Geological, geophysical, and petrochronological constraints on the interplay between magmatism and deformation in magmatic arc systems

By

Sarah F. Trevino

A dissertation submitted in partial fulfillment of
The requirements for the degree of

Doctor of Philosophy
(Geoscience)

at the
UNIVERSITY OF WISCONSIN – MADISON
2022

Date of final oral examination: August 1, 2022

The dissertation is approved by the following members of the Final Oral Committee:

Basil Tikoff, Professor, Department of Geoscience
Laurel Goodwin, Professor, Department of Geoscience
Annie Bauer, Assistant Professor, Department of Geoscience
Hiroki Sone, Assistant Professor, Geological Engineering
John Geissman, Emeritus Professor, University of Texas – Dallas

Table of Contents

Dedication

Dissertation introduction

References

Chapter 1: Multiple, Coeval Silicic Magma Storage Domains Beneath the Laguna Del Maule Volcanic Field Inferred from Gravity Investigations

Abstract
1. Introduction
2. Geologic Setting and Previous Work
- 2.1 Regional setting
- 2.2 Eruption age dating

3. Data
- 3.1 Gravity data
- 3.2 Density estimates from plutonic rocks

4. Gravity Inversion Method
5. Inversion Model Results and Uncertainty
6. Discussion
- 6.1 Implications of plutonic rock equivalents for gravity anomaly interpretation
- 6.2 Thermodynamic models and density anomalies
- 6.3 Effect of hydrothermal activity
- 6.4 Present state of the Barrancas and broader Laguna del Maule magma reservoir

7. Conclusion
8. Figures and Figure Captions
9. References

Chapter 2: Determining the initiation of shear zone deformation using titanite petrochronology

Abstract
1. Introduction
2. Geologic Background
3. Materials and methods
- 3.1. Sample description
- 3.2. Pb isotopic compositions of feldspar
- 3.3. Zircon petrochronology
- 3.4. Titanite petrochronology

3.4.1. Microstructures
3.4.2. Trace element geochemistry
3.4.3. Geochronology

4. Results

4.1. Pb isotopic compositions of feldspar
4.2. Zircon petrochronology
4.3. Titanite petrochronology
4.3.1. Microstructures
4.3.2. Trace element geochemistry
4.3.3. Geochronology

5. Discussion

5.1. In situ versus microsampled isotope dilution geochronology
5.2. Bracketing shear zone initiation: a maximum age from titanite recrystallization
5.3. Bracketing shear zone initiation: a minimum age from titanite neoblastic growth
5.4. Mid-Cretaceous WISZ

6. Conclusions

7. Figures and Figure Captions

8. References

Appendix

Chapter 3: Exploring the emplacement of Cretaceous arc granites and dextral shear zones in northwestern Nevada, USA, using the StraboSpot data system

Abstract

1. Introduction

1.1 Cretaceous Deformation
1.2 Northwestern Nevada plutons
1.3 An Introduction to StraboSpot

2. StraboSpot Log

3. Summary

4. Figures and Figure Captions

5. References

Chapter 4: Two phases of Cretaceous dextral shearing recorded in the plutonic rocks of NW Nevada: A tectonic link between intra-arc shearing in the Sierra Nevada and Idaho batholiths

Abstract

1. Introduction

2. Geologic setting

2.1 The Sierra Nevada batholith

2.1.1 Magmatism
2.1.2 Mid-Cretaceous deformation
2.1.3 Late Cretaceous deformation

2.2 The Idaho batholith and its gneissic western margin

2.2.1 Magmatism
2.2.2 Dextral shearing 100-85 Ma in Idaho

2.3 The Sahwave batholith and intrusions of northwest Nevada

3. Methods

3.1 Fields Methods

3.2 Petrology, chemistry, field fabrics, and microstructures

3.2.1 Sahwave granodiorite
3.2.2 The granodiorite of Bob Spring
3.2.3 The granodiorite of Juniper Pass
3.2.4 The Power Line intrusive complex

3.3 Microstructural characterization of the fabrics from the Sahwave Range intrusive suite and the Power Line intrusive complex

3.3.1 Fabric characterization of the Sahwave Range intrusive suite inferred from microstructures
3.3.2 Fabric characterization of the Power Line intrusive complex inferred from microstructures

3.4 Anisotropy of Magnetic Susceptibility and Magnetic Mineralogy

3.4.1 Background: Anisotropy of Magnetic Susceptibility (AMS)
3.4.2 Background: Magnetic Mineralogy
3.4.3 Sahwave granodiorite
3.4.4 The granodiorite of Bob Spring
3.4.5 The granodiorite of Juniper Pass
3.4.6 The Power Line intrusive complex

4. Discussion

4.1 Emplacement of the Sahwave Range intrusive suite

4.1.1 Synthesis of microstructural and magnetic fabrics
4.1.2 Comparison of the syntectonic Sahwave Range intrusive suite with simultaneous intrusions Sierra Nevada batholith
4.1.3 Tectonic-assisted, pull-apart syntectonic emplacement model for the Sahwave Range intrusive suite

4.2 Deformation of the Power Line intrusive complex

4.2.1 Synthesis of solid-state fabrics in the Power Line intrusive complex
4.2.2 Kinematics of shearing within the Power Line intrusive complex and constraints on emplacement
4.2.3 Comparison with the western Idaho shear zone and a regional ~100 Ma deformation in the magmatic arcs of the western U.S.

5. Conclusions

6. Figures and Figure Captions

7. References

Appendix

Dedication

Science, like life, is collaborative.
For every person that has trusted and supported me as I sought to understand this small aspect of truth.

But most especially,
For Clare

Dissertation Introduction

Deformation and magmatism are two fundamental products of orogenesis. Deformation is expressed as fault systems and shear zones that evolve to accommodate plate motion and since the advent of plate tectonic theory, structural geologists have investigated these physical features to reconstruct a region's spatial deformation history. Similarly, geochemical and petrologic techniques can be used to investigate the temporal and thermodynamic history of magmatic processes during tectonic plate motion. When integrated, these structural and petrological tools can lend insight into Earth's past and present tectonic processes on a range of spatiotemporal scales, from individual shear margins to regional arc deformation.

Convergent plate boundaries, where an oceanic plate subducts below a continental plate, often result in the formation of a magmatic arc on the overriding plate. This arc magmatism is driven by dehydration reactions in the subducting plate and accounts for much of the margin-parallel magmatism (e.g., Gill, 1981). Where there is a component of margin parallel slip, there is often a strike-slip fault within the magmatic arc (e.g., Fitch, 1972). Strike-slip faults appear to play a major role in partitioning slip at obliquely convergent plate boundaries (e.g., Beck, 1983; McCaffrey, 1996). The relation between subduction-related magmatism and strike-slip deformation, however, remains controversial.

Chapter 1 of my dissertation describes gravity investigations to observe patterns of magma emplacement and storage at Laguna Del Maule. Laguna Del Maule is a volcanic field (LdMVF) within a modern magmatic arc, where rhyolitic volcanism is associated with strike-slip faults. Our new density model of the broader LdMVF captured what we interpret as at least two magma bodies at different stages of maturity. A larger, low-density body beneath the lake represents an active melt storage system, whereas the newly discovered Barrancas magma body represents the still warm remains of a melt storage system that last erupted 1-2 ka ago. The

remnant magma melt content is uncertain, but it is likely to be < 30 %; further, it may contain <2.5% volatile phase and is thus in a non-eruptible condition. These geophysical observations paired with the published geochemical data from other researchers indicate that the spatially and petrologically discrete magma bodies have persisted and evolved during at least the last 25 ka, producing rhyolite eruptions. These data suggest that the multiple discrete plutons captured in the present-day geophysical models are the norm, rather than the exception, at the LdMVF. **Chapter 1 was published in the Journal of Geophysical Research in 2021. The author list is: S. Trevino, C. Miller (New Zealand) B. Tikoff (University of Wisconsin – Madison), D. Fournier (Mira Geoscience), and B. Singer (University of Wisconsin – Madison).**

Chapters two, three, and four investigate how magma emplacement is connected to strike-slip faulting/shearing by investigating exhumed examples of magmatic arcs emplaced during oblique convergence. The relative time scales between the two processes is a point of debate, as magmatism is commonly assumed to be more rapid than tectonism (e.g., Paterson and Tobisch, 1992). However, it has been demonstrated that at least some arc batholiths are incrementally assembled over millions of years as melt is progressively and cyclically generated, differentiated, migrated, and emplaced into a dynamic crustal column (e.g., Coleman et al., 2004).

Geochronological and petrological data reveals the temporal and thermodynamic evolution of arc emplacement and are an invaluable record of the tectonic history, but it is also critical to understand the high-temperature deformation within the magmatic arc shear zones systems. These studies use both geochronological and microstructural methods to provide high resolution and precision data poised to reveal new insight on solid state and magmatic fabric development, deformation rates, and strain localization behavior in sub-solidus environments.

Chapter 2 of my dissertation is a collaborative study with Claire Harrigan at Boise State University. Together we used petrochronology to investigate high-temperature crustal strain partitioning and localization on the micro- to macro-scale using the western Idaho shear zone (WISZ), west-central Idaho. The WISZ is a crustal-scale structure that localized arc magmatic process and deformation related to terrane accretion and translation along the North American Cordillera. We used a WISZ orthogneiss to examine how fabric develops on the micro-scale during high temperature deformation. Claire Harrigan conducted geochemical and geochronological data analyses for this chapter, and I conducted all of the microstructural, textural, and petrological fabric characterizations of titanite for in-situ geochemical and geochronological analyses. By integrating the geochronometric, geochemical, and microstructural titanite record using statistical and petrologically relevant visualizations, we document the local preservation of titanite related to magmatic and subsolidus processes. Importantly, this petrochronological workflow resulted in a date for the onset of deformation in the WISZ, confirming tectonic interpretations of WISZ deformation as a separate event from terrane suturing. Chapter 2 is in preparation for submission to the Journal of Earth and Planetary Science Letters 2022. **The author list is: C. Harrigan (Boise State University), S.F. Trevino (University of Wisconsin – Madison), M. Schmitz (Boise State University), and B. Tikoff (University of Wisconsin – Madison).**

Chapters 3 and 4 expand this work to the Cretaceous intrusive suites of Nevada in the central United States Cordillera. Chapter 3 investigates and characterizes the Cretaceous – present day geology of the central Nevada region of interest and represents a first order investigation of any fabrics preserved in middle and Late Cretaceous north central Nevada granodiorites. **Chapter 3 was published in 2021 GSA Section Meeting Guides: Geological**

Society of America Field Guide 61. The author list is: S.F. Trevino, B. Tikoff (University of Wisconsin–Madison), N. Van Buer (California State Polytechnic University, Pomona), S.J. Wyld (MapTect LLC), and H. McLachlan.

Chapter 4 expands on this original dataset to track the spatial-temporal patterns of pluton emplacement and deformation within the Sahwave Range intrusive suite and the Power Line intrusive complex. This chapter compares fabric data from the Sahwave Range intrusive suite and the Power Line intrusive complex with fabric data from middle Cretaceous and Late Cretaceous intrusive suites of the Sierra Nevada batholith and the Idaho batholith. The goal was to test if magma emplacement and associated dextral shearing was simultaneous along the continental margin. We determined that the Sahwave Range intrusive suite and the Power Line intruisve complex record two distinct dextral transpressional deformation events, ~100 Ma and ~88 Ma. These data provide evidence for continuous shearing between the Sierra Crest shear zone in the Sierra Nevada batholith and the western Idaho shear zone in the Idaho batholith. **Chapter 4 is in preparation for submission to the Geological Society of America Bulletin 2022. The author list is: S.F. Trevino (University of Wisconsin – Madison), C. Harrigan (Boise State University), and B. Tikoff (University of Wisconsin – Madison).**

In summary, this dissertation uses structural geologic, geophysical, and petrochronologic tools to investigate the feedbacks between magmatism and deformation and how that they are expressed temporally and spatially in large magmatic arcs.

References:

Beck, M.E., 1983. On the mechanism of tectonic transport in zones of oblique subduction: Tectonophysics, v. 93, no. 1–2, p. 1-11, https://doi.org/10.1016/0040-1951(83)90230-5.

Coleman, D.S., Gray, W., and Glazner, A.F., 2004. Rethinking the emplacement and evolution of zoned plutons: Geochronologic evidence for incremental assembly of the Tuolumne Intrusive Suite, California: Geology, v. 32, no. 5, p. 433–436, https://doi.org/10.1130/G20220.1.

Fitch, T.J., 1972. Plate convergence, transcurrent faults, and internal deformation adjacent to Southeast Asia and the western Pacific: Journal of Geophysical Research v. 77, 4432–4460.

Gill, J.B., 1981. Orogenic Andesites and Plate Tectonics: Minerals and Rocks, v. 16, xiv-390 pp.

McCaffrey, B., 1996. Estimates of modern arc-parallel strain rates in fore arcs: Geology, v. 24, no. 1, p. 27–30. doi: https://doi.org/10.1130/0091-7613(1996)024<0027:EOMAPS>2.3.CO;2

Paterson, S.R., and Tobisch, O.T., 1992. Rates of processes in magmatic arcs: implications for the timing and nature of pluton emplacement and wall rock deformation: Journal of Structural Geology, v. 14, p. 291-300.

Chapter 1: Multiple, Coeval Silicic Magma Storage Domains Beneath the Laguna Del Maule Volcanic Field Inferred from Gravity Investigations

Abstract

The rhyolite-producing Laguna del Maule volcanic field (LdMVF), Chile, has had numerous post-glacial eruptions that produced large explosions and voluminous lava flows. During the Holocene ~60 meters of surface uplift is recorded by paleo-shorelines of the freshwater Laguna del Maule, with an inflation source near the Barrancas volcanic complex. Rhyolites from the Barrancas complex erupted over ~14 ka including some of the youngest (1.4 ± 0.6 ka) lava flows in the field. New gravity data collected on the Barrancas complex reveals a residual gravity low (-6 mGal, "Barrancas anomaly") that is distinct from the pronounced gravity low (-19 mGal; "Lake anomaly") associated with present-day ground uplift to the northwest. Three-dimensional inversion of the Barrancas anomaly indicates the presence of a magma body with a maximum density contrast with the host rock of -250 kg/m^3 centered at a depth of ~ 3 km below surface. Nearby Miocene high-silica granites represent frozen remnants of highly evolved rhyolitic magma. Comparison of the densities measured from samples of these plutons with the geophysical model densities, and integration of thermodynamic modeling of silicic melt evolution, provide constraints on our interpretation. We propose a magma body, containing < 30 % melt phase and low volatile content, exists beneath Barrancas. The Barrancas and Lake gravity lows represent magma in different physical states, associated with past and present-day storage beneath LdMVF. The gravity model mirrors geochemical observations which independently indicate that at least two distinct rhyolites were generated and stored as discrete magma bodies within the broader LdMVF.

1. Introduction

Snapshots of the evolution of shallow silicic plutonic and magmatic systems through to their ultimate expression as explosive and effusive rhyolite eruptions are rare in the geologic record. Recent geochemical and geochronological studies (Glazner et al., 2004; Cooper & Kent, 2014; Barboni et al., 2016; Rubin et al., 2017; Andersen et al., 2017a; 2018; Schaen et al., 2017) of eruptive products and exhumed plutons propose that shallow silicic reservoirs exist as "mush" systems containing discrete batches of eruptible interstitial melt within a larger mostly crystalline framework (Bachmann & Bergantz, 2004; Hildreth, 2004). Over time, these bodies may cool to form plutons or, with the addition of heat and volatiles delivered via basaltic to andesitic intrusions, melting or defrosting of the mush can rapidly produce eruptible pools of crystal-poor rhyolitic melt (Druitt et al., 2012; Cooper & Kent, 2014; Till et al., 2015; Andersen et al., 2018). These petrological and geochemical data and models propose a continuum between the end members of cold plutonic storage systems and systems that are heated and incubated such that they may produce explosive eruptions.

Geophysical imaging can provide insight into the location, geometry, and present state of silicic plutonic and magmatic systems (e.g., Magee et al., 2018). Seismic, magnetotelluric, and gravity surveys (Bachmann & Bergantz, 2008; Bertrand et al., 2012; Represas et al., 2012; del Potro et al., 2013; Comeau et al., 2015; Pritchard & Gregg, 2016; Gaynor et al., 2019; Paulatto et al., 2019) have imaged silicic plutonic and magmatic systems in a variety of tectonic settings, including at the Laguna del Maule Volcanic Field (LdMVF) (Miller et al., 2017a; 2017b; Cordell et al., 2018; Wespestad et al., 2019; Bai et al., 2020; Peterson et al., 2020). These geophysical studies infer the physical state of magma bodies from the distribution of material properties such

as density, conductivity, and P and S-wave velocities. However, crustal-scale geophysical models are non-unique and have an inherent low resolution that homogenize and smear out anomalous rock volumes, making the imaging of individual melt lenses within the broader crystal matrix difficult to resolve.

The LdMVF comprises at least 40 km^3 of post-glacial (younger than 20 ka) rhyolite encircling a 20 x 16 km lake basin and is thus the largest such concentration of rhyolite erupted in the Andes (Hildreth et al., 2010). The LdMVF is an exemplar field area owing to: (1) rapid rates of surface inflation of over 25 cm/year since 2007 (Feigl et al., 2014; Le Mével et al., 2015; 2016) that have re-accelerated recently (Le Mével et al., 2019), and more than 60 meters of surface warping during the Holocene (Singer et al., 2018), that reflect active growth of a large underlying magma reservoir system (Singer et al., 2014); (2) geochronology, petrology, and geochemistry of the LdMVF eruptive products reveal at least two physically discrete, chemically distinct, long-lived rhyoliteproducing domains in the upper crust (Andersen et al., 2017b; 2018; 2019), and melt inclusions indicate an H2O-rich, CO2-charged, magma reservoir system producing rhyolitic liquids from 14 to 4 km depth (Klug et al., 2020); and (3) the late Miocene Risco Bayo-Huemul plutonic complex, exposed only 20 km to the west, spans a compositional range of gabbro to high-silica granite very similar to the LdMVF, is of comparable dimensions to the LdMVF, and is interpreted to be the frozen equivalent of a rhyolitic melt such as that erupted at LdMVF (Schaen et al., 2017; 2018; Garibaldi et al., 2019).

Here we significantly expand the 3D density model of Miller et al. (2017b) to include new gravity data from the Barrancas complex (Sruoga et al., 2015; 2018) in the southern part of the Laguna del Maule volcanic field (LdMVF) as well as extending the data coverage north of Laguna del Maule. The new observations reveal a previously unmapped -6 mGal Bouguer

gravity anomaly below the Barrancas complex ("Barrancas anomaly") that is physically independent of the larger (-19 mGal) negative anomaly associated with current surface inflation at LdMVF ("Lake anomaly") (Le Mével et al., 2016; Miller et al., 2017b). We also report new density measurements from granites comprising the nearby Risco Bayo and Huemul plutons (Schaen et al., 2017) as a novel means of exploring the full density evolution of silicic magmas in this part of the Andes. We interpret these new geophysical data in context of the extensive petrological (Andersen et al., 2017b, 2018, 2019; Cáceres et al., 2018; Klug et al., 2020) and geomorphic (Singer et al., 2018) findings from LdMVF. These new findings provide important new constraints on the structural geology of the LdMVF. The multidisciplinary approach allows us to reduce the non-uniqueness inherent in geophysical models and to better understand the hazards posed by silicic magma systems (Till et al., 2018). Our high-resolution geophysical observations of the broad magmatic system at LdMVF provides the first images of multiple embedded magma bodies in different developmental stages within a large silicic reservoir.

2. Geologic setting and previous work

2.1 Regional setting

The Laguna del Maule volcanic field (LdMVF) (Fig. 1), located on the crest of the Andes (36◦ S) within the Southern Volcanic Zone, comprises the region's largest concentration of crystal poor rhyolite and has hosted at least 50 post-glacial rhyolitic eruptions comprising >40 km3 since 25 ka (Andersen et al., 2017b; Hildreth et al., 2010). The LdMVF lies 20-30 km south east of the 7.2 to 6.2 Ma Risco Bayo and Huemul plutonic complexes (Schaen et al., 2017, 2018; Garibaldi et al., 2018). The Huemul pluton is a high silica granite that has a compositional gap from 70 to 75 wt % SiO2 and strong depletion of Ba and Eu. This composition suggests these

granites are frozen remnants of rhyolitic melt extracted from a mush that solidified at 4-6 km depth analogous to those that likely are growing beneath the present day LdMVF (Schaen et al. 2017; Le Mevel et al., 2016; Andersen et al., 2017b; 2018; Wespestad et al., 2019). As such, they offer a unique perspective on how the LdMVF magmatic system has evolved that is complimentary to that derived solely from the eruptive products of the LdMVF.

2.2 Eruption age dating

Plagioclase and zircon petrochronologic data reveal that the two distinct eruptive episodes at 23-19 ka and 8–2 ka also reflect rhyolite generation in compositionally and physically distinct domains beneath the LdMVF (Andersen et al., 2018; 2019). The four youngest vents and eruptive complexes are in the south and eastern part of the LdMVF, suggesting that this region once contained a significant volume of eruptible melt. The youngest eruptions, dated by $^{40}Ar/^{39}Ar$ methods or inferred from geomorphology, are the Cari Launa (<3.3 ±0.6 ka), the rhyolite of Colada Divisoria (2.1 ± 0.7 ka), Colada Las Nieblas (~1.8 ka), and the Barrancas complex (14.5-1.9 ka) (Andersen et al., 2017b, 2019). The Colada Las Nieblas flow lacks pumice cover and displays an uneroded morphology and is considered of comparable age to the younger portions of the Barrancas complex and eastern Barrancas complex lavas (around 2.1 to 1.9 ka). The $^{40}Ar/^{39}Ar$ chronology is supported by ^{36}Cl surface exposure dates of 2.5 ± 0.7 ka and 1.4 ± 0.6 ka for the youngest Barrancas flows (Singer et al., 2018). In addition, the younger flow from the Cari Launa vent yields an imprecise ^{36}Cl surface exposure date of 0.8 ± 0.6 ka, indicating a late Holocene age (Singer et al., 2018).

Within the LdMVF, the Barrancas volcanic complex is the site of multiple domes and contains some of the youngest (1.4 ± 0.6 ka) erupted lavas of the LdMVF, forming high-standing

relief 600 m above the surrounding topography. Up to eight overlapping lava flows from three main eastwest aligned vents cover an area of approximately 50 km2 (Fig. 1) (Sruoga et al., 2015). Between 14.5 and 8.4 ka, rhyolite erupted only from the Barrancas complex. Eruptive material from Barrancas forms a large portion (~ 6 km3) of the post Last Glacial Maximum eruptive history of LdMVF. The western Barrancas dome complex was erupted between 14.5 and 11.4 ka and partially collapsed to produce large block and ash flows that traveled ~13 km filling valleys with deposits ~60 - 120 m thick, decreasing to 10 m in distal areas (Fig. 1; Sruoga et al., 2015, 2018). The younger eastern domes (5.6 to 1.4 ka) produced 8 obsidian flows and several tephra falls and pyroclastic flows.

2.3 Geochemistry and petrology

The Barrancas rhyolites are distinguished from the older 22-19 ka rhyolites erupted in the north from a magma source coincident with the Lake gravity anomaly by their elevated Sm and Y abundances, low TiO_2 in magnetite, and high Ce in plagioclase crystals (Andersen et al., 2017b; 2018; 2019; Klug et al., 2020). The Barrancas rhyolites show no evidence for having mixed with other spatially discrete rhyolites, strongly suggesting compartmentalization of eruptible domains within the wider magma reservoir (Andersen et al., 2018; 2019). Petrologic evidence from melt inclusion composition and entrapment pressures (Klug et al., 2020) suggests that crystal poor rhyolite melt beneath the LdMVF accumulated in the shallow crust (50 – 350 MPa, ~ 2 to 8 km depth) after ascending out of rhyodacitic mush at ~8 – 14 km. The crystal poor rhyolite accumulation pressures derived from melt inclusions are at the lower end of those derived from analysis of amphibole crystals in the rhyodacites (Andersen et al., 2017b; Cáceres et al., 2018) that suggest crystallization pressures of 190 – 400 MPa. The voluminous pyroclastic

flow on the south flank of the Barrancas complex (geologic unit rcb-py in Fig. 1) has some of the lowest melt inclusion derived pressures (50 – 150 MPa) from LdMVF, consistent with its origin via collapse of shallowly emplaced, and thoroughly degassed, endogenous and exogenous domes (Sruoga, et al., 2018; Klug et al., 2020). The Barrancas complex shows the only evidence of shallow hydrothermal alteration in the LdMVF. Advanced argillic alteration has affected the domes of the Barrancas complex, as well as block and ash flow deposits, suggesting that circulation of > 300 °C hydrothermal fluids may have contributed to dome collapse (Sruoga et al., 2018).

2.4 Geophysical models

The identification of rapid surface inflation within the LdMVF, at rates greater than 25 cm/yr since 2007, has prompted several geophysical studies that have imaged a trans-crustal magma system and a small upper crustal fault system beneath the eponymous lake using topographic analysis (Singer et al. 2018), teleseismic tomography (Bai et al., 2020), surface wave tomography (Wespestad et al., 2019), seismic reflection and magnetics (Peterson et al., 2020), magnetotellurics (Cordell et al., 2018, 2019, 2020), geodesy (Feigl et al., 2014; Le Mével et al., 2015, 2016; Zhan et al., 2019), and gravity (Miller et al., 2017b). The summit of the Barrancas complex is < 5 km south of a paleoshoreline that formed when the lake was dammed by the Espejos rhyolite coulée at 19.0 ka. This shoreline is inferred to have been a horizontal surface when the lake catastrophically drained at 9.4 ka. (Singer et al., 2018). The present day paleoshore is uplifted 62 m in the southern part of the lake basin relative to the northern part. This pattern is consistent with surface warping produced by an inflating magma reservoir located below the

southeastern portion of the lake basin, beneath the northern flank of the Barrancas complex (Singer et al., 2018).

Gravity inversion, teleseismic tomography, and surface wave tomography inferred overlapping low-density and low-velocity anomalies (referred to here as the "Lake" anomaly) interpreted as crystal-rich, dacitic to rhyodacitic magma reservoirs with volumes between 100 and 500 km3 at depths between 2 and 12 km, containing domains including 20-70 km3 of volatile-rich rhyolite melt that is spatially coincident with the deformation source.

Teleseismic and surface wave tomography suggests that melt contents in the Lake magma body range from 5 to 14 %, however these are likely to be minimum due to inherent vertical smearing and wide grid cell widths (3 to 4 km) (Wespestad et al., 2019; Bai et al., 2020). Teleseismic tomography (Bai et al., 2020) resolves a low-Vp anomaly in the southeast of the LdMVF beneath the Barrancas complex. This feature is elongated northeast-southwest, dips to the southwest, and is resolvable to about 25 km depth. The velocity perturbation of this feature is -100 to -200 m/s compared to -400 m/s for the main Lake anomaly. However, its location on the edge of the seismic array leads to greater uncertainty as to the geometry of this feature. Group velocity maps from surface wave tomography show a negative group velocity anomaly across the 0.29 to 0.39 Hz range in the southeast corner of the basin towards the Barrancas complex suggesting a melt phase may be present (Wespestad et al., 2019).

Using 3D MT inversion, Cordell et al. (2018, 2020) imaged the deeper portion of the magma system that extends north of the lake and likely represents a deep crustal zone of magma storage, mixing, and assimilation (Andersen et al., 2017b). The Barrancas complex is on the edge of the MT array, although there is a suggestion of a shallow (~1-2 km) conductive body (~10

Ωm) beneath Barrancas, above a 5-10 Ωm body at 4-5 km depth (D. Cordell, pers. comm., 2020).

These geophysical observations strongly point to a trans-crustal magma system extending to within 2 km of the surface, which is consistent with the petrologic and geochemical observations. Imaging of the Lake anomaly and identification and modeling of the source of paleoshoreline warping prompted further geophysical investigation of the Barrancas complex, which was on the edge of previous geophysical imaging campaigns.

3. Data

3.1 Gravity Data

We collected 105 additional terrestrial gravity measurements over two summer campaigns in December 2017 and March 2018, significantly expanding the work of Miller et al. (2017b) to the southeast and north of the original dataset (Fig. 1). The new data coverage adds approximately 500 km^2 of previously un-surveyed area to the original data set. Measurements were taken every 500–1000 m in a series of 3–4 km long, radial and valley parallel profiles within a 15 km radius of the main Barrancas complex. Of the 105 measurements, 19 were collected in two E-W transects in valleys north of the lake and four far-field gravity measurements were collected south and east into Argentina to improve the regional gravity field definition.

Gravity stations are precisely located using post processed differential GPS with 15-minute occupations times, resulting in height errors better than 15 cm (< 0.05 mGal). GPS data are corrected using continuous GPS stations that are part of the Observatorio Volcanológico de Los Andes del Sur (OVDAS) network, with maximum baselines of 10 km.

Corrections for Earth tide and drift are applied to the daily raw gravity data using gTOOLS (Battaglia et al., 2012), to produce gravity values relative to the local base which is tied to two nearby absolute gravity stations (Miller et al., 2017b). We follow the same Bouguer reduction procedures as outlined in Miller et al (2017b) which follows Hinze et al. (2005), using the WGS84 ellipsoid as the reference datum.

Reference densities, representing the bulk density of the topography, of 2375 and 2361 kg/m3 are derived from our updated dataset using topographic correlation methods (Nettleton, 1939; Parasnis, 1966) while previous analysis of a commercial data set (unpublished data from Energy Development Corporation) from the nearby Maroposa geothermal prospect yields values of 2350 and 2452 kg/m^3 (Miller et al. 2017b). Conversion of the OVDAS 1-D P-wave velocity model to density (Brocher, 2005), yields densities of 2429 to 2448 kg/m^3 in the top 7 km (Miller et al. 2017b). The average of all the density estimations is 2413 kg/m^3 that we approximate as 2400 kg/m^3 for use as the reference density. Continental scale gravity models (Tašárová, 2007; Folguera et al., 2012) of the south-central Andes, around latitude 36°S, obtain an upper crustal density of 2450 kg/ m^3, so our local scale density values are similar to larger continental-scale values.

The new dataset was merged with the published (Miller et al., 2017b) gravity data to produce an expanded Bouguer anomaly map of the LdMVF (Fig. 2). The new Bouguer anomaly map identifies a gravity low on the southeast region of the LdMVF, spatially coincident with the Barrancas complex and distinct from the gravity low beneath the lake (Fig. 2A). A second-order polynomial (Uieda, 2018) (Fig. 2B) best approximates the measured regional field gradient, oriented approximately parallel to the South American/Nazca tectonic plate boundary. We removed the second-order polynomial from the Bouguer anomaly data to produce a residual

gravity anomaly dataset suitable for inversion. Experiments with removing first- and third-order polynomials to approximate the regional field produce similar residual anomalies to the 2nd order.

We prefer the 2nd order polynomial since this is the lowest order surface that approximates the regional anomaly.

Our data spacing and survey coverage is suitable for mapping density changes of larger features (cubic km scale) in the top approximately 1 to 10 km of the crust which is the target zone for shallow rhyolitic magma reservoirs at Laguna del Maule volcanic field (Andersen 2017b). However, our closest data spacing (approximately 500 m) means we are less able to accurately map small (< ~500 m horizontal extent) very shallow (top few hundred) density changes, which will appear smeared out, lower-than-true amplitude features in our anomaly maps.

The new residual gravity map (Fig. 2C) shows the previously identified Lake anomaly (Miller et al., 2017b), as well as two distinct low gravity anomalies in the east of the field spatially associated with the Barrancas complex and Cari Launa vents. These two anomalies are separated by a region of neutral gravity change constrained by several measurement points. The -6 mGal anomaly is located on the southeastern flank of the Barrancas complex. The Barrancas anomaly consists of a small lobe located beneath the summit of the Barrancas eruption vents and the rest of the anomaly extends 5 km to the SE. The southern part of the Barrancas anomaly is broadly coincident with the location of a ~ 60 - 120 m thick valley filling block and ash flow deposit (Sruoga et al., 2015) that was emplaced south of the main volcanic domes and vents at 11.5 ka. It is possible that part of the gravity anomaly reflects this pyroclastic material, a hypothesis that we investigate further in the discussion. The -3 mGal anomaly is associated with

the Cari Launa and Divisoria vents, however it is not particularly well resolved as station coverage is sparser in this area.

3.2 Density estimates from plutonic rocks

Density measurements of plutonic rocks that represent an end member state of silica magma systems, are important to interpret the densities derived from gravity models of silicic systems. Plutonic rocks are often inferred to represent the "frozen", sub-solidus cumulates of magma reservoirs (Glazner et al., 2004; Bachmann et al., 2007). The 7.2-6.2 Ma, high silica granites in the Huemul pluton, located 30 km NW of the LdMVF, are interpreted to be the frozen remnants of a once eruptible, crystal-poor, rhyolitic melt (Schaen et al., 2017; 2018). This melt is inferred to be extracted out of deeper residual mush at pressures of 100 to 200 MPa or about 3.7 to 7.2 km depth, but not necessarily erupted. This interpretation is consistent with numerical models that consider crustal rheology, exsolved volatile contents, and magma recharge which imply a narrow depth range, 6 to 8 km (200 ± 50 MPa), where silicic magma reservoirs can incubate large bodies of potentially eruptible rhyolite (Huber et al., 2019).

Petrologic and structural studies of the Risco Bayo and Huemul plutons (Schaen et al., 2017; 2018; Garibaldi et al., 2018) have revealed miarolitic cavities and rock fabrics indicative of volatile and melt transport through an underlying crystal mush, including accumulation of vapor bubbles at the roof of the reservoir. These observed features are similar to those proposed to exist within the present-day magma body represented by the Lake anomaly (Miller et al., 2017b; Andersen et al., 2018). As such, the geochemical composition and observed textures of these exhumed granites make them a crystallized, end-member representative of a present-day silicic melt storage system.

Direct density measurements of the high silica granites can be compared to geophysically derived densities of the nearby silicic melt storage system at LdMVF to provide constraints for interpreting the gravity anomalies. Drill cores taken for Anisotropy of Magnetic Susceptibility measurements (Garibaldi et al. 2018) with a volume of 3.2cm^3 were used for density measurements. Density measurements were conducted using a glass pycnometer on two to five specimens per intrusive unit of the Risco Bayo – Huemul plutonic complex (Table 1). Two of the five Huemul high silica granite drill core samples contain visible bubbles; these samples were taken near the miarolitic cavity zone in the middle of the intrusion (Schaen et al. 2018). All other samples did not show observable bubbles or cavities and were drilled in main interior pluton regions. A map of sample location is shown in Supporting Information.

We measured the densities of a suite of samples spanning the observed compositional range fromgabbro to high silica granite at the Risco Bayo and Huemul plutonic complex. The density range varies by 260 kg/m^3, reflecting the density increase from high silica granite to silica poor gabbro. Samples from the Huemul high silica granite - which is interpreted to be the solidified analog of a crystal poor, high silica melt extracted from the granite cumulate framework - have an average density of 2439 ± 15 kg/m^3. Density measurements of high silica granite samples that contain miarolitic cavities varied by < 10 kg/ m^3 from cavity free samples. As only a fraction of the entire pluton was sampled (Supporting Figure S2), it is possible there are regions with greater cavity abundance that could more significantly lower the density of the high silica granite. The samples representing the cumulate residual phase have an average density of 2502 ± 46 kg/m^3. The Bouguer correction density of 2400 kg/ m^3 means that if plutonic rocks, such as those found at the Risco Bayo and Huemul plutons, are present within the survey area, they should create a small positive gravity anomaly.

4. Gravity Inversion Method

We inverted the gravity data from 306 of the 342 stations (excluding the more distant stations away from the LdMVF) for 3D density distribution using the SimPEG inversion framework (Cockett et al., 2015), implementing a mixed ℓ_p norm inversion scheme. Further details on the inversion method are given in Miller et al. 2017b, Fournier and Oldenburg (2019), and Miller et al. (2020) and are briefly summarized below.

The 3D model mesh (rectangular box in Fig. 1) has a 250 x 250 m horizontal cell size with vertical cells that expand from 100 m thick in the top 500 m to 420 m at the base of the mesh at -7000 m a.s.l.. Three layers of padding cells in the horizontal dimensions outside the data coverage are included to reduce edge effects.

The inverse problem (Tikhonov & Arsenin, 1977) is formulated as an optimization problem of the form:

$$\phi(\mathbf{m}) = \phi_d(\mathbf{m}) + \beta\phi_m(\mathbf{m})$$

where β is the tradeoff or Tikhonov parameter. A small β produces a model that tightly fits the data but may include excessive structure resulting in a large model norm, $\phi_m(\mathbf{m})$. Conversely if β is large, the optimization results in a larger data misfit, $\phi_d(\mathbf{m})$ and a model with minimal structure. The optimization is nonlinear, so a gradient-based, Gauss-Newton method is used and continues until the algorithm converges to a minimum and the misfit tolerance is achieved.

The data misfit, $\phi_d(m)$, is a metric which measures the difference between observed and predicted data and is defined as:

$$\phi d(m) = \frac{1}{2}||\boldsymbol{W}_d(F[m] - \boldsymbol{d_{obs}})||\frac{2}{2}$$

where $\boldsymbol{d}_{obs}$ is the observed data, F[m] is the forward model, and $\boldsymbol{W}_d$ is a diagonal matrix with elements equal to $\mathbf{W}_{dii} = 1/\varepsilon$ where ε_{ii} is the standard deviation of the ith data point. We set ε to 0.1 mGal.

Regularizations can be tuned to produce smooth or sparse models depending on the prior knowledge of the interpreter using the ℓ_p norm where $0 \leq p \leq 2$. We follow the procedure of Fournier and Oldenburg (2019) where sparsity assumptions are introduced though a Scaled Iteratively Re-weighted Least Squares (S-IRLS) method. This regularization function is flexible and allows us to explore a range of possible solutions by varying the p values. The inversion starts with a smooth model (ℓ_2 norm) that is used as a starting point to impose the sparse ℓ_p constraint in a two-step process. Our regularization norm consists of four terms, representing the amplitude (density) and the three directional gradients. Instead of choosing a single regularization we implement many, using all combinations of ℓ_p. The 3 gradient terms remain equal while the amplitude term varies to create 9 possible models with norms [0,0,0,0], [0,1,1,1], [0,2,2,2], [1,0,0,0], [1,1,1,1], [1,2,2,2], [2,0,0,0], [2,1,1,1], [2,2,2,2]. For example, the regularization [0111] places a 0 norm on the density value and 1 norms on the three directional density gradients (e.g., Fournier and Oldenburg, 2019). We then calculate the median model from the complete suite of models (e.g. Miller et al., 2020). From the model ensemble we also calculate the probability of a density value occurring in a model cell, providing a method of assessing uncertainty of the model (Miller et al. 2020). Figure 3 illustrates the effect of the different inversion norms on the model. Note that all the models fit the data within the errors.

5. Inversion Model Results and Uncertainty

Depth slices at 1600 and 1100 m a.s.l. (Fig. 4A, B) display a patchwork of high- and lowdensity regions reflecting near surface variations in lithologies (lavas vs. pyroclastic material)

(Fig. 1). One of these shallow low-density regions is at the eastern end of Laguna Fea (Fig. 5) and represents an accumulation of pyroclastic material that dams the lake.

Below 0 m a.s.l the negative density contrast anomalies coalesce into 3 regions: 1) The Lake anomaly; 2) The Barrancas anomaly and; 3) The Cari Launa and Divisora anomalies, although the model is poorly constrained in later area by sparser data coverage. Figure 5 shows the three-dimensional representation of these bodies as isosurfaces of <1900 kg/ m^3 (red) and 2200 to 2300 kg/m^3 (grey). Positive density anomalies are interpreted as either crystalized plutonic rocks of similar composition to that found at the Risco Bayo – Huemul plutons (see section 3.2) or Pleistocene lavas and metavolcanic wall rocks dividing magmatic domains.

The Lake anomaly - identified by Miller et al. (2017b) and Wespestad et al. (2019) - is interpreted to represent a magma reservoir containing a 20-30 km^3 interstitial melt volume localized within a larger (>100 km^3) crystal rich mush. In this paper we focus on the interpretation of the newly identified Barrancas and Cari Launa anomalies.

Our model reveals a 64 k km^3 low-density body beneath the vent labelled rng on Figure 1, on the south-east part of the Barrancas complex that extends from near surface to 4 km below sea level. Model resolution degrades below 4 km b.s.l. (Fig.4 X-X' and Z-Z' sections). This body has a maximum density contrast of around -220 kg/m^3 or an estimated absolute density of 2180 kg/m^3.

North of the Barrancas complex, our model reveals a shallower anomaly in the subsurface beneath the Cari Launa and Divisoria vents that extends to around 2 km below sea level (Fig 4; W-W' and Z-Z' sections). This 51 km^3 low-density body is resolved with a density contrast of - 100 to -150 kg/m^3 or 2250 to 2300 kg/m^3 absolute density. These anomalies are poorly constrained because of a lack of measurements from that region.

6. Discussion

Andersen et al. (2017b; 2018; 2019) and Klug et al. (2020) propose a conceptual model of the LdMVF magma system based on geochronology, whole rock and trace geochemical distinctions, mineral barometry/thermometry, mineral textures, diffusion chronometry, and melt inclusion volatile contents. In this model, the sub-LdMVF magma reservoir exists as an extensive, largely crystalline mush (85% melt). These studies identify two geochemically distinct rhyolite compositions that did not interact with one another; one that erupted during early postglacial time (22-19 ka), and another, that includes the Barrancas complex, that erupted during the Holocene. These two distinct rhyolite magmas may reflect differences in crystal phase proportions in the mush and thermal heterogeneity of the reservoir with hot zones reflecting regions of variable basaltic intrusion (Andersen et al., 2019). We use this conceptual petrological model as a framework to interpret and integrate our geophysical model findings (Fig. 8). To constrain our interpretations of the new gravity anomaly data and inversion model, we used measured densities of rock samples from the exhumed Risco Bayo – Huemul plutonic complex inferred to represent a frozen analog of a silicic melt storage system.

We further constrain our interpretations with thermodynamic modeling of dacite and rhyolite melt data to estimate the present-day melt, volatile, and crystal phases beneath the Barrancas complex that last erupted 2 ka. We investigate if valley filling pyroclastic deposits can account for the Barrancas anomaly and briefly discuss the effect of hydrothermal activity on our interpretation. Finally, we discuss the physical interpretation of the density models and implications for magma storage within the LdMVF, in comparison to previously published findings on the LdMVF magma system (Miller et al., 2017b; Andersen et al., 2018; Cordell et

al., 2018; Wespestad et al., 2019; Bai et al., 2020; Klug et al., 2020). Our expanded gravity coverage and updated inversion model reveals with high confidence that the low-density bodies at Barrancas and Cari Launa are discrete from the Lake gravity anomaly. The Lake anomaly has been previously interpreted as caused by a shallow melt rich lens within a broader mush (Miller et al., 2017b; Wespestad et al., 2019; Bai et al., 2020). We focus on the Barrancas anomaly as the Cari Launa anomaly is poorly resolved by our dataset. The Barrancas gravity low (Fig. 2) partially coincides with a 60 – 120 m thick block and ash flow deposit from the 11.5 ka eruption, which filled the valley south of the edifice (Sruoga et al., 2015; 2018) (Fig. 1). We calculated the gravity effect of the pyroclastic deposit using a simple two-dimensional model of a 120 m deep, 2 km wide V-shaped valley, filled with material having a density contrast of -400 kg/m^3 which results in a -1.6 mGal anomaly. The absolute density of the valley fill (approximately 2000 kg/ m^3) is the same as used to model the shallow infill from the 1.8 ka Taupo caldera eruption (Davy & Caldwell, 1998) and is the same as the average bulk density of 106 samples measured from the 2.36 ka Mt Meagre block and ash flow (Michol et al., 2008). To recreate the magnitude of the observed anomaly requires filling a valley 600 m deep or for the density of the material to be around 900 kg/m^3; both parameters are unrealistic. Further, the valley filling model does not reflect the longer wavelengths of the observed anomaly. Therefore, the entire -6 mGal Barrancas anomaly cannot be explained by the presence of thick low-density pyroclastic material. A small (> -1 to < approximately 40 % melt) and finally solidify. Therefore, combined with the recent (<2 ka) and long-lived eruptive history of the Barrancas complex, we interpret this large low-density body, and the low velocity bodies from seismic tomography, to be remnants of magmatic storage systems that fed the most recent eruptions between 1 and 2 ka. In the following sections we discuss the likely state of the magma beneath the Barrancas complex.

6.1 Implications of plutonic rock equivalents for gravity anomaly interpretation

The 7.2 to 6.0 Ma Risco Bayo - Huemul plutonic complex was emplaced at 3.7 to 7.2 km depth and spans a similar range in rock composition as the LdMVF, including crystal-rich rhyodacites, and the crystal-poor rhyolites that produced the entire Barrancas complex (Schaen et al., 2017; 2018) (Supporting Information Figure S2). Thus, the Risco Bayo and Huemul plutonic rocks provide analogues for portions of the magma reservoir underlying the LdMVF. Relative to metamorphosed basement rocks, granites commonly yield negative Bouguer anomalies (e.g., Cordell et al., 1985; Gaynor et al., 2019) if the Bouguer correction (i.e., surrounding crustal) density is approximately 2600-2700 kg/m^3. Metamorphosed basement rocks in the Chilean Central Andes near Laguna del Maule are typically at 2-3 km depth (Godoy et al., 1999) and have densities of approximately 2700 kg/m^3. Overlying these basement rocks are sedimentary and volcanic rock packages of density between 2300 and 2600 kg/m3 , consistent with the correction density obtained for the Laguna del Maule and Barrancas area of 2400 kg/m3 . If frozen plutonic bodies of similar composition and density to the Risco Bayo and Huemul plutons were present at shallow depth (2-3 km) beneath Barrancas, they would create a small positive Bouguer anomaly, relative to our correction density of 2400 kg/m^3. If the density of the crust increases with depth, then these granites would produce neutral or negative anomalies. The lowest density rocks of the exhumed Risco Bayo and Huemul plutonic complex that represent "frozen melt" have an average density of 2439±15 kg/m^3 (section 2.1) similar to the Bouguer correction density. This density is higher than the density values returned by the inversion model for the body beneath the Barrancas complex (2180 kg/m3) and suggests that the Barrancas body cannot be a cold, solidified pluton. Rather, it may contain some percent melt and perhaps an

exsolved volatile phase, as also inferred from the slowing of seismic waves through this region (Wespestad et al., 2019, Bai et al., 2020), and the high H2O contents of the rhyolitic melts (Klug et al., 2020). We therefore propose that the low-density body beneath the Barrancas complex is a combination of low-density surface lavas and pyroclastic material, and a deeper remnant magma storage system that contains some proportion of residual melt left over from the last eruption at 1- 2 ka. We investigate this hypothesis in the following section using MELTS thermodynamic modelling tool.

6.2 Thermodynamic models and density anomalies

Our gravity model of the Barrancas complex - constrained by independent density measurements, cooling models, and seismic tomography evidence - suggests that a melt phase is present in the storage system at 3-4 km depth. To further investigate the presence of melt or fluid phases within the modeled low-density body beneath the Barrancas complex, we use Rhyolite MELTS for Excel (Gualda & Ghiorso, 2015) to construct phase diagrams that relate magma density (melt, crystal, and fluid phases) to temperature and pressure. The magma body is assumed to be a crystal-rich mush of andesitic to dacitic bulk composition, which contains volumetrically minor interstitial rhyodacitic to rhyolitic melt. Within the relatively cool upper crust, a mush is a more likely state for long-term storage and incubation of silicic magma than a large, long-lived body of rhyolitic melt (Cooper & Kent, 2014; Andersen et al., 2018). Andersen et al. (2018) show that for a dacite magma at 200 MPa (ca. 8 km depth), using the external volatile flux model, a density of 2200-2300 kg/m^3 can be produced with less than 10% exsolved fluid volume fraction at a temperature of around 750°C. This estimate is consistent with the high H2O content of melt inclusions and volatile saturation of most rhyolite erupted within the

LdMVF (Klug et al., 2020). However, unlike these rhyolites, the Barrancas domes show evidence of hydrothermal alteration and collapse to produce a large pyroclastic flow, in which melt inclusions contain little CO_2 and low H_2O contents (Klug et al., 2020). These features are interpreted by Klug et al. (2020) to reflect much shallower emplacement (50-100 MPa; less than 4 km depth) and extensive degassing of rhyolitic magma prior to eruption.

To model the densities of residual magmas that equilibrate at low pressures and lose volatiles, simulating conditions thought to occur beneath the Barrancas complex, we use the rhyodacite of Laguna sin Puerto containing 69% silica, 2.5% H2O and no CO2 (Hildreth et al., 2010; Klug et al., 2020) as a starting composition. We normalize the composition to retain the H2O phase within the melt and then cool the magma to its solidus at a constant pressure of 110 MPa. The modeled values allow us to track density changes as the magma cools and crystallizes (Fig. 7A). The liquidus is ~960 °C (not shown on the plot) and as cooling occurs the magma density rises to a peak of 2420 kg/m^3 at 762 °C. At these conditions, quartz begins to crystallize and at 760 °C the H2O begins to exsolve, lowering the density. Between 744 and 742 °C, with 40 % melt remaining, the exsolved fluid phase doubles in mass from 0.64 to 1.31 wt. % at which point the density drops further. The density range of Barrancas gravity models span from 2200 - 2350 kg/m3 matching conditions that include the solidus and up to ~30 % melt plus exsolved H2O (Fig. 7A). In contrast, Figure 7B shows the total system densities of a LdMVF rhyolite containing 5 wt. % H2O at 90 and 110 MPa, with the expected pressure at the approximate depth range (2.5-3.5 km) of the Lake body imaged by the gravity inversion and teleseismic tomography. Five weight % H_2O is likely a minimum, as melt inclusions contain up to 8 wt.% H2O (Klug et al., 2020) that would further lower the density. The latter MELTS model replicates the densities recovered by the gravity inversion for the Lake anomaly (1800 to 1900 kg/m^3). To

reproduce the model densities required for Lake anomaly, the magma system must contain an exsolved fluid phase, although the proportion of melt is less certain. A lower bound of 5-14 % melt is obtained by coarser gridded seismic tomography models (Wespestad et al., 2019; Bai et al., 2020), while the closer spaced gravity data suggests small pockets with ~50 % melt is possible in parts of the system depending on the pressure.

6.3 Effect of hydrothermal activity

Miller et al. (2017a) proposed that gravity changes associated with the Lake anomaly in the top 2 km are caused by the influx of hydrothermal fluids into the Troncoso fault zone (e.g., Garibaldi et al., 2019). As our modelled low-density bodies extend close to the surface, we consider whether the top portion of these bodies may in fact represent a rock hosted hydrothermal system as suggested by Andersen et al. (2018) to explain in part the low densities observed. In a liquid-dominated hydrothermal system within a porous rock, pore space initially filled by air is replaced by brine resulting in a small gravity increase. Hence, the presence of an active liquid dominated hydrothermal system would slightly increase the observed gravity relative to the surrounding area.

The Barrancas domes show widespread evidence for advanced argillic alteration caused by circulation of > 300° C fluids during the Holocene (Sruoga et al., 2015). Hydrothermal alteration can often lower the density of rock (e.g., Miller & Williams-Jones, 2016), although the magnitude of the density decrease from alteration is typically 1-2 mGal and not enough to explain the gravity lows observed. Magneto-telluric models of the Barrancas area (Cordell et al., 2018) show a small, shallow (1-2 km) conductive anomaly (10 Ωm) near the summit of Barrancas that may be consistent with conductive clay minerals formed by hydrothermal

alteration. However, the gravity anomaly extends far south from the altered domes. As such, hydrothermal alteration is likely to play only a minor part in the observed gravity anomaly.

6.4 Present state of the Barrancas and broader Laguna del Maule magma reservoir

Our interpretation of the density model (Fig. 8) of the LdMVF is partially constrained by equivalent plutonic rocks from the nearby Risco Bayo – Huemul pluton, employed as a "frozen" analog. These rocks have densities > 2400 kg/m^3, which would result in positive gravity anomalies if they existed in our residual anomaly map. We note that positive gravity anomalies exist in the older, northern part of the volcanic field suggesting they may represent the cold, frozen portions that may have become plutons. A ridge of positive gravity anomaly divides the Lake anomaly from the Barrancas anomaly. The inversion model indicates that this ridge is a shallow feature extending towards the surface and may represent a buried sequence of Pliocene andesitic lavas comprising the Cola de Zorro Formation within the uppermost 2 km (Hildreth et al., 2010), as opposed to a frozen pluton. Our new density model of the broader LdMVF has captured what we interpret as at least two magma bodies at different stages of maturity. The key geophysical and geochemical features of these magma bodies are summarized in Figure 8. The large low-density body beneath the Lake represents an active melt storage system containing a substantial free volatile phase (5-8 %), driven by deeper injection of basalt, supplying heat and volatiles and propelling the present-day uplift (Le Mével et al., 2016; Zhan et al., 2019; Klug et al., 2020). The depth of the reservoir is consistent with melt inclusion derived pressure estimates (Klug et al., 2020) and suggests that gravity is imaging the top portion of a trans-crustal magmatic system that extends to >25 km depth (Andersen et al., 2017b; Cordell et al., 2018; Bai et al., 2020). The geochemical data indicate spatially and petrologically discrete magma bodies

have persisted during at least the last 25 ka, producing rhyolite eruptions. This data suggest that the multiple discrete bodies captured in the present-day geophysical models are the norm, rather than the exception, at the LdMVF.

Given the spatial coincidence of the teleseismic low-Vp anomaly and the Lake gravity anomaly, joint inversion of the two, either via structural gradients or by analytic relationships that link Vp and density, is likely to yield greater insight into the physical properties of this magma body, with ramifications for its present state and future trajectory. The newly discovered Barrancas magma body represents the still warm remains of a magma body within the reservoir that last erupted 1-2 ka. The melt content is uncertain, but it is likely to be < 30 %; further, it may contain - although on the edge of the seismic array - imply some degree of melt remains. Melt contents inferred by teleseismic tomography suggests the body beneath Barrancas volcanic field, by comparison to the Lake low VP anomaly, has < 14 % melt. The deeper portion of the low-density body under the Barrancas complex may represent the cooling, volatile-depleted, cumulate framework of a dacitic magma body, which was once the “warm storage” source of rhyolite melt (Anderson et al., 2017). One possible end point in the development of the Barrancas magma is the formation of a high silica pluton, similar to the exhumed Huemul pluton to the west of the LdMVF. However, future injection of basalt beneath the Barrancas complex, as is postulated to be occurring beneath the Lake anomaly, could reactivate this magma body and continue to drive the paleoshoreline upwarping observed since 9.4 ka. This scenario is supported by petrochronologic evidence from the Barrancas complex (Andersen et al., 2019), which suggests that the erupted rhyolites were sourced from a long lived “warm” part of the magma reservoir. This magma reservoir experienced external additions of heat and volatiles that remobilized interstitial melt shortly prior to successive eruptions.

7. Conclusions

The new residual gravity anomaly map of the LdMVF shows a -6 mGal gravity low extending from the summit of the Barrancas complex to 5 km southeast of the summit at depth. The inversion model of the Barrancas anomaly shows a 64 km3 body dipping to the south east at a depth of 2-4 km (sea level to 2 km below sea level) with a modelled density of ~2200 to 2350 kg/m3 . Our interpretation - guided by measured densities from the nearby Risco Bayo - Huemul plutonic rocks, thermodynamic modeling, and petrologic observations - is that the Barrancas low density body represents a volatile poor magma with a interpretation is consistent with the presence of magma that degassed at depths less than 3-4 km and produced domes comprising the Barrancas volcanic complex. We propose this magma represents the cooling remnant of a once active melt pocket that last erupted 1-2 ka. Moreover, the growth of this magma reservoir in the shallow crust is likely responsible for the >60 m uplift of the paleoshoreline in the southern part of the LDM basin since 9.4 ka.

Our new geophysical observations of the location, geometry, and state of the magmatic anomalies in the SE basin provide geophysical evidence that integrates with petrological models of melt storage. The Barrancas gravity anomaly represents a rhyodacite melt stored in the shallow crust in warm zones that can be melted, differentiated, extracted, and erupted. Thermodynamic modelling shows that these bodies may transition from moribund to melt rich over a relatively small temperature range. A temperature increase could result from basalt intrusion, proposed as a mechanism for the present-day inflation above the Lake anomaly (e.g., Le Mével et al., 2016).

The new gravity model of the LdMVF corroborates extensive petrologic findings and provides geophysical evidence for at least two separate magma bodies within the same volcanic field. The emerging picture is one in which a broader magma reservoir can coevally host multiple melt-bearing domains in differing physical states. This finding has important implications for future hazard monitoring of the LdMVF, in both Chile and Argentina, as the Barrancas complex straddles this border.

8. Figures and Captions

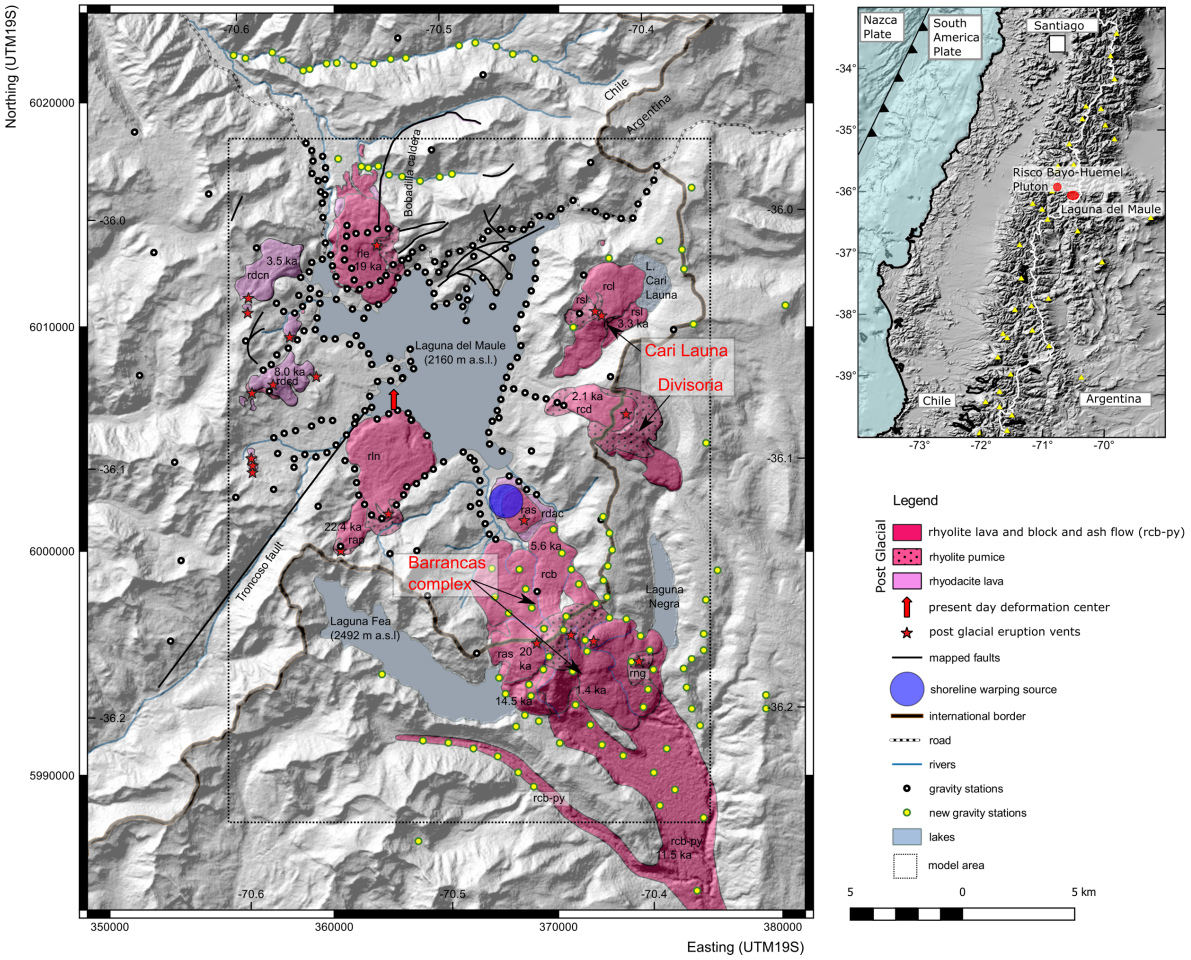

Figure 1. Geological map of the Laguna del Maule volcanic field showing post glacial silicic lavas and pyroclastic deposits. White dots are the gravity data from Miller et al. (2017b), yellow dots are new data from this study. Modified from Miller et al. (2017b) and Andersen et al. (2017b) to show the expanded gravity coverage and Barrancas pyroclastic flow.

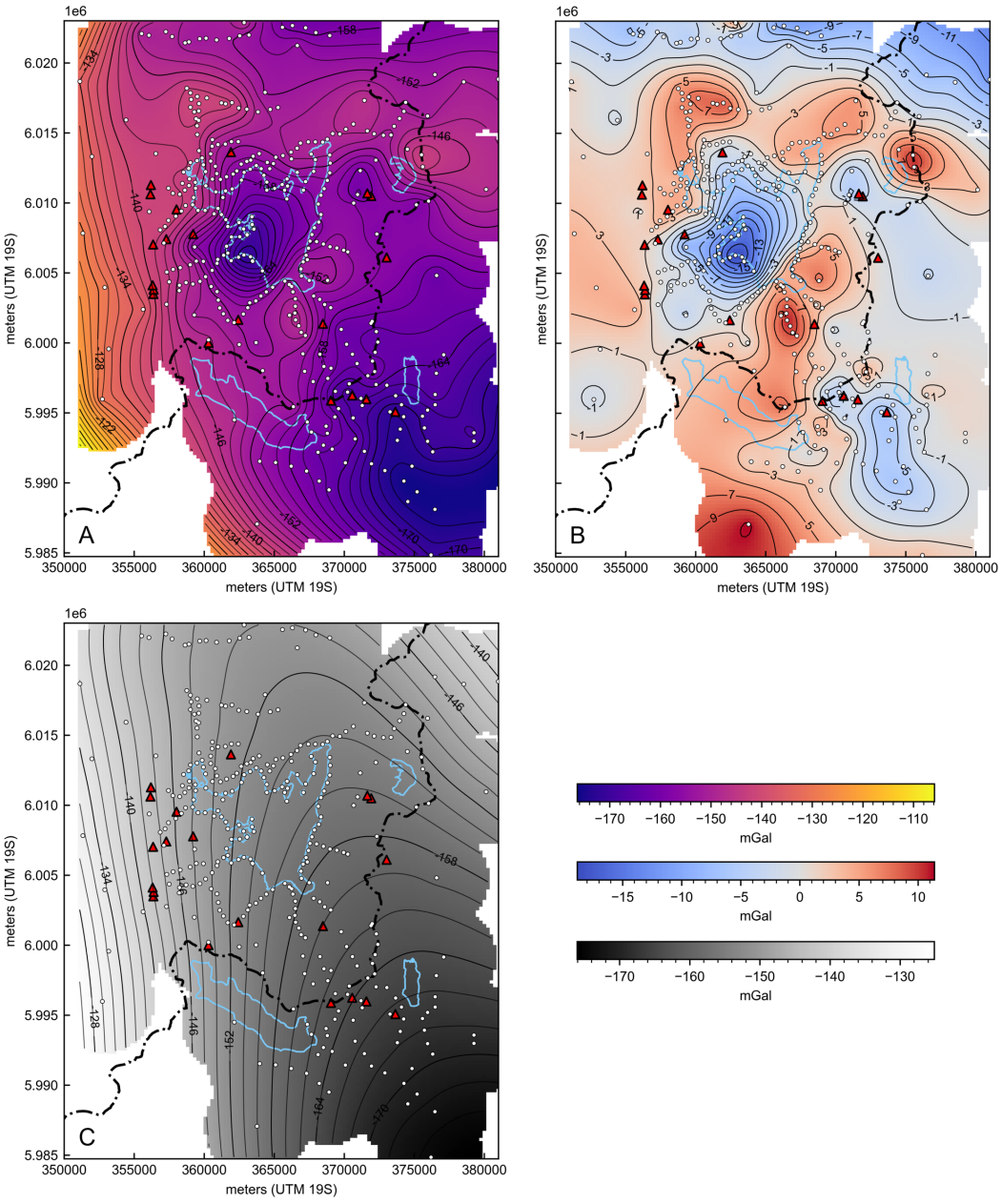

Figure 2. Gravity data collected at the Laguna del Maule volcanic field. A) Expanded coverage Bouguer anomaly map, B) residual gravity anomaly, C) Second order regional field. Red triangles are post-glacial eruption vents. The dot-dashed line is the Chile – Argentina border and the lakes are outlined in light blue. White dots are gravity station locations. Modified from Miller et al. (2017b) to include additional data from Barrancas and north of Laguna del Maule as well as showing the 2nd order regional field.

Table 1: *Density Measurements*

Geologic Unit	**Sample No.**	**Avg. density (kg/m3)**	**St. dev. (kg/m3)**	**SiO2 content (Schaen 2018)**
Huemul High Silica Granite	5	2,439	15	75-77
Huemul Granite	5	2,502	46	68-70
Risco Bayo Granodiorite	5	2,544	7	62-66
Huemul Qtz. Monzonite	5	2,546	21	62-63
Risco Bayo Microdiorite	5	2,642	18	55
Risco Bayo Gabbro	2	2,699	NA	51

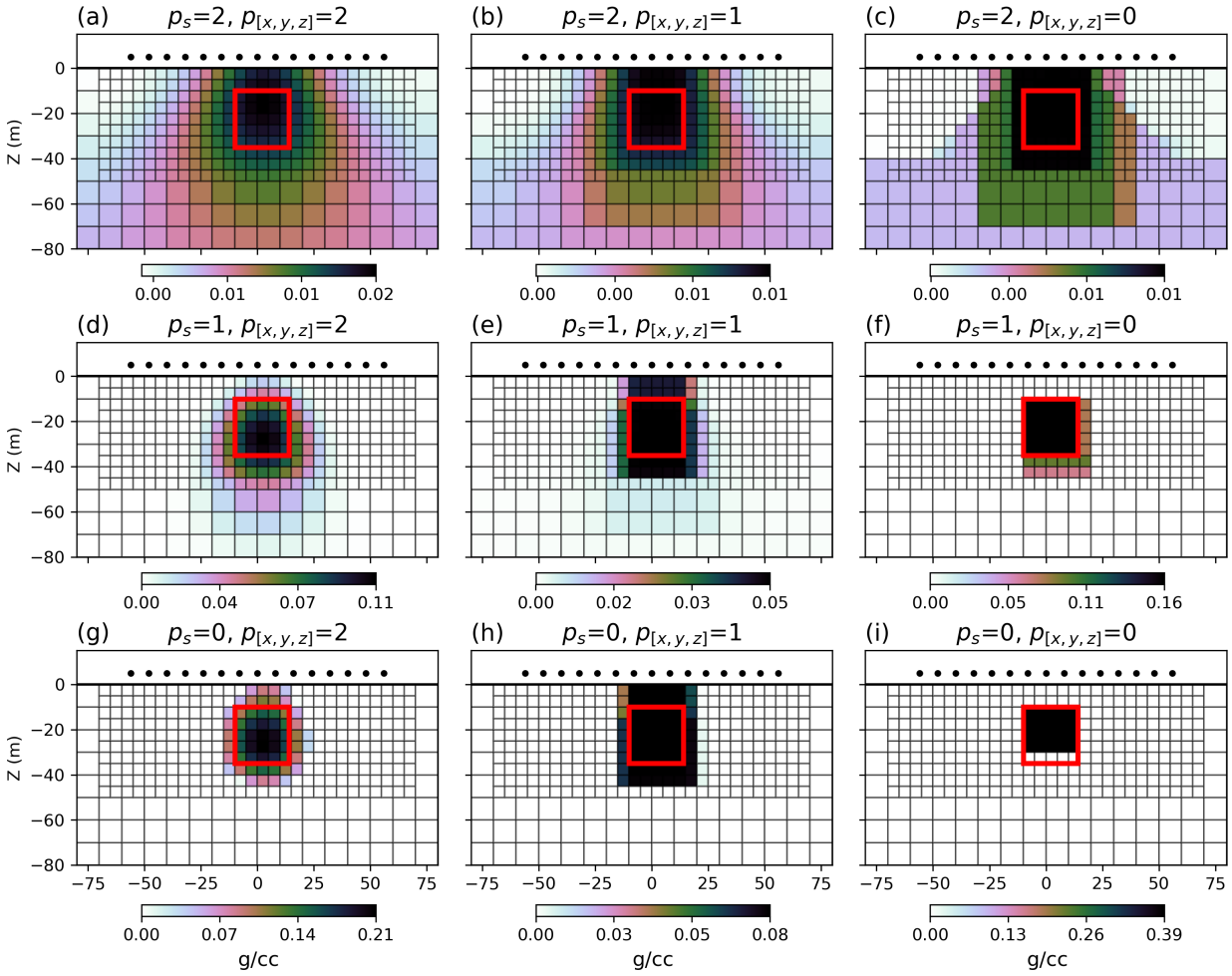

Figure 3. The effect of different model norms on the final model from a synthetic dataset. The input model outline is shown by the red square and has a density contrast of 0.4 g/cc. The top row (a-c) show norms with a smooth amplitude constraint i.e. [2,2,2,2], [2,1,1,1], [2,0,0,0]. The middle row (d-f) shows models with an intermediate amplitude constraint, i.e. [1,2,2,2], [1,1,1,1], [1,0,0,0] and the bottom row (g-i) shows models with a compact amplitude constraint, i.e. [0,2,2,2], [0,1,1,1], [0,0,0,0].

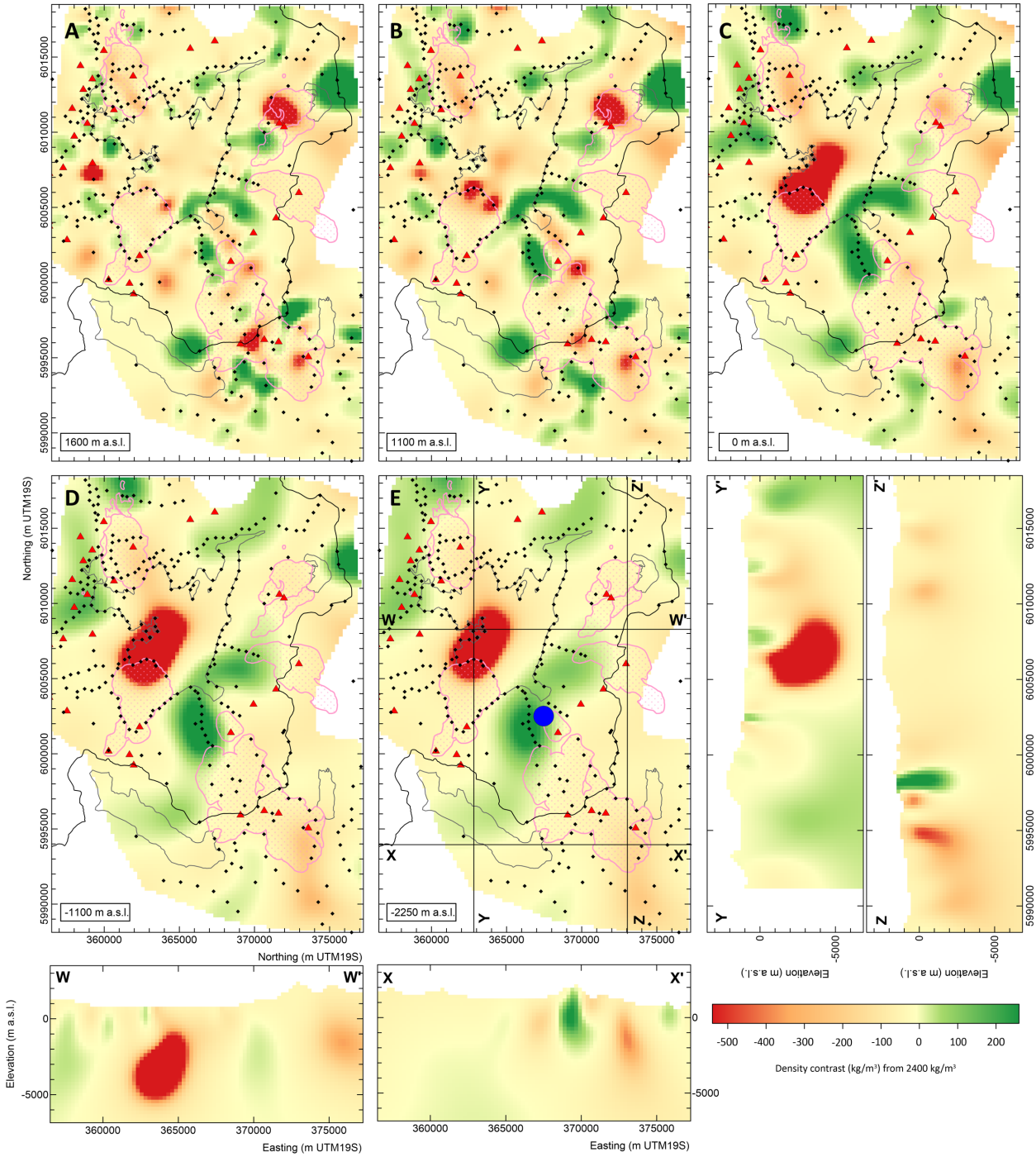

Figure 4. Depth slices and cross sections from the median inverse model. The blue dot is the inferred source of shoreline warping from Singer et al. (2018). Modified from Miller et al. (2017b) to include the expanded survey and model area, additional cross-sectional slices and the location of the shoreline warping source from Singer et al. (2018).

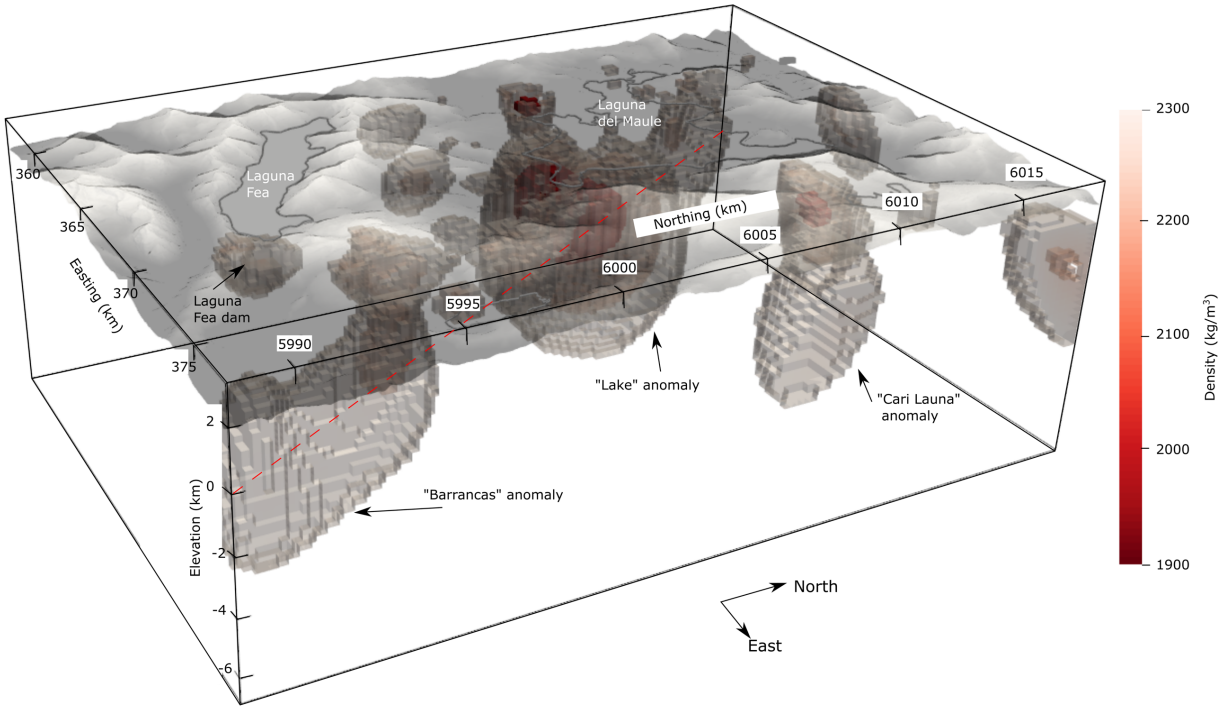

Figure 5. Three-dimensional representation of the inverse model showing isosurfaces of <1900 kg/m3 material (red) and 2200-2300 kg/m3 (grey) material. Dashed red line shows the cross-section view in Figure 8. The Lake low density body is labelled along with the Barrancas and Cari Launa bodies. Other smaller bodies have limited depth extent and likely represent shallow variations in the thicknesses of pyroclastic deposits. The most important of these is the shallow body at the eastern end of Laguna Fea that dams the outlet and poses a flooding hazard should it fail. View is from the south east looking to the north west.

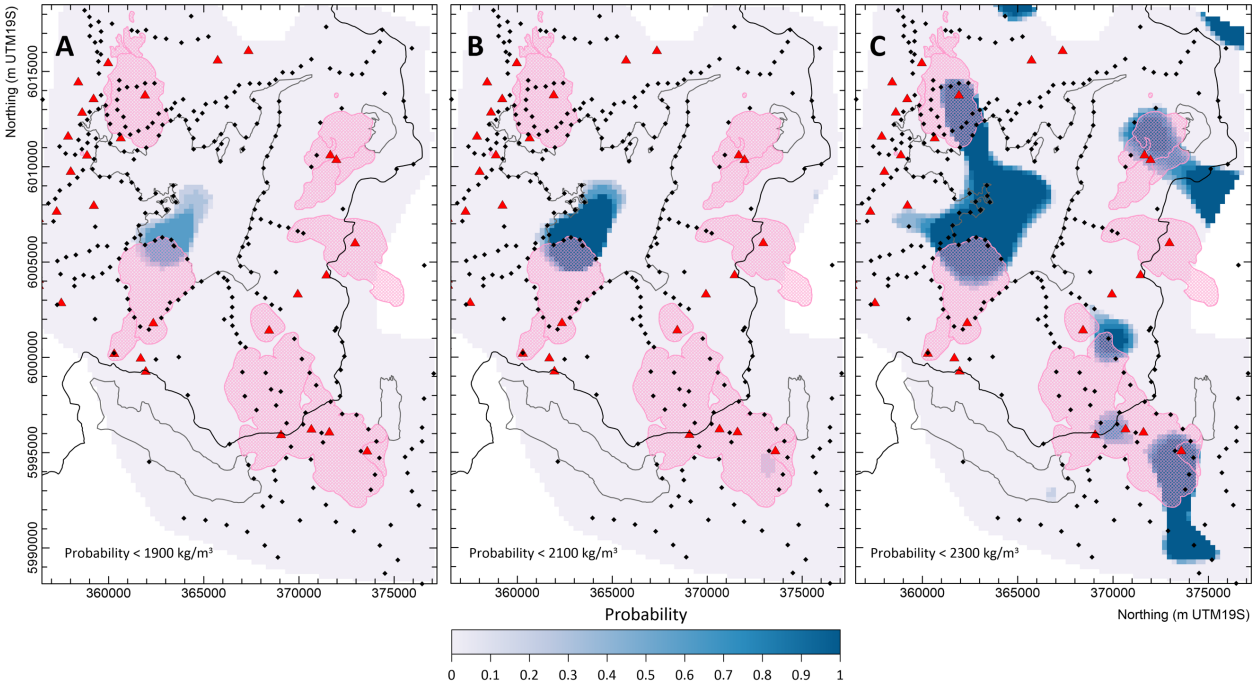

Figure 6. Probability of a density value occurring in the model, A) < 1900 kg/m3, B) <2100 kg/m3 and C) <2300 kg/m3. Depth slice is at 0 m a.s.l. (approximately 2.5 km depth).

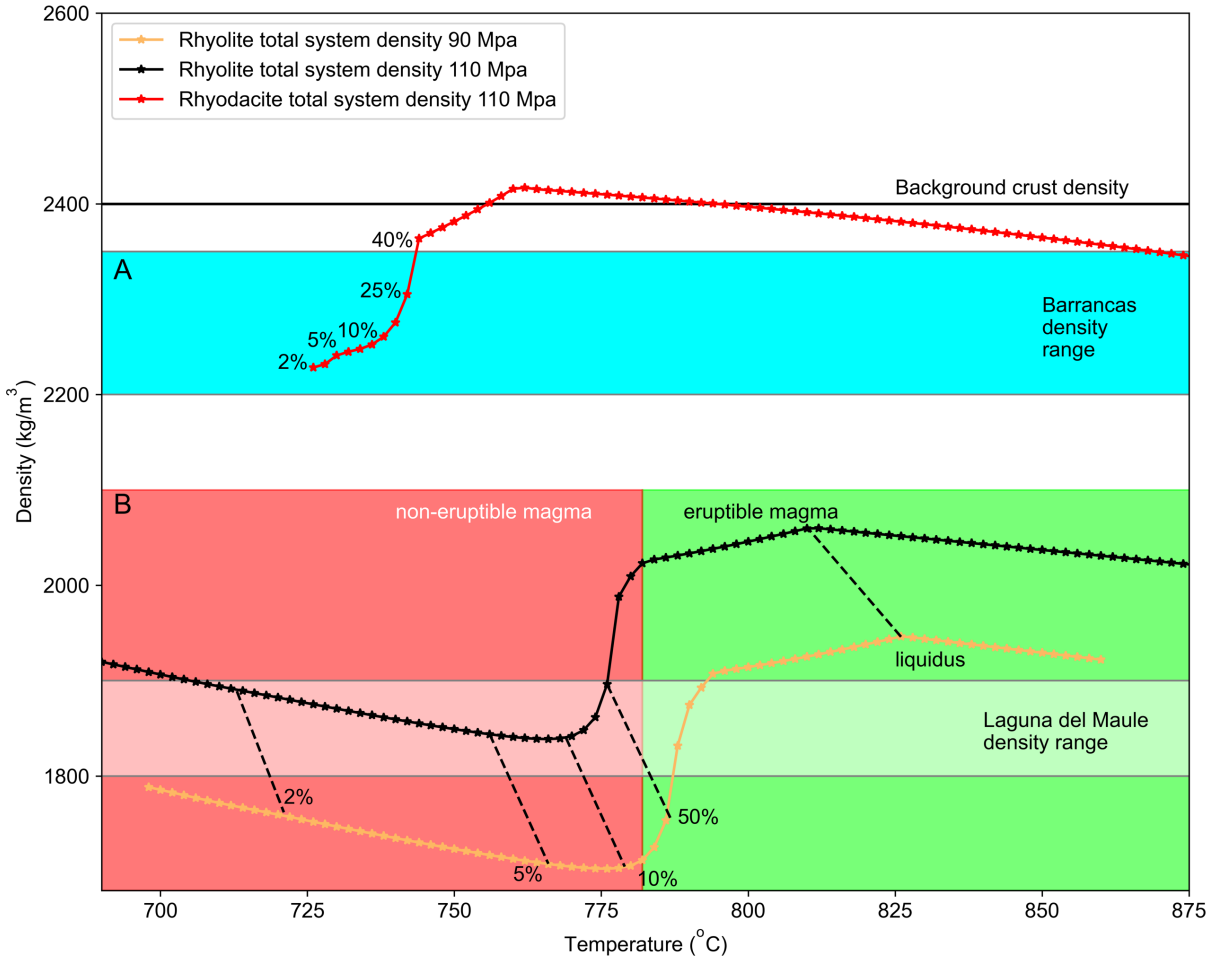

Figure 7. Plots of density as a function of temperature estimated by rhyolite MELTS simulations. In both plots the annotated percentages indicate melt percent. A) Total system densities (crystal, melt, volatile) of rhyodacite magma containing 2.5% H2O (red). The range of densities from the gravity inversion model at Barrancas are shaded light blue. B) Total system densities of rhyolite magma at 90 and 110 MPa (approx. 2.5 to 4.5 km depth) with melt proportions (dashed lines). The range of densities from the inversion model of the Lake anomaly are shaded grey. Eruptible versus non-eruptible magma is shaded red and green, corresponding to the temperature for which approximately 50 melt percent is present.

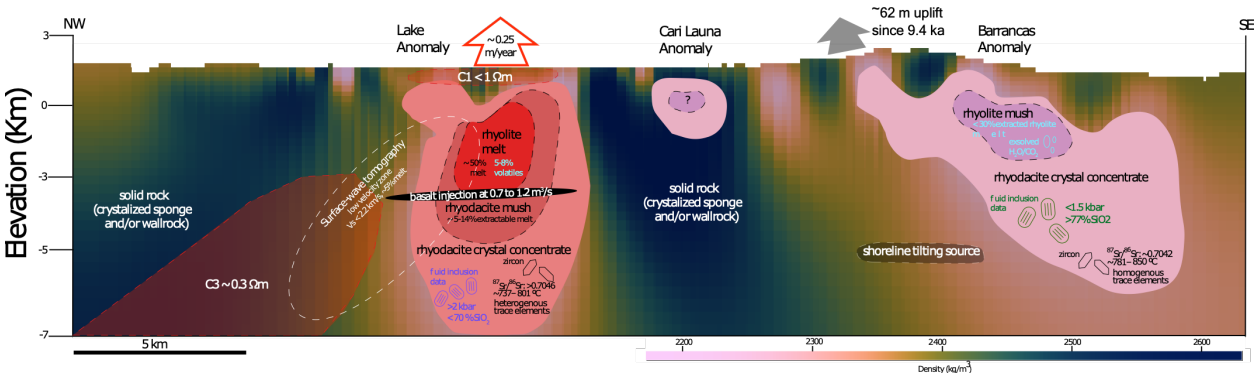

Figure 8: Compilation of geological and geophysical data from Laguna del Maule Volcanic Field onto a cross section from the median inverse density model (Refer Fig. 5 for section line). Anomalies are schematically annotated to describe the physical states (crystal/liquid/volatile) present in the system. The Lake anomaly is denoted by the dark pink to red magma body and is compositionally distinct from the pale pink to pale purple magmas that illustrate the Cari Launa and Barrancas anomalies (Andersen et al., 2017b; 2018; 2019). Holocene rhyolites erupted from Cari Launa and Barrancas yield higher temperatures, different geochemical trends and volatile contents than older LdMVF magmas (Andersen et al., 2017b; 2018; 2019). Melt inclusion entrapment pressures, and H2O and CO2 contents imply discrete magma batches associated with Early Post Glacial and Holocene eruptions (Klug et al., 2020). The low velocity anomaly from surface-wave tomography (Wespestad et al., 2019) is represented by the white dashed ellipse. Red dashed regions represent electrical resistivity anomalies (Cordell et al., 2018). The inclined elongate black ellipse under the Lake anomaly, shows the position of the inflating sill driving current surface inflation denoted by the red surface uplift arrow (Feigl et al., 2013; Le Mevel et al., 2015). The grey ellipse denotes the approximate location of the modeled source of the shoreline tilting (Singer et al., 2018).

9. References

Andersen, N. L., Jicha, B. R., Singer, B. S., & Hildreth, W. (2017a). Incremental heating of Bishop Tuff sanidine reveals preeruptive radiogenic Ar and rapid remobilization from cold storage. Proceedings of the National Academy of Sciences, 201709581. https://doi.org/10.1073/pnas.1709581114

Andersen, N. L., Singer, B. S., Jicha, B. R., Beard, B. L., Johnson, C. M., & Licciardi, J. M. (2017b). Pleistocene to Holocene Growth of a Large Upper Crustal Rhyolitic Magma Reservoir beneath the Active Laguna del Maule Volcanic Field, Central Chile. Journal of Petrology, 58(1), 85–114. https://doi.org/10.1093/petrology/egx006

Andersen, N. L., Singer, B. S., Costa, F., Fournelle, J., Herrin, J. S., & Fabbro, G. N. (2018). Petrochronologic perspective on rhyolite volcano unrest at Laguna del. Earth and Planetary Science Letters, 493, 57–70. https://doi.org/10.1016/j.epsl.2018.03.043

Andersen, N. L., Singer, B. S., & Coble, M. A. (2019). Repeated Rhyolite Eruption From Heterogeneous Hot Zones Embedded Within a Cool, Shallow Magma Reservoir. Journal of Geophysical Research: Solid Earth, 124(3), 2582–2600. https://doi.org/10.1029/2018JB016418

Bachmann, O., Miller, C. F., & de Silva, S. L. (2007). The volcanic-plutonic connection as a stage for understanding crustal magmatism. Journal of Volcanology and Geothermal Research, 167(1–4), 1–23. https://doi.org/10.1016/j.jvolgeores.2007.08.002

Bachmann, Olivier, & Bergantz, G. (2008). The magma reservoirs that feed supereruptions. Elements, 4(1), 17–21. https://doi.org/10.2113/GSELEMENTS.4.1.17

Bai, T., Thurber, C., Lanza, F., Singer, B. S., Bennington, N., Keranen, K., & Cardona, C. (2020). Teleseismic tomography of the Laguna del Maule Volcanic Field in Chile. Journal of Geophysical Research: Solid Earth. https://doi.org/10.1029/2020JB019449

Barboni, M., Boehnke, P., Schmitt, A. K., Mark Harrison, T., Shane, P., Bouvier, A. S., & Baumgartner, L. (2016). Warm storage for arc magmas. Proceedings of the National Academy of Sciences of the United States of America, 113(49), 13959–13964. https://doi.org/10.1073/pnas.1616129113

Battaglia, M., Poland, M. P., & Kauahikaua, J. (2012). GTools: An interactive computer program to process gravity data for high resolution applications. In AGU Fall Meeting (pp. GP43B1143).

Bertrand, E. A., Caldwell, T. G., Hill, G. J., Wallin, E. L., Bennie, S. L., Cozens, N., et al. (2012). Magnetotelluric imaging of upper-crustal convection plumes beneath the Taupo Volcanic Zone, New Zealand. Geophysical Research Letters, 39(2), 1–6. https://doi.org/10.1029/2011GL050177

Blundy, J. D., & Annen, C. J. (2016). Crustal Magmatic Systems from the Perspective of Heat Transfer. Elements, 12(2), 115–120. https://doi.org/10.2113/gselements.12.2.115 Brocher, T. M. (2005). Empirical Relations between Elastic Wavespeeds and Density in the Earth's Crust. Bulletin of the Seismological Society of America, 95(6), 2081–2092. https://doi.org/10.1785/0120050077

Cáceres, F., Castruccio, Á., & Parada, M. A. (2018). Morphology, Effusion Rates, and Petrology of Postglacial Lavas of Laguna del Maule Volcanic Field, Chilean Andes, and Implications for Their Plumbing System. Geochemistry, Geophysics, Geosystems, 19(12), 4925–4944.

Cockett, R., Kang, S., Heagy, L. J., Pidlisecky, A., & Oldenburg, D. W. (2015). SimPEG: An open source framework for simulation and gradient based parameter estimation in geophysical applications. Computers and Geosciences, 85, 142–154. https://doi.org/10.1016/j.cageo.2015.09.015

Comeau, M. J., Unsworth, M. J., Ticona, F., & Sunagua, M. (2015). Magnetotelluric images of magma distribution beneath Volcán Uturuncu, Bolivia: Implications for magma dynamics. Geology, 43(3), 243–246. https://doi.org/10.1130/G36258.1

Cooper, K. M., & Kent, A. J. R. (2014). Rapid remobilization of magmatic crystals kept in cold storage. Nature, 506(7489), 480–483. https://doi.org/10.1038/nature12991

Cordell, D., Unsworth, M. J., & Díaz, D. (2018). Imaging the Laguna del Maule Volcanic Field, central Chile using magnetotellurics: Evidence for crustal melt regions laterally-offset from surface vents and lava flows. Earth and Planetary Science Letters, 488, 168–180. https://doi.org/10.1016/j.epsl.2018.01.007

Cordell, D., Unsworth, M. J., Diaz, D., Reyes-Wagner, V., Currie, C. A., Hicks, S. P.(2019) Fluid and melt pathways in the central Chilean subduction zone near the 2010 Maule earthquake (35–36°S) as inferred from magnetotelluric data. Geochemistry, Geophysics, Geosystems 20(4), 1818-1835.

Cordell, D., Unsworth, M. J., Lee, B., Diaz, D., Bennington, N. (2020) Integrating magnetotelluric and seismic images of silicic magma systems: A case study from the Laguna del Maule Volcanic Field, central Chile. Journal of Geophysical Research: Solid Earth.

Cordell, L., Long, C. L., & Jones, D. W. (1985). Geophysical expression of the batholith beneath Questa Caldera, New Mexico. Journal of Geophysical Research, 90(4), 11263. https://doi.org/10.1029/JB090iB13p11263

Davy, B. W., & Caldwell, T. G. (1998). Gravity, magnetic and seismic surveys of the caldera complex, Lake Taupo, North Island, New Zealand. Journal of Volcanology and Geothermal Research, 81, 69–89. https://doi.org/10.1016/S0377-0273(97)00074-7

Druitt, T. H., Costa, F., Deloule, E., Dungan, M., & Scaillet, B. (2012). Decadal to monthly timescales of magma transfer and reservoir growth at a caldera volcano. Nature, 482(7383), 77–80. https://doi.org/10.1038/nature10706

Feigl, K. L., Le Mevel, H., Tabrez Ali, S., Cordova, L., Andersen, N. L., DeMets, C., & Singer, B. S. (2014). Rapid uplift in Laguna del Maule volcanic field of the Andean Southern Volcanic zone (Chile) 2007-2012. Geophysical Journal International, 196(2), 885–901. https://doi.org/10.1093/gji/ggt438

Folguera, A., Alasonati Tašárová, Z., Götze, H.-J., Rojas Vera, E., Giménez, M., & Ramos, V. a. (2012). Retroarc extension in the last 6 Ma in the South-Central Andes (36°S–40°S) evaluated through a 3-D gravity modelling. Journal of South American Earth Sciences, 40, 23–37. https://doi.org/10.1016/j.jsames.2012.08.003

Garibaldi, N., Tikoff, B., Schaen, A. J., & Singer, B. S. (2018). Interpreting Granitic Fabrics in Terms of Rhyolitic Melt Segregation, Accumulation, and Escape Via Tectonic Filter Pressing in the Huemul Pluton, Chile. Journal of Geophysical Research: Solid Earth. https://doi.org/10.1029/2018JB016282

Garibaldi, N., Tikoff, B., Peterson, D., Davis, J.R., and Keranen, K. (2019). Statistical separation of tectonic and inflation-driven components of deformation on silicic reservoirs, Laguna del Maule volcanic field, Chile. Journal of Volcanology and Geothermal Research, 389, doi: 10.1016/j.jvolgeores.2019.106744.

Gaynor, S. P., Coleman, D. S., Rosera, J. M., & Tappa, M. J. (2019). Geochronology of a Bouguer Gravity Low. Journal of Geophysical Research: Solid Earth, 124(3), 2457–2468. https://doi.org/10.1029/2018JB015923

Glazner, A. F., Bartley, J. M., Coleman, D. S., Gray, W., & Taylor, R. Z. (2004). Are plutons assembled over millions of years by amalgamation from small magma chambers? GSA Today, 14(4), 4. https://doi.org/10.1130/1052-5173(2004)0142.0.CO;2

Godoy, E., Yañez, G., & Vera, E. (1999). Inversion of an Oligocene volcano-tectonic basin and uplifting of its superimposed Miocene magmatic arc in the Chilean Central Andes: First seismic and gravity evidences. Tectonophysics, 306(2), 217–236. https://doi.org/10.1016/S0040-1951(99)00046-3

Gualda, G. A. R., & Ghiorso, M. S. (2015). MELTS_Excel: A Microsoft Excel-based MELTS interface for research and teaching of magma properties and evolution. Geochemistry,Geophysics,Geosystems, 16, 315–324. https://doi.org/10.1002/2014GC005545.Received

Hildreth, W., Godoy, E., Fierstein, J., & Singer, B. S. (2010). Laguna del Maule volcanic field: Eruptive history of a Quaternary basalt to rhyolite distributed volcanic field on the Andean range crest in central Chile. Servicio Nacional de Geologia y Mineria, Bolletin, 63, 145.

Hinze, W. J., Aiken, C., Brozena, J., Coakley, B., Dater, D., Flanagan, G., et al. (2005). New standards for reducing gravity data: The North American gravity database. GEOPHYSICS, 70(4), J25–J32. https://doi.org/10.1190/1.1988183

Huber, C., Townsend, M., Degruyter, W., & Bachmann, O. (2019). Optimal depth of subvolcanic magma chamber growth controlled by volatiles and crust rheology. Nature Geoscience. https://doi.org/10.1038/s41561-019-0415-6

Klug, J. D., Singer, B. S., Kita, N. T., & Spicuzza, M. J. (2020). Storage and evolution of Laguna del Maule rhyolites: insight from volatile and trace element contents in melt inclusions. Journal of Geophysical Research: Solid Earth. https://doi.org/10.1029/2020JB019475

Le Mével, H., Feigl, K. L., Cordova, L., Demets, C., & Lundgren, P. (2015). Evolution of unrest at Laguna del Maule volcanic field (Chile) from InSAR and GPS measurements , 2003 to 2014. Geophysical Research Letters, 1–24. https://doi.org/10.1109/36.662741.Pitz

Le Mével, H., Gregg, P. M., & Feigl, K. L. (2016). Magma injection into a long-lived reservoir to explain geodetically measured uplift: Application to the 2007-2014 unrest episode at Laguna del Maule volcanic field, Chile. Journal of Geophysical Research: Solid Earth, 121(8), 6092–6108. https://doi.org/10.1002/2016JB013066

Le Mével, H., Feigl, K. L., Cordova, L., Bekaert, D.P., & Singer, B.S. (2019) Re-acellerating deformation at Laguna del Maule volcanic field, Southern Andes. American Geophysical Union Fall Meeting Abstracts, 2019AGUFM.G33C0701L

Magee, C., Stevenson, C. T. E., Ebmeier, S. K., Keir, D., Hammond, J. O. S., Gottsmann, J. H., et al. (2018). Magma Plumbing Systems: A Geophysical Perspective. Journal of Petrology, (July), 1–35. https://doi.org/10.1093/petrology/egy064

Mastrandrea, M. D., Mach, K. J., Plattner, G. K., Edenhofer, O., Stocker, T. F., Field, C. B., et al. (2011). The IPCC AR5 guidance note on consistent treatment of uncertainties: A common approach across the working groups. Climatic Change, 108(4), 675–691.

Michol, K. A., Russell, J. K., & Andrews, G. D. M. (2008). Welded block and ash flow deposits from Mount Meager, British Columbia, Canada. Journal of Volcanology and Geothermal Research, 169(3–4), 121–144. https://doi.org/10.1016/j.jvolgeores.2007.08.010

Miller, Craig A, & Williams-Jones, G. (2016). Internal structure and volcanic hazard potential of Mt Tongariro, New Zealand, from 3D gravity and magnetic models. Journal of Volcanology and Geothermal Research, 319, 12–28. https://doi.org/10.1016/j.jvolgeores.2016.03.012

Miller, C. A., Le Mével, H., Currenti, G., Williams-Jones, G., & Tikoff, B. (2017a). Microgravity changes at the Laguna del Maule volcanic field: Magma-induced stress changes facilitate mass addition. Journal of Geophysical Research: Solid Earth, 122(4), 3179–3196. https://doi.org/10.1002/2017JB014048

Miller, Craig A., Williams-Jones, G., Fournier, D., & Witter, J. (2017b). 3D gravity inversion and thermodynamic modelling reveal properties of shallow silicic magma reservoir beneath Laguna del Maule, Chile. Earth and Planetary Science Letters, 459, 14–27. https://doi.org/10.1016/j.epsl.2016.11.007
Nettleton, L. L. (1939). Determination of density for reduction of gravimeter observations. Geophysics, 4(3). https://doi.org/10.1190/1.1437088

Parasnis, D. S. (1966). Mining Geophysics. Elsevier, Amsterdam-London-New York.

Paulatto, M., Moorkamp, M., Hautmann, S., Hooft, E., Morgan, J. V., & Sparks, R. S. J. (2019). Vertically Extensive Magma Reservoir Revealed From Joint Inversion and Quantitative Interpretation of Seismic and Gravity Data. Journal of Geophysical Research: Solid Earth, 124(11), 11170–11191. https://doi.org/10.1029/2019JB018476

Peterson, D., Garibaldi, N., Keranen, K., Tikoff, B., Miller, C., Lara, L. E., et al. (2020). Active normal faulting, diking, and doming above the rapidly inflating Laguna del Maule volcanic field, Chile imaged with CHIRP, magnetic, and focal mechanism data. Journal of Geophysical Research: Solid Earth. https://doi.org/10.1029/2019JB019329

del Potro, R., Díez, M., Blundy, J., Camacho, A. G., & Gottsmann, J. (2013). Diapiric ascent of silicic magma beneath the Bolivian Altiplano. Geophysical Research Letters, 40(10), 2044–2048. https://doi.org/10.1002/grl.50493

Pritchard, M. E., & Gregg, P. M. (2016). Geophysical Evidence for Silicic Crustal Melt in the Continents: Where, What Kind, and How Much? Elements, 12(2), 121–127. https://doi.org/10.2113/gselements.12.2.121

Represas, P., Catalão, J., Montesinos, F. G., Madeira, J., Mata, J., Antunes, C., & Moreira, M. (2012). Constraints on the structure of Maio Island (Cape Verde) by a three-dimensional gravity model: imaging partially exhumed magma chambers. Geophysical Journal International, 190(2), 931–940. https://doi.org/10.1111/j.1365-246X.2012.05536.x

Rubin, A. E., Cooper, K. M., Till, C. B., Kent, A. J. R., Costa, F., Bose, M., et al. (2017). Rapid cooling and cold storage in a silicic magma reservoir recorded in individual crystals. Science, 1156(June), 1154–1156. https://doi.org/10.1126/science.aam8720

Schaen, A. J., Cottle, J. M., Singer, B. S., Brenhin Keller, C., Garibaldi, N., & Schoene, B. (2017). Complementary crystal accumulation and rhyolite melt segregation in a late Miocene Andean pluton. Geology, 45(9), 835–838. https://doi.org/10.1130/G39167.1

Schaen, A. J., Singer, B. S., Cottle, J. M., Garibaldi, N., Schoene, B., Satkoski, A. M., & Fournelle, J. (2018). Textural and Mineralogical Record of Low Pressure Melt Extraction and Silicic Cumulate Formation in the late Miocene Risco Bayo-Huemul Plutonic Complex,

Southern Andes. Journal of Petrology, 59(10), 1991–2016. https://doi.org/10.1093/petrology/egy087

Singer, B S, Andersen, N. L., Le Mével, H., Feigl, K. L., DeMets, C., Tikoff, B., et al. (2014). Dynamics of a large, restless, rhyolitic magma system at Laguna del Maule, southern Andes, Chile. GSA Today. https://doi.org/10.1130/GSATG216A.1

Singer, B.S., Le Mével, H., Licciardi, J.M., Córdova, L., Tikoff, B., Garibaldi, N., Andersen, N.L., Diefenbach, A.K. & Feigl, K.L. (2018). Geomorphic expression of rapid Holocene silicic magma reservoir growth beneath Laguna del Maule, Chile.Science advances,4(6), p.eaat1513.

Sruoga, P., Elissondo, M., Fierstein, J., Garcia, S., Gonzalez, R., & Rosas, M. (2015). Actividad explosiva postglacial del centro barrancas, complejo volcanico Laguna del Maule. In Congreso Geologico Chileno (pp. 49–52). Sruoga, P., Elissondo, M., Rosas, M., Fierstein, J., & Singer, B. S. (2018). Cerro Barrancas, Laguna Del Maule Volcanic Field, Chile: unraveling its eruptive history to constrain hazard assessment. In AGU Chapman Conference. AGU. Retrieved from https://agu.confex.com/agu/18chapman1/webprogram/Paper328208.html

Tašárová, Z. A. (2007). Towards understanding the lithospheric structure of the southern Chilean subduction zone (36°S-42°S) and its role in the gravity field. Geophysical Journal International, 170(3), 995–1014. https://doi.org/10.1111/j.1365-246X.2007.03466.x

Tikhonov, A. N., & Arsenin, V. Y. (1977). Solutions of Ill-posed Problems.
Till, C. B., Vazquez, J. A., & Boyce, J. W. (2015). Months between rejuvenation and volcanic eruption at Yellowstone caldera, Wyoming. Geology, 43(8), 695–698. https://doi.org/10.1130/G36862.1

Till, C. B., Pritchard, M. E., Miller, C. A., Brugman, K. K., & Ryan-davis, J. (2018). Supervolcanic investigations. Nature Geoscience. https://doi.org/10.1038/s41561-018-0100-1
Uieda, L. (2018). Verde: Processing and gridding spatial data using Green's functions. Journal of Open Source Software, 3(30), 957. https://doi.org/10.21105/joss.00957

Wespestad, C. E., Thurber, C. H., Andersen, N. L., Singer, B. S., Cardona, C., Zeng, X., et al. (2019). Magma Reservoir Below Laguna del Maule Volcanic Field, Chile Imaged with Surface-Wave Tomography. Journal of Geophysical Research: Solid Earth, 1–15. https://doi.org/10.1029/2018JB016485

Zhan, Y., Gregg, P. M., Le Mével, H., Miller, C. A., & Cardona, C. (2019). Integrating Reservoir Dynamics, Crustal Stress, and Geophysical Observations of the Laguna del Maule Magmatic System by FEM Models and Data Assimilation. Journal of Geophysical Research: Solid Earth, 124(12), 13547–13562. https://doi.org/10.1029/2019JB018681

Chapter 2: Determining the timing of initiation of shear zone deformation using titanite petrochronology

Abstract

We present a new methodology to date the initiation of shear zone deformation in granitic rocks using an integrative method of titanite petrochronology, zircon geochronology, microstructural analysis, and trace element mapping. This method is applied to a porphyritic orthogneiss in the western Idaho shear zone, Idaho. U-Pb zircon petrochronology dates crystallization of this unit at ca. 103 Ma. High-precision isotope dilution U-Pb geochronological measurements on titanite crystal fragments are used to constrain the timing of shear zone initiation. Using microstructural techniques - crystallographic misorientations, fabric context, backscattered electron images – relict magmatic, partially to fully recrystallized, and neoblastic titanite crystals are distinguished. Further, principal component analysis of trace element compositional variance of titanite is able to distinguish relict magmatic titanites from recrystallized and neoblastic titanites. The ages of partially recrystallized and neoblastic titanite grains constrain the initiation of the western Idaho shear zone to between ca. 98 and 96 Ma. The 5-7 m.y. lag between pluton emplacement and the onset of deformation indicates that mid Cretaceous deformation in the western Idaho shear zone was temporally distinct from Jurassic-Early Cretaceous accretionary tectonics. Our integrated petrochronological investigation documents that: 1) deformation induces textural, chemical, and isotopic changes in titanite; 2) the geochemical properties of primary magmatic titanite collapse into a discernible trend of subsolidus syn-deformational titanite compositions; and 3) the timing of onset of deformation and progression of strain accumulation are preserved in the U-Pb ages of these titanite crystals.

1. Introduction

High-temperature shear zones play a major role in partitioning oblique slip at transpressional and transtensional plate boundaries (e.g., Fitch, 1972) and have been called upon to solve the "room problem" of plutonism in dominantly contractional arc settings (e.g., Hutton et al., 1990; Tikoff and Teyssier, 1992). Much of the interplay between deformation and magmatism takes place in the roots of continental arcs at lower to mid-crustal depths, and the interaction of these processes can be explored using accessory mineral petrochronology in deformed granitoids. The timing of shear zone deformation in continental arc settings can be used to reconstruct ancient tectonic processes related to lithospheric assembly and modification, such as coupling of the magmatic arc to the subducting plate (e.g., Krueger and Yoshinobu, 2018) or terrane accretion (Tikoff et al., 2022).

It is difficult to directly date high temperature (>550°C) deformation in shear zones. Most geochronological methods used in continental arc settings date either timing of melt crystallization (e.g., U-Pb zircon) or a lower temperature cooling interval (e.g., Ar/Ar biotite and hornblende), which while useful for broadly bracketing the timing of deformation, does not date high-temperature fabrics directly. Titanite ($CaTiSiO_5$), a mineral common in granitoid plutons, recrystallizes and grows in response to changes in pressure, temperature, and differential stress and thus can record evidence of fabric-forming events (Kohn, 2017). The high Pb closure temperature of titanite (>750°C; Hartnady et al., 2019 and references therein) makes it a useful U-Pb chronometer for high-temperature systems, albeit one necessitating correction for initial Pb incorporated during crystallization (Bonamici and Blum, 2020; Frost et al., 2000; Storey et al., 2006). When titanite (re)crystallization can be associated with deformation fabrics, the U-Pb age of titanite dates shear zone deformation directly. Techniques such as electron backscattered

diffraction (EBSD) that quantify intragrain crystallographic misorientation domains have been successfully used to associate the partial recrystallization of titanite with deformation (Bonamici et al., 2015; Gordon et al., 2021).

However, because titanite commonly crystallizes at magmatic through subsolidus temperatures, relict igneous, recrystallized, and neoblastic titanite can coexist in the same mesoscale volume of a deformed granitoid, complicating the association of titanite ages with a specific process (Getty and Gromet, 1992). This can be remedied by characterizing and dating titanite at the single crystal or intracrystalline scale. Numerous studies have: 1) documented a range of natural titanite compositions (Frost et al., 2000; El Korh et al., 2009); 2) attributed different morphologies to magmatic and metamorphic titanite crystals (Getty and Gromet, 1992; Resor et al., 1996; Torvela et al., 2008); 3) leveraged those morphological differences to categorize titanite and extract chemical characteristics from those categories (Garber et al., 2017); and 4) used in situ titanite ages of metamorphic titanite to explore the relationship between magmatism and deformation (Papapavlou et al., 2017; Rossetti et al., 2017). Despite these and other efforts to use titanite petrochronology to date deformation, more work remains to apply these techniques to settings of syntectonic plutonism where igneous titanite crystallization and deformation-related titanite (re)crystallization may differ in age by only a few million years.

We use zircon and titanite petrochronology to date pluton emplacement and the initiation of shear zone deformation. We identify magmatic through subsolidus titanite growth by integrating textural information from backscattered electron (BSE) imaging and electron backscatter diffraction (EBSD) crystallographic misorientation maps with trace element chemistry as measured by laser ablation inductively coupled plasma mass spectrometry (LA-ICPMS). Recent empirical calibration of tracer diffusion rates in titanite (Garber et al., 2017;

Gordon et al., 2021; Holder et al., 2019; Kohn, 2017) suggest that crystal domains sufficiently recrystallized to modify Nb, Zr, and rare earth element (REE) concentrations will experience U-Pb isotopic resetting. Thus, the expulsion or incorporation of high field strength elements and REE can indicate crystal domains whose U-Pb ages reflect deformation-related recrystallization and neoblastic growth. Using tandem LA-ICPMS and isotope dilution–thermal ionization mass spectrometry (ID-TIMS) geochronology, we assess the range of zircon and titanite ages in the rock. We specifically target zircon domains to date pluton emplacement and recrystallized and neoblastic titanite to date shear zone initiation. We use the precision of initial Pb-corrected ID-TIMS ages to distinguish a 5-7 m.y. lag between pluton crystallization and the onset of deformation.

2. Geological Background

Coeval plutonism and deformation was common during the Cretaceous construction of the North American Cordillera (e.g., Bartley et al., 2018; Braudy et al., 2017; Tikoff and St. Blanquat, 1997). In the Idaho section of the North American Cordillera, the Cretaceous western Idaho shear zone (WISZ) is a crustal-scale, dextral transpressive, high-temperature shear zone that deformed syntectonic intrusive rocks (Figure 1; (Giorgis et al., 2008; Manduca et al., 1993; Tikoff et al., 2001). In the McCall, Idaho area, three plutonic complexes were deformed by the WISZ: the Hazard Creek complex, the Little Goose Creek complex, and the Payette River Tonalite complex (Manduca et al., 1993). Previous work in the area constrained pluton emplacement to ca. 118 Ma (Hazard Creek complex), ca. 105 Ma (Little Goose Creek complex), and ca. 90 Ma (Payette River Tonalite complex) and constrained deformation to older than ca. 90 Ma (Giorgis et al., 2008; Manduca et al., 1993).

The strongly deformed Little Goose Creek complex contains the $^{87}Sr/^{86}Sr$ 0.706 isopleth which currently delineates the boundary between accreted terranes to the west and the Idaho Batholith to the east (Fleck and Criss, 1985; Manduca et al., 1992). The WISZ lies within, and is parallel to, the Salmon River suture zone, a Late Jurassic-Early Cretaceous structure that encompasses the transition from Mesozoic accreted terranes to cratonic North America (McClelland et al., 2000). Suturing in western Idaho was dated at 128 ± 3 Ma using a multi-mineral Sm-Nd isochron (Getty et al., 1993). It is debated whether the WISZ overprints the Jurassic terrane accretion episode as a distinct shearing event (McClelland et al., 2000; Montz and Kruckenberg, 2017) or if the WISZ is the expression of continuous deformation following terrane accretion (Gray et al., 2012). WISZ deformation that post-dates magmatism would support the hypothesis of Late Jurassic-Early Cretaceous suturing and mid-Cretaceous transpressional shearing as distinct events. Below we describe the detailed, contextualized accessory mineral petrochronology that allows us to distinguish between magmatism and solid-state deformation with million to sub-million year resolution.

3. Material and methods

3.1. Sample description

We examined a highly deformed porphyritic orthogneiss (14WZ3-2; 44.9669°, -116.18085°, WGS84) from the Little Goose Creek Complex of the Border Zone Suite of the Idaho Batholith near McCall, Idaho (Figure 1; Gaschnig et al., 2010; Manduca et al., 1993). Approximately 1 kg of sample was extracted for thin and thick sections as well as feldspar, zircon, and titanite mineral separates following standard petrographic and separation techniques.

3.2. Pb isotopic compositions of feldspar

The isotopic composition of initial Pb in this sample was estimated from the measured Pb isotope composition of feldspar crystals, following methods modified from Housh and Bowring, (1991). An approximately 8 cm^3 K-feldspar porphyroclast was isolated with a wafer saw from the hand sample and analyzed separately from matrix K-feldspar extracted during standard crushing and density separation of the geochronology sample. Fifty milligrams of each subsample of feldspar crystals was prepared by Frantz magnetic barrier separation (non-magnetic at 0.5 A magnet current, 10° side slope, 7° forward slope), lithium metatungstate density separation ($\rho < 2.64$ g/cm^3), and hand-picked for mineral clarity and lack of inclusions. Each subsample was sequentially leached in 6M HCl (30 min), 8M HNO_3 (30 min), 1M HF (1 hour) and again in 1M HF (1 hour), before collecting a series of three 1M HF (30 min) leaches that were processed through 1M HBr-based anion-exchange chromatography (Strelow and Toerien, 1966). Pb isotope ratios were measured by static multicollection on 1011 Ω resistor amplifiers on an IsotopX Phoenix X62 thermal ionization mass spectrometer. Instrumental mass bias was corrected using external calibration to repeated measurements of NBS 981 at the same sample quantity and run temperature conditions.

3.3. Zircon petrochronology

Zircon was separated, annealed at 900°C for 60 hours, mounted, imaged via cathodoluminescence, and dated at the Boise State University Isotope Geology Laboratory using methods detailed in Macdonald et al. (2018). LA-ICPMS analysis of >200 spots on approximately 47 zircon crystals resulted in age determinations and trace element concentrations. We used LA-ICPMS ages and CL images to inform grain selection for ID-TIMS, targeting domains that represented the main phase of magmatic crystallization or metamorphism.

We subsampled 16 zircon crystals into 26 crystal fragments using the laser from the LA-ICPMS system as a cutting tool and treated the fragments with chemical abrasion at 180° or 190°C to mitigate Pb loss modified from Mattinson (2005). Samples were spiked with an in-house ^{205}Pb-^{233}U-^{235}U tracer (BSU-1B) calibrated to EARTHTIME gravimetric standards (Condon et al., 2015; McLean et al., 2015), dissolved, and processed for U and Pb separation by HCl-based anion-exchange chromatography (Krogh, 1973). Isotopic measurements were made on an IsotopX GV Isoprobe-T or an IsotopX Phoenix X62 multicollector TIMS with a Daly photomultiplier detector. Details of instrumental fractionation, common Pb correction, and error propagation are given in Table 1.

3.4. Titanite petrochronology

3.4.1. Microstructures

We analyzed lineation parallel, foliation perpendicular (XZ) thick sections with BSE imaging and EBSD analysis at the University of Wisconsin–Madison using a Hitachi S3400 Variable Pressure scanning electron microscope fitted with a Hitachi High-Sensitivity BSE detector and an Oxford EBSD detector. Data were processed using Aztec software and the MTEX toolbox for MATLAB (Bachmann et al., 2010) with code modified from Michels et al. (2015). We identified the crystal phases present and measured the three-dimensional orientation of crystallographic lattice at micron-scale resolution (Prior et al., 2002, 1999). Mineralogical phase maps were used to investigate the textural context of titanite within the rock fabric. Lattice misorientation maps were used to visualize the magnitude of intracrystalline misorientation and patterns of misorientation relative to titanite grain boundaries.

3.4.2. Trace element geochemistry

All titanite trace element chemistry and geochronology analyses were performed at the Boise State University Isotope Geology Laboratory. BSE imaging was conducted on titanite separates at the Boise State University and on titanite in thick sections at the University of Wisconsin–Madison. We analyzed >700 spots on approximately 220 titanite crystals from separates and within thick sections to capture the full range of titanite trace element chemistry. Trace element measurements were made on a ThermoElectron X-Series II quadrupole ICPMS and New Wave Research UP-213 Nd:YAG UV (213 nm) laser ablation system and followed the procedures described in Macdonald et al. (2018), except Sr and Zr were measured instead of P and Ti (analytical parameters described in Harrigan et al., 2022)

To examine the trace element variability in titanite from this sample, we did principal component analysis in R on a non-normalized suite of trace elements (Sr, Y, Zr, Nb, La, Ce, Pr, Nd, Sm, Eu, Gd, Tb, Dy, Ho, Er, Tm, Yb, Lu, Ta, Th, U, Hf) without any a priori categorization of the analyzed spots (i.e., microstructural characterization of titanite grains into magmatic, recrystallized, and neoblastic categories did not inform the principal component analysis).

3.4.3. Geochronology

Titanite crystals chosen for ID-TIMS geochronology were selected based on texture, internal misorientation pattern, fabric context, and trace element chemistry with the aim of capturing the range of variability in the sample. BSE images of ID-TIMS-dated titanite crystals are given in Supplemental Figure S1. Titanite crystals with sufficiently high U concentrations to yield measurable radiogenic Pb were subsampled by fracturing grains with a sharpened steel dental tool. To extract titanite from thick sections, the laser on the LA-ICPMS system was used to ablate material surrounding the titanite grain in a moat shape. Titanite was plucked from thick

sections using a sharpened steel dental tool, transferred to a glass vial filled with deionized water, and sonicated in 5 second bursts for 10 minutes to clean the titanite crystal faces.

In preparation for dissolution, titanite crystals or crystal fragments were sonicated with 3.5 M HNO_3 for 15 min and rinsed twice with ultra-pure H^2O. Samples were spiked with an in-house 205Pb-233U-235U tracer (BSU-1B) calibrated to EARTHTIME gravimetric standards (Condon et al., 2015; McLean et al., 2015) and dissolved following the methods described in Macdonald et al. (2018). Titanite was processed for U and Pb separation by HBr- and HCl-based anion-exchange chromatography (Krogh, 1973; Strelow and Toerien, 1966). Isotopic measurements were made with the same instrumentation and methods as zircon.

4. Results

4.1. Pb isotopic compositions of feldspar

The Pb isotopic compositions of matrix and porphyroclast K-feldspar are given in Harrigan et al., 2022. Leachates 3-5 have reproducible compositions, suggesting that the pretreatment and two 1-hour 1M HF leaches sufficiently eliminated reservoirs of surface-correlated or mineral inclusion Pb. For initial Pb estimates, we averaged the values of Leachates 3-5 and found that the Pb isotopic composition of the porphyroclast was indistinguishable, within uncertainty, from matrix K-feldspar. As our matrix K-feldspar sample averages the full analytical volume from which zircon and titanite were extracted, we use its composition for the initial Pb correction of zircon and titanite dates.

4.2. Zircon petrochronology

Excluding crystals with Jurassic and earliest Cretaceous dates, zircon dates range from 112.62 ± 0.09 Ma to 96.21 ± 0.48 Ma (Figure 2). CL imaging (Supplemental Figure S1) revealed inherited cores in nearly every zircon, and the subsampling of zircon crystals allowed us to

largely, but not completely, avoid Jurassic and earliest Cretaceous inherited cores, as evidenced in some ID-TIMS dates. Six zircon crystals were subsampled and yielded multiple dates. In some cases, crystal fragments from a single crystal were the same age within uncertainty (e.g., z1b: 110.464 ± 0.086 Ma; z1d: 110.635 ± 0.088 Ma), and in other cases, multiple fragments from a single crystal spanned >3 Ma (e.g., z6a: 105.10 ± 0.10 Ma; z6b: 107.71 ± 0.37 Ma; z6c: 109.01 ± 0.08 Ma). The dispersion in dates from a single crystal is strongly correlated with variation in CL texture of sampled domains. All zircon grains from this sample have a significant sector and oscillatory zoned volume (e.g., z16d: 106.59 ± 0.12 Ma), and we interpreted these portions of the crystals as crystallizing during the main period of super-solidus zircon saturation. Some zircon grains have dark-banded and sector-zoned rims (e.g., z10, z18, z20), the youngest fragment of which we interpreted to constrain the end of magmatic zircon growth in this sample (z20a: 103.20 ± 0.13 Ma). The two youngest zircon dates are associated with CL-bright rims truncating interior zoning, a texture commonly associated with metamorphic growth (Corfu et al., 2003). Crystal fragments z15 (97.71 ± 0.44 Ma) and z14b (96.21 ± 0.48 Ma) are mixtures of interiors, dark-banded and sector-zoned rims, and CL-bright rims that crosscut interior zoning. These dates reflect mixtures between magmatic (>103 Ma) and metamorphic (<98 Ma, after shear zone initiation, described in section 4.2.) zircon domains and thus were interpreted as maximum ages of zircon rim growth.

4.3. Titanite petrochronology

4.3.1. Microstructures

Titanite grains within oriented thick sections show a range of morphologies and degrees of crystallographic distortion because of both changes in crystallization conditions and crystal plastic deformation. Using internal zoning observed in BSE images, EBSD misorientation maps,

and petrographic context, we recognized several distinct types of titanite grains (Figure 3; Table 1). Rounded diamond-shaped titanite grains within K-feldspar porphyroclasts have oscillatory zoning in BSE images and small degrees of misorientation (less than 1°) where the titanite c-axis is parallel to the lineation (e.g., t702). Subhedral, elongate titanite grains with little to no BSE zoning (e.g., t909) and with their c-axis parallel to the margin of K-feldspar porphyroclasts and ribboned quartz domains display the most significant misorientation gradient (0 to 5°) with the highest degrees of misorientation found at grain tips. Rounded and lenticular titanite grains characteristic of neoblastic growth are found within ribboned quartz and myrmekitic feldspar domains. These grains display minimal degrees of misorientation (less than 2°) despite commonly having elongate and locally boudinaged morphologies (e.g., t902). Some lenticular grains show no observable variations in composition (e.g., t902), while others display core and rim zones in BSE images (e.g., t903).

4.3.2. Trace element geochemistry

We applied principal component analysis on a suite of trace element concentrations measured by LA-ICPMS to distinguish titanite compositional types and trends. The chemical variability reduced to three branches defined by divergence in Y + Nb, Th + light rare earth element, and U + heavy rare earth element concentrations (Figure 4A). When coded by Zr-in-titanite temperatures (Figure 4A; Hayden et al., 2008 with P = 0.44 GPa from Braudy et al., 2017) or age of ID-TIMS-dated crystals (Figure 4B; ages described in section 3.3.), systematic variations are observed between the branches of the principal component analysis score plot, with the coolest and youngest titanite crystals restricted to one branch of the data.

The dimensional reduction of principal component analysis efficiently highlights the trace elements most responsible for the chemical variance of titanite in this sample. However, by

accentuating that variance through summing or ratioing certain geochemical parameters, we can more clearly visualize and interpret the differences between titanite compositional domains and their origins. By featuring geochemical parameters associated with the main titanite valence substitution groups (tri-, tetra-, and pentavalent), we examined the effect of different trace element substitution mechanisms during titanite (re)crystallization. A trivariate plot of rare earth elements (REE)–U–Nb/Th displays two "spurs" oblique to a main compositional trend of decreasing REE and high field strength elements (Figure 4C-D). The two spurs are distinctive because of their high Nb/Th and REE concentration, respectively. Titanite crystals that plot on the spurs commonly display sector (e.g., t1) or oscillatory zoning (e.g., t13a) in BSE images. Titanite in the spurs grew at high temperatures, up to about 770°C. By contrast, titanite crystals in the main trend typically have a patchy or homogenous BSE response, and their temperatures decrease in a correlated fashion from about 725°C at high REE + U + Nb/Th to about 625°C at low REE + U + Nb/Th.

4.3.3. Geochronology

We dated titanite grains sampled directly from varying positions within thick sections as well as across chemical trends exhibited by grains from mineral separates e.g., Fig. 3, to link textural and chemical indicators of titanite recrystallization and neoblastic growth to timing of deformation. Subsampling and dating intragrain titanite domains by ID-TIMS, including an initial Pb correction utilizing coexisting K-feldspar, achieved a median precision of 0.2% (2σ) on our individual crystal or crystal fragment titanite $^{206}Pb/^{238}U$ dates. A ^{204}Pb-based initial Pb correction of titanite data allowed us to plot titanite dates in the same Wetherill concordia space typically used for zircon dates, providing a graphical way to compare the ages and uncertainties of the different mineral chronometers. Apart from the four youngest, lowest U and least

radiogenic reversely discordant titanite analyses, our ^{204}Pb-corrected titanite analyses are concordant, attesting to the accuracy of the K-feldspar based initial Pb correction strategy. In fact, our preferred initial ^{207}Pb/^{206}Pb value from K-feldspar is similar to modeled terrestrial Pb isotopic compositions for 100, 90, and 80 Ma (Stacey and Kramers, 1975) and overlaps with the range of modern whole rock ^{207}Pb/^{206}Pb from the Idaho Batholith (Figure 5F, inset; (Gaschnig et al., 2011).

ID-TIMS dates from all titanite types range from 105.0 ± 0.1 Ma to 82.6 ± 2.9 Ma (Figure 2). The two oldest dated titanite crystals or crystal fragments (t9: 104.98 ± 0.14 Ma; t17a: 103.53 ± 0.36 Ma) are older or equivalent in age to the magmatic zircon fragment which constrains pluton emplacement in this sample (z20a: 103.20 ± 0.13 Ma), demonstrating that magmatic titanite is preserved. Importantly, subsampled titanite crystals yielded different dates for the crystal fragments (e.g., four t15 fragments span from 99.64 ± 0.25 Ma to 93.98 ± 0.17 Ma), consistent with U-Pb ages being conserved in multidomain, multigenerational titanite. Some titanite dates are likely mixed ages due to the physical mixing of different age domains. Several titanite crystals or crystal fragments (t106a, t106b, t15b, t4, t2) overlap within uncertainty with the dates of the zircon rim fragments that have both magmatic and metamorphic zones visible in CL (z15, z14b). This suggests a possible magmatic + metamorphic age interpretation for these titanite crystals and crystal fragments. However, titanite crystals t4 and t2 lenticular, a morphology associated with metamorphic titanite growth (Getty and Gromet, 1992). Though they overlap with the age uncertainty of z14b, we interpreted the dates of t4 and t2 (t4: 95.93 ± 0.11 Ma; t2: 95.67 ± 0.12 Ma) as relating to neoblastic growth during solid-state deformation, as discussed in section 4.3. in conjunction with the geochemical and microstructural data. Consequently, we interpreted all titanite dates younger than t4 and t2 as

dominantly reflecting (re)crystallization during deformation since magmatic processes must have concluded before the growth of neoblastic grains such as t4 and t2.

5. Discussion

5.1. In situ versus microsampled isotope dilution geochronology

Multiple approaches exist for correcting titanite dates for the incorporation of initial Pb. A ^{204}Pb-based initial Pb correction is the standard approach for both ID-TIMS (Schmitz and Bowring, 2001) and SIMS titanite geochronology (Bonamici and Blum, 2020; Stern, 1997). The 204Pb-based correction assumes an isotopic composition for initial Pb, either from a standard Earth Pb evolution model (Stacey and Kramers, 1975) or the measured isotopic composition of a co-existing low U phase (Frost et al., 2000), and allows the calculation of all three radiogenic ^{207}Pb*/^{206}Pb*, ^{207}Pb*/^{235}U and ^{206}Pb*/^{238}U chronometers to assess concordance. However, accurately measuring ^{204}Pb via LA-ICPMS is a challenge because of a ^{204}Hg isobaric interference related to contaminants in the Ar plasma, and thus most LA-ICPMS titanite dates are corrected with a ^{207}Pb-based initial Pb correction, in which either individual analyses are corrected based upon an estimated initial ^{207}Pb/^{206}Pb and U-Pb isotope ratios assumed concordant, or groups of analyses are regressed in Tera-Wasserburg concordia space to return both an initial ^{207}Pb/^{206}Pb value and an age from the concordia and ^{207}Pb/^{206}Pb axis intercepts (Bonamici and Blum, 2020; Storey et al., 2006).

To assess the ^{207}Pb-based correction for both LA-ICPMS and ID-TIMS U-Pb dates, we regressed titanite data on Tera-Wasserburg plots to determine estimates for initial ^{207}Pb/^{206}Pb compositions and titanite ages in this sample (Figure 5). When the LA-ICPMS isotopic data are plotted and colored by temperature or ID-TIMS date, no clear temperature- or age-defined

populations emerge through which to regress the LA-ICPMS data to determine multiple initial $^{207}Pb/^{206}Pb$ values corresponding to different titanite populations. This does not preclude the existence of multiple titanite populations in the sample; rather, the in situ isotopic data lacks the resolution to identify these populations. Single titanite grains with multiple LA-ICPMS spots only occasionally have sufficient spread in $^{207}Pb/^{206}Pb$ to produce robust intragrain regressions in Tera-Wasserburg space and do not reliably return reproducible initial $^{207}Pb/^{206}Pb$ estimates. Regression of the ID-TIMS titanite data in Tera-Wasserburg space revealed significant over-dispersion from a linear fit (MSWD = 11000), discernible due to the high precision of ID-TIMS dates, strongly suggesting that these titanite crystals are not a single-age population and warning against indiscriminate grouping of analyses to define regression lines.

In ID-TIMS measurements, ^{204}Pb is the quantitative proxy for initial Pb. Measurements of ^{204}Pb can be used to subtract the initial Pb component from the total Pb budget and calculate radiogenic $^{207}Pb/^{235}U$ and $^{206}Pb/^{238}U$ dates using an estimate of the initial $^{207}Pb/^{204}Pb$ and $^{206}Pb/^{204}Pb$ ratios. A coeval low $^{238}U/^{204}Pb$ mineral, like K-feldspar, can provide the estimate of the pool of initial Pb incorporated into minerals that (re)crystallize during deformation (Frost et al., 2000). Notably, this technique for recovering radiogenic isotope ratios and corresponding dates does not rely on the grouping of multiple analyses to define regression lines, nor does it sacrifice the $^{207}Pb/^{235}U$ chronometer, like the commonly used "semi-total Pb" projection or "^{207}Pb-correction" technique in Tera-Wasserburg space (Ludwig, 1998; Stern, 1997; Storey et al., 2006). By using both the $^{206}Pb/^{238}U$ and $^{207}Pb/^{235}U$ chronometers, we can evaluate concordancy as well as confirm that titanite crystals and crystal fragments can—and in this case, do—record distinct ages representing different stages of fabric development in a deformed rock (Figure 2). Our concordant ID-TIMS dates document >22 Ma of magmatic and deformation-

related titanite (re)crystallization, demonstrating that, for this sample, a single intercept age in Tera-Wasserburg space of all LA-ICPMS isotopic data is effectively meaningless for making geological interpretations.

5.2. Bracketing shear zone initiation: a maximum age from titanite recrystallization

Textural, geochemical, and age information can be used to ascribe a (re)crystallization process to different titanite crystal types within a single sample. It is apparent that titanite records multiple (re)crystallization processes within different fabric contexts. Specifically, EBSD phase and titanite crystallographic misorientation maps showed that most euhedral, diamond-shaped titanite grains are found included in K-feldspar porphyroclasts rather than the matrix. The inclusion of titanite within the core of K-feldspar, a magmatic phase, indicates that some of the titanite within the rock formed during pluton emplacement and solidification. We interpreted these diamond -shaped titanite grains with low degrees of internal crystallographic misorientation as relict magmatic titanite, prevented from recrystallizing during shear zone deformation by the surrounding K-feldspar porphyroclast. However, some titanite grains included in K-feldspar porphyroclasts, particularly those grains whose c-axis is at a high angle to the rock fabric, do show crystallographic misorientation evidence of recrystallization. We interpreted these diamond -shaped crystals with moderate to high crystallographic misorientation on titanite grain edges as partially recrystallized titanite that contains both relict magmatic and recrystallized domains. This shows that not all titanite grains included in porphyroclasts are shielded from and therefore immune to deformation effects. Rather, even titanite grains within porphyroclasts respond to fabric-forming processes if their primary orientation is at a high angle to the developing solid-state fabric, which is - by inference - inducing local recrystallization of the K-feldspar porphyroclasts.

By integrating trace element chemistry and age data on the trivariate plot, a more resolved correlation between chemistry and age is evident: the spurs are associated with older ages, whereas within the main trend, total REE, U, and Nb/Th decrease with time (Figure 4D). The spurs represent different magmatic compositions probably related to sector zoning (e.g., t1 LA-ICPMS spots were placed on different sector zones (Supplemental Figure S1) and plot on both spurs). The trivariate plot colored by temperature (Figure 4C) supports this interpretation with the hottest temperatures generally restricted to the spurs.

Intragrain geochemistry variations, commonly associated with high crystallographic misorientation, confirm that some crystals are physical mixtures of relict magmatic and newly recrystallized domains. On the trivariate REE–U–Nb/Th plot, LA-ICPMS spots on partially recrystallized titanite grains plot in a trend along the spurs. The spurs collapse from the two magmatic compositions of high Nb/Th and REE, respectively, into the main trend at intermediate REE + U + Nb/Th due to REE and high field strength element expulsion during partial to full recrystallization. For example, two individual crystals approximately 200 μm from each other within a feldspar porphyroclast (Figure 3) yield dates that overlap within uncertainty (t106a: 98.13 ± 0.86 Ma; t106b: 97.54 ± 0.68 Ma). The backscattered oscillatory zoning and low degrees of misorientation in t106a (the small area of 1-2° of misorientation along the edge of t106a is likely an artifact of polishing) seemingly suggest that t106a is a relict magmatic grain, though its date (t106a: 98.13 ± 0.86 Ma) is a few million years younger than the pluton emplacement age as determined by zircon (ca. 103 Ma). This younger-than-expected date for t106a is explained by the space it occupies in the low-U spur of the trivariate REE–U–Nb/Th plot (Figure 4D). When the trivariate plot is rotated to highlight the spur visible in REE versus U space (Figure 6), it is evident that grains t106a and t106b plot in an array between the high-REE end of the spur toward

the main trend. One LA-ICPMS spot from t106a is a magmatic composition at the end of the spur, and another spot with a lower REE concentration indicates that some domains recrystallized, expelling trace elements, and therefore also resetting the U-Pb isotopic systematics in the recrystallized domains. This recrystallization is not evident in the BSE image or the crystallographic misorientation map of t106a. The moderate to high degrees of the crystallographic misorientation along the edges of t106b, as well as the REE concentrations that plot along the spur and towards the main trend, are both indicative of deformation-induced recrystallization. Crystals or crystal fragments that contain both relict magmatic and recrystallized domains will yield a mixed age that reflects both pluton emplacement-related magmatism and solid-state deformation. Since the chemistry of t106b plots closer to the main trend than t106a, it has recrystallized more than t106a, and its date of (97.54 ± 0.68 Ma) provides an upper limit for the age of deformation initiation: ca. 98 Ma. Similarly, titanite grains older than ca. 98 Ma also plot in the spurs of the trivariate REE–U–Nb/Th plot and are interpreted as partially recrystallized, though to a lesser degree than t106b. Fragments of grain t15 are older, equivalent in age to, and younger than t106a and t106b (Figure 2). Grain t15 plots within the spurs and main trend on the REE–U–Nb/Th plot, consistent with the interpretation that magmatic to subsolidus titanite compositions will plot along the spurs and intersect with the main trend through partial recrystallization, though we focused here on t106a and t106b because of the additional contextualization that the misorientation maps and fabric context provide.

5.3. Bracketing shear zone initiation: a minimum age from titanite neoblastic growth

In addition to within K-feldspar porphyroclasts, titanite recrystallization is observed in the ribboned quartz and myrmekitic domains of the rock. Quartz dynamic recrystallization

features such as grain-size reduction and grain boundary migration are consistent with strain localizing in these domains. Titanite grains in these fabric domains tend to be highly to completely recrystallized with patchy crystallographic misorientation patterns, consistent with the strong reactivity of titanite to changes in differential stress (cf. Kohn, 2017). These fabric domains also contain neoblastic titanite grains with a lenticular morphology and low degrees of crystallographic misorientation (<1°).

The interpretation of some titanite grains as neoblastic is consistent with their geochemical character. In the trivariate REE–U–Nb/Th plot, the lenticular or elongate and boudinaged titanite grains located within the ribboned quartz and myrmekitic feldspar fabric domains plot in the main trend of the data (Figure 4C-D). Critically, the spurs of magmatic and partially recrystallized titanite intersect the main trend at intermediate REE + U + Nb/Th, which means that titanite crystals with higher REE + U + Nb/Th grew with access to a trace element reservoir separate from the relict magmatic titanite. Nucleation of neoblasts was likely in response to an increase in available titanite-forming elements due to the local breakdown of magmatic phases during solid state-deformation. We observed mineral breakdown textures in K-feldspar and hornblende in thin section for this rock. Therefore, the oldest neoblastic titanite age that plots within the high REE + U + Nb/Th portion of the main trend (t4: 95.93 ± 0.11 Ma; Figure 6), above the spurs, reflects crystal nucleation during deformation and thus provides a minimum age for shear zone initiation: ca. 96 Ma.

Additionally, some crystals contain intragrain domains that plot in an array along the main trend, suggesting progressive growth and/or recrystallization with decreasing temperature. Some lenticular grains have distinct core and rim zones in BSE images, suggestive of multiple generations of neoblastic growth (e.g., t903; Figure 3). The neoblastic and recrystallized titanite

grains that plot in the mid to lower REE + U + Nb/Th portions of the main trend reflect continued deformation until at least 82.6 ± 2.9 Ma (t312). We interpreted the U-Pb ages of these titanite crystals as (re)crystallization ages rather than cooling ages because the Pb closure temperature in titanite is >750°C (Hartnady et al., 2019 and references therein). Titanite ages will record shear zone deformation until the pressure, temperature, and differential stress that control titanite reactivity diminishes to the point where titanite stops (re)crystallizing. Therefore, titanite likely does not capture the coolest end stages of shearing and is a poor constraint on the end of deformation. The Little Goose Creek complex was rapidly exhumed through hornblende and biotite 40Ar/39Ar closure temperatures (550°C and 325°C, respectively) between 85 and 70 Ma (Giorgis et al., 2008). The temperature range and age of our youngest ID-TIMS-dated titanite grain (t312: 659-694°C, 82.6 ± 2.9 Ma) extends the evidence for rapid exhumation of the WISZ to higher temperatures.

5.4. Mid-Cretaceous WISZ

The new petrochronological data show that WISZ deformation started between 98 and 96 Ma at this location. Solid-state deformation occurred 5-7 m.y. after crystallization of the pluton at ca. 103 Ma. Because deformation in this sample did not occur during or immediately after pluton emplacement, the implication is that shearing in the WISZ initiated at 98-96 Ma. As such, the dextral tranpressional deformation recorded in the WISZ is distinct from suturing events in the Late Jurassic and Early Cretaeous (e.g., McClelland et al., 2000). Both the timing and the style of deformation is consistent with the growing recognition of a ca. 100 Ma event within the central Cordillera (Tikoff et al., 2022 and references therein).

The titanite ages younger than 96 Ma (e.g., post shear zone initiation) indicate continued, protracted WISZ deformation. These results suggest that the WISZ was actively deforming during the intrusion of the ca. 90 Ma Payette River Tonalite complex (Giorgis et al., 2008; Manduca et al., 1993). However, some WISZ studies have concluded that deformation ended by ca. 90 Ma based on zircon U-Pb ages of non-deformed dikes and plutons (Braudy et al., 2017; Giorgis et al., 2008). These findings apparently contradict our youngest titanite ages that indicate that the shear zone was active until at least 82.6 ± 2.9 Ma. We suggest that this discrepancy reflects strain localization in different lithologies across the shear zone, causing the focus of deformation to shift, such that deformation ceases at different times in different locations. Further work on petrochronology across the WISZ could evaluate this interpretation.

6. Conclusions

Tandem zircon and titanite petrochronology can determine when shear zone deformation initiated. Coexisting relict magmatic, recrystallized, and neoblastic titanite were distinguished using BSE images, EBSD microstructures, and trace element geochemistry. Age-integrated principal component analysis of geochemical trends document the changes induced by progressive fabric development at high temperatures. A trivariate plot of REE–U–Nb/Th resolves a main geochemical trend of neoblastic and fully recrystallized titanite compositions and spurs of magmatic and partially recrystallized titanite compositions. The titanite crystals with higher REE + U + Nb/Th than relict magmatic, partially recrystallized titanite are associated with ribboned quartz and myrmekite formation, exhibit low degrees of crystallographic misorientation, have a homogenous or patchy BSE response, and must have grown from a geochemical reservoir distinct from magmatic titanite. This would suggest that changes in

titanite geochemistry reflect changing P-T- fluid conditions during deformaiton, with active deformation providing microstructural pathways for fluids. These titanite are ca. 96 Ma and younger and represent neoblastic nucleation and growth during active deformation, providing a minimum deformation initiation age. Thus, the shear zone thus initiated between 98 and 96 Ma. Systematic correlations between U-Pb age, crystallographic misorientation trends, and changing trace element geochemistry indicate that titanite deformation ages are robust.

The precision of titanite ID-TIMS geochronology is necessary to distinguish between near-synchronous magmatism and deformation. In the Little Goose Creek Complex of the western Idaho shear zone, Idaho, deformation lagged pluton emplacement by 5 to 7 m.y.. This result indicates that WISZ shearing is a distinct event from Late Jurassic-Early Cretaceous terrane accretion. WISZ deformation beginning between 98 and 96 Ma is consistent with a major ca. 100 Ma event within the North American Cordillera.

The presented approach is broadly applicable to any range of titanite compositions. The combination of statistical tools and enhanced petrological visualizations can be used to identify key components of the geochemical variance that isolate titanite's response to strain and fabric development. This petrochronological workflow complements and extends diffusion-based thermochronometers to higher temperature deformation processes. and can become a valuable tool for tectonics research in granitoid-hosted shear zones.

7. Figure captions

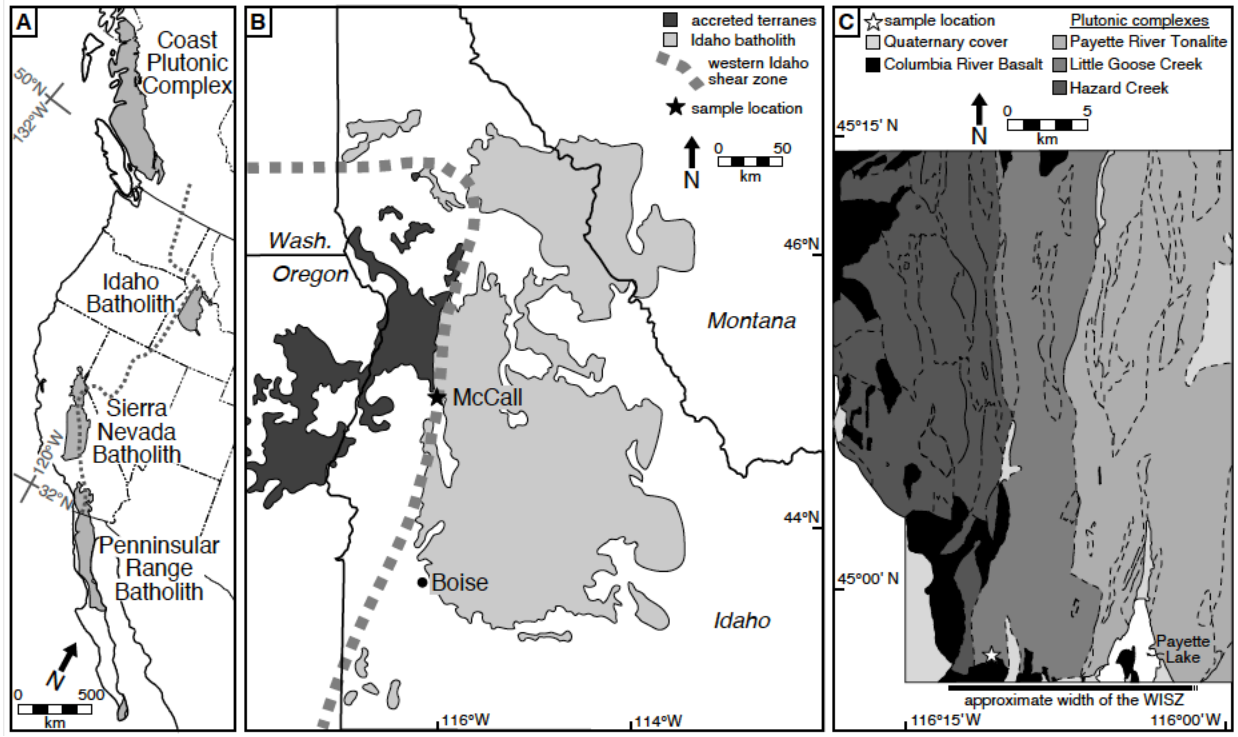

Figure 1. (A) Map of the North American Cordillera with batholiths (gray polygons) and the $^{87}Sr/^{86}Sr = 0.706$ isopleth (thick dashed line). (B) Map of the location of the western Idaho shear zone (dashed line) in relation to accreted terranes and the Idaho Batholith. Modified from (Lund, 1995). Wash. – Washington. (C) Map of the plutonic complexes deformed by the western Idaho shear zone near McCall, Idaho. Contacts between mapped units within each plutonic complex are indicated with solid (observed) and dashed (interpreted) lines. Modified from

(Manduca, 1988). WISZ – western Idaho shear zone.

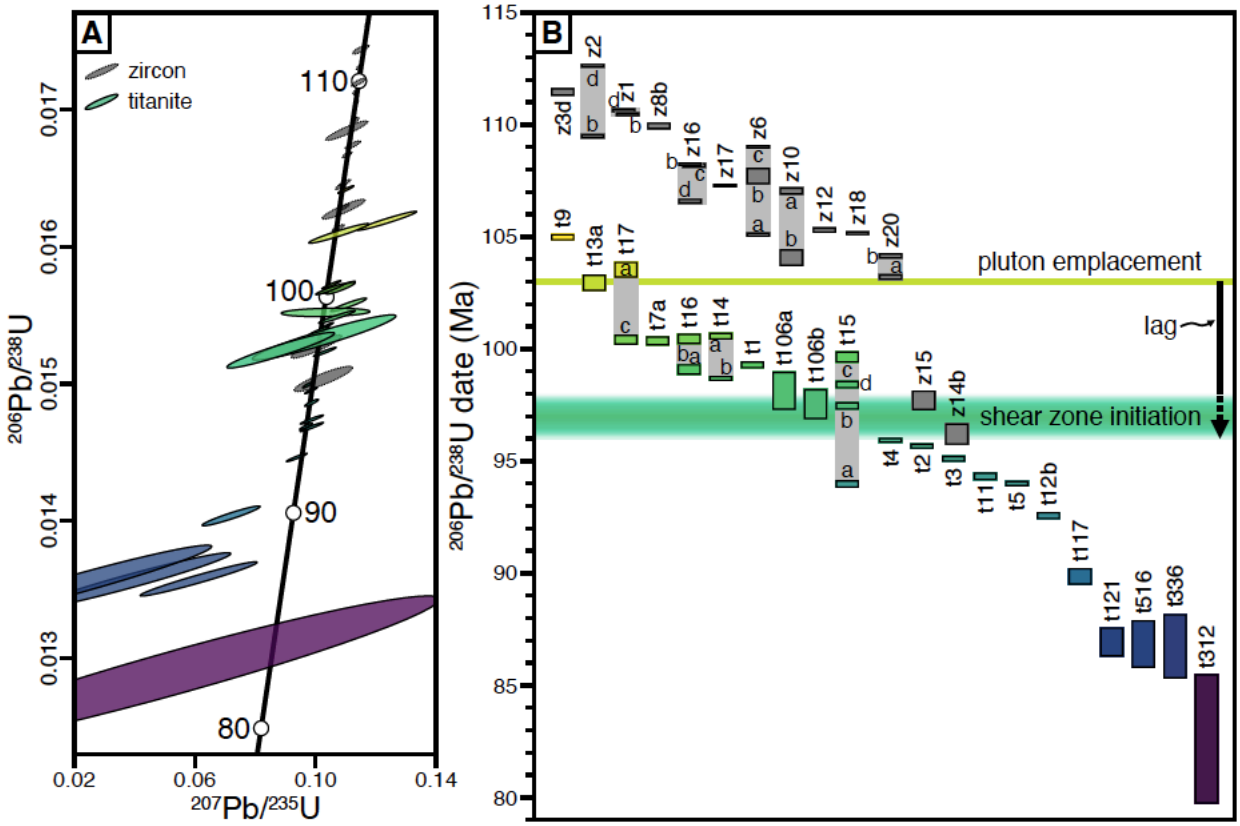

Figure 2. (A) Zircon (gray ellipses with dotted borders) and titanite (colored ellipses with solid borders) ID-TIMS dates in Wetherill concordia space. Titanite is colored according to $^{206}Pb/^{238}U$ date. (B) Ranked date plot of zircon (dark gray) and titanite (colored) ID-TIMS dates. The height of the rectangles is the 2σ uncertainty on the $^{206}Pb/^{238}U$ dates. Light gray bars connect fragments of the same crystal. Titanite crystals are colored according to $^{206}Pb/^{238}U$ date. The horizontal light green line indicates the timing of pluton emplacement. The horizontal dark green band indicates the interval during which the shear zone initiated, 98 to 96 Ma. The vertical black arrow represents the time lag between pluton emplacement and the start of shear zone

deformation.

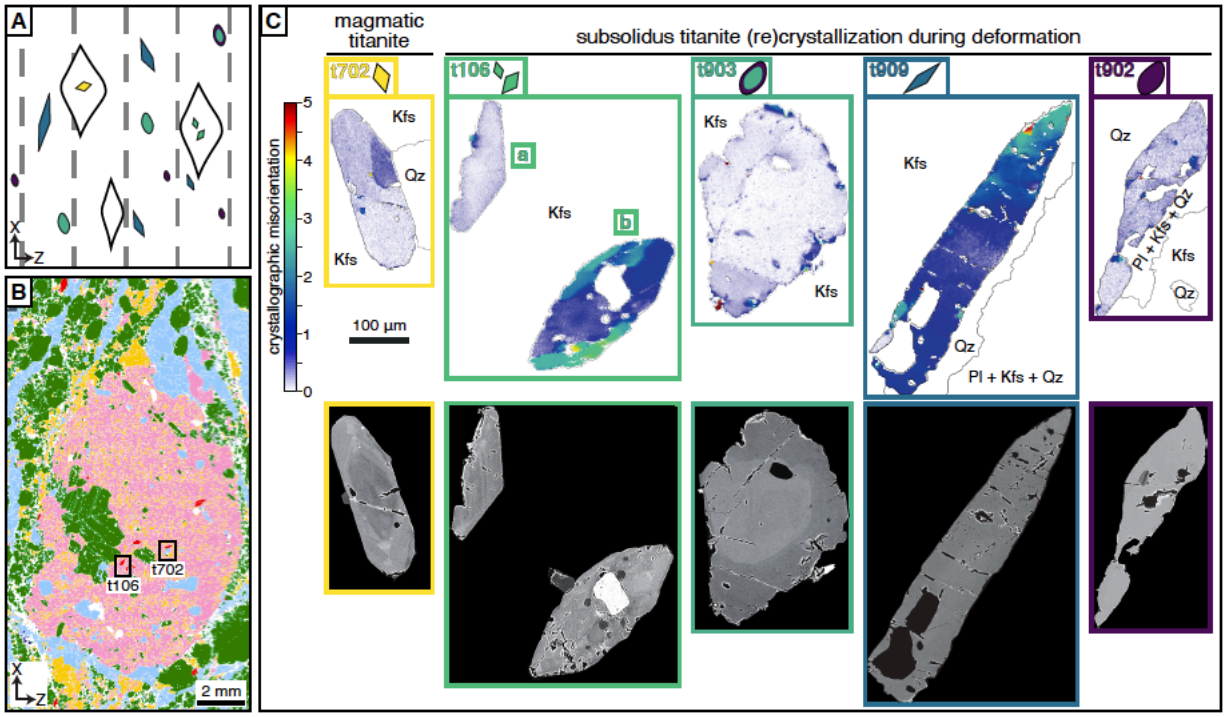

Figure 3. (A) Schematic XZ section (dashed lines parallel to lineation) with feldspar porphyroclasts (solid black lines) and titanite grains (colored shapes). This schematic highlights different titanite populations: euhedral diamonds are magmatic or partially recrystallized grains; elongate, subhedral shape are recrystallized grains; and rounded shapes represent neoblastic grains. (B) EBSD phase map of an XZ section with a K-feldspar porphyroclast (pink) surrounded by quartz ribbons (blue) and calcic and sodic plagioclase (green and yellow, respectively). Titanite grains (red) can be observed both within and outside the porphyroclast. Black boxes indicate titanite grains from this section that are highlighted in (C). (C) Grain numbers and schematic grain shapes are paired with grains representative of the characteristic types. Boxes and labels are colored according to estimated age based on position within geochemical trends shown in Figure 4. Top row: titanite crystallographic maps colored for misorientations from 0-5°, with quartz (Qz), plagioclase (Pl), and K-feldspar (Kfs) labeled. Bottom row: BSE images of

each grain.

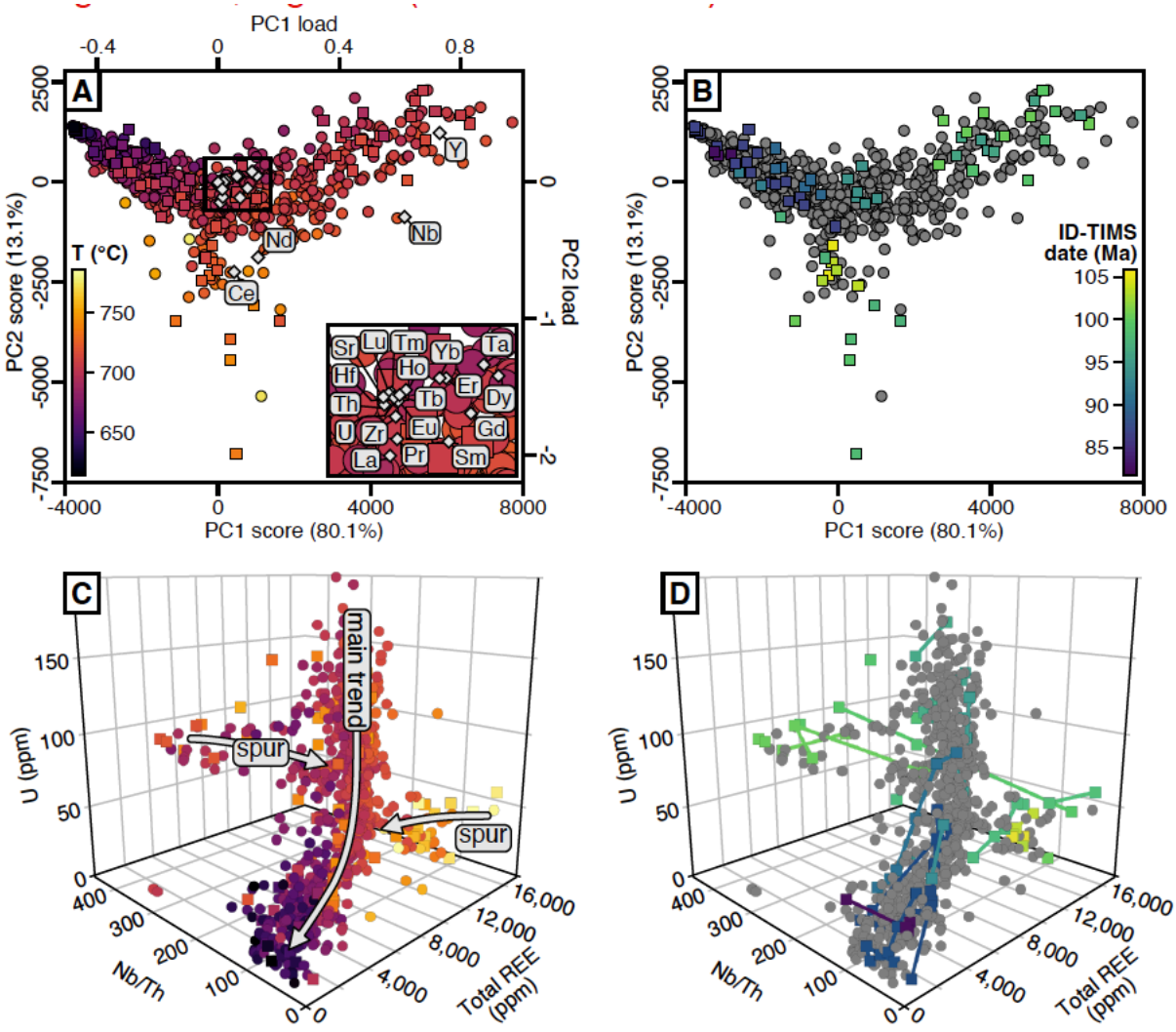

Figure 4. Trace element chemistry of titanite with ID-TIMS-dated crystals indicated by squares and undated crystals indicated by circles. Principal component analysis plots colored by (A) temperature and (B) ID-TIMS date. Principal component loads are shown as gray diamonds in (A). 80.1% and 13.1% are the percent contributions of principal components 1 and 2, respectively. Trivariate total REE–U–Nb/Th plots colored by (C) temperature and (D) ID-TIMS date. In (D), colored lines connect fragments of the same titanite crystal. Color bars in (A) and (B) also apply to (C) and (D), respectively. T – temperature, PC1 – principal component 1, PC2

– principal component 2.

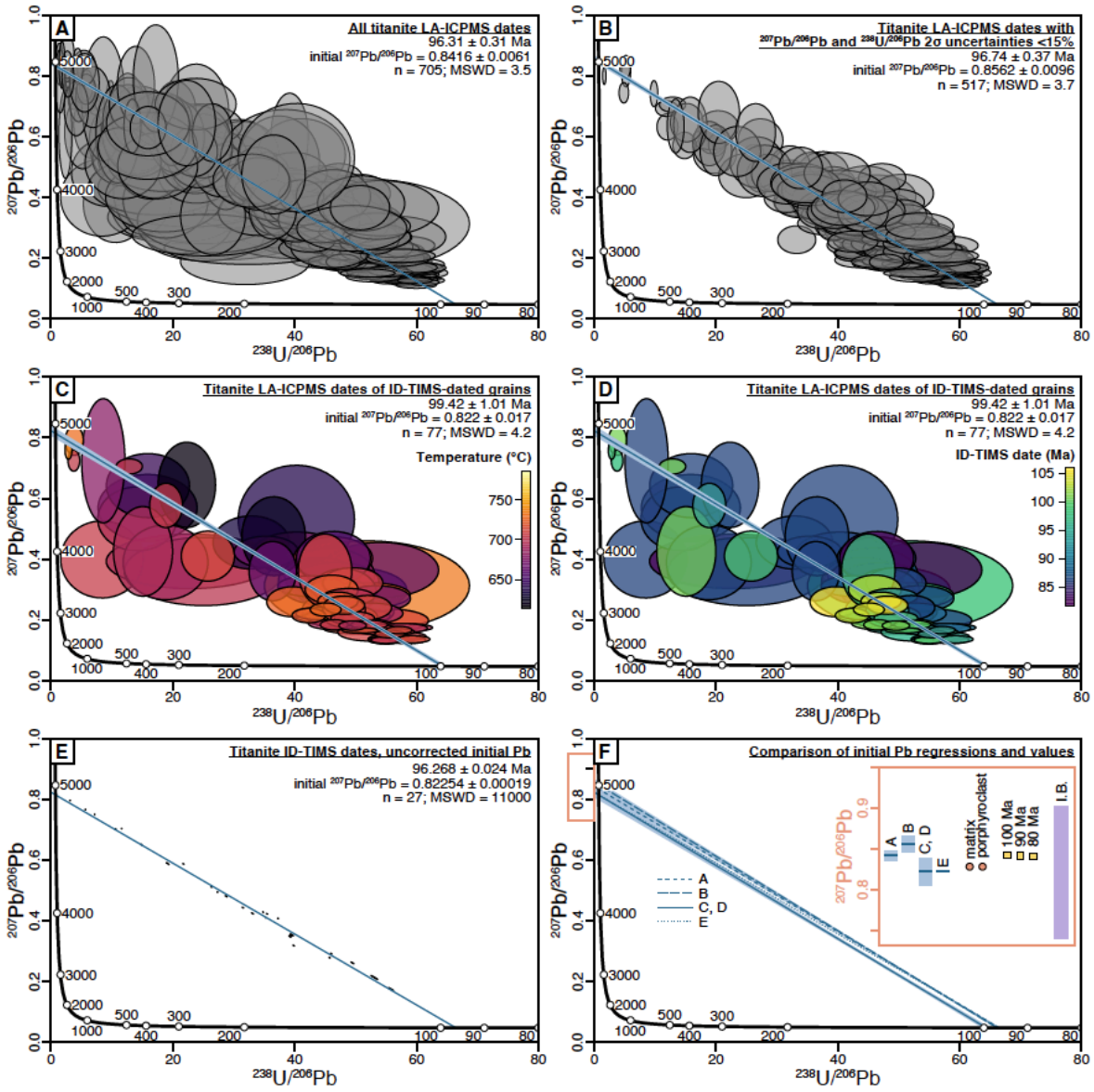

Figure 5. Comparison of titanite LA-ICPMS and ID-TIMS dates and regressions in Tera-Wasserburg concordia space. The concordia intercept age ± 95% confidence interval and the initial $^{207}Pb/^{206}Pb$ value ± 95% confidence interval are determined using the maximum likelihood algorithm of (Ludwig, 1998) and represented in the plots as dark blue lines in panels A-F with light blue error envelopes. Uncertainty in the isotopic measurements is shown as 95% confidence ellipses. (A) All titanite LA-ICPMS dates. (B) Titanite LA-ICPMS dates with $^{207}Pb/^{206}Pb$ and $^{238}U/^{206}Pb$ 2σ uncertainties <15%. (C, D) Titanite LA-ICPMS dates of spots on crystals or crystal fragments later dissolved for ID-TIMS colored by temperature (C) or ID-TIMS date (D). (E)

Titanite ID-TIMS dates with no initial Pb correction applied. (F) Comparison of the regressions in panels A-E. (F, inset) Comparison of initial $^{207}Pb/^{206}Pb$ regression values and uncertainties from panels A-E (blue rectangles), measured $^{207}Pb/^{206}Pb$ values from matrix and porphyroclast K-feldspar (orange circles; 95% confidence interval analytical uncertainty is smaller than the size of the symbols), modeled $^{207}Pb/^{206}Pb$ using a two-stage isotope evolution model (Stacey and Kramers, 1975; yellow squares), and the range of modern whole rock $^{207}Pb/^{206}Pb$ values from the Idaho Batholith (Gaschnig et al., 2011; purple rectangle; I.B.–Idaho Batholith).

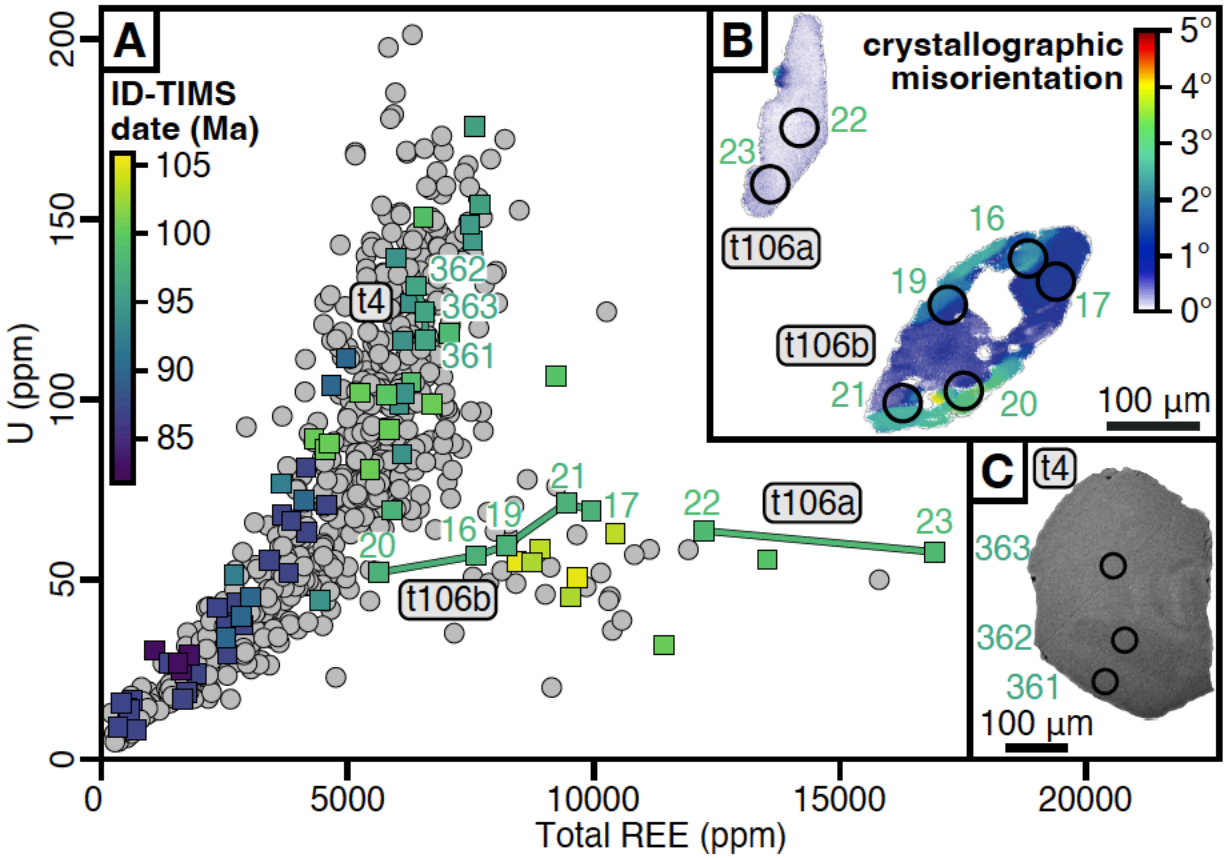

Figure 6. (A) Rotated view of the trivariate REE–U–Nb/Th plot (symbols as in Figure 4D) showing the main trend and lower U spur in total REE vs. U space. LA-ICPMS spot numbers for key titanite grains (t4, t106a, t106b) are highlighted in the geochemistry plot and mapped on (B) crystallographic misorientation maps of t106a and t106b and (C) a BSE image of t4.

Table 1: Summary of microstructural and textural titanite characteristics.

Example grain	t702	t106b	t903	t909	t902
Morphology	wedge-shaped	wedge-shaped	rounded and lenticular	subhedral, elongate	elongate and boudinaged
Fabric context	within K-feldspar porphyroclasts, titanite c-axis is parallel to the lineation	within K-feldspar porphyroclasts, titanite c-axis at high angle to the fabric	within ribboned quartz and myrmekitic feldspar domains	titanite c-axis parallel to the margin of K-feldspar porphyroclasts and ribboned quartz domains	within ribboned quartz and myrmekitic feldspar domains
Backscattered electron zoning	oscillatory	oscillatory	core and rim zones	minimal variation	minimal variation
Degree of misorientation	low (< 1°)	moderate to high (up to 4°)	low (< 2°)	high (up to 5°), highest misorientation at grain tips	low (< 2°)
Interpreted category	magmatic	partially recrystallized	neoblastic	fully recrystallized	neoblastic

8. References

Bachmann, F., Hielscher, R., Schaeben, H., 2010. Texture Analysis with MTEX – Free and Open Source Software Toolbox. Solid State Phenomena 160, 63–68.

Bartley, J.M., Glazner, A.F., Coleman, D.S., 2018. Dike intrusion and deformation during growth of the Half Dome pluton, Yosemite National Park, California. Geosphere 14, 1283 1297. https://doi.org/10.1130/ges01458.1

Bonamici, C.E., Blum, T.B., 2020. Reconsidering initial Pb in titanite in the context of in situ dating. Am Mineral 105, 1672–1685. https://doi.org/10.2138/am-2020-7274

Bonamici, C.E., Fanning, C.M., Kozdon, R., Fournelle, J.H., Valley, J.W., 2015. Combined oxygen-isotope and U-Pb zoning studies of titanite: New criteria for age preservation. Chem Geol 398, 70 84. https://doi.org/10.1016/j.chemgeo.2015.02.002

Braudy, N., Gaschnig, R.M., Wilford, D.E., Vervoort, J.D., Nelson, C.L., Davidson, C., Kahn, M.J., Tikoff, B., 2017. Timing and deformation conditions of the western Idaho shear zone, West Mountain, west-central Idaho. Lithosphere-us 9, 157–183. https://doi.org/10.1130/l519.1

Condon, D.J., Schoene, B., McLean, N.M., Bowring, S.A., Parrish, R.R., 2015. Metrology and traceability of U–Pb isotope dilution geochronology (EARTHTIME Tracer Calibration Part I). Geochim Cosmochim Ac 164, 464–480. https://doi.org/10.1016/j.gca.2015.05.026

Corfu, F., Hanchar, J.M., Hoskin, P.W.O., Kinny, P., 2003. Atlas of Zircon Textures. Rev Mineralogy Geochem 53, 469–500. https://doi.org/10.2113/0530469

El Korh, A.E., Schmidt, S.T., Ulianov, A., Potel, S., 2009. Trace Element Partitioning in HP–LT Metamorphic Assemblages during Subduction-related Metamorphism, Ile de Groix, France: A Detailed LA-ICPMS Study. J Petrol 50, 1107–1148. https://doi.org/10.1093/petrology/egp034

Fitch, T.J., 1972. Plate convergence, transcurrent faults, and internal deformation adjacent to Southeast Asia and the western Pacific. Journal of Geophysical Research 77, 4432–4460.

Fleck, R.J., Criss, R.E., 1985. Strontium and oxygen isotope variations in Mesozoic and Tertiary plutons of central Idaho. Contributions to Mineralogy and Petrology 90, 291–308. https://doi.org/10.1007/bf00378269

Frost, R.B., Chamberlain, K.R., Schumacher, J.C., 2000. Sphene (titanite): phase relations and role as a geochronometer. Chemical Geology 172, 131–148. https://doi.org/10.1016/s0009-2541(00)00240-0

Garber, J.M., Hacker, B.R., Kylander-Clark, A.R.C., Stearns, M.A., Seward, G., 2017. Controls on Trace Element Uptake in Metamorphic Titanite: Implications for Petrochronology. J Petrol 58, 1031–1058. https://doi.org/10.1093/petrology/egx046

Gaschnig, R.M., Vervoort, J.D., Lewis, R.S., McClelland, W.C., 2010. Migrating magmatism in the northern US Cordillera: in situ U–Pb geochronology of the Idaho batholith. Contrib Mineral Petr 159, 863–883. https://doi.org/10.1007/s00410-009-0459-5

Gaschnig, R.M., Vervoort, J.D., Lewis, R.S., Tikoff, B., 2011. Isotopic Evolution of the Idaho Batholith and Challis Intrusive Province, Northern US Cordillera. J Petrol 52, 2397 2429. https://doi.org/10.1093/petrology/egr050

Getty, S.R., Gromet, L.P., 1992. Geochronological constraints on ductile deformation, crustal extension, and doming about a basement-cover boundary, New England Appalachians. American Journal of Science 292, 359–397. https://doi.org/10.2475/ajs.292.6.359
Getty, S.R., Selverstone, J., Wernicke, B.P., Jacobson, S.B., Aliberti, E., Lux, D.R., 1993. Sm-Nd dating of multiple garnet growth events in an arc-continent collision zone, northwestern U.S. Cordillera. Contributions to Mineralogy and Petrology 115, 45–57.

Giorgis, S., McClelland, W., Fayon, A., Singer, B.S., Tikoff, B., 2008. Timing of deformation and exhumation in the western Idaho shear zone, McCall, Idaho. Gsa Bulletin 120, 1119–1133. https://doi.org/10.1130/b26291.1

Gordon, S.M., Kirkland, C.L., Reddy, S.M., Blatchford, H.J., Whitney, D.L., Teyssier, C., Evans, N.J., McDonald, B.J., 2021. Deformation-enhanced recrystallization of titanite drives decoupling between U-Pb and trace elements. Earth Planet Sc Lett 560, 116810. https://doi.org/10.1016/j.epsl.2021.116810

Gray, K.D., Watkinson, A.J., Gaschnig, R.M., Isakson, V.H., 2012. Age and structure of the Crevice pluton: overlapping orogens in west-central Idaho? Can J Earth Sci 49, 709–731. https://doi.org/10.1139/e2012-016

Hartnady, M.I.H., Kirkland, C.L., Clark, C., Spaggiari, C.V., Smithies, R.H., Evans, N.J., McDonald, B.J., 2019. Titanite dates crystallization: Slow Pb diffusion during super-solidus re-equilibration. J Metamorph Geol 37, 823–838. https://doi.org/10.1111/jmg.12489

Hayden, L.A., Watson, E.B., Wark, D.A., 2008. A thermobarometer for sphene (titanite). Contrib Mineral Petr 155, 529–540. https://doi.org/10.1007/s00410-007-0256-y

Holder, R.M., Hacker, B.R., Seward, G.G.E., Kylander-Clark, A.R.C., 2019. Interpreting titanite U–Pb dates and Zr thermobarometry in high-grade rocks: empirical constraints on elemental diffusivities of Pb, Al, Fe, Zr, Nb, and Ce. Contrib Mineral Petr 174, 1–19. https://doi.org/10.1007/s00410-019-1578-2

Housh, T., Bowring, S.A., 1991. Lead isotopic heterogeneities within alkali feldspars: Implications for the determination of initial lead isotopic compositions. Geochim Cosmochim Ac 55, 2309–2316. https://doi.org/10.1016/0016-7037(91)90106-f

Hutton, D.H.W., Dempster, T.J., Brown, P.E., Becker, S.D., 1990. A new mechanism of granite emplacement: Intrusion in active extensional shear zones. Nature 343, 452–455.

Jaffey, A.H., Flynn, K.F., Glendenin, L.E., Bentley, W.T., Essling, A.M., 1971. Precision measurement of half-lives and specific activities of 235U and 238U. Physical Review C 4, 1889–1906.

Klein, B.Z., Jagoutz, O., 2021. Construction of a trans-crustal magma system: Building the Bear Valley Intrusive Suite, southern Sierra Nevada, California. Earth Planet Sc Lett 553, 116624. https://doi.org/10.1016/j.epsl.2020.116624

Kohn, M.J., 2017. Titanite Petrochronology. Rev Mineralogy Geochem 83, 419–441. https://doi.org/10.2138/rmg.2017.83.13

Krogh, T.E., 1973. A low-contamination method for hydrothermal decomposition of zircon and extraction of U and Pb for isotopic age determinations. Geochim Cosmochim Ac 37, 485 494. https://doi.org/10.1016/0016-7037(73)90213-5

Krueger, R.J., Yoshinobu, A.S., 2018. Structures in the Jackass Lakes pluton−host-rock system, central Sierra Nevada, California, and inferred mid-Cretaceous Farallon−North America plate kinematics. GSA Bulletin 130, 1940–1958. https://doi.org/10.1130/b31992.1

Ludwig, K.R., 1998. On the treatment of concordant uranium-lead ages. Geochimica et Cosmochimica Acta 62, 665–676.

Lund, K., 1995. Metamorphic and structural development of island-arc rocks in the Slate Creek-John Day Creek area, west-central Idaho, in: Vallier, T.L., Brooks, H.C. (Eds.), Geology of the Blue Mountains Region of Oregon, Idaho, and Washington: Petrology and Tectonic Evolution of Pre-Tertiary Rocks of the Blue Mountains Region. pp. 517–540.

Macdonald, F.A., Schmitz, M.D., Strauss, J.V., Halverson, G.P., Gibson, T.M., Eyster, A., Cox, G., Mamrol, P., Crowley, J.L., 2018. Cryogenian of Yukon. Precambrian Res 319, 114–143. https://doi.org/10.1016/j.precamres.2017.08.015

Manduca, C.A., Kuntz, M.A., Silver, L.T., 1993. Emplacement and deformation history of the western margin of the Idaho batholith near McCall, Idaho: Influence of a major terrane boundary. Geological Society of America Bulletin 105, 749–765. https://doi.org/10.1130/0016-7606(1993)105<0749:eadhot>2.3.co;2

Manduca, C.A., Silver, L.T., Taylor, H.P., 1992. 87Sr/86Sr and 18O/16O isotopic systematics and geochemistry of granitoid plutons across a steeply-dipping boundary between contrasting lithospheric blocks in western Idaho. Contrib Mineral Petrol 109, 355–372. https://doi.org/10.1007/bf00283324

Manduca, C.C.A., 1988. Geology and geochemistry of the oceanic arc-continent boundary in the western Idaho Batholith near McCall.

Mattinson, J.M., 2005. Zircon U–Pb chemical abrasion ("CA-TIMS") method: Combined annealing and multi-step partial dissolution analysis for improved precision and accuracy of zircon ages. Chem Geol 220, 47–66. https://doi.org/10.1016/j.chemgeo.2005.03.011

McClelland, W.C., Tikoff, B., Manduca, C.A., 2000. Two-phase evolution of accretionary margins: examples from the North American Cordillera. Tectonophysics 326, 37–55. https://doi.org/10.1016/s0040-1951(00)00145-1

McLean, N.M., Condon, D.J., Schoene, B., Bowring, S.A., 2015. Evaluating uncertainties in the calibration of isotopic reference materials and multi-element isotopic tracers (EARTHTIME Tracer Calibration Part II). Geochim Cosmochim Ac 164, 481–501. https://doi.org/10.1016/j.gca.2015.02.040

Michels, Z.D., Kruckenberg, S.C., Davis, J.R., Tikoff, B., 2015. Determining vorticity axes from grain-scale dispersion of crystallographic orientations. Geology 43, 803–806. https://doi.org/10.1130/g36868.1

Papapavlou, K., Darling, J.R., Storey, C.D., Lightfoot, P.C., Moser, D.E., Lasalle, S., 2017. Dating shear zones with plastically deformed titanite: New insights into the orogenic evolution of the Sudbury impact structure (Ontario, Canada). Precambrian Res 291, 220–235. https://doi.org/10.1016/j.precamres.2017.01.007

Pennacchioni, G., Zucchi, E., 2013. High temperature fracturing and ductile deformation during cooling of a pluton: The Lake Edison granodiorite (Sierra Nevada batholith, California). J Struct Geol 50, 54 81. https://doi.org/10.1016/j.jsg.2012.06.001

Prior, D.J., Boyle, A.P., Brenker, F., Cheadle, M.C., Day, A., Lopez, G., Peruzzi, L., Potts, G., Reddy, S., Spiess, R., Timms, N.E., Trimby, P., Wheeler, J., Zetterstrom, L., 1999. The application of electron backscatter diffraction and orientation contrast imaging in the SEM to textural problems in rocks. American Mineralogist 84, 1741–1759. https://doi.org/10.2138/am-1999-11-1204

Prior, D.J., Wheeler, J., Peruzzi, L., Spiess, R., Storey, C., 2002. Some garnet microstructures: An illustration of the potential of orientation maps and misorientation analysis in microstructural studies. Journal of Structural Geology 24, 999–1011.

Resor, P.G., Chamberlain, K.R., Frost, C.D., Snoke, A.W., Frost, B.R., 1996. Direct dating of deformation: U-Pb age of syndeformational sphene growth in the Proterozoic Laramie Peak shear zone. Geology 24, 623–626. https://doi.org/10.1130/0091-7613(1996)024<0623:ddodup>2.3.co;2

Rossetti, F., Asti, R., Faccenna, C., Gerdes, A., Lucci, F., Theye, T., 2017. Magmatism and crustal extension: Constraining activation of the ductile shearing along the Gediz detachment, Menderes Massif (western Turkey). Lithos 282, 145–162. https://doi.org/10.1016/j.lithos.2017.03.003

Schmitz, M.D., Bowring, S.A., 2001. U-Pb zircon and titanite systematics of the Fish Canyon Tuff: an assessment of high-precision U-Pb geochronology and its application to young volcanic rocks. Geochim Cosmochim Ac 65, 2571–2587. https://doi.org/10.1016/s0016-7037(01)00616-0

Schmitz, M.D., Schoene, B., 2007. Derivation of isotope ratios, errors, and error correlations for U-Pb geochronology using 205Pb-235U-(233U)-spiked isotope dilution thermal ionization mass spectrometric data. Geochem Geophys Geosystems 8, 1–20. https://doi.org/10.1029/2006gc001492

Stacey, J.S., Kramers, J.D., 1975. Approximation of terrestrial lead isotope evolution by a two-stage model. Earth and Planetary Science Letters 26, 207–221.

Stern, R.A., 1997. The GSC Sensitive High Resolution Ion Microprobe (SHRIMP): analytical techniques of zircon U-Th-Pb age determinations and performance evaluation. Geological Society of Canada, Current Research, Radiogenic Age and Isotopic Studies: Report 10 1997-F, 1–31. https://doi.org/10.4095/209089

Storey, C.D., Jeffries, T.E., Smith, M., 2006. Common lead-corrected laser ablation ICP–MS U–Pb systematics and geochronology of titanite. Chem Geol 227, 37–52. https://doi.org/10.1016/j.chemgeo.2005.09.003

Strelow, F.W.E., Toerien, F.V.S., 1966. Separation of Lead(ll) from Bismuth(lll), Thallium(lll), Cadmium(ll), Mercury(ll), Gold(lll), Platinum(IV), Palladium(ll), and Other Elements by Anion Exchange Chromatography. Analytical Chemistry 38, 545–548.

Tikoff, B., et al., 2022. Hit and Run.

Tikoff, B., Kelso, P., Manduca, C., Markley, M.J., Gillaspy, J., 2001. Lithospheric and crustal reactivation of an ancient plate boundary: the assembly and disassembly of the Salmon River suture zone, Idaho, USA. Geological Soc Lond Special Publ 186, 213–231. https://doi.org/10.1144/gsl.sp.2001.186.01.13

Titus, S.J., Clark, R., Tikoff, B., 2005. Geologic and geophysical investigation of two fine-grained granites, Sierra Nevada Batholith, California: Evidence for structural controls on emplacement and volcanism. Gsa Bulletin 117, 1256 16. https://doi.org/10.1130/b25689.1

Torvela, T., Mänttäri, I., Hermansson, T., 2008. Timing of deformation phases within the South Finland shear zone, SW Finland. Precambrian Res 160, 277–298. https://doi.org/10.1016/j.precamres.2007.08.002

Appendix

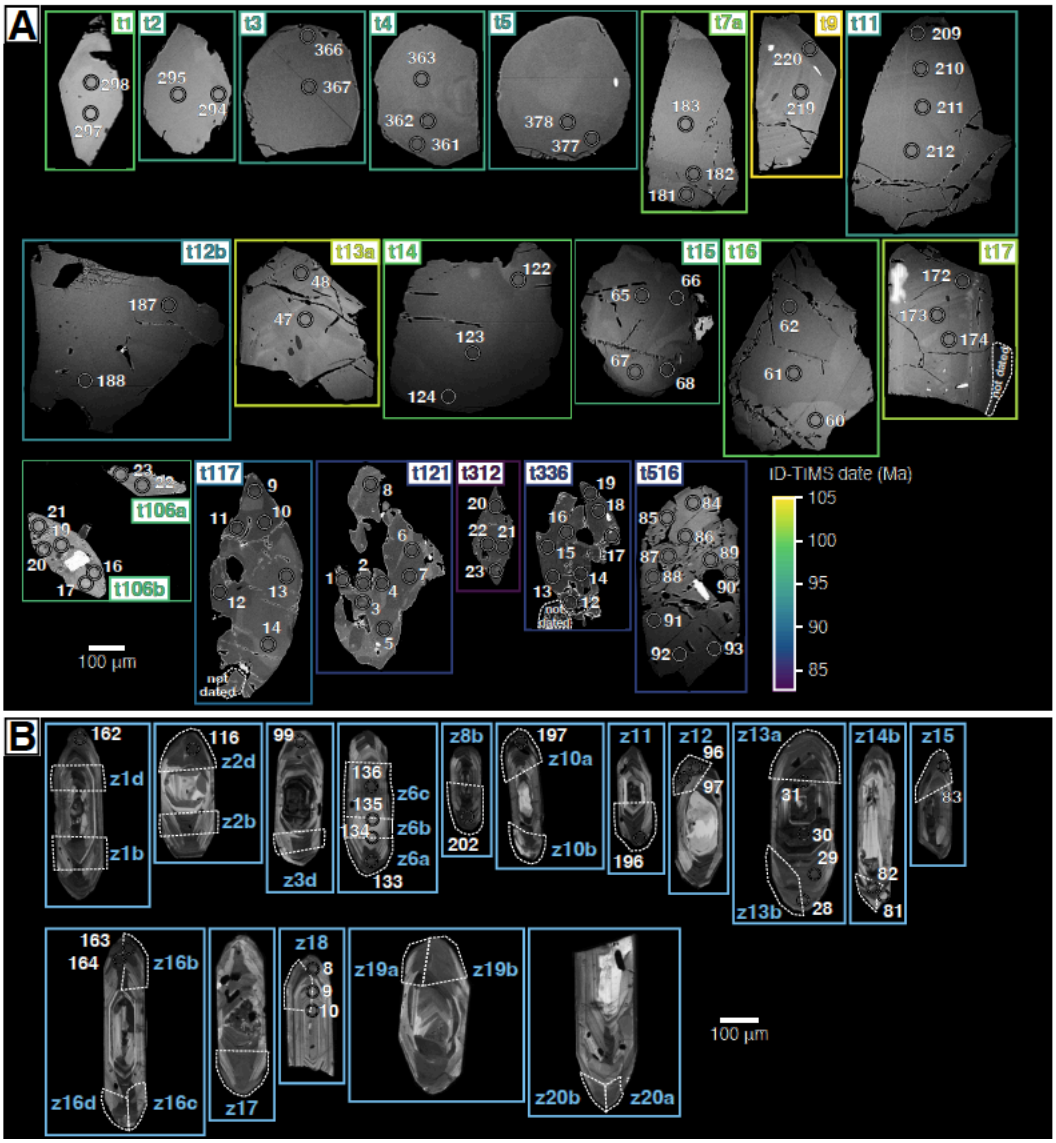

Supplemental Figure S1. (A) Backscattered electron (BSE) images of isotope dilution–thermal ionization mass spectrometry (ID-TIMS)–dated titanite crystals with borders colored by ID-TIMS date. White open circles and white numbers on the BSE images indicate laser ablation–inductively coupled plasma mass spectrometry (LA-ICPMS) spot placement and reference number. Locations of subsampled titanite crystal fragments not indicated because some

fragments were taken from entirely below the plane of the BSE image. (B) Cathodoluminescence images of zircon dated by ID-TIMS with dated fragments indicated (white dashed polygons). White open circles and white numbers indicate LAICPMS spot placement and reference number.

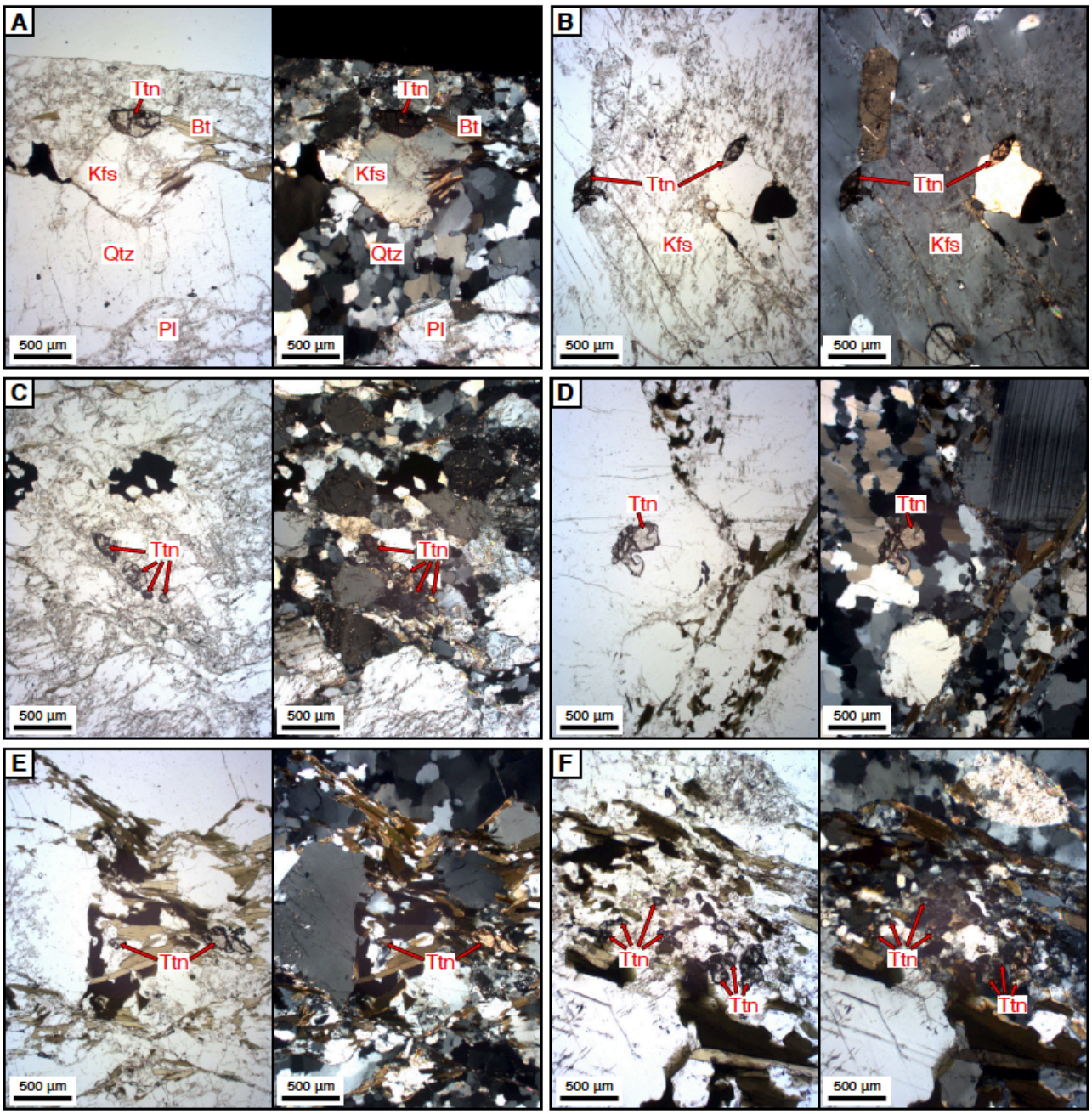

Supplemental Figure S2. Plane polarized light (left) and cross polarized light (right) photomicrographs of sample 14WZ3-2, a K-feldspar porphyritic granodiorite orthogneiss composed of K-feldspar (Kfs), plagioclase (Pl), quartz (Qtz), biotite (Bt) ± hornblende, titanite (Ttn), allanite, apatite, zircon, and oxides. Quartz subgrains have cuspate and lobate boundaries (e.g., A). Titanite is present as inclusions in potassium feldspar megacrysts and in the matrix. Titanite grains included in the megacrysts are euhedral and dark brown (e.g., B). In the matrix, titanite ranges from suhedral (e.g., C) to anhedral (e.g., D) and tends to be lighter in color than the euhedral grains included in the megacrysts. Titanite in the matrix is primarily found in areas with a higher concentration of biotite, like the folia surrounding a K-feldspar porphyroclast (e.g., A, E). Where a titanite grain in the matrix has a subhedral wedge shape, the longest axis of the wedge tends to align with nearby biotite folia (e.g., E). Titanite is also found in clusters of anhedral grains (e.g., F), and these grains are typically smaller than solitary matrix titanite (e.g., D).

Chapter 3: Exploring the emplacement of Cretaceous arc granites and dextral shear zones in northwestern Nevada, USA, using the StraboSpot data system

Abstract

This field trip traverses the Sahwave and Nightingale Ranges in central Nevada, USA, and northward to Gerlach, Nevada, to the Granite, northern Fox, and Selenite Ranges. Plutonic bodies in this area include the ca. 93–89 Ma Sahwave nested intrusive suite of the Sahwave and Nightingale Ranges, the ca. 106 Ma Power Line intrusive complex of the Nightingale Range, the ca. 96 Ma plutons in the Selenite Range, and the ca. 105–102 Ma plutons of the Granite and Fox Ranges. Collectively these plutons occupy nearly 1000 km^2 of bedrock exposure. Plutons of the Sahwave, Nightingale, and Selenite Ranges intrude autochthonous rocks east of the western Nevada shear zone, while plutons of the Granite and Fox Ranges intrude displaced terranes west of the western Nevada shear zone. Integrated structural, geochemical, and geochronological studies are used to better understand magmatic and deformation processes during the Early Cretaceous, correlations with Cretaceous plutons in adjacent areas of Idaho and California, and regional implications.

Field-trip stops in the Sahwave and Nightingale Ranges will focus on: (1) microstructure and orientation of magmatic and solid-state fabrics of the incrementally emplaced granodiorites-granites of the Sahwave intrusive suite; and (2) newly identified dextral shear zones hosted within intrusions of both the Sahwave and Nightingale Ranges. The Sahwave intrusive suite exhibits moderate to weak magnetic fabrics determined using anisotropy of magnetic susceptibility, with magnetic foliations that strike NW-NE and magnetic lineations that plunge moderately to steeply. Microstructural analysis indicates that these fabrics formed during

magmatic flow. The older Power Line intrusive complex in the Nightingale Range is cross-cut by the Sahwave suite and contains a N-S–trending solid-state foliation that reflects ductile dextral shearing. Field-trip stops in the plutons of the Gerlach region will focus on composition, texture, and emplacement ages, and key differences with the younger Sahwave suite, including lack of evidence for zoning and solid-state fabrics. The field trip will utilize StraboSpot, a digital data system for field-based geology that allows participants to investigate the relevant data projects in the study areas.

1. Introduction

The Mesozoic–Cenozoic history of the U.S. Cordillera is dominated by subduction, accreted terrane collision, arc magmatism during the Mesozoic, and younger extensional deformation starting at ca. 30 Ma (e.g., Oldow, 1984; Burchfiel et al., 1992; Dickinson, 2008; Lund, 2008). The eastward subduction of the oceanic plates below North America are inferred to have caused punctuated arc magmatism from the Triassic through the Cretaceous, although there have been arguments for a period of westward subduction (e.g., Hildebrand, 2013) For this guide, we will focus on summarizing the background for Cretaceous magmatism and deformation in the central Cordillera region (California to Idaho).

Volumetrically significant Cretaceous magmatism occured on the western margin of the North American Cordillera (Fig. 1). It is evidenced by the coeval 120–85 Ma Cordilleran batholiths exposed in the Peninsular Ranges of Baja California and southern California, Sierra Nevada mountains, desert ranges of NW Nevada, the western margin of a batholith in NW Idaho, and the Coast Range of coastal Canada (e.g., Armstrong, 1988; Bateman, 1992; Manduca et al., 1993; Ducea, 2001; Schmidt and Paterson, 2002; Van Buer and Miller, 2010). This magmatic

flare-up event has been attributed to various causes, including episodic mantle and crustal processes that lead to magmatism-tectonism feedback (e.g., Ducea, 2001; Ducea and Barton, 2007; DeCelles et al., 2009; Ducea et al., 2015; Martínez Ardila et al., 2019) and/or tectonically driven processes (e.g., Tikoff and Teyssier, 1992; de Saint Blanquat et al., 2011; Kirsch et al., 2016). The timing and nature of magmatism, however, varies from south to north along the U.S. continental margin. Metaluminous magmatism in the Peninsular Range batholith ceases at ca. 90 Ma (Silver and Chappell, 1988; Gaschnig et al., 2017) but persists in the Sierra Nevada batholith until ca. 83 Ma (Everden and Kistler, 1970; Chen and Moore, 1982; Kistler et al., 1986; Bateman, 1992; Coleman et al., 2004). In the Idaho batholith, the timing and nature of magmatism is significantly different from the Peninsular Range and Sierra Nevada batholiths. Metaluminous magmatism in the Idaho batholith—mostly located on the western margin of the batholith—ceases at 85 Ma (Gaschnig et al., 2010; 2011; Manduca et al., 1993; Lund, 2008), while peraluminous magmatism in the main section of the Idaho batholith—the Atlanta and the Bitteroot lobes—starts at 85 Ma and ceases by 60 Ma (Gaschnig et al., 2010).

Episodes of Cretaceous magmatism were accompanied by major dextral terrane displacment inferred to have occurred in the Early Cretaceous. This offset is manifested by the proposed Mojave–Snow Lake fault in the Sierra Nevada (Lahren et al., 1990; Schweickert and Lahren, 1990), and the western Nevada shear zone in northwest Nevada and southeast Oregon (Wyld and Wright, 2001). Subsequently, major Cretaceous arc magmatism occurred along or near this older shear zone, which corresponds to a terrane margin in northwestern Nevada and arguably also within the Sierra Nevada. Magmatic and solid-state fabrics, preserved in these Cretaceous plutons, provide the first direct evidence for dextral transpression. These shear zones initiate at ca. 100 Ma, with deformation in the central Sierra Nevada (Krueger and Yoshinobu,

2018) and the western Idaho shear zone (e.g., Giorgis et al., 2008; Braudy et al., 2017). In the Sierra Nevada batholith, the shearing migrated eastward with the magmatism. The youngest dextral transpression episode is recorded by the Sierra Crest shear zone in the Sierra Nevada batholith, in which deformation lasts until ca. 80 Ma. Interestingly, the deformation in the western Idaho shear zone is now thought to also extend until 85 Ma, with the youngest shearing occurring on the east side of the zone (Ostwald et al., 2017). In general, the Sierra Crest shear zone preserves lower strains and less documented offset than the western Idaho shear zone (Tikoff and de Saint Blanquat, 1997; Cao et al., 2015).

The key to resolving these along-strike differences can be found in the plutons in northwestern Nevada. In the intervening region of northwest Nevada, there was little direct evidence for syn-magmatic Cretaceous dextral transpressional deformation that could be correlated with either the Sierra Crest or western Idaho shear zones. In this field guide, we will focus on the region from the Sahwave and Nightingale Ranges to the area around the town of Gerlach (Selenite, Granite and Fox Ranges), where multiple large Cretaceous plutons are exposed. We will focus on composition and structural relations of the Cretaceous plutons that ~~will~~ facilitate links with areas to the north (western Idaho) and south (Sierra Nevada).

In the first half of the field guide, we present U-Pb zircon geochronology, field and microstructural analysis, and anisotropy of magnetic susceptibility results from intrusive units of the Sahwave and Nightingale Ranges (Sahwave batholith and Power Line intrusive complex). These data indicate magmatism from ca. 106–88 Ma, mostly of granodiorite composition, with evidence for an episode of solid-state deformation and dextral shearing between ca. 106–94 Ma, followed by more limited synplutonic deformation from ca. 94–88 Ma.

In the second half of the field guide, we present geochronologic, compositional, and structural relations of Gerlach area plutons to the north and northwest. This area also contains multiple large granodioritic Cretaceous plutons, including those of the Selenite Range (ca. 96 Ma), Granite Range (ca. 102 Ma), and Fox Range (ca. 105–103 Ma). Plutonic rocks of the Selenite Range show a variably developed, magmatic foliation, but plutonic rocks of the Granite Range and Fox Ranges are generally undeformed. Interpreting how data from plutons of this area relate to data from the Sahwave and Nightingale Ranges is a focus of the guide.

1.1 Cretaceous Deformation

A major change in plate motion in the central-western United States is hypothesized to have occurred at ca. 100 Ma (Saleeby et al., 2007, 2008; Matthews et al., 2012; Hildebrand, 2013). A major shift from left-lateral to right-lateral motion along the continental boundary was hypothesized to occur at ca. 100 Ma (Oldow, 1984) but the amount of dextral shearing and intra-arc deformation preserved in these arc systems varies significantly along strike in the Cordillera. For context we will discuss deformation characteristics preserved in the Sierra Crest shear zone in the Sierra Nevada batholith, the western Nevada shear zone in northern Nevada, and the western Idaho shear zone in Idaho.

The main dextral strike-slip deformation within the Sierra Nevada arc initiated at ca. 92 Ma within the Sierra Crest shear zone (Tikoff and de Saint Blanquat, 1997; Fig. 2). The Sierra Crest shear zone formed along the eastern boundary of the Sierra Nevada batholith (e.g., Tikoff and Greene, 1997; Tikoff and de Saint Blanquat, 1997) and comprises several structures. From south to north, these are the proto–Kern Canyon fault (Busby-Spera and Saleeby, 1990), the Rosy Finch shear zone (Tikoff and Teyssier, 1992), the Gem Lake shear zone (Greene and

Schweickert, 1995), and the Cascade Lake shear zone (Tikoff et al., 2005; Cao et al., 2015). These dextral shear zones are thought to have been active during the last stage of arc magmatism (Busby-Spera and Saleeby, 1990; Tikoff and Teyssier, 1992; Greene and Schweickert, 1995; Tikoff and de Saint Blanquat, 1997). Foliation in the Sierra Crest shear zone is NNW trending and subvertical, but lineation varies from horizontal to vertical, a pattern that could be indicative of wrench-dominated transpressional deformation (Tikoff and Greene, 1997). Sierra Crest shear zone fabric textures and orientations from the youngest plutonic units of the Tuolumne intrusive suite, the Mono Pass intrusive suite, and Mount Whitney intrusive suite are indicative of lower strains with greater strains preserved in Triassic and Jurassic units (e.g., Cao et al., 2015). Dextral transpressional deformation at ca. 100 Ma in the Sierra Nevada batholith is recorded by isolated shear zones intruded by younger granitic bodies (Krueger and Yoshinobu, 2018).

In contrast, the highly telescoped plutons and wall rocks in the western Idaho shear zone preserve higher strains produced by deformation that initiated at ca. 100 Ma (McClelland et al., 2000; Tikoff et al., 2001; Fig. 3). The western Idaho shear zone is a steeply dipping, dextral transpressive shear zone coincident with the locally N-S–trending Sr_i 0.706 line (Armstrong et al., 1977; Fleck and Criss, 1985; Tikoff et al., 2001). Giorgis et al. (2008) attributed the dextral transpressional deformation in the western Idaho shear zone to the docking of the Insular superterrane outboard of the magmatic arc (Fig. 3). Western Idaho shear zone deformation is preserved in the fabrics of the preexisting Hazard Creek complex and syntectonically emplaced Payette River tonalite of the Idaho batholith (McClelland et al., 2000). The solid-state foliation—defined by aligned mica, amphibole, and ribboned quartz grains—strikes N-S and dips steeply to the east. Finite strain in the western Idaho shear zone is much higher than strain in the Sierra

Crest shear zone, such that all intrusive contacts have been rotated into parallelism with the shear zone (e.g., Tikoff et al., 2001).

From northwest Nevada to southeast Oregon, Wyld and Wright (2001) documented a segment of dextral strike-slip shearing known as the western Nevada shear zone (Fig. 4). The western Nevada shear zone is a localized band of N-striking shear zones separating the Pueblo terrane and Gerlach area rocks from the Black Rock terrane. The timing of northward strike-slip displacement of the Pueblo terrane along the western Nevada shear zone is broadly constrained to the Early Cretaceous/Late Jurassic as it displaced Middle Jurassic (Pueblo terrane) assemblages.

Part of the difficulty in providing direct evidence for Cretaceous strike-slip tectonism in northwestern Nevada is that NE-trending granitoid bodies are sparsely distributed within the Basin and Range province. Such present-day exposures may represent a highly fragmented magmatic arc with segmented shear zones overprinted by the Basin and Range extension. Further, the Miocene–present Eastern California shear zone causes ~300 km of northward motion of the Sierra Nevada block (Atwater and Stock, 1998; Wernicke and Snow, 1998; McQuarrie and Wernicke, 2005). In the study area, there is evidence of deformation in 106–88 Ma plutons, which we will explore more in this field guide.

1.2 Northwestern Nevada plutons

The Late Cretaceous Sahwave batholith located ~100 km NE of Reno, Nevada, is a particularly continuous, nested intrusive suite emplaced between 105 and 89 Ma. The granodiorite plutons of the Sahwave batholith are broadly similar in composition, age, and emplacement pattern (Van Buer and Miller, 2010) to the Tuolumne intrusive suite but are

chemically more primitive ($^{87}Sr/^{86}Sr = 0.7046$, $\varepsilon_{Nd} = -0.2$). The plutons of the Sahwave and Nightingale Ranges are separated from the plutons of the Trinity Range, the Selenite Range, the Fox Range, and the Granite Range (Fig. 4) by several kilometers of metamorphic wall rocks which vary from east to west. In general, wall rocks to the east can be assigned to one of two well-established terranes: the Black Rock arc terrane or the back-arc Jungo basinal terrane (Fig. 4; Silberling et al., 1987; Quinn et al., 1997; Wyld, 2000). The Black Rock arc terrane consists of a thick Paleozoic substrate of deep marine siliciclastic and lesser volcanic rocks, overlain by a distinctive assemblage of deep marine Late Triassic to Early Jurassic mafic to intermediate volcanogenic arc rocks, and lesser sedimentary strata, all of which are intruded by Early to Middle Jurassic plutons (Wyld, 1990; Quinn et al., 1997). The Late Triassic Jungo terrane, which lies generally east and south of the Black Rock terrane, consists dominantly of very fine-grained siliciclastic strata (now slate and phyllite), with minor interbedded quartzose sandstone and scarce limestone (Lupe and Silberling, 1985; Wyld, 2000, 2002). The metamorphic wall rocks of the Sahwave and Nightingale plutons have been referred to as the Nightingale Sequence, but they are readily correlated with the Late Triassic Jungo terrane on the basis of stratigraphy and structural history (Silberling et al., 1987).

The plutons of the Sahwave and Nightingale Ranges (Fig. 5) are the Power Line granodiorite at 104.9 ± 0.8 Ma; the granodiorite of Juniper Pass at 92.7 ± 1.4 Ma; the granodiorite of Bob Spring at 92.8 ± 1.7 Ma; the School Bus granodiorite at 91.2 ± 1.2; and the Sahwave granodiorite at 88.5 ± 2 Ma (Table 1 and Fig. 5; U-Pb SHRIMP-RG [sensitive high-resolution ion microprobe–reverse geometry] zircon ages; Van Buer and Miller, 2010). The granodiorite of Juniper Pass, the granodiorite of Bob Spring, and the Sahwave granodiorite are the main units of the Sahwave batholith. The Power Line granodiorite is part of an earlier

intrusive event. The plutons of the Sahwave batholith have very similar compositions and crystallization ages to the plutons within the Tuolumne intrusive suite. This similarity is compelling evidence that the Sahwave batholith is a northward continuation of the Late Cretaceous Sierra Nevada magmatic arc into Nevada (Fig. 6).

Granodiorite plutons of similar composition and age to the Sahwave batholith intrude the western Trinity Range (90.3 ± 0.6 Ma; Van Buer and Miller, 2010), the Selenite Range (96.3 ± 0.8 Ma; Van Buer and Miller, 2010), the Fox Range, and the Granite Range. Preliminary mapping indicates that wall rocks in the southwest Selenite Range are very similar to Late Triassic strata of the Jungo terrane (S. Wyld, personal observ.). Rocks that can be assigned to the Jungo terrane are also found to the west in the Lake Range, and to the east in the Bluewing Mountains, Lava Beds, Seven Troughs Mountains, and Trinity Range. Farther north, wall rocks to the Cretaceous intrusions in the northern Selenite Range are similar to Late Triassic to Early Jurassic rocks found in the Black Rock terrane (S. Wyld, personal observ.). Farther west, wall rocks to the Cretaceous intrusions of Granite Mountain and the Fox Range belong to the Granite and Fox terranes, respectively, and are considered to lie west of the western Nevada shear zone (Kinsella et al., 2007; Wyld and Wright, 2019). The western Nevada shear zone, although now concealed by Cenozoic strata and Cretaceous plutons in the study area, thus trends NNE, east of Granite Mountain and the Fox Range, separating the Jungo and Black Rock terranes from allochthonous western assemblages, and obliquely truncating the Black Rock–Jungo terrane boundary.

1.3 An Introduction to StraboSpot

We will utilize the StraboSpot data system throughout the guide (Fig. 7). StraboSpot was designed for the recording, manipulation, analysis, and storage of geology data in a digital

format for structural geology and tectonics (Walker et al., 2019). This data system has been further expanded to include field-based petrology. We are using the StraboSpot system in the Sahwave batholith study area to facilitate a synchronous guided virtual trip (May 2021) and to also allow for an asynchronous self-guided trip using both this guide and the data stored in StraboSpot. The data set is "GSA Sahwave" in the StraboSpot system.

2. StraboSpot Log

Spot 1.1. Overview of the Nightingale and Sahwave Ranges

The Nightingale and Sahwave Ranges together form a single, synclinally folded horst block composed of predominantly granodiorite-composition plutonic rocks (Fig. 5). In the Nightingale Range, the Sahwave batholith (School Bus granodiorite ca. 91 Ma; all ages U-Pb zircon unless otherwise specified) intrudes older intrusive rocks of the Power Line intrusive complex (106 Ma). The Power Line intrusive complex is compositionally variable, but the main unit is a medium-grained biotite-hornblende-granodiorite with ribboned quartz, mafic folia, and potassium feldspar porphyroclasts. The Sahwave Range is composed of the compositionally zoned Sahwave batholith (Van Buer and Miller, 2010): the granodiorite of Juniper Pass (ca. 93 Ma), the granodiorite of Bob Spring (ca. 93 Ma), and the Sahwave granodiorite (ca. 88 Ma). This suite grades from an equigranular tonalite/granodiorite to a more felsic, potassium feldspar megacrystic granodiorite in the center. Units of the Sahwave batholith are intruded into the thick metasedimentary strata of the Jungo terrane.

Geochemical data from Van Buer and Miller (2010) suggest that the Sahwave batholith contains more primitive initial $^{87}Sr/^{86}Sr$ and εNd values (~0.7047 and –0.2, respectively) than the Sierra Nevada batholith, indicative of a slightly different magma source within underlying

mantle lithosphere. Major-element chemistry suggest that the Sahwave batholith represents a magnesian, metaluminous to weakly peraluminous, calc-alkaline series, with an alkali-lime index of 59.6. Major- and trace-element variations with respect to silica show trends consistent with fractional crystallization and mixing (Van Buer and Miller, 2010). However, chondrite-normalized rare-earth-element diagrams of whole-rock and zircon data from the units do show some variation and deviation between the felsic and more mafic units, specifically for the granodiorite of Juniper Pass (Fig. 8).

Optional Spot 1.1a. Holocene Fault Scarps along Sahwave Range Front (40.2895° N, 118.9952° W)

The entire eastern flank of the Sahwave Range is marked by relatively fresh fault scarps and triangular facets related to its active range-bounding normal fault. East of Juniper Pass, clear scarps cutting Holocene alluvium can be viewed from the road intersection. Trenching studies by Wesnousky et al. (2005) have dated the most recent earthquake rupture to ca. 5500 cal. yr B.P.

Optional Spot 1.1b. Sahwave Batholith Intrusive Margin, Southwest Nightingale Range (40.0472° N, 119.2877° W))

In the southwest Nightingale Range, where the granodiorite of Juniper Pass intruded marine metasedimentary strata, the wall rocks exhibit strong ductile deformation within an ~100-m-wide structural aureole (Fig. 9D). Wall rocks in this zone are marked by a strong subvertical mineral lineation as well as tight coaxial ductile curtain folds, and have been metamorphosed to siliceous hornfels and tremolite-diopside-grossular calc-silicates. Outside this aureole, the wall rocks are only lower greenschist facies, and are not lineated. They do, however, contain a NW-trending foliation, parallel to the intrusive contact as much as 5 km from the Sahwave batholith, which is anomalous relative to the regional NE-trending foliations related to the Late Jurassic Luning-Fencemaker thrust belt (e.g., Oldow, 1984; Wyld, 2002). The relative abundance of 10–

100-m-thick marble and calc-silicate layers in these strata also distinguishes them from the generally carbonate-free strata north and east of the Sahwave batholith. This difference in lithology is consistent with the possibility that there may be a significant mid-Jurassic to mid-Cretaceous strike-slip fault running down the length of the batholith.

To access the best contact exposures, park at the location above, and walk 1.35 km up the vehicle-impassible road (to 40.0389° N, 119.2773° W), and then turn up the side canyon to the left. The best wall rock exposures are ~300 m up this side canyon (40.0391° N, 119.2744° W), and you reach good outcrops of the granodiorite of Juniper Pass another 100 m up the canyon (40.0393° N, 119.2736° W).

Optional Spot 1.1c. Nightingale Mine
(40.0099° N, 119.2276° W)

The Nightingale Range is named for the Nightingale Mining District, which straddles the southern intrusive contact of the Sahwave batholith. At the Nightingale Mine itself, the contact between the granodiorite of Juniper Pass and the wall rock marbles occurs in the middle of the extensive (and dangerous) open stopes. Along the contact, skarn mineralization includes quartz, diopside, clinozoisite, grossular/almandine garnet, and scheelite. Tungsten was mined here from 1917 through the 1950s.

Spot 1.2. The Sahwave Granodiorite
(40.133650° N, 119.05830° W; Rock Box Sample: GSA 21-04)

The Sahwave granodiorite is one of the most well-exposed units of the Sahwave batholith, and is of both similar age and composition to the Cathedral Peak and Mono Creek granodiorites of the Tuolumne and John Muir intrusive suites, respectively. The Sahwave granodiorite is the youngest unit of the Sahwave batholith and was emplaced at ca. 87 Ma (Table 1). Van Buer and Miller (2010) mapped all units of the Sahwave batholith and characterized this

unit as a potassium feldspar megacrystic biotite granodiorite. Potassium feldspar phenocrysts are present throughout the Sahwave and Nightingale Range plutons, but only in the Sahwave unit do potassium feldspar megacrysts (4–6 cm**)** occur in pods and stringers that are reminiscent of textures observed in the Cathedral Peak granodiorite of the Tuolumne intrusive suite. The Sahwave granodiorite preserves a weak magmatic foliation defined by the shape-preferred orientation of potassium feldspar megacrysts and alignment of biotite laths. Field measurements of the magmatic foliation trend N-S throughout the unit. Lineation, however, was difficult to identify and measure in the field. Optical microstructural analysis of thin sections of samples from across the Sahwave granodiorite indicates magmatic to submagmatic textures. Quartz grains display patchy undulose extinction and sharp cuspate/lobate boundaries indicative of high-temperature deformation (Fig. 10A). both potassium feldspar and plagioclase feldspar are euhedral and show no evidence of internal deformation.

The Sahwave granodiorite intrudes the granodiorite of Bob Spring along a generally shallowly dipping contact that is sharp on the north side but gradational along its south side. The contact in the south was difficult to define, and we used magnetic susceptibility along an E-W transect to determine the shift from Sahwave granodiorite to the granodiorite of Bob Spring (Fig. 11A). The Sahwave granodiorite yields a magnetic susceptibility range from 0.50 to 3.00, whereas the granodiorite of Bob Spring yields a higher magnetic susceptibility of 4.00–6.50.

Laser ablation-inductively coupled plasma-mass spectroscopy (LA-ICP-MS) yielded a U-Pb zircon age of ca. 88 Ma from two samples (17SW-20, 17SW-40). Zircon grains from the Sahwave granodiorite display significant oscillatory and sector zoning and many grains contain inherited cores (Fig. 12B)

Anisotropy of magnetic susceptibility (AMS) was utilized to further examine the orientation of the fabrics preserved within in the Sahwave granodiorite unit and further expanded across all other units of the Sahwave batholith. AMS results yield weak anisotropy and shape ellipsoids that cluster along the prolate and oblate boundary (Fig. 13). AMS fabrics from the Sahwave granodiorite are consistent with field measurements and yield a steep N-S magnetic foliation, but reveal a weak, moderately to shallowly plunging magnetic lineation (Fig. 14).

Spot 1.3. The Granodiorite of Bob Spring
(40.22753° N, 119.14187° W; Rock Box Sample: GSA 21-05)

The granodiorite of Bob Spring outcrops poorly but is characterized as a medium-grained biotite granodiorite or granite with poikilitic potassium feldspar phenocrysts up to ~2 cm long with homogenously distributed biotite, titanite, and altered hornblende (Van Buer and Miller, 2010). The granodiorite of Bob Spring is texturally variable, and some outcrops display a much finer-grained and equigranular texture. The unit also contains abundant aplite and pegmatite dikes dominated by quartz and potassium feldspar. The granodiorite of Bob Spring contains equant and rounded quartz grains that are generally only ~1 mm in size, but reach 3–5 mm in the southern outcrops. Biotite and hornblende are highly chloritized, and feldspars sometimes show signs of sericitization. Titanite grains are euhedral, large, and abundant (Fig. 10B). Field observations of the granodiorite of Bob Spring suggest that this unit is perhaps equivalent to the Half Dome unit of the Tuolumne intrusive suite in the central Sierra Nevada due to similarities in age, composition, and texture.

Zircons from the granodiorite of Bob Spring are similar to those of the Sahwave granodiorite in that they display significant oscillatory zoning and sector zoning and abundant

inherited cores. LA-ICP-MS zircon ages of the granodiorite of Bob Spring (17BS-1) suggest a crystallization age of ca. 95 Ma (Fig. 12).

A magmatic foliation weakly defined by mafic minerals is occasionally observed in this unit but was difficult to measure in the field, and trends were variable. The AMS shape ellipsoids are only slightly more oblate with low anisotropy (Fig. 13). The AMS magnetic fabrics from the granodiorite of Bob Spring yield a subvertical N-S–striking magmatic foliation, with a weak and irregular lineation (Fig. 14).

Spot 1.4. Juniper Pass Granodiorite
(40.31255° N, 119.01728° W; Rock Box Sample: GSA 21-08)

The Juniper Pass granodiorite is the outermost unit of the Sahwave batholith, out cropping at the furthest north and south exposures of the Sahwave Range and in small outcrops in the Nightingale Range. It is characterized as a medium- to coarse-grained equigranular biotite-hornblende-granodiorite with large (4–8 mm) biotite and hornblende phenocrysts (Fig. 9F). Van Buer and Miller (2010) observed that hornblende and titanite are present throughout all units of the Sahwave intrusive suite, but only in the granodiorite of Juniper Pass does the hornblende form crystals notably larger than the 1–3 mm euhedral titanite. The granodiorite of Juniper Pass is also the most compositionally variable of the units, such that this unit could also be characterized as a tonalite or a quartz diorite depending on the outcrop. Microstructural observations reveal potassium feldspar and plagioclase are euhedral, but lenticular deformation twins are observed in some plagioclase. Plagioclase crystals are often associated with myrmekite along grain boundaries. Quartz grains show cuspate-lobate boundaries, some evidence of grain boundary migration, and patchy undulatory extinction. Biotite is relatively unaltered, but hornblende shows significant resorption with embayment of quartz and feldspar (Fig. 10C).

Mafic enclaves are found throughout the unit but are common within 1–2 km of the exterior contact, and are flattened by a ratio of 2:1–10:1. Many of these enclaves also display dextral shear sense with the shear planes paralleling the mineral foliation (Fig. 11C). The Juniper Pass granodiorite has the most discernible magmatic to submagmatic fabric of all the Sahwave Range units. The foliation is defined by the alignment of mafic minerals and euhedral plagioclase. Mafic schlieren and enclaves parallel the mineral fabric (Fig. 11D). In contrast to the N-S foliation trends in the Sahwave granodiorite and granodiorite of Bob Spring, the granodiorite of Juniper Pass displays a strong E-W foliation in the northern outcrops, especially at this spot.

The Juniper Pass granodiorite is the most mafic of the units of the Sahwave batholith, and by contact relationships, it is considered the oldest intrusive unit. The U-Pb zircon ages (SHRIMP and LA-ICP-MS) suggest that the Juniper Pass granodiorite was emplaced synchronously or even after the granodiorite of Bob Spring (94.7 Ma). LA-ICP-MS zircon ages from the granodiorite of Juniper Pass (17JP-7) indicate that this unit is slightly younger than the granodiorite of Bob Spring, with a crystallization age of ca. 93.5 Ma (Fig. 12A). However, the uncertainties for these new ages are still large, and high-resolution U-Pb geochronology is needed to resolve the emplacement history of these units.

In contrast to all other units of both the Sahwave and the Nightingale Ranges, the Juniper Pass granodiorite yields some of the highest magnetic susceptibilities, measuring from 0.50–8.15. Approximately 50% of the specimens from the Juniper Pass granodiorite record a strong degree of anisotropy; collectively samples from this unit yield the most scatter (Fig. 13). AMS results from the Juniper Pass granodiorite record an E-W magnetic foliation fabric that is coincident with field fabric measurements as well as oblate shape ellipsoids (Fig. 14). The magnetic lineation direction is not consistent within this unit.

Optional Spot 1.4a. Juniper Pass Pegmatite
(40.24457° N, 119.01434° W; Rock Box Sample: GSA 21-06)

The granodiorite of Juniper Pass contains the largest mapped unit of pegmatite in the Sahwave Range intrusive complex. This pegmatite body contains 3–6 cm books of muscovite; 2 cm–2 m crystals of potassium feldspar and quartz and often form graphic granite textures; and stringers of small 1–3 mm garnets. Some outcrops also contain an abundance of 1–8 cm prisms of black tourmaline (Fig. 9C). These tourmaline-rich areas are found in distinct zones throughout the pegmatite and along the intrusive contacts with the Juniper Pass granodiorite, where they grow radially away from the contact (Fig. 9F). The pegmatite contact also contains xenoliths of the Juniper Pass granodiorite.

Optional Spot 1.4b. Andalusite Occurrence, Eastern Bluewing Mountains
(40.3357° N, 118.9620° W; Rock Box Sample: GSA 21-07)

Andalusite and cordierite are often found as small, altered grains throughout the northern metamorphic aureole of the granodiorite of Juniper Pass in the Bluewing Mountains, where it intrudes deep-marine slates of the Triassic Jungo terrane. These minerals are interpreted to reflect contact metamorphism in the aureole of the intrusion. At this location in the eastern Bluewing Mountains, about a kilometer from the inferred intrusive contact, andalusite crystals reach up to 5 cm or more in length and cut almost randomly across the slaty foliation in wall rocks (Fig. 9A).

Optional Spot 1.4c. Sahwave Batholith Intrusive Margin, Southwest Bluewing Mountains
(40.3263° N, 119.0831° W)

The intrusive contacts surrounding much of the Sahwave Range intrusive suite are sometimes marked by contact-parallel foliation indicative of ductile deformation associated with pluton emplacement, and sometimes by highly irregular contacts indicative of stoping and

diking. At this location, both features can be observed. Both magmatic foliation in the granodiorite of Juniper Pass, and also metamorphic foliation in the wall rocks within ~200 m of the contact, strike WNW. These fabrics cut across the older, regional NE-striking foliation in wall rocks inherited from Luning-Fencemaker thrust belt deformation. This WNW foliation is parallel to the km-scale strike of the intrusive margin, which is apparently offset a few kilometers left-laterally by a NE-striking fault west of Juniper Pass. However, at the 100 m scale, the contact zigzags across that foliation as it trends generally NE up the hillside above the road. In many locations, granodiorite dikes extend into the wall rocks. Further, stoped blocks of the wall rocks can be observed surrounded by granodiorite. The next ridge, ~300 m past the contact, is already out of the structural aureole, and NE-striking foliations are observed at that location.

Spot 1.5. The School Bus Granodiorite
(40.13196° N, 119.27930° W; Rock Box Sample: GSA 21-01)

Van Buer and Miller (2010) dated and characterized the School Bus granodiorite as a ca. 91 Ma, leucocratic granodiorite. Similar to the granodiorite of Bob Spring and the Sahwave granodiorite, it contains phenocrysts of potassium feldspar, biotite, and titanite. Unlike these main units, the School Bus granodiorite outcrops show no compositional or textural variation, and a magmatic fabric is difficult to discern in the field. The School Bus granodiorite intrudes both the Power Line intrusive complex and the Juniper Pass granodiorite along sharp, vertical contacts (Fig. 11A). This unit only contains a few preliminary AMS drill sites and more will be needed to assess magnetic fabrics preserved in the unit.

Optional Spot 1.5a. Diorite Phase of the Sahwave Batholith
(39.9970° N, 119.2205° W; Rock Box Sample: GSA 21-02)

Near the southern margin of the Sahwave batholith, there are several small intrusions of fine- to medium-grained biotite-hornblende-diorite and quartz diorite, from roughly 10 m to 1

km in size. These frequently contain ~5 mm euhedral plagioclase phenocrysts~~,~~ and ~~contain~~ hornblende phenocrysts that are sometimes acicular. In several areas, these intrusions record magma-mixing relationships with the granodiorite of Juniper Pass, such as lobate and interfingering contacts, streaky fine-scale intermingling, and outcrop-scale gradational contacts. Contemporaneous mafic intrusions such as may be the source of mafic enclaves found elsewhere in the Juniper Pass unit may have formed (Fig. 9E).

Spot 1.6. Power Line Intrusive Complex
(40.2084° N, 119.28393° W; Rock Box Sample: GSA 21-03)

The oldest intrusive unit in the Sahwave-Nightingale region is referred to as the Power Line intrusive complex (Van Buer and Miller, 2010). This complex outcrops in the northwestern Nightingale Range and is intruded to both the north and south by units of the Sahwave batholith. The main Power Line intrusive complex is a medium-grained biotite-hornblende-granodiorite with ribboned quartz, mafic folia, and porphyroclasts of potassium feldspar. The Power Line intrusive complex, however, is compositionally variable and includes many unmapped dikes and pods of darker granodiorite and diorite ranging from centimeters to hundreds of meters in long dimensions (Van Buer and Miller, 2010). Some of these are fine grained, weathering to a blue-grayish color, but all subunits share a similar, generally N-S–oriented, steeply dipping solid-state foliation (Van Buer and Miller, 2010). This unit also contains many large inclusions of metamorphic rock, mostly 5–200 m in length, but including a 4-km-long potential roof pendant as well as small elongated enclaves. These xenoliths and enclaves are aligned subparallel to the medium-temperature solid-state fabrics of the Power Line intrusive complex. The solid-state fabric and extremely low magnetic susceptibility (0.01–1.05) distinguish the Power Line intrusive complex from all other intrusive units in the area, including the School Bus intrusive

suite, which intrudes the complex (Figs. 11A, 11B). The subvertical foliation is defined by mafic folia and ribboned quartz, with potassium feldspar porphyroclasts forming sigma shear sense indicators that define a dextral shear sense in the horizontal plane. Mafic minerals define a strong subvertical lineation within the foliation plane, characterizing the Power Line intrusive complex as an L-S tectonite. Microstructures record recrystallized biotite and quartz (grain-size reduction, subgrain rotation recrystallization, etc.). Feldspar record some minor recrystallization within the tails of sigma clasts (Fig. 10D).

LA-ICP-MS analyses were conducted on zircon separates from 17PL-3, yielding a U-Pb zircon age of 106 Ma. Zircons from the Power Line intrusive complex are visibly distinct from the highly zoned zircons of the Sahwave units, with very little zoning, and large zircon crystals showing some possible metamorphic rims (Fig. 12B).

AMS data from the Power Line intrusive complex yields mostly oblate fabrics and only slightly high values of anisotropy (Fig. 13). This low degree of magnetic anisotropy combined with an extremely low magnetic susceptibility is likely the result of the lack of titanomagnetite phases in the Power Line intrusive complex. The magnetic fabric preserved in the Power Line intrusive complex is defined by predominately paramagnetic minerals (hornblende and biotite). The magnetic foliation and lineation are consistent with field measurements and yield a subvertical N-S foliation and a steeply plunging lineation (Fig. 14).

Optional Spot 1.6a. Southwest Nightingale Range Normal Fault Triangular Facets (40.012° N, 119.298° W)

Whereas the Sahwave Range is bounded by an east-dipping normal fault along its eastern side, and is tilted westward up to ~30°, the Nightingale Range is bounded by a west-dipping normal fault along its west side and is tilted up to ~15° eastward. There is no evidence for

rupture on this fault postdating the formation of the Lake Lahontan shorelines, but there is a beautiful pair of 400-m-tall triangular facets along the normal fault scarp here, indicating normal offset earlier in the Quaternary.

Optional Spot 1.6b. Oligocene Paleovalley in the Southern Nightingale Range (39.9984° N, 119.2875° W)

Northern Nevada is traversed by several kilometer-deep paleovalleys that appear to have been established by the Eocene and then served as conduits for long-distance distribution of Oligocene ignimbrites (e.g., Henry, 2008). At this location, the south-dipping contact between soft-weathering, dark-gray metamorphic rocks below and cliffy, relatively flat-lying orange tuffs above has been identified as a buttress unconformity along the north side of one of these paleovalleys. This paleovalley contains at least 11 separate ignimbrite flows ranging from 31.3 to 24.9 Ma in age (Faulds et al., 2005).

Optional Spot 1.6c. Winnemucca Lake (39.9775° N, 119.2976° W)

As recently as the 1930s, the floor of the now-dry valley west of the Nightingale Range was covered by shallow Winnemucca Lake, which was fed by the Truckee River before diversion via Derby Dam reduced its water supply. Winnemucca Lake was a remnant of Pleistocene Lake Lahontan, which filled the valley to a depth of almost 200 m, leaving lacustrine deposits at elevations up to 1340 m along the west side of the Nightingale Range. These lacustrine deposits include coarse sand and gravel beach deposits, delta deposits, and fine-grained lake muds. Many of these deposits are tufa-cemented, and tufa also coats bedrock surfaces and occasionally forms freestanding towers. At this location, a volcanic outcrop was coated in nearly 2 m of tufa, which has now begun to peel off, revealing palisades of “thinolite”

crystals up to 10 cm in length, probably pseudomorphs after the icy carbonate, ikaite, $CaCO_3.6H_2O$.

Spot 1.7. Concluding Statements about the Sahwave Batholith and Power Line Intrusive Complex

1. The Power Line intrusive complex was emplaced ca. 106 Ma.
2. The Power Line intrusive complex shows evidence of mid- to low-temperature solid-state deformation and the development of N-S–striking vertical foliation and subvertical lineation. Dextral shear indicators (horizontal movement direction) perpendicular to stretching lineation (vertical) suggest that the unit experienced dextral transpressional shearing. The deformation geometry of this unit is reminiscent of the pure-shear–dominated transpression recorded in the western Idaho shear zone (e.g., Tikoff et al., 2001). Internal fabrics of the Power Line intrusive complex (both field-measured and magnetic foliations) are relatively concordant to wall rock foliation. This concordance may indicate extensive post-emplacement deformation cross-cutting the pluton/country rock contact.
3. Deformation occurred after the emplacement of the Power Line intrusive complex, possibly ca. 100 Ma.
4. The Sahwave batholith was incrementally emplaced from ca. 95–87 Ma.
5. All units of the Sahwave batholith show predominately magmatic textures with large grains showing highly irregular boundaries indicative of high-temperature deformation. AMS magnetic fabrics for all units yield both prolate and oblate ellipsoids. The AMS fabrics for the Sahwave granodiorite and the granodiorite of Bob Spring yield a steeply dipping N-S– to NW-SE–striking magnetic foliation and moderately plunging lineation with a variable trend,

but the granodiorite of Juniper Pass yields an E-W striking foliation with no interpretable lineation.

6. The fabrics of the Sahwave batholith (field-measured and AMS foliations) are indicative of a second period of deformation, which records more distributed shear than in the Power Line intrusive complex. Internal fabrics of the Sahwave batholith are moderately discordant to wall rock foliation, which may indicate the absence of extensive post-emplacement deformation cross-cutting the pluton/country rock contact. If the area experienced ductile deformation on a regional scale after cooling of the pluton, concordant fabrics would be expected in both the wall rock and intrusive body (e.g., Castro, 1987). Therefore, the shearing fabrics within the Sahwave batholith likely formed synchronous with pluton emplacement and cooling. Similar to other syn-emplacement shear zones in the Sierra Nevada (e.g., Rosy Finch shear zone; Tikoff and Teyssier, 1992; de Saint Blanquat and Tikoff, 1997), it remained a wide zone of distributed shear that did not experience localized strain (e.g., Pennacchioni and Mancktelow, 2018). Further detailed AMS analysis is in progress to investigate the emplacement of each unit.

Spot 1.8. Overview of the Cretaceous Plutons of the Gerlach Area

Several large Cretaceous plutons are found in mountain ranges near the town of Gerlach, including in the Selenite, Granite, and Fox Ranges (Fig. 4). Selenite Range plutons intrude rocks assigned to the Jungo and Black Rock terranes (Wyld, personal observ.), whereas those in the Granite and Fox Ranges intrude allochthonous terranes that lie west of the western Nevada shear zone (Wyld, personal observ.; Kinsella et al., 2007; Wyld et al., 2007; Kinsella, 2010; Wyld and Wright, 2019). These plutons thus intrude across, and postdate, the western Nevada shear zone boundary. The Selenite Range plutons share similarities in composition and internal fabric to

plutonic rocks of the Sahwave batholith but lack internal zoning and are slightly older (ca. 96 Ma). Plutons in the Granite and Fox Ranges are distinctly older (ca. 105–102 Ma) than the Sahwave batholith, and differ from the latter in lack of zoning, compositions ranging from granodiorite to quartz diorite, and rare evidence for any internal foliation.

Spot 1.9. Kumiva Peak Pluton
(40.43573° N, 119.22614° W; Rock Box Sample: GSA 21-09)

Plutonic rocks underlie most of the Selenite Range (Fig. 15), with an exposed area of ~200 km^2. Wall rocks of these plutonic rocks are inferred to belong to the Triassic Jungo terrane on the southwest side and the Triassic to Early Jurassic part of the Black Rock terrane farther north. Contacts with wall rock are sharp and bordered by a contact aureole up to ~100 m wide. There is also a short intrusive contact exposed in a small uplift east of the southern Selenite Range, where Selenite Range plutonic rocks are intruded by the granodiorite of Juniper Pass along a sharp contact. Elsewhere, the intrusive rocks are overlapped by Tertiary or Quaternary strata or cut by Cenozoic normal faults.

Although originally described altogether as the “Selenite pluton” (Smith et al., 1971), the intrusion is actually composed of at least two distinct units. South of Luxor Peak, plutonic rocks are composed of medium-coarse hornblende-biotite-granodiorite to quartz diorite or tonalite, with a strong, generally subvertical, north-south magmatic foliation, and a color index around 20. These intrusive rocks are referred to here as the Kumiva Peak pluton. The rock is mostly equigranular but, distinctively, contains seriate porphyritic euhedral plagioclase up to 1.5 cm in long dimension, with twinning visible to the naked eye. These euhedral plagioclase grains make up 10%–20% of the rock. While hornblende and biotite are the predominant mafic phases, minor clinopyroxene is also locally found. Mafic enclaves are rare. This unit has a distinctively rugged

outcrop habit, often forming rocky tors (Fig. 16F). The Kumiva Peak pluton has been dated at 96.3 ± 0.8 Ma via U-Pb SHRIMP analysis of zircon (sample NVB-212 in Table 1; Van Buer and Miller, 2010).

Spot 1.10. Selenite Peak Pluton
(40.68734° N, 119.25083° W; Rock Box Sample: GSA 21-10)

North of Luxor Peak, the plutonic rock is described as a medium-grained hornblende-biotite-granodiorite. Relative to the Kumiva Peak pluton, however, they are generally more equigranular, richer in potassium feldspar, and have a lower color index (closer to 10). These rocks are referred to here as the Selenite Peak pluton (Fig. 15). A magmatic foliation is common but not as strongly defined as in the Kumiva Peak pluton. Rocks of the Selenite Peak pluton contain euhedral plagioclase phenocrysts, but they do not comprise as significant a fraction of the rock as in the Kumiva Peak pluton. Contact between the two plutonic units is reasonably sharp at (1:24,000) map scale, but outcrop in the area is insufficiently continuous to determine the nature of the contact at outcrop scale.

One sample from the Selenite Peak pluton (SL-11) has been analyzed for U-Pb zircon geochronology. The sample location is shown in Figure 15. Analyses were performed at the Stanford-USGS Micro-isotopic Analytical Center using the SHRIMP-RG instrument. Ten zircon grains from this pluton gave a ^{207}Pb-corrected, ^{206}Pb/^{238}U weighted average age of 96.3 ± 1.5 Ma (Fig. 17; Table 1). This is indistinguishable from the 96.3 ± 0.8 Ma age determined for the Kumiva Peak pluton in the southern Selenite Range (Van Buer and Miller, 2010).

Optional Stop 1.10a. Black Rock Desert and Black Rock Point
(40.655606° N, 119.348167° W)

From this point on Hwy. 447, just before it turns south into the town of Gerlach, there is a good view to the NNE of the Black Rock Desert and, in the distance, Black Rock Point (Fig. 18).

The Black Rock Desert is a vast playa deposit, extending ~100 km to the north, that was once part of Pleistocene Lake Lahontan. At peak lake height, the desert was covered by 150 m of water. The desert has gained fame for hosting the World Land Speed races of 1983 and 1997, in the last of which Andy Green achieved a speed of 763 m.p.h. and broke the speed of sound in his vehicle ThrustSSC (Thrust supersonic car); and as the site of the yearly Burning Man festival, at which time population on the desert makes it temporarily the third largest city in Nevada. At the north end of the desert at the southern end of the Calico Hills is a hill called Black Rock Point (Fig. 18). While most of the Calico Hills consist of red to tan Tertiary volcanic strata, Black Rock Point consists of Permian shallow marine mafic volcanic rocks and minor limestone (Gianella and Larson, 1960). These rocks do not correlate with Permian strata of the Black Rock terrane and are considered part of the displaced terranes west of the western Nevada shear zone.

Black Rock Point was an important landmark, because of its striking dark color, for emigrants traveling across the desert on their way to California via the Applegate Trail in the mid-1800s. At the base of Black Rock Point is a large hot spring that was an important source of water for emigrants after crossing the desert; an abandoned wagon can still be seen there.

Spot 1.11. Granite Range Pluton
(40.707631° N, 119.353167° W; Rock Box Sample: GSA 21-12)

The Granite Range pluton underlies most of the Granite Range; the total exposed area is ~150 km^2. On its northwest and northeast sides, the pluton intrudes Permian to Early Jurassic strata of the Granite subterrane, but elsewhere it is in fault contact with or overlapped by Cenozoic valley deposits. The intrusive contact with wall rocks is sharp and steeply dipping. Small pods and apophyses of the pluton are locally found in wall rocks around the margins of the pluton, but there is a notable absence of dikes. A contact metamorphic aureole extends up to 500

m from the pluton margin, and both stratigraphic layering and structures in wall rocks on the north side appear to have been warped outward into a broad N-facing fold during intrusion (Fig. 19). In the southeast and west, the Granite Range pluton is flanked by major Cenozoic normal faults and thus rises prominently above the surrounding area (Fig. 20). Normal faulting on the west side of the pluton was accompanied by a smaller component of right-lateral strike-slip offset (Faulds and Ramelli, 2005), whereas faulting on the southeast side of the pluton appears to reflect dominantly normal-sense offset.

The Granite Range pluton appears to be compositionally and texturally homogenous throughout, with no evidence of zoning. Predominant rocks are medium- to coarse-grained, hornblende biotite or biotite-hornblende-granodiorite, containing 20%–30% quartz and 15%–20% mafics (Fig. 16D), although more leucocratic rocks are locally present near the pluton margins. Titanite is a characteristic mineral phase, comprising 1%–2% of the rock. Most rocks are equigranular, but phenocrysts of potassium feldspar up to 7 mm in size are locally found. Small granitic aplite to pegmatite dikes cut the pluton in some areas but are not common. Mafic enclaves are rare and small. Unlike plutons of the Sahwave, Nightingale, and Selenite Ranges, the Granite Range pluton shows no evidence of any magmatic or subsolidus foliation.

One sample (NVB-293; see Fig. 19 for location) from the Granite Range [[everything should be Granite Range]] pluton has been analyzed for U-Pb zircon geochronology. Analyses were performed at the Stanford-USGS Micro-Isotopic Analytical Center using the SHRIMP-RG instrument. Data from 13 zircon grains yielded a ^{207}Pb-corrected, ^{206}Pb/^{238}U weighted average age of 102.4 ± 1.3 Ma (Fig. 17), which is interpreted as the crystallization age of the Granite Range pluton.

Optional Spot 1.11a. Lake Lahontan Shorelines
(40.753808° N, 119.277064° W)

Return to Hwy. 34 and proceed north ~5.25 miles to the coordinates for Optional Spot 1.11a, where a subsidiary road to the south and southeast provides entrance to the Black Rock Desert. Looking to the northeast, you can see spectacular exposure of Lake Lahontan shorelines carved into mafic metavolcanic rocks of the Granite terrane (Fig. 21). At least eight distinct shorelines are visible, from an elevation of 1221 m to 1303 m, attesting to a Pleistocene maximum depth here of 82 m.

Optional Spot 1.11b. Granitic Fault Breccia in Southeast Granite Range
(40.666889° N, 119.371356° W)

Take Hwy. 34 south to just before it takes a sharp turn into the town of Gerlach. At ~40° 39′ 57.54″ N, 119° 22′ 10.70″ W, you can turn off onto a road that closely parallels Hwy. 34 to the west. Take this road northeast and follow it as it turns sharply to the northwest, climbing uphill, and then turns southwest, following the front of the Granite Range. Follow the southwest-trending section of the road ~0.5 mi., then park and walk southeast a short distance along the relatively flat hilltop. Here, you can find outcrops of fault breccia associated with two parallel range-front normal faults (Fig. 19). The eastern strand evidently cuts off the western strand at depth and has uplifted fine examples of indurated fault breccia (or cataclasite), composed of variably comminuted fragments of the Granite Range pluton (Fig. 16E).

Spot 1.12. Northern Fox Range Pluton
(40.619311° N, 119.461672° W; Rock Box Sample: GSA 21-11)

Several large Cretaceous intrusions are found in the Fox Range, including the Pah-Rum Peak, Juniper Flat, and northern Fox Range plutons (Kinsella, 2010; Fig. 22). Wall rocks of these plutons are Triassic or Jurassic metasediments of the Fox terrane (Fig. 22; Kinsella et al., 2007;

Kinsella, 2010). The Pah-Rum Peak and Juniper Flat plutons, found in the central Fox Range, are both leucocratic biotite granodiorite and are likely related intrusions. Kinsella (2010) reports a U-Pb zircon age of 105.35 ± 0.58 Ma for the Juniper Flat pluton. Our focus here is on the northern Fox Range pluton, which underlies the northern part of the range. The northern Fox Range pluton has been studied by Kirkham (1982), Leshendok (1997), Kinsella (2010), and Wyld and J.E. Wright (personal observ.), on which the following description is based.

The total exposed area of the northern Fox Range pluton is ~10 km^2 (Fig. 22). Tertiary strata overlap the pluton in several areas, including at high elevations, indicating that the upper part of the pluton was close to the basal Tertiary unconformity. On the west, it is partially bound by a major Cenozoic normal fault system that flanks the west side of the Fox Range. To the south, intrusive contacts with older wall rocks are observed. Contact with wall rocks is generally sharp and is bounded by a contact metamorphic aureole that extends to 100–200 m. Although previously considered to be responsible for localized amphibolite grade metamorphism in wall rocks farther south (Bonham, 1969; Kirkham, 1982; Thiesse, 1988), new work by Kinsella (2010) documents that high-grade metamorphism of wall rocks is not spatially associated with the intrusion, but rather reflects an older episode of tectonism.

The northern Fox Range pluton is relatively homogeneous in texture and composition throughout, with no evidence of zoning. The predominant rock type is clinopyroxene-biotite-hornblende-granodiorite to quartz diorite. Medium grain size and equiangular texture are typical, although some areas have sparse phenocrysts of plagioclase. The percent of mafic minerals ranges from 15%–30%, with more mafic compositions dominating to the south. Hornblende and biotite are subequal in abundance, and clinopyroxene is minor. Enclaves of finer-grained biotite-hornblende-diorite are present throughout the pluton, but are generally scarce and small, except

in the northeasternmost part of the pluton where enclaves are unusually abundant (up to 60% of rock volume) and much larger (up to 2 m or more in maximum dimension) (Fig. 16C). Leucocratic aplite to pegmatite dikes of granitic composition are found locally throughout the pluton, but are especially common near the southern contact with wall rocks and in the northeast part of the pluton. The rock box sample is from typical clinopyroxene-biotite-hornblende-quartz-diorite of the northern Fox Range pluton.

Throughout most of the pluton, there is no observable subsolidus or magmatic fabric. One exception is near the southern contact with wall rocks, where the pluton has a foliation extending up to 250 m from the contact that is defined by alignment of mafic minerals and plagioclase laths. This fabric is parallel to the pluton–wall rock contact and is interpreted to be of magmatic origin. The other exception is in the northeastern exposures of the pluton, where a steeply dipping foliation is manifested only by ellipsoidal shapes of mafic enclaves (Fig. 16C), and a weak preferred alignment of plagioclase and mafic minerals within the enclaves. Host plutonic rock in this area, however, is undeformed.

One sample (FR-22z; see Fig. 22 for location) from the northern Fox Range pluton has been analyzed for U-Pb zircon geochronology. Analyses were performed using laser ablation multicollector ICP-MS at the University of Arizona. Data from 15 zircon grains yielded a concordant ^{207}Pb-corrected, ^{206}Pb/^{238}U weighted average age of 102.7 ± 0.9 Ma (Fig. 23; Table 1), which is interpreted as the crystallization age of the northern Fox Range pluton. The age of the northern Fox Range pluton is very similar to that of the Granite Range pluton.

At this stop, we will examine exposures in the northeasternmost part of the northern Fox Range pluton (Fig. 22), where large mafic enclaves are particularly abundant in an area called the “zebra outcrop” by Leshendok (1997). The stop is at a small hill that requires a short walk

from the end of the nearest road. Enclaves here consist of fine-grained biotite-hornblende-diorite, with a high percentage (30%) of mafic minerals, and variably abundant phenocrysts of plagioclase and hornblende. As we will see, there is only limited evidence of an internal foliation within the enclaves, despite the preferred orientation of enclave long axes. Detailed study of enclaves in this general part of the northern Fox Range pluton led Leshendok (1997) to conclude that they are most likely a manifestation of magma mixing, as fresh injections of mafic magma were emplaced into the more felsic host magma chamber. Evidence of this interpretation includes gradation of enclaves into local mafic dikes of similar composition, chilled borders of enclaves, and enclave shapes that vary from round to elongate. The enclave-defined foliation in this area is likely related to dismemberment of mafic dikes during magmatic flow, based on evidence of Leshendok (1997) that mafic dikes are observed in transitional relation with enclave swarms.

Optional Spot 1.12a. Rocks of the Fox Terrane and Pre-Intrusion Deformation (40.568469° N, 119.47395° W)

From the previous stop, return to the Power Line Road and take it ~1.5 mi. south to where it makes a large jog going over a creek. Park and walk up the creek bed to a final point ~ 300 m to the west. This traverse will introduce you to some features of the Cottonwood Canyon unit (Fig. 22), which was divided by Kinsella (2010) into the lower Smith Canyon argillite and the upper, depositionally overlying, Cottonwood Canyon quartzite. Age of the Cottonwood Canyon unit is constrained to the interval between ca. 204–103 Ma, based on ages of youngest detrital zircons from the unit and the age of the cross-cutting northern Fox Range pluton. However, detrital zircon signature from quartz-rich sandstones of the Cottonwood Canyon unit, as well as from all other units of the Fox terrane, are remarkably similar to zircon age signatures

of Early to Middle Jurassic eolianites of the Colorado Plateau, and the unit is thus considered to be of Jurassic age. All units of the Fox terrane were affected by polyphase deformation (folds, foliation) that pre-dates intrusion of Cretaceous plutons.

The unit we will see on this traverse is the Smith Canyon argillite. Slate in the lower part of the drainage is contact metamorphosed by the nearby northern Fox Range pluton, as manifested by mimetic growth of contact metamorphic biotite parallel to the older slaty foliation. Proceeding upcanyon, you cross into a thick limestone horizon. Contact metamorphic effects in the limestone give it a coarser-grained texture more characteristic of marble. Multiple tight to isoclinal ductile folds of bedding can be found in the limestone (Figs. 16A, 16B). These folds attest to the intense deformation affecting the unit prior to Cretaceous intrusion.

3. Summary

This guide has presented data, at various different levels of detail, from multiple large Cretaceous plutons found in the area from northeast of Pyramid Lake to around the town of Gerlach in northwest Nevada. The results provide a considerably updated understanding of Cretaceous plutonism and deformation in northwest Nevada, and present a new basis for comparing the record of Cretaceous plutonism and deformation from western Idaho to the Sierra Nevada of California.

Cretaceous plutons in the study area are primarily granodiorite in composition, with predominant mafic phases including biotite or hornblende and biotite; however, granite, quartz diorite, tonalite, and diorite are locally found. Potassium feldspar megacrysts are common in rocks of the Sahwave batholith, but not in other plutons. Leucocratic aplite to pegmatite dikes of granitic composition are found locally, but are large only within parts of Sahwave batholith.

Mafic enclaves are generally scarce and small, although locally they are more abundant and larger in size. Overall, the composition of Cretaceous plutons in the study area is more similar to those of the Sierra Nevada than those found along the western Idaho shear zone. The zoned Sahwave batholith, in particular, shares significant similarities with the Tuolumne and John Muir intrusive suites in Sierra Nevada, although rocks of the Sahwave batholith contain more primitive initial $^{87}Sr/^{86}Sr$ and εNd values (~0.7047 and –0.2, respectively), indicating a slightly different magma source within the underlying mantle lithosphere.

Geochronologic data indicate that there were two broad phases of magmatism. The first phase occurred from ca. 105–102 Ma, as represented by the Power Line complex of the Nightingale Range, and by plutons of the Granite and Fox Ranges. The second phase occurred from ca. 96–89 Ma, as represented by the Kumiva Peak and Selenite Peak plutons of the Selenite Range, and the Sahwave batholith of the Sahwave and Nightingale Ranges. The total age range of ca. 105–89 Ma is comparable to that of many Cretaceous plutons in the Sierra Nevada batholith, slightly younger than Cretaceous plutons found along the western Idaho shear zone in western Idaho (ca. 120–85 Ma), and generally older than the main phases of the Idaho batholith (ca. 85–60 Ma).

Structural field measurements of fabrics from plutons in the study area yield variable results. Magmatic foliations are common internally within rocks of the ca. 91–88 Ma Sahwave batholith and in ca. 96 Ma plutons of the Selenite Range, but are absent or scarce in the ca. 105–102 Ma plutons of the Granite and Fox Ranges. The Sahwave batholith and Selenite plutons contain submagmatic to magmatic fabrics that vary from weak to strong, and are defined by the preferred orientation of mafic minerals, potassium feldspar megacrysts, and plagioclase crystals. In addition, there is scarce textural evidence of dextral shear. The magmatic foliation in the

Sahwave granodiorite and the granodiorite of Bob Spring (Sahwave batholith) and Selenite Range units, is N-S striking and steeply dipping; however, an E-W foliation is also found in the granodiorite of Juniper Pass (Sahwave batholith). In contrast, the only evidence for magmatic foliation in the Fox and Granite Ranges is found along the southern contact of the northern Fox Range pluton with wall rocks. In this area, the fabric parallels the E-W contact and is defined by preferred orientation of mafic minerals and feldspar crystals.

Solid-state fabrics within plutonic rocks of the study area are preserved in the ca. 105 Ma Power Line intrusion in the Nightingale Range. Here, the fabric is a steeply dipping, N-S–striking, subsolidus foliation defined by mafic folia, potassium feldspar porphyroclasts, and ribboned quartz, with a strong subvertical lineation defined by mafic minerals. Microstructures record evidence for grain-size reduction and subgrain rotation recrystallization. This deformation reflects moderate-temperature ductile shearing, with sigma clasts indicative of dextral shear.

Magmatic fabrics are difficult to observe in the field, which leads to further AMS studies of the plutons of the Nightingale and Sahwave Ranges to constrain the deformation. AMS data from the Sahwave granodiorite and the granodiorite of Bob Spring yield weak magnetic anisotropy with prolate and oblate shape ellipsoids, but also reveal evidence of a NW-SE magnetic foliation and variable magnetic lineation. Data from the granodiorite of Juniper Pass indicate stronger magnetic anisotropy, with oblate shape ellipsoids, revealing an E-W magnetic foliation. Data from the Power Line intrusive suite yield high values of magnetic anisotropy, oblate shape ellipsoids defining a subvertical N-S foliation, and a steeply plunging lineation.

Collectively, structural data reveal an episode of ductile dextral shearing in the Power Line intrusive suite between ca. 105 and 91 Ma, forming a N-S–striking foliation and subvertical lineation, but that this deformation did not affect the ca. 105–102 Ma plutons of the Granite and

Fox Range, the ca. 96 Ma plutons of the Selenite Range, or the younger rocks of the Sahwave batholith. The relation of the NW-SE–oriented foliations found in plutons of the Selenite Range and Sahwave batholith to this localized ductile deformation is not clear. In terms of correlation with Cretaceous plutons of nearby regions, structural data from the study area are more consistent with the lower strains recognized in the Sierra Crest shear zone of the Sierra Nevada than with the high strain deformation recorded in the western Idaho shear zone.

4. Figure Captions

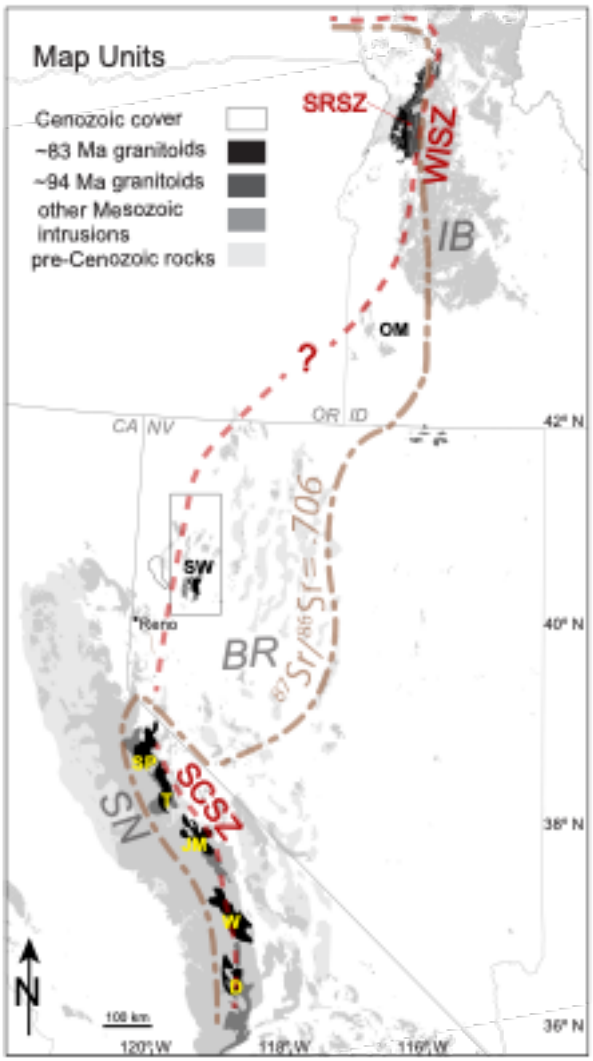

Figure 1. Simplified map of the central U.S. Cordillera showing the Sierra Nevada batholith and the Idaho batholith (darker-gray shades). The Jurassic arc (lightest gray) with respect to the location of the $^{87}Sr/^{86}Sr = 0.706$ line (brown dashed line), and associated shear zone systems (red; Sierra Crest shear zone—SCSZ, Salmon River suture zone—SRSZ, and western Idaho shear zone—WISZ). Compositionally zoned intrusions emplaced during the Cathedral Range intrusive epoch (95–83 Ma) are shown as dark gray and black: D—Domelands

intrusive suite; JM—John Muir intrusive suite; SP—Sonora Pass intrusive suite; T—Tuolumne intrusive suite; W—Mount Whitney intrusive suite; SW—Sahwave batholith; IB—Idaho batholith, SN—Sierra Nevada; BR—Basin and Range province; and OM—Owyhee mountains.

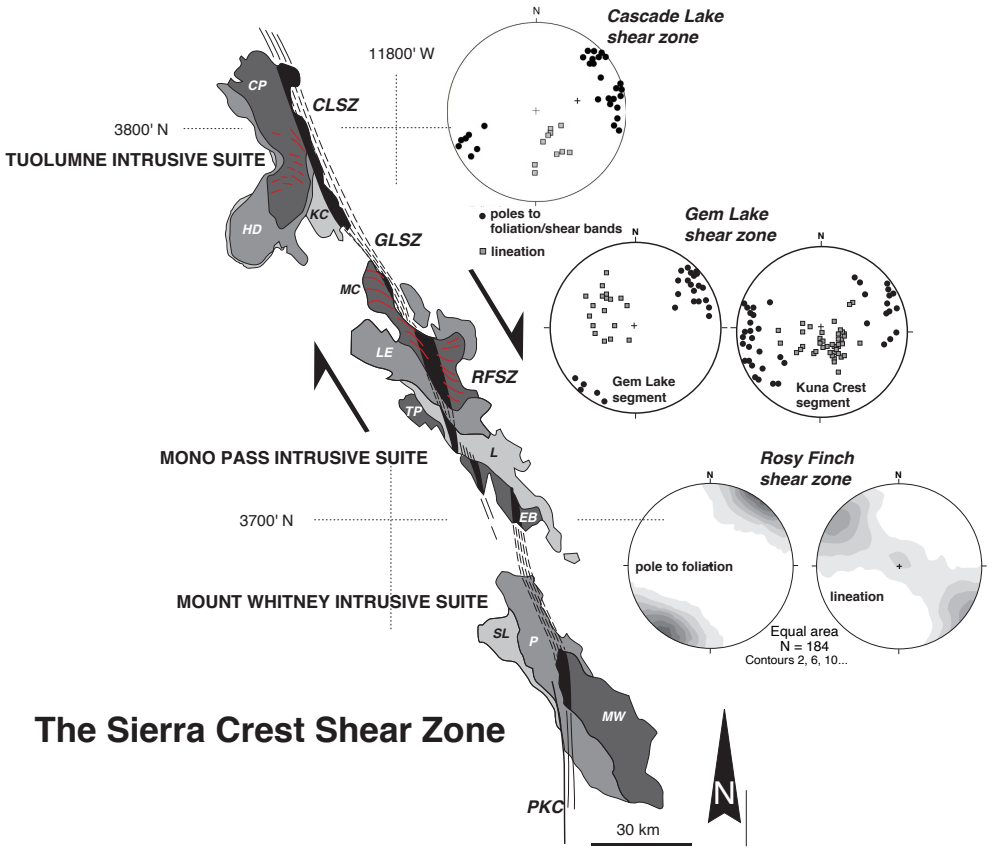

Figure 2. Simplified geologic map of the N25W trending en echelon intrusive suites of the Late Cretaceous Sierra Nevada arc, as well as the multiple dextral shear zones that comprise the Sierra Crest shear sone (SCSZ); Cascade Lake shear sone—CLSZ, Gem Lake shear zone—GLSZ, Rosy Finch shear zone—RFSZ. The John Muir intrusive suite serves as the host for the RFSZ and the proto–Kern Canyon fault (PKC). Plutons include CP—Cathedral Peak; HD—Half Dome; KC—Kuna Crest; MC—Mono Creek; LE—Lake Edison; L—Lamarck; TP—Turret Peak; EB—Evolution Basin; MW—Mount Whitney; P—Paradise; and SL—Sugarloaf. Black dashed lines and map pattern indicate known dextral shearing. Dextral shear is inferred for the RFSZ from the deflected magnetic foliation trajectories (red). Dextral shear from the GLSZ and the CLSZ is inferred from deformed sigma clasts and shear bands. Stereonets show compiled field fabric data from the CLSZ (Tikoff et al., 2005), the GLSZ (Greene and Schweickert, 1995),

and magnetic fabric data from the RFSZ (Tikoff and de Saint Blanquat, 1997). Modified from Tikoff and de Saint Blanquat (1997).

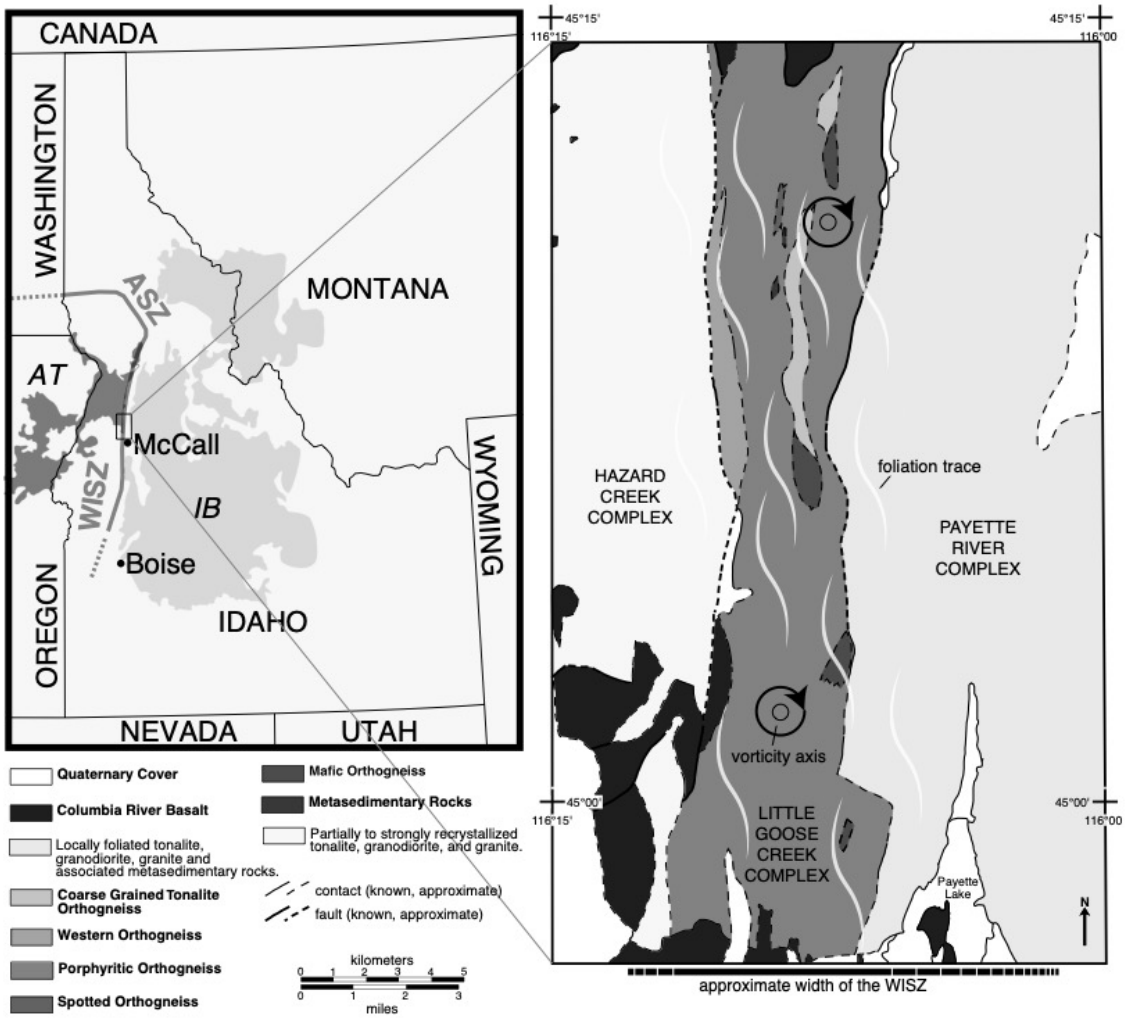

Figure 3. Simplified geologic map of the western Idaho shear zone (WISZ) and deformed magmatic complexes of the Cretaceous Idaho arc. ASZ—Ahsahka shear zone, AT—accreted terranes, and IB—Idaho batholith. Modified from Ostwald et al. (2017).

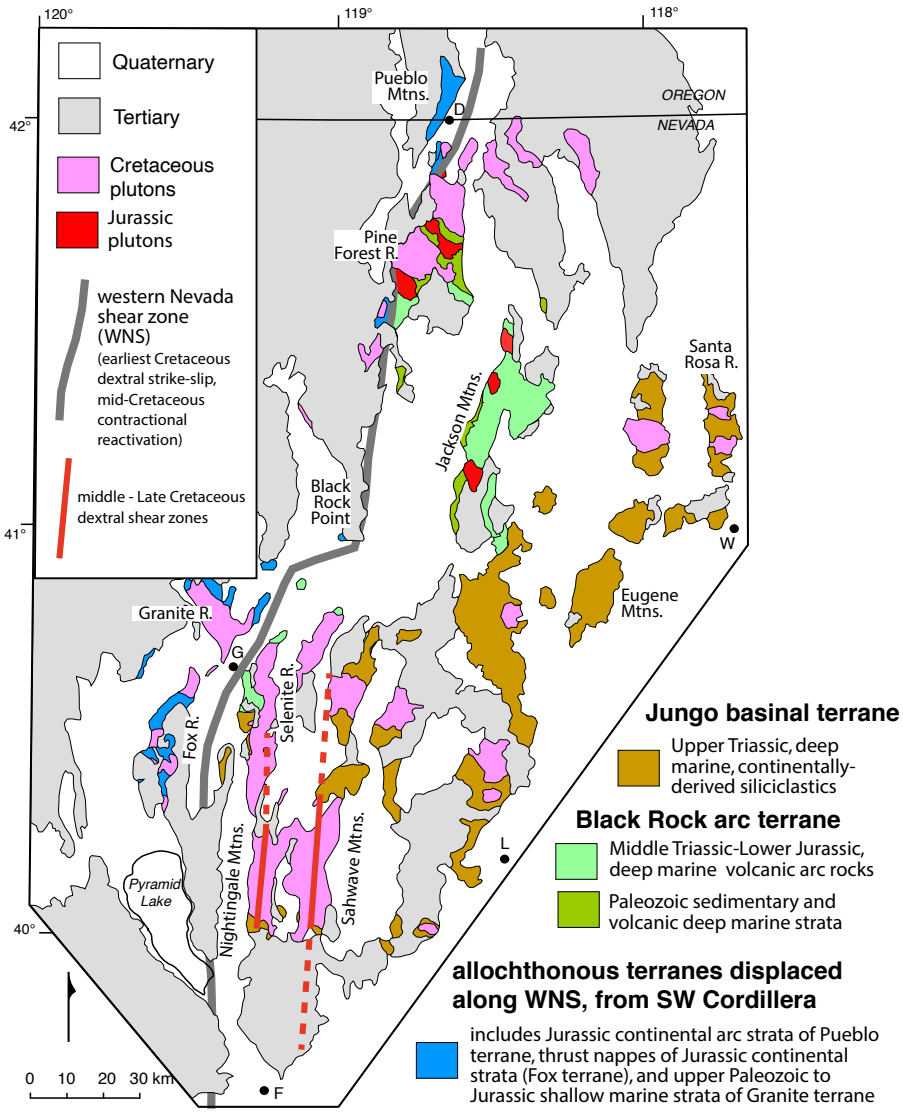

Figure 4. Simplified geology of northwest Nevada (see Fig. 1 for location). Towns are Denio (D), Fernley (F), Gerlach (G), Lovelock (L), and Winnemucca (W). Western Nevada shear zone drawn to show broad location without obscuring geologic units. Boxes show locations of Figures 5, 15, 19, and 22. Sources of data in boxed areas are listed in associated figure captions. Principal other sources of data are Stewart and Carlson (1976), Wyld (1996, 2002), Quinn et al. (1997), Wolak (2002), Wyld and Wright (2001), and Wyld et al. (2007).

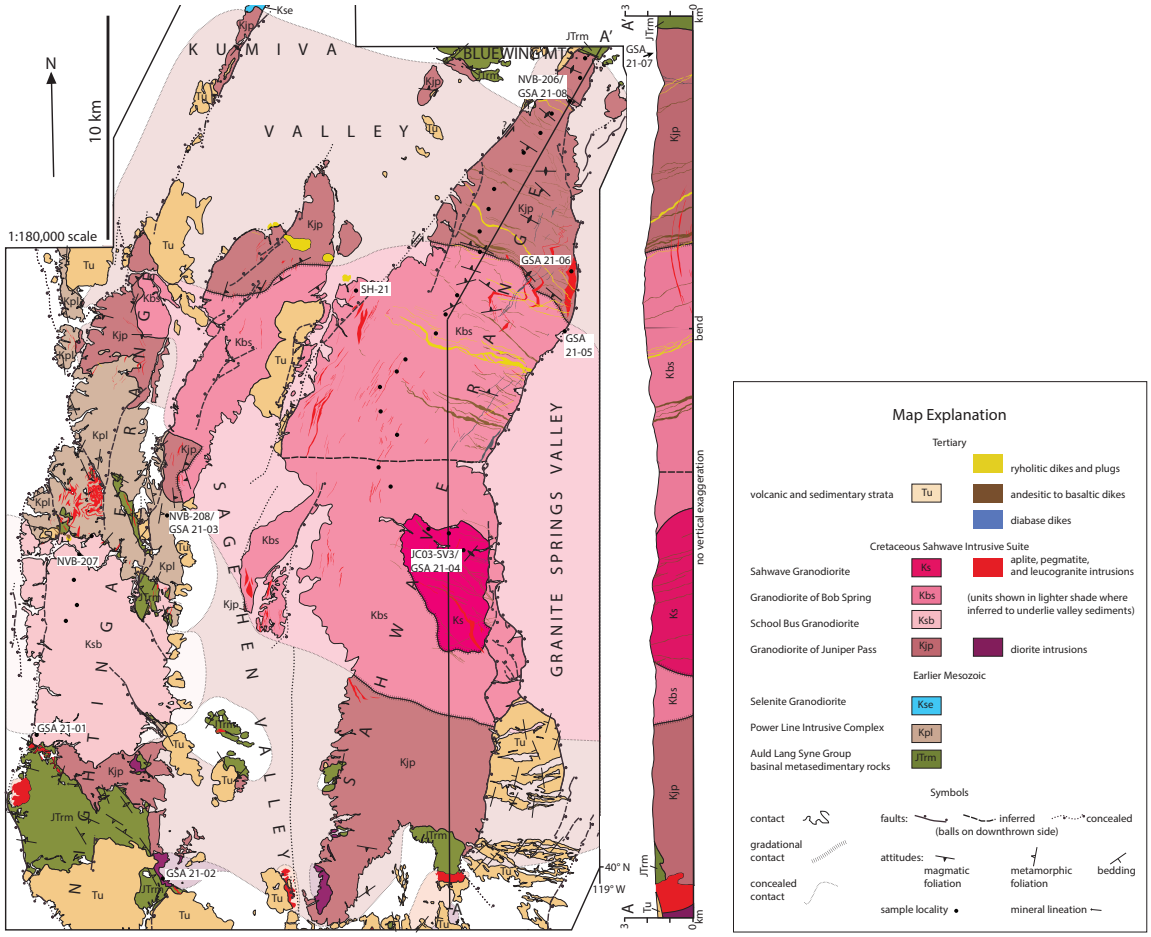

Figure 5. Detailed geologic map of the intrusive units within the Sahwave and Nightingale Ranges. Based on mapping at the 1:24,000 scale but shown as ~1:180,000. Modified from Van Buer and Miller (2010).

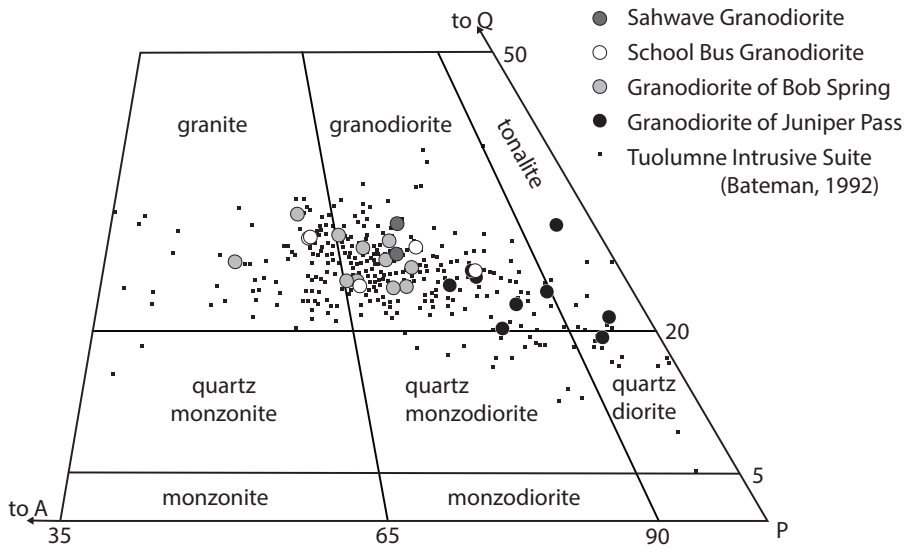

Figure 6. Portion of quartz–alkali-feldspar–plagioclase (Q-A-P) ternary plot showing samples from Sahwave and Tuolumne intrusive suites, together with International Union of Geological Sciences classifications. From Van Buer and Miller (2010).



Figure 7. StraboSpot outputs from a Mac (Apple) computer. The photo on the left shows a map view of the field-trip region with a white tool bar containing line, point, and polygon tools that can be utilized to map features in the field. The photo on the right shows an example spot location with an embedded field photo, which can be accessed when one has selected a specific spot. Tabs along the top (Spot, Notes, Orientation, etc.) allow you to access more detailed information about the selected spot.

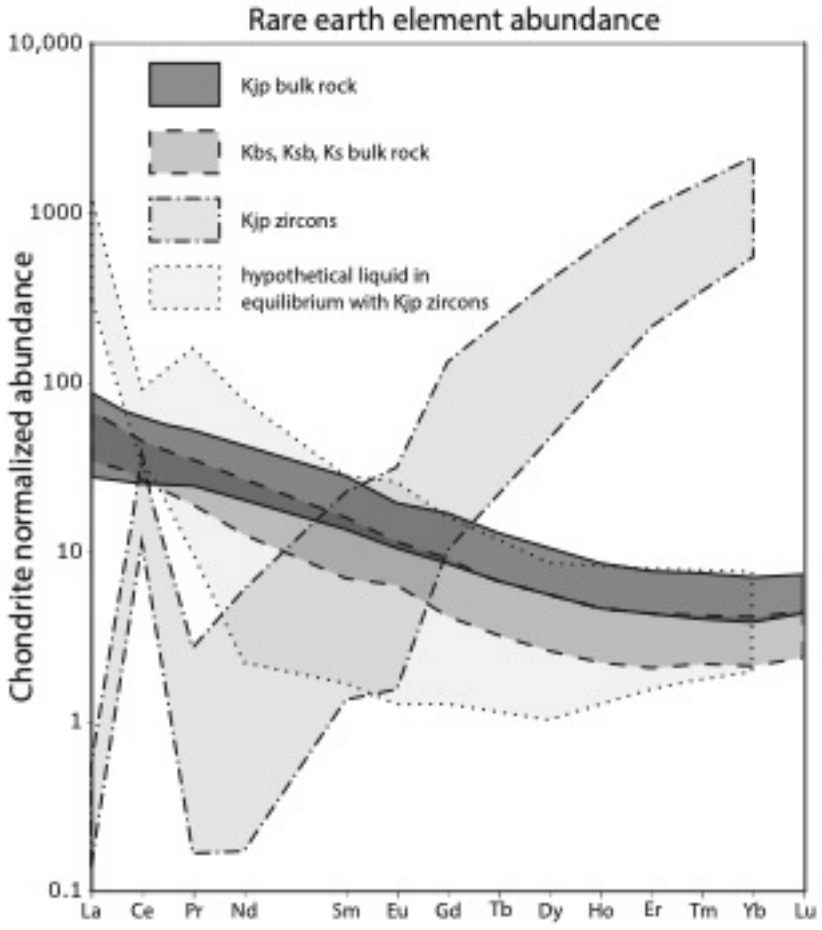

Figure 8. Chondrite-normalized rare-earth-element diagram comparing whole-rock analyses from the granodiorite of Juniper Pass with zircons from the same unit, and the modeled composition of the liquid that would have been in equilibrium with the zircons. Data from the rest of the Sahwave batholith are grouped together for comparison. See key in Figure 5 for unit descriptions. From Van Buer and Miller (2010).

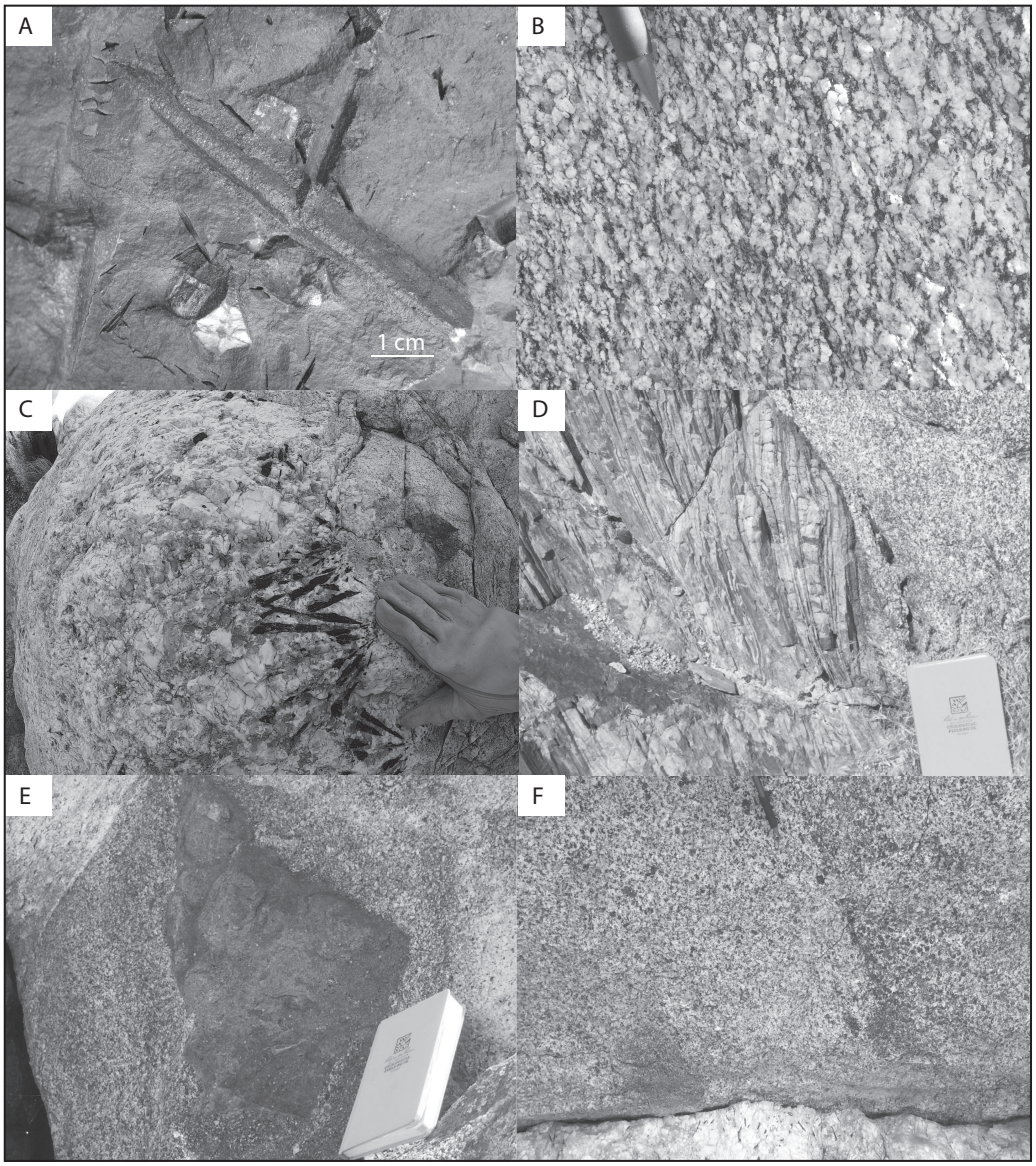

Figure 9. Field photographs from the Sahwave and Nightingale Ranges and the Bluewing Mountains. (A) Andalusite porphyroclasts in Triassic–Jurassic Auld Lang Syne Group, 1 km from Sahwave batholith intrusive contact at Optional Spot 1.4b. (B) Solid-state texture and steeply dipping foliation fabric trace from the Power Line intrusive suite at Spot 1.5. Pencil for scale. (C) Tourmaline pegmatite intruding Granodiorite of Juniper Pass at Optional Spot 1.4a. Gloved hand for scale. (D) Southwest intrusive contact of the Power Line intrusive suite with the deformed walk rock. Field notebook for scale. (E) Xenoliths, magma mingling textures, and compositional variations observed between diorite and granodiorite units of Juniper Pass near

Optional Spot 1.5a. Field notebook for scale. (F) Subvertical trace of the E-W–striking magmatic fabric observed in the granodiorite of Juniper Pass. Magmatic fabric is crosscut by a pegmatite intrusion. Pencil for scale.

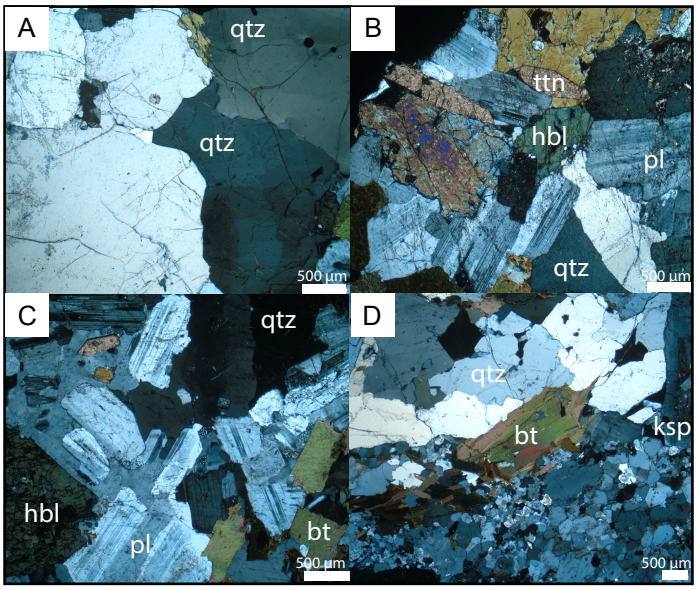

Figure 10. (A) XPL (Cross-polarized) photomicrograph of the Sahwave granodiorite. Quartz (qtz) grains show cuspate-lobate grain boundaries and chessboard subgrains indicative of high-temperature deformation (~500–600 °C) and magmatic fabrics. (B) XPL photomicrograph of the granodiorite of Bob Spring. Thin section displays euhedral magmatic grains of titanite (ttn), plagioclase (plg) and quartz with hornblende (hbl) grains showing the alteration. (C) XPL photomicrograph of the granodiorite of Juniper Pass. Euhedral grains of plagioclase, biotite (bt), hornblende, and titanite, surrounded by amorphous K-feldspar and quartz grains. (D) XPL photomicrograph from an XZ [parallel to lineation] section from the main unit of the Power Line intrusive complex. Large quartz grains show grain boundary migration and bulging recrystallization, recrystallization of biotite in strands parallel to lineation along with domains of recrystallized quartz and feldspar that show significant grain-size reduction and subgrain development.

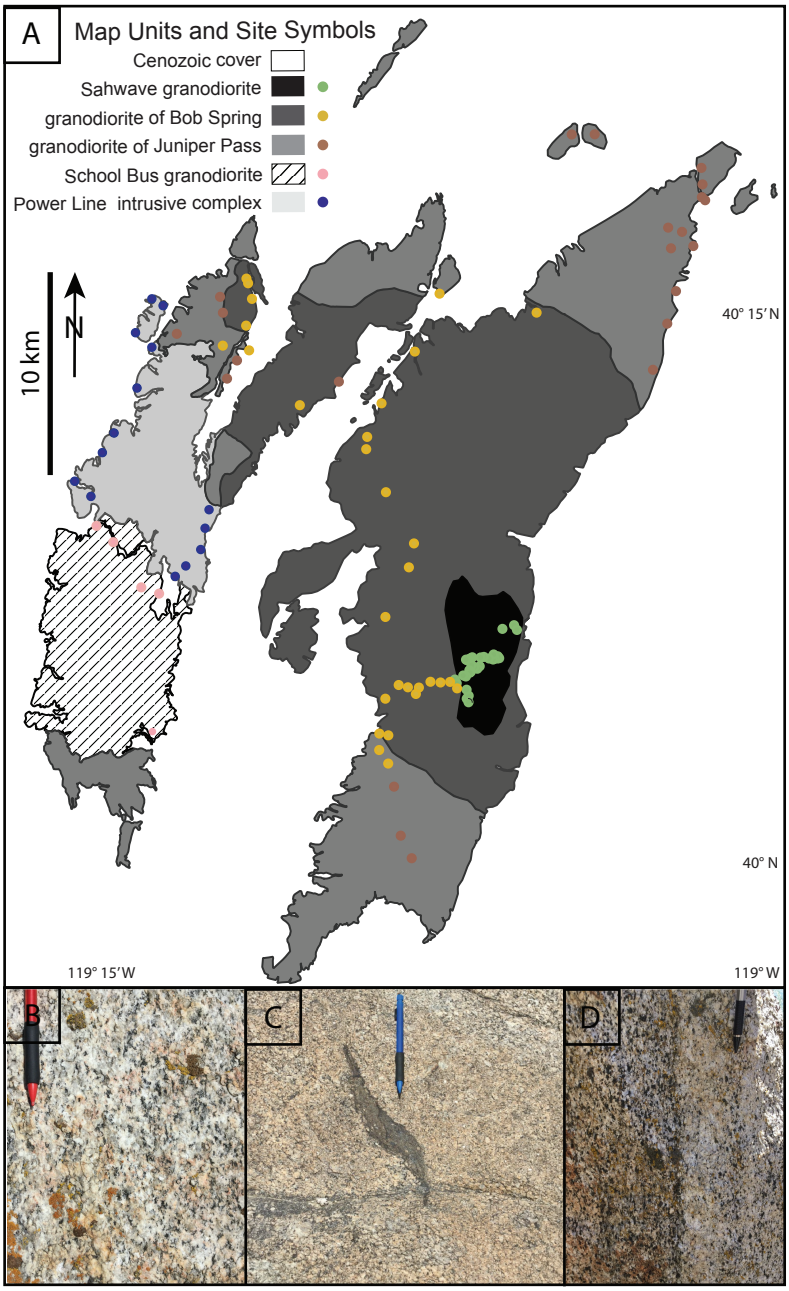

Figure 11. (A) Simplified map of the intrusive units within the Sahwave and Nightingale Ranges. Colored dots correspond to 88 site locations across the five different units. (B) Field photographs from the Power Line granodiorite showing a strong solid-state foliation defined by mafic minerals, ribboned quartz, and potassium feldspar porphyroclasts. Red pencil is aligned north-south with the pencil tip indicating south. (C) Sheared mafic enclave from the southern exposures of the Juniper Pass unit. (D) Mafic schlieren and vertical foliation defined by large

biotite and hornblende observed in the northern exposure of the Juniper Pass unit. Photograph was taken looking east.

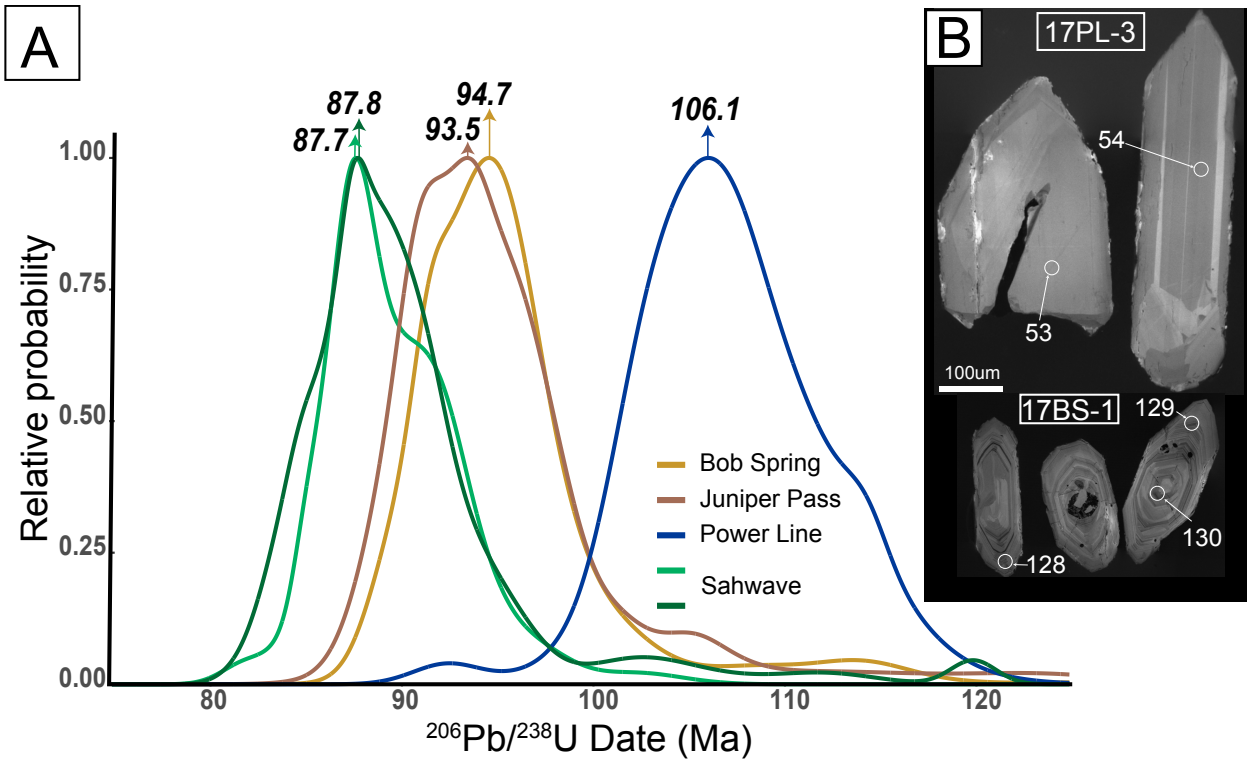

Figure 12. (A) U-Pb zircon ages from in situ laser ablation-inductively coupled plasma-mass spectroscopy (LA-ICP-MS). (B) Cathodoluminescence images of representative zircons from the Power Line intrusive complex and the Granodiorite of Bob Spring. White numbers indicate the spot locations; circles represent the spot size. All units from the Sahwave Range intrusive suite contain zircon with magmatic oscillatory zoning. Zircon from the Power Line intrusive complex display less oscillatory zoning, with some grains showing metamorphic rims.

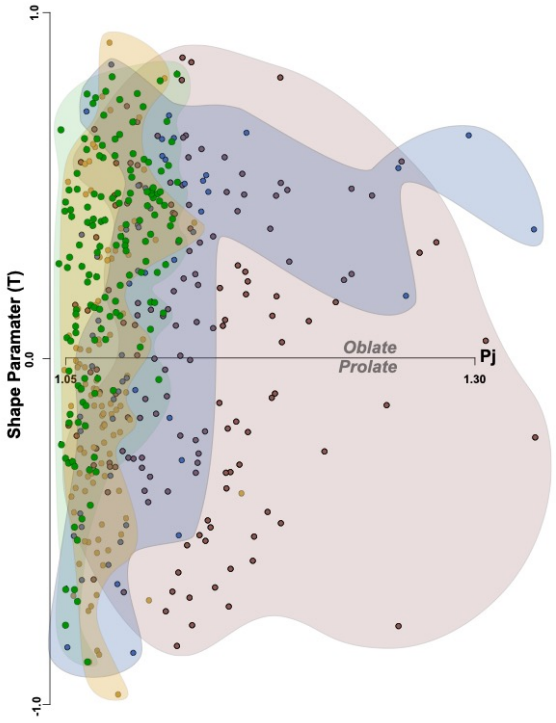

Figure 13. Anisotropy degree (Pj) versus shape parameter (T) of all the measured samples from the Sahwave intrusive suite and the Power Line complex. Color corresponds to the colored site locations on the site map (Fig. 11). Note the scatter of the data and the low Pj values for the Sahwave granodiorite (green) and the granodiorite of Bob Spring (yellow). The Power Line granodiorite and the granodiorite of Juniper Pass (red) have slightly higher Pj values, with the Power Line granodiorite (blue) being more oblate.

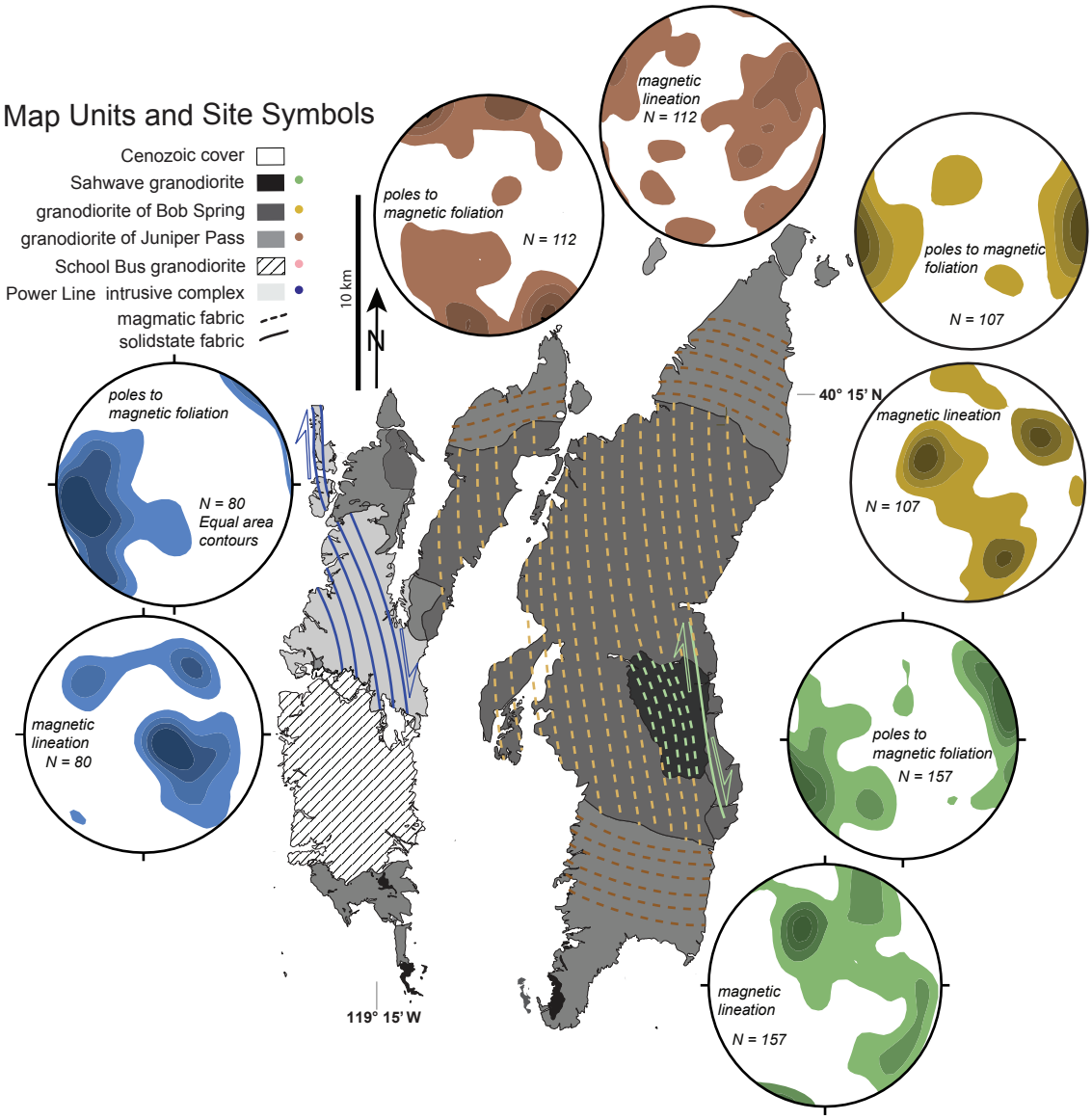

Figure 14. Summary map of the Sahwave batholith that illustrates the microstructural and magnetic foliations from anisotropy of magnetic susceptibility analyses. The dotted lines represent the interpreted magmatic foliation trajectories colored by unit. Dextral shear and solid-state deformation fabrics are observed for locations on the western and eastern margins of the batholith, indicated by solid lines with shear arrows along with an inferred magnetic foliation trajectory. Lower hemisphere equal area projections are colored by unit and show the variable orientation of magnetic foliation and lineation directions.

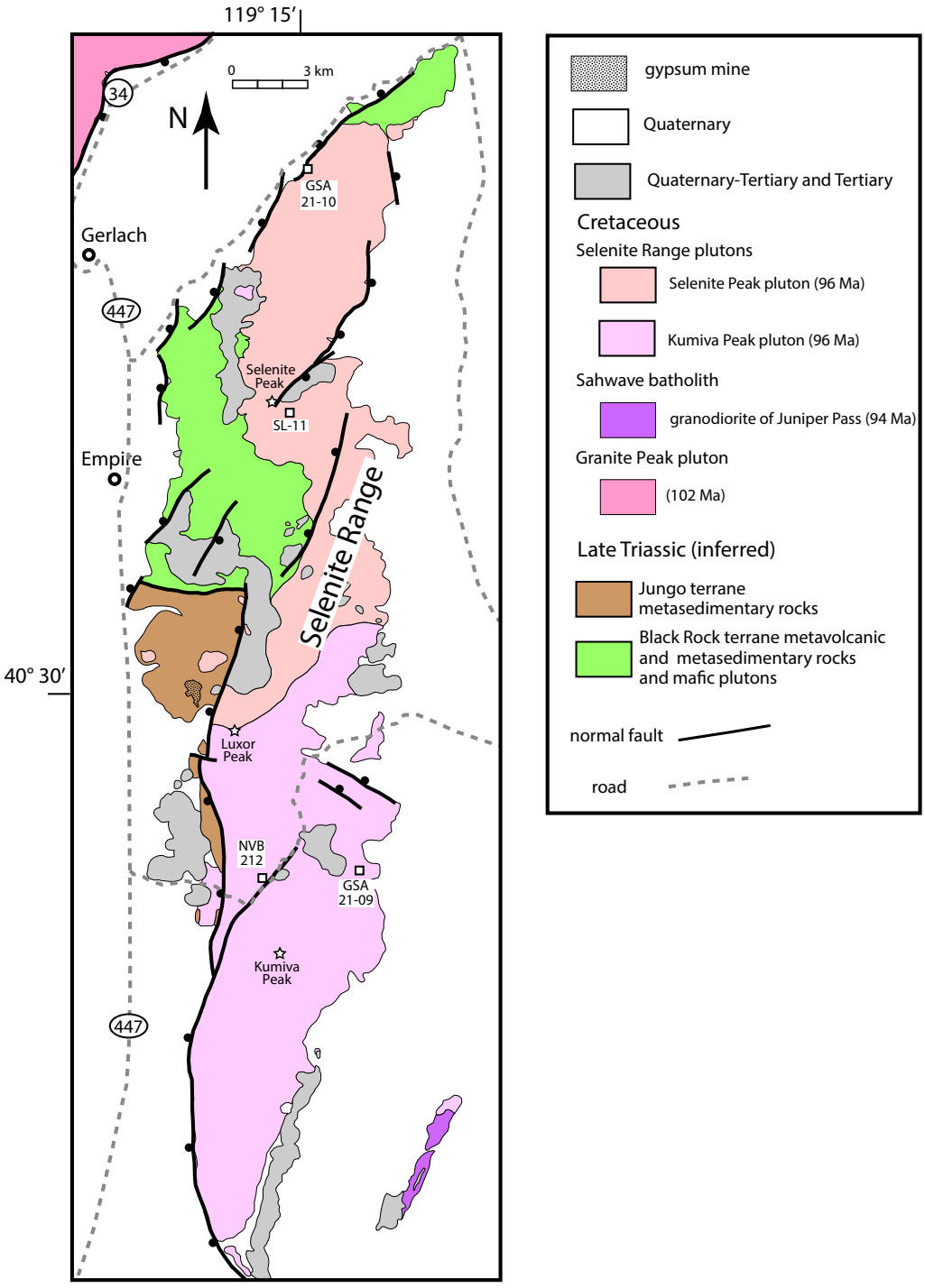

Figure 15. Simplified geologic map of the Selenite Range based on unpublished mapping at 1:24,000 scale by S. Wyld.

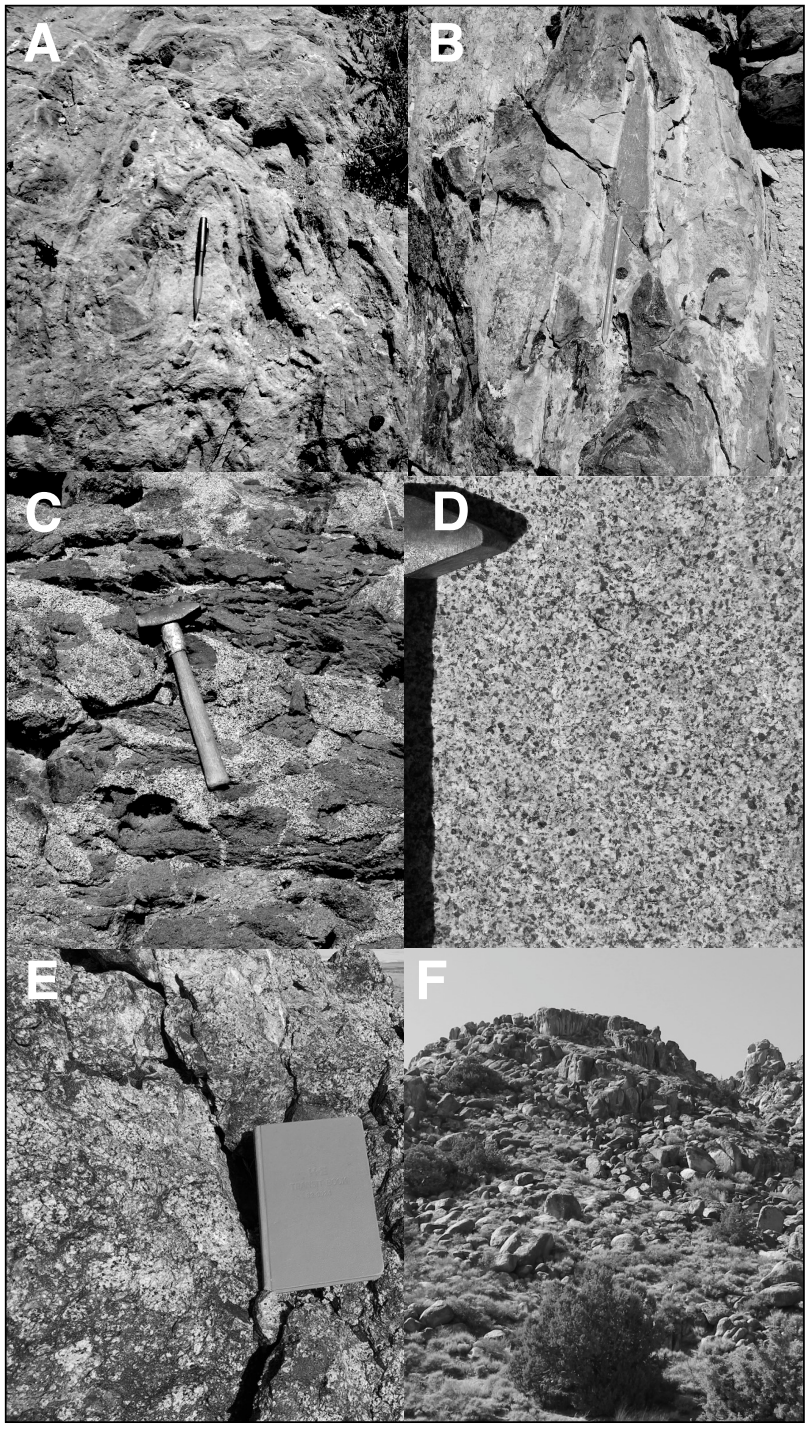

Figure 16. (A–B) Isoclinal folds in carbonate of the Cottonwood Canyon unit (Fox Range). Folds are of bedding and axial trace is parallel to pencil in both images. (A) Folds visible at optional Stop 1.12a. (B) Folds located farther up the canyon. Both images show views to northeast. (C) "Zebra outcrop" of northerneasternmost Fox Range pluton, showing abundant

mafic enclaves (dark, fine grained) enclosed within lighter-colored host quartz diorite. (D) Photograph showing typical medium-grained, equigranular biotite-hornblende-granodiorite of Granite Range pluton. Partial hammer head for scale is ~3 cm long. (E) Photograph of fault breccia exposed at the stop location. Clasts (lighter) are composed of granitic fragments derived from the Granite Range pluton. Matrix (darker) is more finely comminuted granitic material stained dark red by Fe-bearing fluids. (F) Photograph (looking north) of typical hornblende-biotite-granodiorite of the Kumiva Peak pluton in the Selenite Range. Photo shows the rocky tor outcrops typical of this plutonic body. Large bush in lower central part of photo is ~2 m tall.

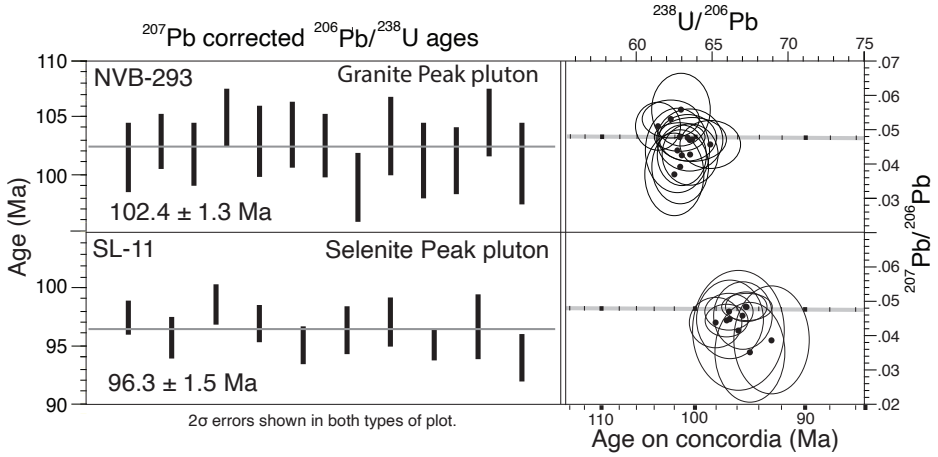

Figure 17. SHRIMP (sensitive high-resolution ion microprobe) U-Pb results for the Granite Range and Selenite Peak plutons. At left, spot ages and uncertainties are shown by solid bars. No spot ages were rejected. Weighted averages are shown by gray lines. Diagrams on right are inverse concordia plots: ages along concordia (gray line with tick marks) are shown on the corresponding tick marks at bottom. All errors are 2σ.

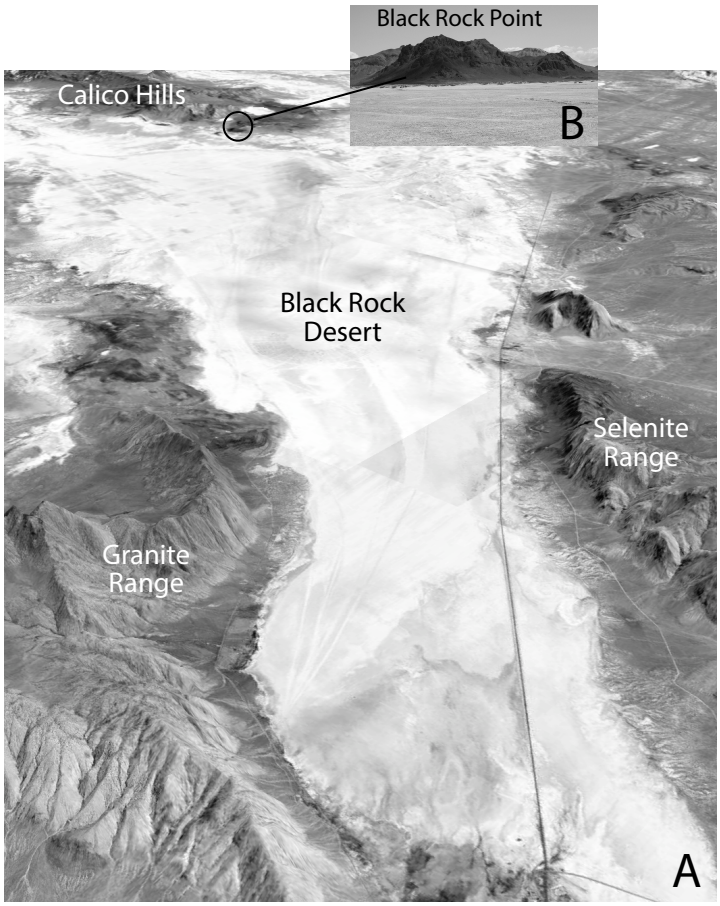

Figure 18. Black Rock Desert and Black Rock Point as viewed from the north side of the town of Gerlach. (A) GoogleEarth image (view to NNE) showing Black Rock Desert and surrounding mountains. (B) Close-up photograph of Black Rock Point taken from farther south in the Black Rock Desert (view to north).

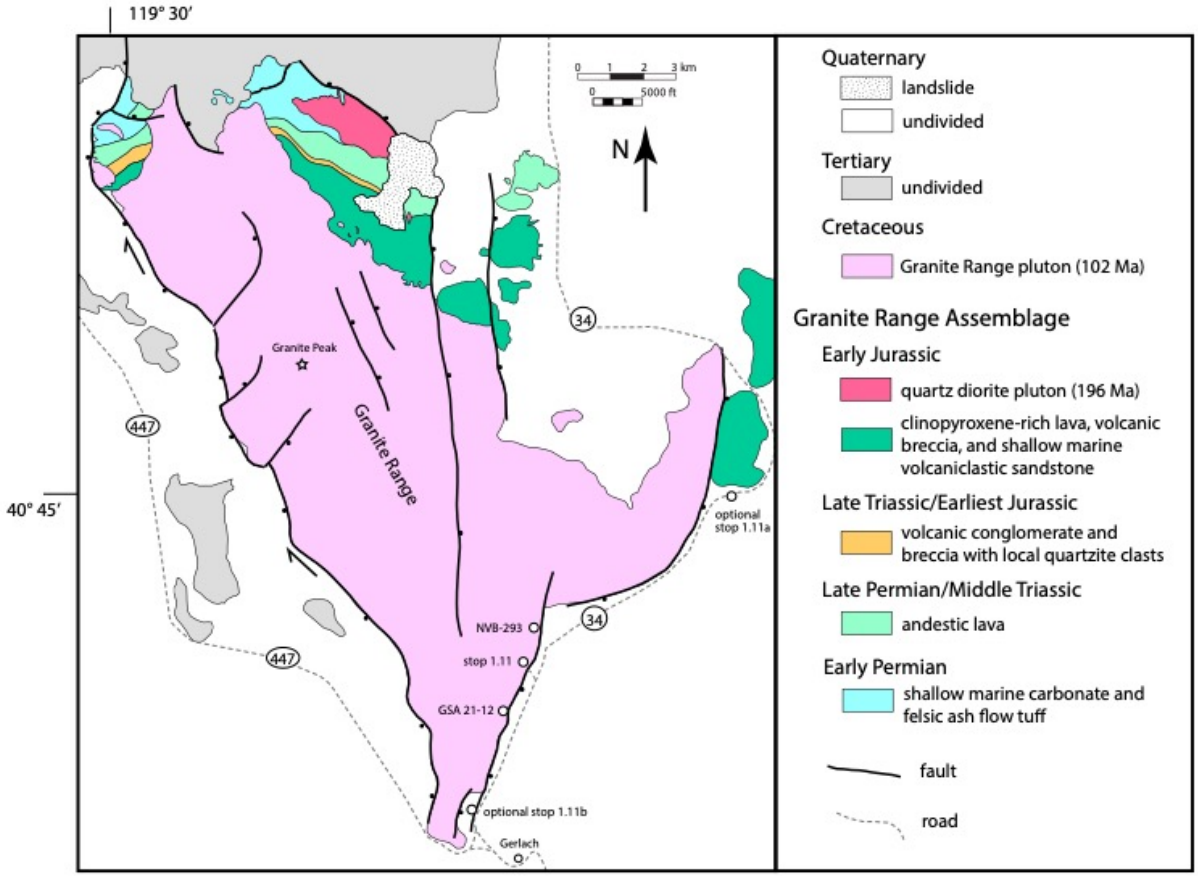

Figure 19. Simplified geologic map of the Granite Range. Distribution of, and structure cutting, Granite terrane rocks, and adjacent parts of Granite Range pluton and Tertiary strata is based on unpublished mapping at 1:24,000 scale by S. Wyld. Geology in the remainder of the figure is based on Bonham (1969), Stewart and Carlson (1978), and Faulds and Ramelli (2005).

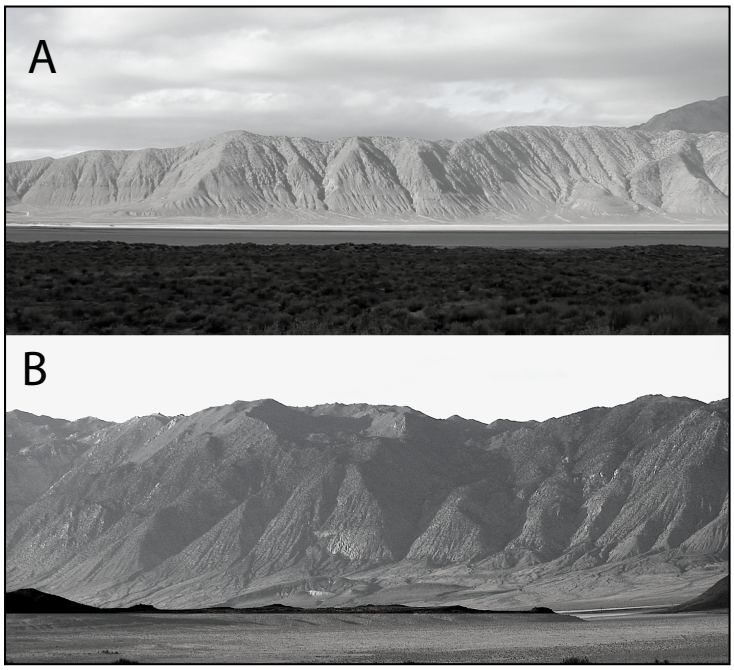

Figure 20. Distance photographs of (A) the southeast side and (B) the southwest side of the Granite Range pluton, showing the prominent normal fault scarps uplifting both sides of the pluton. Triangular faceted ridges are evident in panel B.

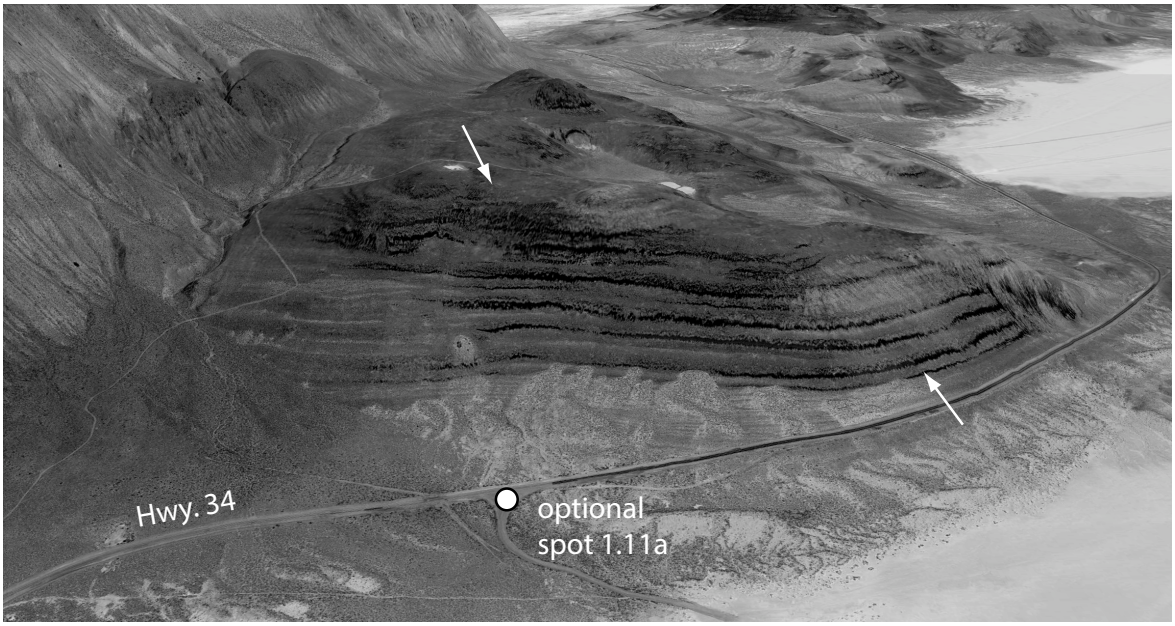

Figure 21. GoogleEarth image (view to north) of multiple Lake Lahontan shorelines cut into mafic metavolcanic rocks of the Granite terrane. Uppermost and lowermost visible shorelines are marked with white arrows. Steep topography to the west is the Granite Range pluton. White lowlands to the east are parts of the Black Rock Desert playa.

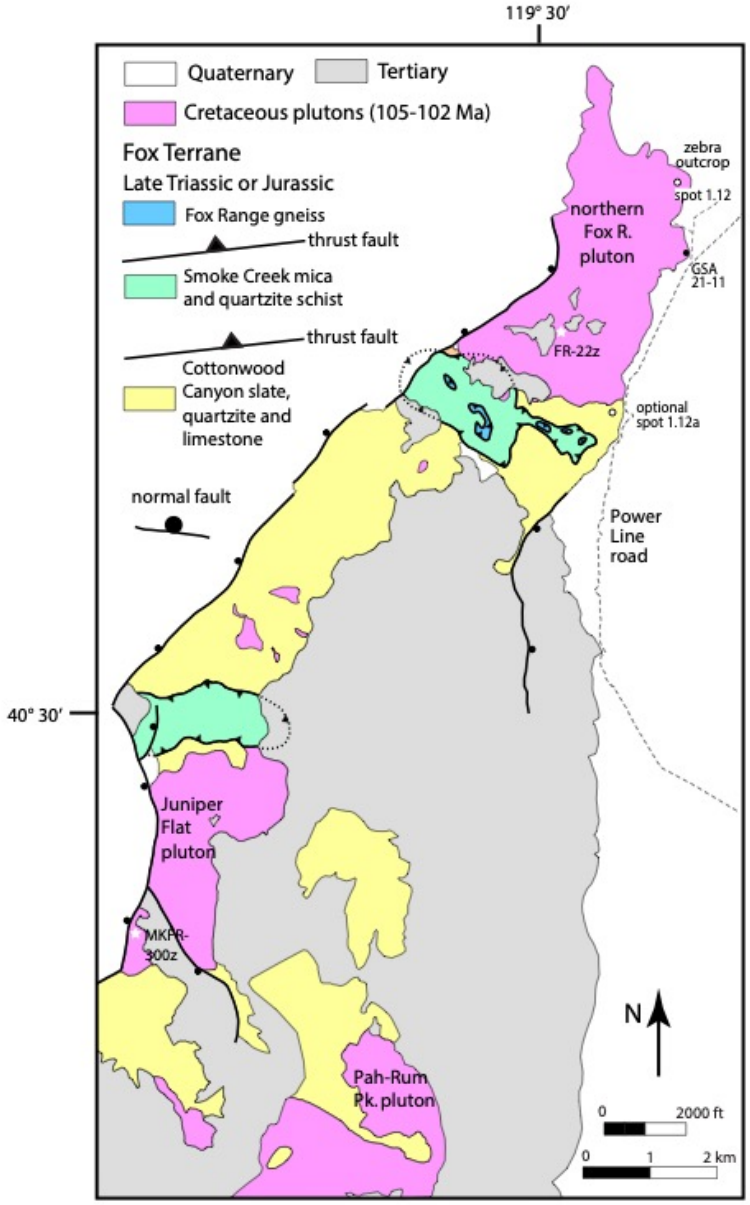

Figure 22. Simplified geologic map of the Fox Range. Based on 1:24,000 scale mapping by Kinsella (2010).

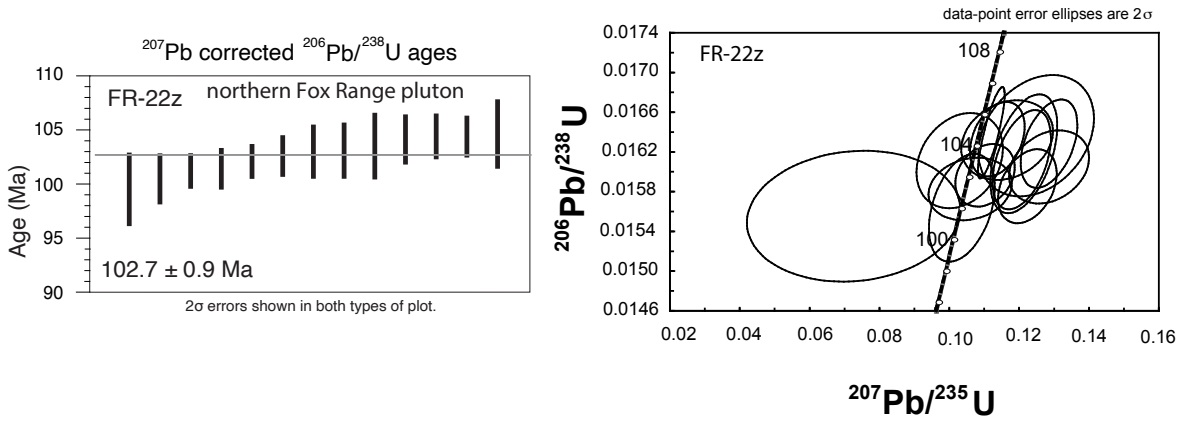

Figure 23. SHRIMP (sensitive high-resolution ion microprobe) U-Pb results for the Fox Range pluton. The left plot shows spot ages and uncertainties denoted by solid bars. No spot ages were rejected. Weighted average is denoted by the gray line. The right diagram is a normal concordia diagram reporting U-Pb zircon data.

TABLE 1. U-Pb GEOCHRONOLOGY SAMPLE DATA

Unit	Sample no.	Latitude (°N)	Longitude (°W)	Age (±2σ, Ma)
Sahwave granodiorite	JC03-SV3	40.13222	119.06806	88.5 ± 2.0
School Bus granodiorite	NVB-207	40.12694	119.26833	91.2 ± 1.2
granodiorite of Bob Spring	SH-21	40.20806	119.10056	92.8 ± 1.7
granodiorite of Juniper Pass	NVB-206	40.31306	119.01778	92.7 ± 1.4
granodiorite in Trinity Range	NVB-286	40.17028	118.77222	90.3 ± 0.6
Power Line intrusive complex	NVB-208	40.14389	119.22222	104.9 ± 0.8
Kumiva Peak pluton	NVB-212	40.4318	119.2705	96.3 ± 0.8
Selenite Peak pluton	SL-11	40.6016	119.2570	96.3 ± 1.5
Granite Peak pluton	NVB-293	40.717	119.347	102.4 ± 1.3
Juniper Flat pluton	MKFR-300z	40.43	119.62	105.4 ± 0.6
northern Fox Range pluton	FR-22z	40.57	119.49	102.7 ± 0.9

Note: Reported ages are ^{207}Pb corrected $^{206}Pb/^{238}U$ weighted-average ages with 2σ error.

5. References

Armstrong, R.L., Taubeneck, W.H., and Hales, P.O., 1977, Rb-Sr and K-Ar geochronometry of Mesozoic granitic rocks and their Sr isotopic composition, Oregon, Washington, and Idaho: Geological Society of America Bulletin, v. 88, p. 397–411, https://doi.org/10.1130/0016-7606(1977)88<397:RAKGOM>2.0.CO;2.

Armstrong, R.L., 1988, Mesozoic and Early Cenozoic magmatic evolution of the Canadian Cordillera, in Clark, S.P., Jr., Burchfiel, B.C., and Suppe, J., Processes in Continental Lithospheric Deformation: Geological Society of America Special Paper 218, p. 55–92, https://doi.org/10.1130/SPE218-p55.

Atwater, T., and Stock, J., 1998, Pacific–North America plate tectonics of the Neogene southwestern United States; an update, in Ernst, W.G., and Nelson, C.A., eds., Integrated Earth and Environmental Evolution of the Southwestern United States: The Clarence A. Hall, Jr. Volume: Columbia, Maryland, Bellwether Publishing, p. 375–402, https://doi.org/10.1080/00206819809465216.

Bateman, P.C., 1992, Plutonism in the Central Part of the Sierra Nevada Batholith, California: U.S. Geological Survey Professional Paper 1483, https://doi.org/10.3133/pp1483, scale: 1:250,000.

Bonham, H. F., 1969, Geology and mineral deposits of Washoe and Storey Counties, Nevada: Nevada Bureau of Mines and Geology Bulletin v. 70, p. 140.

Braudy, N., Gaschnig, R.M., Wilford, D., Vervoort, J.D., Nelson, C.L., Davidson, C., Kahn, M.J., and Tikoff, B., 2017, Timing and deformation conditions of the western Idaho shear zone, West Mountain, west-central Idaho: Lithosphere, v. 9, no. 2, p. 157–183, https://doi.org/10.1130/L519.1.

Burchfiel, B.C., Cowan, D.S., and Davis, G., 1992, Tectonic overview of the Cordilleran orogen in the western United States, in Burchfiel, B.C., Lipman, P.W., and Zoback, M.L., eds., The Cordilleran Orogen: Conterminous U.S.: Boulder, Colorado, Geological Society of America, Geology of North America v. G-3, p. 407–480, https://doi.org/10.1130/DNAG-GNA-G3.407.

Busby-Spera, C.J., and Saleeby, J.B., 1990, Intra-arc strike-slip fault exposed at batholithic levels in the southern Sierra Nevada, California: Geology, v. 18, p. 255–259, https://doi.org/10.1130/0091-7613(1990)018<0255:IASSFE>2.3.CO;2.

Cao, W., Paterson, S., Memeti, V., Mundil, R., Anderson, J.L., and Schmidt, K., 2015, Tracking paleodeformation fields in the Mesozoic central Sierra Nevada arc: Implications for intra-arc cyclic deformation and arc tempos: Lithosphere, v. 7, no. 3, p. 296–320, https://doi.org/10.1130/L389.1.

Castro, A., 1987, On granitoid emplacement and related structures. A review: Geologische Rundschau, v. 76, p. 101–124, https://doi.org/10.1007/BF01820576.

Chen, J.H., and Moore, J.G., 1982, Uranium-lead isotopic ages from the Sierra Nevada Batholith, California: Journal of Geophysical Research, v. 87, p. 4761–4784, https://doi.org/10.1029/JB087iB06p04761.

Coleman, D.S., Gray, W., and Glazner, A.F., 2004, Rethinking the emplacement and evolution of zoned plutons: Geochronologic evidence for incremental assembly of the Tuolumne Intrusive Suite, California: Geology, v. 32, no. 5, p. 433–436, https://doi.org/10.1130/G20220.1.

DeCelles, P.G., Ducea, M.N., Kapp, P., and Zandt, G., 2009, Cyclicity in Cordilleran orogenic systems: Nature Geoscience, v. 2, p. 251–257, https://doi.org/10.1038/ngeo469.

de Saint Blanquat, M., and Tikoff, B., 1997, Development of magmatic to solidstate fabrics during syntectonic emplacement of the Mono Creek granite, Sierra Nevada batholith, California, in Bouchez, J.-L., Stephens, W.E., and Hutton, D.H., eds., Granite: From Melt Segregation to Emplacement Fabrics: Norwell, Massachusetts, Kluwer Academic, p. 231–252.

de Saint Blanquat, M., Horsman, E., Habert, G., Morgan, S., Vanderhaeghe, O., Law, R., and Tikoff, B., 2011, Multiscale magmatic cyclicity, duration of pluton construction, and the paradoxical relationship between tectonism and plutonism in continental arcs: Tectonophysics, v. 500, no. 1–4, p. 20–33, https://doi.org/10.1016/j.tecto.2009.12.009.

Ducea, M.N., 2001, The California arc: Thick granitic batholiths, eclogitic residues, lithospheric-scale thrusting and magmatic flare-ups: GSA Today, v. 11, p. 4–10, https://doi.org/10.1130/1052-5173(2001)011<0004:TCATGB>2.0.CO;2.

Ducea, M.N., and Barton, M.D., 2007, Igniting flare-up events in Cordilleran arcs: Geology, v. 35, no. 11, p. 1047–1050, https://doi.org/10.1130/G23898A.1.

Ducea, M.N., Paterson, S.R., and DeCelles, P.G., 2015, High-volume magmatic events in subduction systems: Elements, v. 11, no. 2, p. 99–104, https://doi.org/10.2113/gselements.11.2.99.

Everden, J.F., and Kistler, R.W., 1970, Chronology of Emplacement of Mesozoic Batholith Complexes in California and Western Nevada: U.S. Geological Survey Professional Paper 623, 42 p. + 2 pls.

Faulds, J.E., and Ramelli, A.R., 2005, Reconnaissance map of the Granite Range fault zone and adjacent areas, Washoe County, Nevada: Nevada Bureau of Mines and Geology Open-File Report 05-11, scale 1:50,000, 6 p. text.

Faulds, J.E., Henry, C.D., and Hinz, N.H., 2005, Kinematics of the northern Walker Lane; an incipient transform fault along the Pacific–North American plate boundary: Geology, v. 33, p. 505–508, https://doi.org/10.1130/G21274.1.

Fleck, R.J., and Criss, R.E., 1985, Strontium and oxygen isotopic variations in Mesozoic and Tertiary plutons of central Idaho: Contributions to Mineralogy and Petrology, v. 90, p. 291–308, doi:10.1007/BF00378269.

Gaschnig, R.M., Vervoort, J.D., Lewis, R.S., and McClelland, W.C., 2010, Migrating magmatism in the northern US Cordillera: In situ U-Pb geochronology of the Idaho batholith: Contributions to Mineralogy and Petrology , v. 159, p. 863–883, doi:10.1007/s00410–009–0459–5.

Gaschnig, R.M., Vervoort, J.D., Lewis, R.S., and Tikoff, B., 2011, Isotopic evolution of the Idaho Batholith and Challis Intrusive Province, northern US Cordillera: Journal of Petrology, v. 52, no. 12, p. 2397–2429, https://doi.org/10.1093/petrology/egr050.

Gaschnig, R.M., Vervoort, J.D., Tikoff, B., and Lewis, R.S., 2017, Construction and preservation of batholiths in the northern U.S. Cordillera: Lithosphere, v. 9, no. 2, p. 315–324, https://doi.org/10.1130/L497.1.

Gianella, V.P., and Larson, E.R., 1960, Marine Permian at Black Rock, Nevada: Geological Society of America Bulletin, v. 71, p. 2061.

Giorgis, S., McClelland, W., Fayon, A., Singer, B.S., and Tikoff, B., 2008, Timing of deformation and exhumation in the western Idaho shear zone, McCall, Idaho: Geological Society of America Bulletin, v. 120, no. 9–10, p. 1119–1133, https://doi.org/10.1130/B26291.1.

Greene, D.C., and Schweickert, R.A., 1995, The Gem Lake shear zone; Cretaceous dextral transpression in the northern Ritter Range pendant, eastern Sierra Nevada, California: Tectonics, v. 14, p. 945–961, https://doi.org/10.1029/95TC01509.

Henry, C.D., 2008, Ash-flow tuffs and paleovalleys in northeastern Nevada: Implications for Eocene paleogeography and extension in the Sevier hinterland, northern Great Basin: Geosphere, v. 4, p. 1–35, https://doi.org/10.1130/GES00122.1.

Hildebrand, R.S., 2013, Mesozoic Assembly of the North American Cordillera: Geological Society of America Special Paper 495, 169 p., https://doi.org/10.1130/SPE495.

Kinsella, M.E., Warren, M.B., Wyld, S.J., and Wright, J.E., 2007, The Fox Range, northwest Nevada: Displaced fragment along an Early Cretaceous dextral strike-slip fault?: Geological Society of America Abstracts with Programs, v. 39, no. 4, p. 8.

Kinsella, M.E., 2010, The Fox Range, northwest Nevada: Displaced fragment along an Early Cretaceous dextral strike-slip fault [M.S. thesis]: Athens, Georgia, University of Georgia, 174 p.

Kirkham, R.A., 1982, The Geology of the northern portion of the Fox Range, Washoe County, Nevada [M.S. thesis]: Reno, University of Nevada, Reno, 98 p.

Kirsch, M., Paterson, S.R., Wobbe, F., Martinez-Ardila, A.M., Clausen, B.L., and Alasino, H.P., 2016, Temporal histories of Cordilleran continental arcs: testing models for magmatic episodicity: American Mineralogist, v. 101, p. 2133

Kistler, R.W., Chappell, B.W., Peck, D.L., and Bateman, P.C., 1986, Isotopic variation in the Tuolumne intrusive suite, central Sierra Nevada, California: Contributions to Mineralogy and Petrology, v. 94, p. 205–220, https://doi.org/10.1007/BF00592937.

Krueger, R.J., and Yoshinobu, A., 2018, Structures in the Jackass Lakes pluton–host-rock system, central Sierra Nevada, California, and inferred mid-Cretaceous Farallon–North America plate kinematics: Geological Society of America Bulletin, v. 130, p. 1940–1958, https://doi.org/10.1130/B31992.1.

Lahren, M.M., Schweickert, R.A., Mattinson, J.M., and Walker, J.D., 1990, Evidence of uppermost Proterozoic to Lower Cambrian miogeoclinal rocks and the Mojave–Snow Lake fault: Snow Lake pendant, central Sierra Nevada, California: Tectonics, v. 9, p. 1585–1608, https://doi.org/10.1029/TC009i006p01585.

Leshendok, M.P., 1997, Magma mixing in the northern Fox Range pluton, Washoe County, Nevada [M.S. thesis]: Reno, University of Nevada, Reno, 105 p.

Lund, K., 2008, Geometry of the Neoproterozoic and Paleozoic rift margin of western Laurentia: Implications for mineral deposit settings: Geosphere, v. 4, no. 2, p. 429–444, https://doi.org/10.1130/GES00121.1.

Lupe, R., and Silberling, N.J., 1985, Genetic relationship between lower Mesozoic continental strata of the Colorado Plateau and marine strata of the western Great Basin: Significance for accretionary history of Cordilleran lithotectonic terranes, in Howell, D.G., ed., Tectonostratigraphic Terranes of the Circum-Pacific Region: Circum-Pacific Council for Energy and Mineral Resources, Earth Science Series, no. 1, p. 263–271.

Manduca, C.A., Kuntz, M.A., and Silver, L.T., 1993, Emplacement and deformation history of the western margin of the Idaho batholith near McCall, Idaho: Influence of a major terrane boundary: Geological Society of America Bulletin, v. 105, p. 749–765, https://doi.org/10.1130/0016-7606(1993)105<0749:EADHOT>2.3.CO;2.

Martínez Ardila, A.M., Paterson, S.R., Memeti, V., Parada, M.A., and Molina, P.G., 2019, Mantle driven Cretaceous flare-ups in Cordilleran arcs: Lithos, v. 326–327, p. 19–27, ttps://doi.org/10.1016/j.lithos.2018.12.007.

Matthews, K.J., Seton, M., and Müller, R.D., 2012, A global-scale plate reorganization event at 105–100 Ma: Earth and Planetary Science Letters, v. 355–356, p. 283–298, https://doi.org/10.1016/j.epsl.2012.08.023.

McClelland, W.C., Tikoff, B., and Manduca, C.A., 2000, Two-phase evolution of accretionary margins: Examples from the North American Cordillera: Tectonophysics, v. 326, no. 1–2, p. 37–55, https://doi.org/10.1016/S0040-1951(00)00145-1.

McQuarrie, N., and Wernicke, B.P., 2005, An animated tectonic reconstruction of southwestern North America since 36 Ma: Geosphere, v. 1, no. 3, p. 147–172, https://doi.org/10.1130/GES00016.1.

Oldow, J.S., 1984, Evolution of a Late Mesozoic back-arc fold and thrust belt, Northwestern Great Basin, U.S.A.: Tectonophysics, v. 102, p. 245–274, https://doi.org/10.1016/0040-1951(84)90016-7.

Ostwald, C., Kahn, M., Schmitz, M.D., and Tikoff, B., 2017, Finding strain localization and dating the onset of deformation in the western Idaho shear zone using titanite U-Pb geochronology and crystallographic vorticity axis analysis: Geological Society of America Abstracts with Programs, v. 49, no. 6, https://doi.org/10.1130/abs/2017AM-307644, abstract 386-4.

Pennacchioni, G., and Mancktelow, N.S., 2018, Small-scale ductile shear zones: Neither extending, nor thickening, nor narrowing: Earth-Science Reviews, v. 184, p. 1–12, https://doi.org/10.1016/j.earscirev.2018.06.004.

Quinn, M.J., Wright, J.E., and Wyld, S.J., 1997, Happy Creek igneous complex and tectonic evolution of the early Mesozoic arc in the Jackson Mountains, northwest Nevada: Geological Society of America Bulletin, v. 109, p. 461–482, https://doi.org/10.1130/0016-7606(1997)109<0461:HCICAT>2.3.CO;2.

Saleeby, J., Farley, K.A., Kistler, R.W., and Fleck, R.J., 2007, Thermal evolution and exhumation of deep-level batholithic exposures, southernmost Sierra Nevada, California, in Cloos, M., Carlson, W.D., Gilbert, M.C., Liou, J.G., and Sorensen, S.S., eds., Convergent Margin Terranes and Associated Regions: A Tribute to W.G. Ernst: Geological Society of America Special Paper 419, p. 39–66, https://doi.org/10.1130/2007.2419(02).

Saleeby, J.B., Ducea, M.N., Busby, C.J., Nadin, E.S., and Westmore, P.H., 2008, Chronology of pluton emplacement and regional deformation in the southern Sierra Nevada batholith, California, in Wright, J.E., and Shervais, J.W., eds., Ophiolites, Arcs, and Batholiths: A Tribute to Cliff Hopson: Geological Society of America Special Paper 438, p. 397–427, https://doi.org/10.1130/2008.2438(14).

Schmidt, K.L., and Paterson, S.R., 2002, A doubly vergent, fan structure in the Peninsular Ranges batholith: Transpression or complex flow along a crustal-scale discontinuity?: Tectonics, v. 21, 1050, https://doi.org/10.1029/2001TC001353.

Schweickert, R.A., and Lahren, M.M., 1990, Speculative reconstruction of the Mojave–Snow Late fault: Implications for Paleozoic and Mesozoic orogenesis in the western United States: Tectonics, v. 9, p. 1609–1629, https://doi.org/10.1029/TC009i006p01609.

Silberling, N.J., Jones, D.L., Blake, M.C., Jr., and Howell, D.G., 1987, Lithotectonic Terrane Map of the Western Conterminous United States: U.S. Geological Survey Miscellaneous Field Studies Map 1874-C, scale 1:2,500,000, 20-p. pamphlet + map.

Silver, L.T., and Chappell, B., 1988, The Peninsular Ranges batholith: An insight into the Cordilleran batholiths of southwestern North America: Royal Society of Edinburgh Transactions: Earth Science, v. 79, p. 105–121.

Smith, J.G., McKee, E.H., Tatlock, D.B., and Marvin, R.F., 1971, Mesozoic granitic rocks in northwestern Nevada: A link between the Sierra Nevada and Idaho Batholiths: Geological Society of America Bulletin, v. 82, p. 2933–2944, https://doi.org/10.1130/0016-7606(1971)82[2933:MGRINN]2.0.CO;2.

Stewart, J. H., and Carlson, J. E., 1976b, Geologic map of north-central Nevada: Nevada Bureau of Mines and Geology Map 50.

Thiesse, M.F., ms, 1988, Geology of Paleozoic basinal rocks in the northern Fox Range, Washoe County, Nevada: M.S. thesis; University of Nevada, Reno, p. 89.

Tikoff, B., Davis, M.R., Teyssier, C., de St. Blanquat, M., Habert, G., and Morgan, S., 2005, Fabric studies within the Cascade Lake shear zone, Sierra Nevada, California: Tectonophysics, v. 400, p. 209–226, https://doi.org/10.1016/j.tecto.2005.03.003.

Tikoff, B., Kelso, P., Manduca, C., Markley, M.J., and Gillaspy, J., 2001, Lithospheric and crustal reactivation of an ancient plate boundary: The assembly and disassembly of the Salmon River suture zone, Idaho, USA, in Holdsworth, R.E., Strachan, R.A., Magloughlin, J.F., and Knipe, R.J., eds., The Nature and Tectonic Significance of Fault Zone Weakening: Geological Society, London, Special Publication 186, no. 1, p. 213–231, https://doi.org/10.1144/GSL.SP.2001.186.01.13.

Tikoff, B., and de Saint Blanquat, M., 1997, Transpressional shearing and strike-slip partitioning in the Late Cretaceous Sierra Nevada magmatic arc, California: Tectonics, v. 16, no. 3, p. 442–459, https://doi.org/10.1029/97TC00720.

Tikoff, B., and Greene, D., 1997, Stretching lineations in transpressional shear zones: An example from the Sierra Nevada batholith, California: Journal of Structural Geology, v. 19, no. 1, p. 29–39, https://doi.org/10.1016/S0191-8141(96)00056-9.

Tikoff, B., and Teyssier, C., 1992, Crustal-scale, en echelon "P-shear" tensional bridges: A possible solution to the batholithic room problem: Geology, v. 20, p. 927–930, https://doi.org/10.1130/0091-7613(1992)020<0927:CSEEPS>2.3.CO;2.

Van Buer, N.J., and Miller, E.L., 2010, Sahwave batholith, NW Nevada: Cretaceous arc flare-up in a basinal terrane: Lithosphere, v. 2, no. 6, p. 423–446, https://doi.org/10.1130/L105.1.

Walker, J.D., Tikoff, B., Newman, J., Clark, R., Ash, J., Good, J., Bunse, E.G., Möller, A., Kahn, M., Williams, R.T., Michels, Z., Andrew, J.E., Rufledt, C., 2019, StraboSpot data system for structural geology: Geosphere, v. 15, n. 2, p. 533–547. doi: https://doi.org/10.1130/GES02039.1

Wernicke, B., and Snow, J.K., 1998, Cenozoic tectonism in the central Basin and Range: Motion of the Sierran–Great Valley block: International Geology Review, v. 40, p. 403–410, https://doi.org/10.1080/00206819809465217.
Wesnousky, S.G., Barron, A.D., Briggs, R.W., Caskey, S.J., Kumar, S., and Owen, L., 2005, Paleoseismic transect across the northern Great Basin: Journal of Geophysical Research, v. 110, B05408, https://doi.org/10.1029/2004JB003283.

Wyld, S.J., 1990, Paleozoic and Mesozoic rocks of the Pine Forest Range, northwest Nevada, and their relation to volcanic arc assemblages of the western U.S. Cordillera, in Harwood, D.S., and Miller, M.M., eds., Late Paleozoic and Early Mesozoic Paleogeographic Relations: Klamath Mountains, Sierra Nevada, and Related Rocks: Geological Society of America Special Paper 255, p. 219–237, https://doi.org/10.1130/SPE255-p219.

Wyld, S.J., 1996, Early Jurassic deformation in the Pine Forest Range, northwest Nevada, and implications for Cordilleran tectonics: Tectonics, v. 15, p. 566–583, https://doi.org/10.1029/95TC03693.

Wyld, S.J., 2000, Triassic evolution of the arc and backarc of northwest Nevada, and evidence for extensional tectonism, in Soreghan, M.J., and Gehrels G.E., eds., Paleozoic and Triassic Paleogeography and Tectonic Evolution of Western Nevada and Northern California: Geological Society of America Special Paper 347, p. 185–208, https://doi.org/10.1130/0-8137-2347-7.185.

Wyld, S.J., and Wright, J.E., 2001, New evidence for Cretaceous strike-slip faulting in the United States Cordillera and implications for terrane-displacement, deformation patterns, and plutonism: American Journal of Science, v. 301, no. 2, p. 150–181, https://doi.org/10.2475/ajs.301.2.150.

Wyld, S.J., 2002, Structural evolution of a Mesozoic back-arc fold-thrust belt in the U.S. Cordillera; new evidence from northern Nevada: Geological Society of America Bulletin, v. 114, p. 1452–1468, https://doi.org/10.1130/0016-7606(2002)114<1452:SEOAMB>2.0.CO;2.

Wyld, S.J., Wright, J.E., Kinsella, M.E., and Warren, M.B., 2007, Identification of a distinct terrane in the Cordillera that is offset along the Early Cretaceous dextral MSNI fault system: Geological Society of America Abstracts with Programs, v. 39, no. 4, p. 81.

Wyld, S.J., and Wright, J.E., 2019, Allochthonous Paleozoic–Jurassic terranes of NW Nevada and SE Oregon displaced dextrally from the southwest Cordillera in the Early Cretaceous. Where is their homeland?: Geological Society of America Abstracts with Programs, v. 50, no. 5, https://doi.org/10.1130/abs/2018RM-313792.</jrn>

Chapter 4: Two phases of Cretaceous dextral shearing recorded in the plutonic rocks of NW Nevada: A tectonic link between intra-arc shearing in the Sierra Nevada and Idaho batholiths

Abstract

The Cretaceous intrusive suites exposed in the Sahwave and Nightingale Ranges of northwestern Nevada are part of the Cretaceous magmatic arc in the western United States, located north of the Sierra Nevada batholith and south of the Idaho batholith. We recognize a 94-88 Ma (U-Pb zircon) Sahwave Range intrusive suite that consists of the Juniper Pass, Bob Springs, and Sahwave plutons. The composition (tonalite to granodiorite) and U-Pb zircon dates of these plutons are similar to plutons in the Tuolumne intrusive suite of the east-central Sierra Nevada batholith. There is also an older, ~106 Ma (U-Pb zircon) Power Line intrusive complex located in the Nightingale Range. We present new field measurements, microstructures, U-Pb zircon geochronology, and anisotropy of magnetic susceptibility analyses on both the Sahwave Range intrusive suite and the Power Line intrusive complex. For the Sahwave Range intrusive suite, an E-W striking magmatic foliation fabric is observed in the older Juniper Pass pluton and a steep NW-SE striking, sub-solidus foliation is observed in the Sahwave pluton. These fabrics are similar to those observed in the Tuolumne Intrusive suite. In contrast, the Power Line intrusive complex is characterized by a vertical, N-S striking solid-state foliation and down-dip lineation. Evidence of dextral shearing is observed on sub-horizontal planes that are perpendicular to the lineation, indicating pure shear dominated transpression. This fabric is similar in style and inferred timing to the western Idaho shear zone adjacent to the Idaho batholith and mid-Cretaceous shear zones of the central Sierra Nevada. The plutons of the Sahwave Range intrusive suite are not affected by the pure-shear-dominated transpression fabric observed in the

Power Line intrusive complex, and thus were emplaced after cessation of that earlier deformation episode. Deformation patterns recorded by the intrusions of northwestern Nevada therefore provide a tectonic link between the Sierra Nevada and Idaho batholiths, recording deformation events observed in these larger, contiguous batholiths. The implication is that two phases of regionally consistent deformation occurred in the magmatic arcs of the western U.S. in the mid-Cretaceous.

1. Introduction

Cretaceous shear zones of varying strike, finite strain, and shear sense (e.g., Armstrong, 1988; Bateman, 1992; Manduca et al., 1993; Tobisch et al, 1995; Tikoff and St. Blanquat, 1997; Andronicos et al., 1999; Ducea, 2001; Schmidt and Paterson, 2002; Van Buer and Miller, 2010; Wolf et al., 2009) from Mexico to Alaska along the North American continental margin record periods of Cretaceous orogenesis within magmatic arcs. These shear zones and their geometries are key structural elements of the North American Cordillera that are commonly addressed as distinct segments, but are a margin-scale expression of Cretaceous tectonism (e.g., Hildebrand and Whalen, 2021a,b; Tikoff et al., 2022). Margin-parallel variations in both orientation and kinematics (wrenching vs. transpression vs. reverse motion) are typical of these major deformation zones. How these shear zones are interpreted with respect to simultaneous magmatism is debated.

Within the western U.S., these shear zones are well exposed in the major batholiths (Fig. 1). The western Idaho shear zone (WISZ), in the western gneissic border of the Idaho batholith, records dextral transpression from ~100-85 Ma (e.g., Tikoff et al., 2001; Giorgis et al., 2008; Harrigan et al., 2022). Simultaneous dextral deformation occurred in the Sawtooth shear zone,

located within the Idaho batholith (Ma et al., 2016). The Sierra Nevada batholith records two phases of dextral deformation during intrusion of the Cretaceous magmatic arc. A ~100 Ma phase of deformation occurs in the central Sierra Nevada, such as in the Sing Peak and Courtright-Wishon shear zones (Krueger and Yoshinobu, 2017; Torres Andrade and Tikoff, 2022). These shear zones are preserved in discontinuous segments, reflecting intrusion by younger magmatism. Hence, these mid-Cretaceous shear zones could have been more regionally extensive than currently mapped or even have formed a continuous shear zone. Second, dextral shear was active in the eastern Sierra in the Sierra Crest shear zone system (SCSZS), which consists of a series of dextral shear zones that were active during the youngest magmatism (e.g., Tikoff and Teyssier, 1992; Greene and Schweikert, 1995; Bartley et al., 1990; Cao et al., 2015). Dextral movement is also inferred to have occurred from ~101-90 Ma in the Bench Canyon shear zone in the Sierra Nevada batholith (McNulty, 1995).

Our understanding of the structural and temporal continuity between the two batholiths is hindered by the effects of Basin and Range deformation. There are, however, exhumed segments of Cretaceous arc plutons in northwest Nevada that reveal the presence of arc magmatism in this region. Detailed mapping, geochronology, and geochemical analyses were conducted by Van Buer and Miller (2010) on the plutons in the Sahwave Range intrusive suite (their Sahwave batholith). They concluded that these plutons constituted a northward continuation of the Sierra Nevada batholith. Specifically, their whole rock geochemistry and U-Pb zircon dates indicated the similarity of the Sahwave batholith and the Tuolumne intrusive suite of the eastern Sierra Nevada batholith. In contrast, older granitic units intruded by the Sahwave Range intrusive suite, such as the ~106 Ma Power Line intrusive complex, showed less geochemical similarity to the Tuolumne intrusive suite. Further, some of the older plutonic units

often exhibit a strong solid-state fabric that is not observed in the Late Cretaceous Sahwave Range intrusive suite (Van Buer and Miller, 2010).

This contribution builds upon previous research to evaluate if the granitic rocks of northwest Nevada provide structural evidence for regional deformation at 100-85 Ma, linking deformation in the Sierra Nevada and Idaho magmatic arcs. We characterize the internal fabrics of the Early Cretaceous Power Line intrusive complex and the Late Cretaceous Sahwave Range intrusive suite (Juniper Pass, Bob Spring, and Sahwave plutons). The Power Line intrusive complex exhibits steeply dipping, NE-SW solid state fabric with shear sense indicators oriented perpendicular to the lineation. New geochronological results constrain deformation as occurring after the 106 Ma emplacement of the intrusive complex, but before emplacement of the earliest plutons in the Sahwave intrusive suite at 95 Ma. This style and timing of deformation are similar to those of the western Idaho shear zone. In addition, we use the Anisotropy of Magnetic Susceptibility (AMS) technique to characterize the magmatic fabrics in the Sahwave Range intrusive suite. We interpret these steeply dipping, E-W to NE-SW striking magmatic fabrics as a record of distributed strain, consistent with fabrics forming in the Sierra Nevada arc at the same time (Tikoff and St Blanquat, 1997; Cao et al., 2015). Together, these new data provide evidence for ~100 Ma and ~88 Ma deformation events in northwest Nevada and provide a structural link between shear zones associated with the Idaho batholith (e.g., western Idaho shear zone) and Sierra Nevada batholith (e.g., the Sierra Crest shear zone system).

2. Geologic Setting

Evidence of deformation at ~100 Ma (mid-Cretaceous) is recognized throughout much of the U.S. Cordillera (e.g., Hildebrand and Whalen, 2021; Busby et al., 2022; Tikoff et al., 2022).

Based on a study of minor structures in northwestern Nevada, Oldow et al. (1984), documented a change from left-lateral to right-lateral motion parallel to the plate boundary at ~100 Ma. This change correlates to a significant plate motion change that is hypothesized to have occurred at 105-100 Ma in the Pacific basin (Matthews et al., 2012). Below we review regional constraints for deformation at ~100-85 Ma in both the Sierra Nevada batholith to the south and the Idaho batholith to the north. We then describe the known Mesozoic magmatic and deformational history in NW Nevada.

2.1 The Sierra Nevada batholith

2.1.1 Magmatism

There are effectively two magmatic arcs in the Sierra Nevada mountains (Bateman, 1992; Saleeby and Dunne, 2015), as constrained by U-Pb zircon geochronology recording pluton crystallization (e.g., Chen and Moore, 1982). The Jurassic magmatic arc was active from 175-150 Ma, whereas the more voluminous Cretaceous magmatic was active from 123-83 Ma. Both are thought to result from subduction of an oceanic plate below North America (Andean style arc) and contain predominantly calc-alkaline intrusive suites. The Jurassic arc is currently preserved on the NW and SE sides of the Cretaceous arc. The Jurassic arc is interpreted to have shut down as a result of multiple terrane collisions, currently exposed in the Sierran Foothills (e.g., Snow and Scherer, 2006). The cessation of the Jurassic arc pre-dates the intrusion of the 149 Ma Independence dike swarm (e.g., Glazner et al., 1999).

The Cretaceous arc is generally considered to have resulted from eastward subduction of oceanic plates from the Pacific basin beneath North America. In general, there is an eastward younging of pluton emplacement ages as well as an eastward increase in K_2O in the Cretaceous

magmatic arc. The boundary between oceanic crust and continental crust is thought to occur in the center of the batholith, as denoted by the $^{87}Sr/^{86}Sr = 0.706$ isopleth (Sr 0.706 line) (e.g., Armstrong et al., 1977; Saleeby, 1981; Kistler, 1990; Lackey et al., 2012). This isopleth is generally used to define the boundary between the accreted oceanic terranes to the west and North American continental crust to the east. This interpretation is constrained by the wallrocks for these intrusions, which locally consist of metamorphosed Paleozoic sedimentary rocks of western North America (e.g., Greene, 1995; Stevens and Greene, 1999).

The pre-100 Ma granites were generally emplaced west of the Sr 0.706 line and are typically tonalitic in composition (e.g., Bateman, 1992; Lackey et al., 2012). In contrast, the post-100 Ma plutons were emplaced east of the Sr 0.706 line and are typically granodioritic in composition. We note that Hildebrand and Whalen (2021a, b) use chemical discrimination diagrams to distinguish between pre-100 Ma "magmatic arc" granites and post-100 Ma "slab breakoff" granites.

The most voluminous magmatism in the Sierra Nevada magmatic arc, the Cathedral Range intrusive event, occurred from 94 to 83 Ma (Evernden and Kistler, 1970; Kistler et al., 1986; Bateman, 1992; Coleman et al., 2005). The Cathedral Range intrusive event consists of several large intrusive suites, which are compositionally zoned. From south to north, these are: the Mount Whitney intrusive suite (e.g., Hirt, 1989); the John Muir intrusive suite; the Tuolumne intrusive suite (e.g., Bateman and Chappell, 1979; Kistler et al., 1986); and the Sonoran intrusive suite (Leopold, 2016). Granitoids in each suite display an inward younging that is generally mirrored by geochemical trends from more mafic to more felsic range (e.g., Stern et al., 1981; Chen and Moore, 1982; Kistler et al., 1986; Coleman and Glazner, 1997). The younger megacrystic K-feldspar granites are often asymmetrically nested within (Tuolumne and Mount

Whitney Intrusive Suites) or aligned *en echelon* (Mono Pass intrusive suite) with older more mafic equigranular granodiorites (Bateman, 1992; John and Robinson, 1982; Hirt, 2007; Saleeby et al., 2008) (Fig. 2). Most intrusive suites and individual plutons are elongate with long axes oriented NNW.

The emplacement level of these intrusive suites is relatively shallow in the east-central Sierra Nevada. Based on Al-in-hornblende barometry (Ague and Brimhall, 1988), and further constrained by the presence of miarolitic cavities (e.g., Bateman, 1992; Titus et al., 2005), these granitoids were emplaced at upper crustal depths (~1–3 kbar; Ague and Brimhall, 1988). The depths of pluton emplacement generally increase southward in exposures of the magmatic arc (Nadin et al., 2016), as a result of Late Cretaceous-Paleogene exhumation of the southern Sierra Nevada (e.g., Wernicke and Snow, 1998).

2.1.2 Mid-Cretaceous deformation

Two phases of dextral transpressional deformation occurred during emplacement of the Cretaceous batholith in the Sierra Nevada. The first phase is recorded by a series of discontinuous mid-Cretaceous shear zones from the central part of the Sierra Nevada batholith. These shear zones were active during magma emplacement in the central part of the batholith. The second is the continuous Late Cretaceous Sierra Crest shear zone system, which was active along the eastern margin of the batholith during magma emplacement.

Evidence for dextral transpressional deformation in the Sierra Nevada at ~100 Ma is found within two shear zones, the Sing Lake and the Courtright-Wishon shear zones (Tobisch et al., 1995; Krueger and Yoshinobu, 2018; Torres Andrade and Tikoff, 2022). The ~98 Ma Sing Lake shear zone deformed the host Jackass Lakes granodiorite and records a continuous

transition from near-solidus to sub-solidus fabrics (e.g., Krueger and Yoshinobu, 2018). The orientation of the Sing Lake shear zone is defined by a steep NW-SE foliation and moderate, north-plunging mineral lineation, with evidence of both dextral shear and west-directed shortening. The vertical foliation and sub-vertical lineation, with dextral shear perpendicular to lineation, is indicative of a transpressional strain regime recorded by the Sing Lake shear zone. Therefore, the Sing Peak shear zone records the earliest documented regional dextral transpression within the central Sierra Nevada batholith during the mid-Cretaceous.

The Courtwright-Wishon shear zone is a high temperature solid state shear zone (Tobisch et al., 1995), with a deformational history similar to that of the Sing Lake shear zone. In the Courtwright area, the shear zone is characterized by northwest-striking, steeply dipping mylonitic and ultramylonitic fabrics superimposed on a magmatic foliation. It deforms the Dinkey Creek (~102 Ma; U/Pb on zircon), Short Hair Creek, and Lost Peak plutons as well as the adjacent wall rock screens that separate these plutons from the undeformed Mount Givens pluton (~90 Ma; U/Pb on zircon). The shear zone is truncated at both ends where it was intruded by younger granitoids. Pre–90 Ma contractional deformation is thought to be predominant along these shear zones. Previous work suggested that normal-sense shearing along steeply dipping foliations is preserved within the Kaiser Peak and Courtwright-Wishon shear zones (Tobisch et al., 1995), interpreted to record minor amounts of extension associated with the construction of the Mount Givens granodiorite between ca. 97 and 90 Ma (Frazer et al., 2014). More recently, Torres Andrade and Tikoff (2022) indicate that the fabrics record dextral tranpressional shearing, with a component of contraction. This interpretation is compatible with the timing and kinematics of the Sing Lake shear zone (Krueger and Yoshinobu, 2018).

The similar deformational history and orientation of these mid-Cretaceous shear zones suggest they may have been part of a larger shear zone system prior to their truncation by younger intrusions (Tobisch et al., 1995; McNulty et al., 2000).

2.1.3 Late Cretaceous deformation

The Sierra Crest shear zone system consists of a series of dextral transpressional shear zones exposed along the eastern margin of the batholith. In the center from north to south of the Sierra Nevada batholith, it is a composed of a series of shallow crustal (1-2 kbars) dextral shear zones including the Cascade Lake shear zone (Tikoff et al., 2005; Cao et al., 2015), Gem Lake shear zone (Greene and Schweickert, 1995), and the Rosy Finch shear zone (Tikoff and Teyssier, 1992; Tikoff and St Blanquat, 1997) (Fig. 2). These shear zones record synmagmatic shearing during the emplacement of the large nested intrusive suites (Tuolumne, Mono Pass, and Whitney) of the Cathedral Range intrusive epoch. In the southern Sierra Nevada, dextral shearing is recorded in more deeply exhumed shear zones, including the proto-Kern Canyon fault (Busby-Spera and Saleeby, 1990; Wood and Saleeby, 1998; Nadin, 2007). Together, these shear zones record dextral deformation for over 300 km along the axis of magmatism preserved in the Sierra Nevada.

Fabrics within the Rosy Finch and Cascade Lake shear zones occur dominantly in plutonic units. Microstructures can quantitatively and qualitatively reveal information regarding the conditions of fabric formation by recording magmatic, sub-magmatic, and sub-solidus deformation processes (Fig. 2). In these locations, sub-solidus foliations and lineations within the shear zones are characterized by aligned biotite and stretched quartz grains. These structures locally anastamose around large K-feldspar megacrysts. Subvertical foliations trend

predominately NNW and lineation varies from horizontal to vertical. This fabric orientation pattern is interpreted to record wrench-dominated transpressional deformation (Tikoff and Greene, 1997). Both shear zones display sub-magmatic to magmatic microstructures indicative of high temperature shearing along with dextral shear sense indicators (K-feldspar sigma clasts, mafic folia, S-C structures, etc.) in the horizontal plane. Further, both shear zones display a strain gradient, with the youngest plutonic units preserving less deformation relative to the wallrocks (e.g., Tikoff and Greene, 1997).

Dextral transpressional deformation is broadly constrained to be coincident with emplacement of the Cathedral Peak and Mono Creek plutons at ~87 Ma (Tikoff et al., 2005; Cao et al., 2015). Bartley et al. (2005) suggest that dextral shearing must have been active at 92 Ma, during emplacement of the oldest member of the Mono Pass intrusive suite (Lamarck granodiorite). Sharp et al. (2000) dated the timing of deformation in the Gem Lake shear zone at 82-80 Ma. Finally, movement on EW-striking sinistral deformation zones, which occur adjacent and are kinematically linked to the larger right-lateral shear zones (Tikoff et al., 1998), are constrained as moving between 79-85 Ma (Segall et al., 1990). We infer from this data that dextral deformation occurred during the emplacement of the intrusive suites from the Cathedral Range intrusive epoch. We note, however, that Cao et al. (2015) suggest that dextral deformation occurred only after 88 Ma.

The simultaneous emplacement and shearing of the intrusive suites suggest a causal link. Tikoff and Teyssier (1992) proposed a p-shear model for emplacement of these large intrusive suites, in which plutons intruded into dilatational jogs/stepovers in the right-lateral shear zone system.

2.2 The Idaho batholith and its gneissic western margin

2.2.1 Magmatism

An Early Cretaceous magmatic arc was built mostly on the western, accreted terrane side of the Idaho batholith (Manduca et al., 1993; Gaschnig et al., 2017a,b). Unlike the Sierra Nevada magmatic arc, it was highly telescoped during ~100-85 Ma western Idaho shear zone deformation and little of this arc remains (Giorgis et al., 2005; Gaschnig et al., 2017b). The transition between the accreted island arc terranes and North American craton is demarcated by a sharp gradient over 5-20 km of the $^{87}Sr/^{86}Sr$ = 0.704, 0.706, & 0.708 isopleths. In the McCall region, there are three Cretaceous intrusive suites associated with the western Idaho shear zone. From W-E, these are: The Hazard Creek complex, the Little Goose Creek complex, and the Payette River tonalite (Fig. 3).

The westernmost Hazard Creek complex (118± 5 Ma, U-Pb on zircon; Manduca et al., 1993), is composed of variably deformed tonalites, trondjhemites, granodiorite, and granites that commonly contain magmatic epidote (Taubeneck, 1971; Manduca et al., 1993), indicative of emplacement depths of at least 7 kbar (Zen and Hammarstrom, 1984). This complex is deformed by the western Idaho shear zone only along its eastern margin. The Little Goose Creek complex – located east and inboard of the Hazard Creek complex – contains tonalites, granodiorite, and granites (110 ± 5 Ma, 105.2 ± 1.5 Ma, U-Pb on zircon; Manduca et al., 1993; Giorgis et al., 2008). This complex displays a pervasive and well-developed solid-state fabric and contains most of the western Idaho shear zone. Based on the wall rocks and screens preserved in the three complexes, the transition from oceanic arc to continental crust is preserved within the Little Goose Creek complex, and occurs over less than 4 km (Manduca, 1988). The Payette River tonalite contains dominantly a distinctive tonalite, but also minor granodiorites and

granites. It is the youngest of the units (91.5±1.1 and 89.7±1.2 Ma; U-Pb on zircon; Manduca et al., 1993; Giorgis et al., 2008), and only contains a strong solid-state fabric on its western side. Amphibolite facies metasedimentary screens in the Payette River tonalite record pressures of 3-6 kbar (Braudy et al., 2017), suggesting mid-crustal emplacement depths.

The Idaho batholith was emplaced east of the intrusive complexes affected by the western Idaho shear zone. Batholith compositions vary, however all rocks contain some muscovite and biotite and are hence two-mica granites (Lewis et al., 1987; Gaschnig et al., 2010). U-Pb zircon ages from the granites of the Atlanta lobe of the Idaho batholith range from ~85-70 Ma (Gaschnig et al., 2010).

2.2.2 Dextral shearing 100-85 Ma in Idaho

The western Idaho shear zone is a north-south–trending boundary between the western continental margin of Laurentia and accreted terranes (e.g., Fleck and Criss, 1985, 2007; Lund and Snee, 1988; Manduca et al., 1992; McClelland et al., 2000; Tikoff et al., 2001, 2017). Steep gradients in strontium (Armstrong et al., 1977; Manduca et al., 1992) and oxygen (Criss and Fleck, 1985; Fleck and Criss, 1985; Manduca et al., 1992; King et al., 2007) isotopes occur across the western Idaho shear zone and varies in width from 2–10-km. WISZ deformation is preserved in the fabrics of pre-existing (Hazard Creek complex, Little Goose Creek complex) and syntectonically emplaced (Payette River tonalite) plutonic units (McClelland et al., 1992). The solid-state foliation — defined by aligned micas, amphiboles, and ribboned quartz grains — strikes N-S and dips steeply to the east. Shear sense in the WISZ is characterized by a vertical vorticity vector nearly parallel to the vertical field lineation consistent with transpressional kinematics (Girogis et al., 2017). Populations of rigidly rotating feldspar porphyroclasts also

reveal a subvertical vorticity vector (Giorgis and Tikoff, 2004). A vertical vorticity vector was also inferred from quartzites in a wall-rock screens using the CVA (Crystallographic Vorticity Axis) method (Michels et al., 2015). Field fabrics, including boudinaged and folded dikes, indicate a right-lateral wrench component of deformation (e.g., Braudy et al., 2017).

Formation of the western Idaho shear zone likely started after ca. 104 Ma (age of Crevice pluton; Gray et al., 2012; Braudy et al., 2017). Recent U-Pb titanite dating has constrained its initiation between ~98 and 96 Ma (Harrigan, 2022). A cross-cutting pegmatite dike in the Little Goose Creek complex was dated at ~90 Ma (Giorgis et al., 2008), suggesting that major shearing had ceased in that unit at that time. The youngest pluton at West Mountain, south of McCall, is the undeformed Rat Creek granite (88.2 ± 3 Ma; U-Pb on zircon), which is consistent with cessation of western Idaho shear zone deformation at ca. 90 Ma. Recent U-Pb titanite dating suggests that deformation continued until ~85 Ma (Harrigan, 2022).

The western Idaho shear zone continues into the Owyhee mountains in southwestern Idaho, where Benford et al. (2010) provided compositional, geochronological, and structural data. Relative to the McCall segment of the western Idaho shear zone, the shear zone in the northern Owyhee segment is wider, less well developed, and contains a 020-oriented foliation. This fabric orientation is consistent with mapping in West Mountain, located between McCall and the Owyhee mountains (Braudy et al., 2017). Along-strike variations in deformation and geochemical characteristic are attributed to the irregularity of the original continental margin (Tikoff et al., 2022).

Dextral Cretaceous shearing is also recorded in the strongly deformed metasedimentary and intrusive rocks of the Sawtooth metamorphic complex exposed east of the central Idaho batholith (Ma et al., 2017). Intrusions from the Sawtooth metamorphic complex exhibit a N-S

oriented fabric. Zircon U-Pb dates on the deformed intrusions indicate that transpressional deformation likely initiated between ~ 95–92 Ma and ca. 84 Ma and ended by ~ 77 Ma. The transpressional deformation in the Sawtooth metamorphic complex and the western Idaho shear zone were kinematically compatible, suggesting that these shear zones may represent a regional transpression system that facilitated both crustal deformation inboard of the continental margin and northward translation of accreted terranes during the Late Cretaceous (Ma et al., 2017). Giorgis et al. (2008) also attributes the dextral transpressional deformation in the WISZ to the docking of the Insular superterrane outboard of the magmatic arc.

2.3 The Sahwave batholith and intrusions of northwest Nevada

Arc-generated granites are sparsely distributed within the western Basin and Range province and may represent a highly fragmented magmatic arc. The current geometry results from both Miocene to present Basin and Range extension paired and ca. 300 km of northward motion of the Sierra Nevada block accommodated by the eastern California shear zone (e.g., Atwater and Stock, 1998; Wernicke and Snow, 1998; McQuarrie and Wernicke, 2005). However, a northward extension of the Cretaceous Sierra Nevada magmatic arc is interpreted to outcrop in northwest Nevada (Van Buer and Miller, 2010; Fig. 4), part of a continuous Cretaceous magmatic arc through the western U.S. (Dickinson, 2004).

From northwest Nevada to southeast Oregon, Wyld and Wright (2001) interpret a segment of dextral strike-slip shearing called the western Nevada shear zone (WNS). The WNS trends NNE and separates the Jungo and Black Rock terranes to the east from allochthonous western assemblages; it also obliquely truncates the Black Rock-Jungo terrane boundary. In fact, the WNS is not exposed, but is concealed by Cenozoic strata and Late Cretaceous plutons.

Consequently, the timing of deformation is broadly constrained to the mid-Cretaceous/Late Jurassic as it displaced Middle Jurassic (Pueblo terrane) assemblages and is crosscut by Late Cretaceous plutons.

The Cretaceous Sahwave batholith and Power Line intrusive complex are the most continuous intrusions and were emplaced into the Late Triassic Jungo terrane. The metamorphic wall rocks of these units are referred to as the Nightingale Sequence and are correlated with the Late Triassic Jungo terrane on the basis of stratigraphy and structural history (Silberling et al., 1987).

The Late Cretaceous Sahwave Range intrusive suite, likely a northward continuation of the Late Cretaceous Sierra Nevada batholith (Van Buer and Miller, 2010), is approximately 100 km NE of the main axis of the Sierra Nevada batholith. It is a nested intrusive suite comprising three NNE-elongated plutons emplaced between 94 and 88 Ma that range in composition from older granodioritic plutons to younger granite plutons. The granodiorite plutons of the Sahwave Range intrusive suite are broadly similar in composition, age, and emplacement pattern (Van Buer and Miller, 2010) to the Tuolumne intrusive suite but are chemically more primitive ($^{87}Sr/^{86}Sr = 0.7046$, $\varepsilon_{Nd} = -0.2$). Major-element chemistry from Van Buer and Miller (2010) characterizes the Sahwave batholith as a magnesian, metaluminous to weakly peraluminous, calc-alkaline series of intrusions, with an alkali-lime index of 59.6. Major- and trace-element variation with respect to silica yields trends consistent with fractional crystallization and mixing. Across a radial transect, major elements become more felsic toward the center of the batholith. The Sahwave batholith tends to have less K_2O and Rb than the Tuolumne intrusive suite, and more Na_2O and Sr, for any given amount of SiO_2.

The plutons of the Sahwave Range intrusive suite are, from oldest to youngest, the granodiorite of Juniper Pass (92.7 ± 1.4 Ma), the granodiorite of Bob Springs (92.8 ± 1.7 Ma), and the Sahwave granodiorite/granite (88.5 ± 2 Ma) (U-Pb zircon ages; Van Buer and Miller, 2010; Fig. 5). The plutons of the Sahwave Range intrusive suite intrude a suite of older granodiorites and diorites, including the Power Line intrusive complex (104.9 ± 0.8 Ma; Van Buer and Miller, 2010) as well as the back-arc Jungo basinal terrane (Silberling et al., 1987; Quinn et al. 1997; Wyld, 2000) that consists of dominantly fine-grained siliciclastic strata (now slate and phyllite), with minor interbedded quartzose sandstone and rare limestone (Lupe and Silberling, 1985; Wyld, 2000, 2002). The Power Line intrusive complex intrudes the Jungo basinal terrane marine metasedimentary strata and host wallrocks exhibit strong ductile deformation within a ca. 100 m wide aureole. Wallrocks in this zone were metamorphosed and developed a strong vertical foliation and subvertical mineral lineation that parallel to the solid-state fabric in the Power Line intrusive complex. Folds in the wallrocks are tight and have axial planes parallel to the foliation.

3. Methods

3.1 Field Methods

Field observations were made in the plutons of the Sahwave Range intrusive suite (Sahwave granodiorite, granodiorite of Bob Spring, and granodiorite of Juniper Pass); this group of plutons was named the Sahwave batholith by Van Buer and Miller (2010). Additional field observations were taken on the Power Line intrusive complex in the Nightingale Range. Field observations included measurements of foliation, lineation, and magnetic susceptibility. Samples were taken for microstructural and Anisotropy of Magnetic Susceptibility analyses. Outcrops

were an assortment of patchy and deeply weathered granodiorite pavements in and along arroyos or steep nobby ridges near the crests of the relatively low relief uplands. Field foliations vary significantly in degree of development, and the lineation was not usually perceptible except along sharp pluton margins. First-order observations and handheld bulk magnetic susceptibility measurements of each of the units from the Sahwave Range intrusive suite suggested they contain abundant medium to coarse grained ferrimagnetic and paramagnetic fabric forming minerals with relatively high averages of bulk magnetic susceptibility (5×10^{-4} to 5×10^{-3}). The Power Line intrusive complex yielded the lowest magnetic susceptibility values of all units in the Sahwave and Nightingale Ranges ($5x10^{-6}$).

Oriented samples were taken from 122 site locations, of which 88 were drilled sites and the remainder were oriented block sample collection sites. Detailed sampling was prioritized for the Sahwave granodiorite and resulted in two roughly N-S and E-W transects where we collected oriented drill core every 100–500 m (Fig. 5).

3.2 Petrology, chemistry, field fabrics, and microstructures

3.2.1 Sahwave granodiorite

The Sahwave granodiorite is the youngest unit of the Sahwave Range intrusive suite and is similar in both age and composition to the Cathedral Peak granodiorite of the Tuolumne intrusive suites. The Sahwave granodiorite contains K-feldspar megacrysts (4-6 cm) that occur in pods and stringers (Fig. 6 A,B). The Sahwave intrusive suite has, on average, a greater modal abundance of mafic minerals, but plagioclase and mafic minerals decrease in abundance toward the center of the intrusion, whereas quartz and K-feldspar generally increase (Van Buer and Miller, 2010).

The Sahwave granodiorite preserves a weak magmatic foliation defined by the shape preferred orientation of K-feldspar megacrysts and alignment of biotite laths. Field measurements of the magmatic foliation trend N-S throughout the unit; lineation was difficult to identify and measure in the field. The eastern margin of the pluton hosts a 2 m thick, N-S striking, solid state shear zone of mylonitized granodiorite (Fig. 7). K-feldspar megacrysts show slight asymmetry indicative of low temperature deformation with both σ clasts and ϕ clasts. Surrounding matrix is strongly recrystallized with grain size reduction of quartz and micas.

The microstructures in the Sahwave granodiorite vary from the margins to the interior of the pluton. Microstructures from the margins of the pluton include "globular" and coarse quartz grains with deeply sutured and cuspate-lobate grain boundaries that display weak checkerboard extinction. Mafic phases - predominately biotite - are typically aligned parallel to a weak foliation defined by quartz elongation and long axis of feldspar clasts. Feldspars show some textural variability with populations of smaller, sub-equant plagioclase feldspar grains with slightly wavy boundaries to large grains with cuspate-lobate boundaries. Potassium feldspar is often poikilitic, contain smaller sub-equant feldspar grains. Poikilitic potassium feldspar domains often display patchy microcline tartan twining and commonly contain myrmekite around the margins (Fig. 8A).

Sites from the center of the unit show a bimodal feldspar population of large and small sub-equant grains. Larger grains of plagioclase feldspar show cuspate-lobate margins and seritization within the core of the grain, with relatively unaltered grain margins. In this sample, we observe both patch tartan twinning and flame perthite nucleating along the margins of both large and small potassium feldspar grains, the latter of which is indicative of high differential stress (Pryer and Robin, 1995; 1996).

Quartz grains show a bi-modal size distribution. The larger grain size population exhibits amoeboidal shapes with evidence for grain boundary migration given by cuspate lobate boundaries and chessboard extinction. The smaller grain size occurs in domains of ribboned quartz, in which relatively equant small quartz exists with abundant triple junctions. Some of the smaller recrystallized quartz grains showing minor bulging recrystallization, shown by bulges and small recrystallized grains along grain boundaries. Subhedral potassium feldspar grains also display a bi-modal size distribution with tartan twining and flame perthite along the grain margins, cuspate-lobate grain boundaries, and the development of myrmekite. Large biotite grains show weak kinking and alignment. Iron oxides and euhedral titanite are more abundant in the center of the pluton.

3.2.2 The granodiorite of Bob Spring

The granodiorite of Bob Spring outcrops poorly. Where observed, it is characterized as a medium-grained biotite granodiorite or granite with poikilitic K-feldspar phenocrysts up to ca. 2 cm long (Fig. 6 C, D). Biotite, titanite, and altered hornblende are homogenously distributed throughout the pluton. A weak magmatic fabric is defined by mafic mineral alignment and is occasionally observed in this unit but was difficult to measure in the field and trends were variable. Most sites were accessed along the western contact with some sites in the western portion of the interior of the unit in the Sahwave Range. Part of the western margin bulges into the Nightingale Range and the weakly observed fabric pattern in the unit approximately parallels the inferred intrusive contact. Lineation was not observed in the field.

The granodiorite of Bob Spring is texturally variable, ranging from a felsic microgranite to a coarser grained equigranular granodiorite texture. The unit also contains abundant aplite and

pegmatite dikes of predominantly quartz and K-feldspar. The granodiorite of Bob Spring is considered equivalent to the Half Dome granodiorite of the Tuolumne intrusive Suite (Van Buer and Miller, 2010).

The granodiorite of Bob Spring contains equant and rounded quartz grains that are generally only ca. 1 mm in size but reach 3–5 mm in the southern outcrops. Biotite and hornblende are often badly chloritized, and sometimes feldspars show signs of sericitization. Titanite grains are euhedral, large, and abundant. Modal percentages from the granodiorite of Bob Spring are are variable, with plagioclase increases inward from the margin to reach its maximum at ~6 km; quartz abundance follows plagioclase's pattern in reverse (Van Buer and Miller, 2010). This pattern is distinct from that in the Sahwave granodiorite, as mafic minerals and plagioclase abundance follows a roughly opposite pattern in that pluton.

Thin sections commonly show infilled fractures in plagioclase, partially recrystallized quartz, and a thin film of alkali feldspar lining many plagioclase laths. Bulging and impingements of plagioclase porphyroclasts with fine quartz grains are common and all sections reveal subordinately plagioclase, recrystallized at the boundaries of large plagioclase porphyroclasts. We also observe deformed polysynthetic albite twins in plagioclase with some examples of kinked crystals. Potassium feldspar crystals also show examples of deformation twins and kinking. Myrmekite textures are common, particularly adjacent to potassium feldspar (Fig. 8B).

3.2.3 The granodiorite of Juniper Pass

The granodiorite of Juniper Pass is the oldest unit of the Sahwave batholith and is exposed predominately in the Sahwave Range with <10 outcrops in the Nightingale Range. The

granodiorite of Juniper Pass is also the most compositionally heterogeneous of the units, varying in composition from a granodiorite to a tonalite or a quartz diorite. It is medium- to coarse-grained and equigranular, with large (4–8 mm) biotite and hornblende phenocrysts (Fig. 6 E, F). Van Buer and Miller (2010) observed that although hornblende and titanite are present throughout all units of the Sahwave Range intrusive suite, only in the granodiorite of Juniper Pass does the hornblende form crystals notably larger than the 1–3 mm euhedral titanite. Mafic enclaves are found throughout the unit but are common within 1–2 km of the exterior contact and are flattened by a ratio of 2:1–10:1. The Juniper Pass granodiorite has the most discernible magmatic to sub-magmatic field fabric in the Sahwave Range intrusive suite with strong E-W foliation in the northern outcrops. The foliation is defined by the alignment of mafic minerals and euhedral plagioclase. Mafic schlieren and enclaves are parallel to the mineral fabric with many of these enclaves displaying elongation parallel to the mineral fabric.

Quartz grains display weak but observable checkerboard undulatory extinction and large grains (>1 mm) are often highly fractured (Fig. 8C). Of the accessory phases present, titanite grains are large (>1 mm) and relatively unaltered but display euhedral to subhedral morphologies. Biotite grains vary in size and degree of alteration. Some biotite grains are unaltered and euhedral, whereas others display some resorption and alteration. Hornblende shows significant resorption with embayments of quartz and feldspar, and alteration to biotite. Grain size populations for both the plagioclase feldspars and the quartz are bimodal. Small plagioclase feldspar grains (< 500 um) are relatively rounded with some grains exhibiting cuspate/lobate boundaries. Smaller quartz grains also show this texture with some evidence for grain size reduction by dynamic recrystallization methods (bulging recrystallization). Large plagioclase grains are more euhedral but often display serrated margins with sharp stepped

boundaries. Further, minor seritization is observed in some plagioclase felspars which also display inclusion-rich cores.

3.2.4 The Power Line intrusive complex

The Power Line intrusive complex (Van Buer and Miller, 2010) is found in the Nightingale Range and is distinct from the Sahwave Range intrusive suite in both age and composition. It is intruded by the granodiorite of Juniper Pass and the School Bus granodiorite. The main unit of the Power Line intrusive complex is a medium-grained biotite hornblende granodiorite. However, the composition of the intrusive complex is variable with numerous dikes and pods of darker granodiorite and diorite ranging from centimeters to hundreds of meters in long dimension. This unit also contains many large inclusions of metamorphic rock, ranging from small, elongated enclaves to inclusions of wallrocks that are 5–200 m in length. There is one wallrock screen on the east side of the pluton that is 4-km long, and may have been attached to the wallrock overlying the pluton (roof pendant). These xenoliths and enclaves are aligned subparallel to the solid-state foliation of the Power Line intrusive complex.

In general, there is a N-S trending, steeply dipping solid-state foliation in the Power Line intrusive complex (Van Buer and Miller, 2010) (Fig. 6 G, H). The solid-state foliation is defined by mafic folia, predominately recrystallized biotite, ribboned quartz, and potassium feldspar porphyroclasts. Lineation is also subvertical, and is defined by biotite, ribboned quartz, and feldspar porphyroclasts. Potassium feldspar sigma type porphyroclast systems in the YZ plane record a dextral shear sense in the horizontal plane. In contrast, no consistent shear sense is observed in the XZ (vertical) plane.

Microstructures in this intrusive complex are distinct from those in the Sahwave Range intrusive suite (Fig. 8 D-I). The fabric consists of a bimodal distribution of medium- (~0.3 mm along the long axis) and coarse-size (~1.5 mm along the long axis) quartz crystals, rounded potassium feldspar porphyroclasts, and mafic folia, dominated by biotite. Relict quartz grains are elongated with recrystallize aggregates of smaller quartz grain, with their long axis parallel to the trace of foliation. Plagioclase and potassium feldspar show some evidence for recrystallization and annealing with core and mantle textures and abundant triple junctions. Sub-magmatic fractures infilled with biotite and quartz occur within plagioclase and larger quartz grains, indicating deformation while melt was still present (Bouchez et al., 1992). Myrmekite is common around the edges of potassium feldspar porphyroclasts and among recrystallized potassium feldspar domains.

3.3 Microstructural characterization of the fabrics from the Sahwave Range intrusive suite and the Power Line intrusive complex

3.3.1 Fabric characterization of the Sahwave Range intrusive suite inferred from microstructures

Microstructural observations from the granodiorite of Juniper Pass reveal both high-temperature solid-state and magmatic fabrics depending on different regions of the pluton. The northernmost outcrop of the granodiorite of Juniper Pass in the Sahwave Range, near the contact with the surrounding Jungo terrane yields more sub-magmatic microstructures. Plagioclase feldspar are euhedral within a poikilitic potassium feldspar texture, with occasional lenticular deformation twins observed in some plagioclase inclusions. Poikilitic potassium feldspar displays patchy microcline tartan twining, commonly characterized as a solid-state deformation

feature (Vernon and Paterson, 2002). Site 17JP12 is more towards the interior of the unit that appears to be more deformed than sites 17JP03 and 17JP09. In thin section, grains from site 17JP12 are irregular in both shape and size; often showing lobate shapes suggesting grain boundary migration indicative of high temperature deformation. There is also evidence for sub-magmatic fabrics at site 17JP12 (e.g., Bouchez et al., 1992). Common potassium feldspar grains show evidence of dynamic recrystallization, but they also contain cracks infilled by quartz and/or plagioclase indicating brittle deformation in the presence of residual melt.

The microstructures in the granodiorite of Bob Spring are indicative of magmatic to sub-magmatic textures. The granodiorite of Bob Spring microstructures from sites in the Sahwave Range and Nightingale Range yield predominately sub-magmatic textures with evidence for solid state deformation overprinted on a magmatic fabric. Mafic minerals are poorly aligned in this unit, but plagioclase, potassium feldspar, hornblende, and biotite all show evidence of minor internal deformation as indicated by grain size reduction along the margins of these phases. Quartz and feldspar grains often show cuspate-lobate boundaries indicating some higher temperature deformation possibly during development of the N-S magmatic fabric. Further, significant fracturing of feldspar and hornblende are attributed to a medium solid-state deformation. Deformation was distributed within the granodiorite of Bob Spring, with no clear evidence for localization from our sites.

Microstructures in the Sahwave granodiorite reveal magmatic to sub-magmatic fabrics that vary from the margins to the interior of the pluton. Thin sections from site 17SW7 (proximal to the eastern margin of the pluton) show a bimodal population of quartz grains. Dynamic recrystallization is indicated by coarse, elongate quartz grains (>2 mm along the long axis) with checkerboard extinction and sharp cuspate/lobate boundaries with evidence for grain

size reduction. Deeply serrated boundaries in quartz are commonly observed and may indicate fast grain boundary migration in the presence of fluids along the margin.

Sites 17SW12 and 17SW16A are from the interior of the Sahwave granodiorite. Site 17SW12 shows a bi-modal potassium and plagioclase feldspar population of large and small, subequant grains. Larger grains of plagioclase feldspar show highly serrated margins and significant seritization of the core of the grain, with relatively unaltered grain margins. Both patch tartan twinning and flame perthite nucleating along the margins of both large and small potassium feldspar grains, which could be indicative of high differential stress (Pryer and Robin, 1995; 1996) within the magmatic state. In addition, high-temperature crack-seal features also occur within plagioclase and potassium feldspar grains, indicating deformation while melt was still present (Bouchez et al., 1992). Some dynamic recrystallization (bulging recrystallization and grain size reduction) along the margins of these feldspar grains is also observed. These features are more indicative of high temperature solid state deformation or sub-magmatic textures within the interior of the Sahwave granodiorite. Although magmatic and sub-magmatic fabric textures characterize the majority of sites in the Sahwave Range, one site (17SW50) documents a thin (~ 2 m) low temperature dextral shear zone along the eastern margin of the Sahwave Range hosted in the Sahwave granodiorite. This small dextral shear zone may postdate the emplacement and deformation of the Sahwave Range intrusive suite.

3.3.2 Fabric characterization of the Power Line intrusive complex inferred from microstructures

The microstructures in the Power Line intrusive complex all show a textural history of both high-temperature to medium-low temperature solid state deformation. This unit is characterized by large and relatively equant matrix grains of potassium feldspar porphyroclasts,

plagioclase feldspar, biotite, and quartz. The unit is distinct from the Sahwave Range intrusive suite in that is contains extremely sparse oxides.

Horizontal surfaces display the trace of the sub-solidus planar fabric and contain dextral shear indicators (potassium feldspar sigma clasts and mafic folia) that were well developed across all sites. Vertical surfaces display a steep mafic mineral lineation. It is worth noting, as a result of available exposures, that most of our data comes from sites along the eastern and western margins of the unit with only a few sites from the interior of the body.

Microstructural observations from the western margin of the Power Line intrusive complex (17PL-04; Fig. 8 D, E, and F) show more medium- to low-temperature solid state deformation and significant recrystallization of biotite and myrmekitic textures associated with the potassium feldspar porphyroclasts. Grain size reduction is present and recrystallized quartz and feldspar domains show core and mantle features and ribbons of recrystallized grains. The bi-modal feldspar and quartz population of large grains show grain boundary migration and small (<200 um) subequant grains indicative of sub-grain rotation. We observe significant subgrain devolvement in larger amygdaloidal quartz with abundant checkerboard extinction indicative of high temperature dynamic recrystallization. Smaller quartz grains have a more polygonal texture and are intermixed with feldspar of equant size. Large feldspar grains display flame perthite nucleating along the margins of both large and small potassium feldspar grains which could be indicative of high differential stress. In addition, crack seal features are also present within plagioclase and potassium feldspar grains, indicating deformation (ductile grain boundary sliding) while melt was still present (Bouchez et al., 1992) (Fig. 8 C, H). The biotite from sites along the margins of the Power Line unit are the most striking feature in the section. Biotite domains reveal a book-sliding texture commonly observed in feldspar that has undergone

shearing (Fig. 8 D, F). As this unit shows dextral shear in the horizonal plane, we interpret this biotite book sliding and recrystallization texture to be an additional dextral shear sense indicator. We also interpret the biotite as fully recrystallized during deformation, possibly in the presence of fluids as grain size is drastically reduced, birefringence is high, and individual lathes are devoid of inclusions. The grains do not exhibit much internal deformation despite their realignment, parallel to the fabric.

Observations from interior sites in the unit (17PL-09; Fig. 8 G, H, and I) show similar quartz and feldspar microstructures to those observed from the western margin sites in the Power Line intrusive complex. We interpret these features to represent a combination of high temperature and mid-low temperature deformation in the interior of the unit. Biotite texture, however, varies significantly between the margin and the interior of the intrusive complex. The more interior sites do not exhibit the same degree of biotite recrystallization. The biotite grains are larger, inclusion rich, and have undergone resorption as grain margins are ratty and smeared. The presence of kinking and wavy extinction suggest that these biotite grains preserve some Internal deformation and did not fully recrystallize during fabric development.

3.4 Anisotropy of Magnetic Susceptibility and Magnetic Mineralogy

3.4.1 Background: Anisotropy of Magnetic Susceptibility (AMS)

Magmatic fabrics preserved in granitoids are often weak and difficult to observe and an alternative method is required to evaluate the strength and orientation of these fabrics. Anisotropy of Magnetic Susceptibility (AMS) is a rapid, non-destructive technique that quantifies the fabric ellipsoid in a rock sample using the magnetic susceptibility of paramagnetic and ferromagnetic grains. Numerous studies have successfully confirmed that AMS fabrics

measured in granitoids accurately reproduce field measurements for both magmatic and solid-state deformation fabrics (e.g., Hrouda, 1982; Tarling and Hrouda, 1993; Bouchez, 1997). Arc granites are ideal candidates for AMS analyses for two main reasons: 1) They contain titanomagnetite and other Fe-rich phases (e.g., I-type granites); and 2) They often contain a medium- to coarse-grained crystalline matrix. These conditions are favorable for the growth of multidomain to pseudosingle domain ferrimagnetic minerals (e.g., titanomagnetite) and mafic paramagnetic minerals (e.g., biotite and hornblende). Both are faithful recorders of magnetic fabrics due to the strength of their bulk susceptibility (5×10^{-4} to 5×10^{-3} SI) and shape preferred orientation. Bulk susceptibility is a unitless parameter, but typically reported in SI units, that records the strength of the rock's magnetic properties. In strongly magnetic rocks, with a bulk susceptibility higher than 5×10^{-3}, the effects of paramagnetic (i.e., biotite and hornblende) and diamagnetic minerals (i.e., feldspar and quartz) are negligible and the AMS is controlled by the ferromagnetic fraction only (e.g., Hrouda and Kahan, 1991). In weakly magnetic rocks, with bulk susceptibility less than 5×10^{-4}, the fraction of ferromagnetic minerals is low, such that the AMS is controlled by the paramagnetic fraction (e.g., Rochette, 1987; Bouchez, 2000). If the bulk susceptibility is less than 5×10^{-5}, the effect of diamagnetic fraction is considerable (e.g., Hrouda, 1986, 2004, 2010).

The AMS ellipsoid is approximated by a symmetrical second-rate tensor, with eigenvalues that define the principal susceptibility magnitudes ($K_1 \geq K_2 \geq K_3$). The bulk magnetic susceptibility (K_m) is the sum of the paramagnetic, ferromagnetic, and diamagnetic mineral contributions to the sample and is the arithmetic mean of the principal susceptibilities measured in low field. The orientation of the AMS ellipsoid is assumed to reflect the alignment of the bulk fabric in most cases. K_1 represents the magnetic lineation and K_3 is the pole to the

magnetic foliation. The corrected degree of anisotropy P_j is the deviation of the AMS ellipsoid from a sphere; the P_j value increases from 1 (sphere) to infinity with increasing anisotropy. Ellipsoid shape, T, is used to approximate the geometry of finite strain for the last major deformation to occur within the intrusive suite. T=0 indicates plane strain, $-1 < T < 0$ indicates prolate strain, and $0 < T < 1$ indicates oblate strain.

For this study, samples from 88 sites in the Sahwave Range intrusive suite and Power Line intrusive complex underwent AMS analysis. On average, 15, 21 mm × 25 mm, cylindrical subspecimens were collected and cut from 8-10 drill cores. AMS was measured on a KLY-3S Kappabridge operating at 300 A/m @ 875 Hz, at the University of Wisconsin – Madison. Of the 88 sites, none were rejected. Averaging from the sites was done in the Anisoft 4.2 package and further reduced using scripts written for AMS in the R programming language from Roberts et al. (2018). The results of AMS analysis are summarized in Supplementary Table S1.

3.4.2 Background: Magnetic Mineralogy

Additional analyses of rock magnetics are required to characterize the composition and domain state of the magnetic grain assemblage in a granitoid. Magnetic susceptibility is affected by variations in both the composition and concentration of the magnetic minerals, when measured as a function of temperature. Magnetic susceptibility vs. temperature analyses are used to: 1) Determine the Curie point temperature of ferrimagnetic minerals; and 2) Separate ferrimagnetic vs. paramagnetic mineral contribution to the sample's magnetic susceptibility.

To assess the domain state of the magnetic mineral assemblage, we conducted hysteresis and isothermal remnant magnetization experiments using the vibrating sample magnetometer (VSM). The VSM is used to magnetize a sample in a uniform magnetic field, which is then

sinusoidally vibrated. The induced voltage in the pickup coil is proportional to the sample's magnetic moment but does not depend on the strength of the applied magnetic field. Using the VSM, it possible to plot the magnetic hysteresis curve and the isothermal remnant magnetization curves for a sample. The magnetic hysteresis curve provides information about the saturation magnetization and the coercivity. The isothermal remnant magnetization provides the coercivity of remanence and saturation isothermal remanent magnetization, which provide information on the domain state of the titanomagnetite grains carrying the characteristic remnant magnetization. Together, these data sets can be evaluated on a Day plot, in which M_{rs}/M_s is plotted against H_{cr}/H_c. The Day plot distinguishes between magnetic minerals have low coercivity values – termed magnetically "soft" and which do not hold a stable remanence – and magnetic minerals have high values are "hard" (e.g., are good magnetic recorders).

Standardized rock magnetic experiments were conducted on six representative sample sites, two from each of the three units. All rock magnetic experiments were carried out at the University of Texas at Dallas Paleomagnetic Laboratory using a VSM for hysteresis and isothermal remnant magnetization to determine domain state and paramagnetic vs. ferrimagnetic grain contribution (Fig. 9).

Magnetic composition was evaluated using a multifunction Kappabridge with a CS4 attachment for thermal experiments. Temperature vs. Susceptibility experiments yield Curie point temperatures ranging from 560-580° C, indicative of titanomagnetite and titanomaghematite as the predominate ferrimagnetic carriers. Hysteresis curves are indicative of multidomain to pseudo-single domain states for the ferrimagnetic components. Curves were corrected for the paramagnetic component.

3.4.3 Sahwave granodiorite

The Sahwave granodiorite yields a bulk magnetic susceptibility range from 0.50 to 3.00 × 10^{-3} and predominantly oblate shape AMS ellipsoids. Bulk magnetic susceptibility is generally higher in the center of pluton (~2.5 x 10^{-3}), relative to the margins (~0.75 x 10^{-3}). The corrected degree of anisotropy does not vary significantly across the Sahwave granodiorite and shape ellipsoids are predominantly oblate with triaxial shape ellipsoids along the eastern margin (Fig. 10). The mean orientation of the K_1-K_2 plane reveals a steeply dipping NNW-SSE magnetic foliation, consistent with field fabrics measurements (Fig. 11). Samples were taken on a detailed transect across the pluton, which reveals variations of the magnetic foliation across the unit. The western margin of the pluton yields a more NW-SE – to even E-W trending – foliation that gradually becomes N-S in the center to eastern margin of the pluton.

The magnetic lineation (K_1) orientation also varies from the interior of the pluton towards either margin (Fig. 11). A steep to subvertical lineation occur in the center of the pluton, gradually shallowing towards the western margin. However, the clustered orientation of K_1 reveals an unobserved average magnetic lineation that plunges ~55° to the NW.

3.4.4 The granodiorite of Bob Spring

The same detailed sampling could not be conducted in the granodiorite of Bob Spring due to limited outcrops; only 23 oriented sample sites were collected and analyzed with AMS. These sites exhibit bulk magnetic susceptibility values from 0.53 to 8.65 × 10^{-3}. Lower magnetic susceptibilities were common in the outcrops of the granodiorite of Bob Spring in the Nightingale Range (0.53-3.74 × 10^{-3}) and higher susceptibilities were more prevalent in the Sahwave Range outcrops (4.18- 8.65 × 10^{-3}). Oblate, triaxial, and prolate shape ellipsoids were identified in the unit, with oblate shape ellipsoids being the most common. Oblate shape

ellipsoids are found in the Sahwave Range outcrops. Prolate and triaxial shape ellipsoids are found predominantly in the Nightingale Range outcrops along the presumed western margin of the unit. The corrected degree of anisotropy values do not vary significantly across the granodiorite of Bob Spring, despite variation in the shape ellipsoid (Fig. 10).

A steeply dipping, N-S trending, magnetic foliation (K_1-K_2) is found throughout the pluton, but orientations do vary (Fig. 11). The western margin of the pluton yields a more NE-SW trending foliation that gradually becomes N-S in the Sahwave Range outcrops. The magnetic lineation pattern varies significantly with several different clusters of K_1 that plunge moderately to shallowly to the north and south (Fig. 11).

3.4.5 The granodiorite of Juniper Pass

The granodiorite of Juniper Pass yields also yields a wide range of bulk magnetic susceptibility values from 0.01-8.02 × 10^{-3}, although average values range between 2.24-3.69 x 10^{-3}. Oblate, prolate, and triaxial shape ellipsoids are found in clusters, with different ellipsoid shape generally found in certain regions of the pluton. Oblate shape ellipsoids (T values of 0.5-1) are found in the northern most outcrops of the Sahwave Range, triaxial shape ellipsoids are found in the southern outcrops of the Sahwave Range (T values of -0.5-0.5), and prolate (T values of -1 to -0.5) and triaxial shape ellipsoids are found in the western outcrops of the Nightingale Range. The corrected degree of anisotropy (P_j) also varies significantly across the granodiorite of Juniper Pass from 1.05 to 1.40, with the highest degrees of anisotropy are found in sites from the Nightingale Range (Fig. 10).

The magnetic foliation plane is E-W striking and steeply dipping in the granodiorite of Juniper Pass, consistent with field measurements. This orientation of the magnetic foliation is

very consistent E-W fabric in the northern and southern outcrops of the granodiorite of Juniper Pass in the Sahwave Range (Fig. 11). In contrast, some variations of the magnetic foliation in outcrops of the pluton in the Nightingale Range. The western margin of the granodiorite of Juniper Pass in the Nightingale Range yields a more NW-SE trending foliation. The lineation fabric for the granodiorite of Juniper Pass is not consistent across the unit and varies from site to site (Fig. 11).

3.4.6 The Power Line intrusive complex

The Power Line intrusive complex yields the lowest magnetic susceptibility values of all units in the Sahwave and Nightingale Ranges (0.01- 0.09 × 10^{-5}). Initial bulk susceptibility measurements from the Power Line intrusive complex indicated that the unit contained little or no ferrimagnetic phases and that the AMS fabric is carried by paramagnetic minerals. Specimens from the Power Line intrusive complex yield a negative susceptibility trend during temperature vs. susceptibility experiments further indicating a predominantly paramagnetic and diamagnetic mineral assemblage for this unit. VSM measurements yield flat hysteresis curves which further indicate a lack of ferrimagnetic phases in this unit. The corrected degree of anisotropy also varies across the Power Line intrusive complex from 1.05 to 1.8. The highest degrees of anisotropy are found along the eastern contact in the southeast portion of the Nightingale Range (Fig. 10).

Distinct clusters of strongly oblate to triaxial shape ellipsoids and triaxial to prolate shape ellipsoids are localized in certain regions of the pluton (Fig. 10). The more oblate shape ellipsoid clusters are found in the western and southeastern margins of the Nightingale Range, whereas the triaxial to prolate shape ellipsoid clusters are found in northern outcrops of the Power Line

intrusive complex in the Nightingale Range. There appears to be no relationship between shape ellipsoid and bulk magnetic susceptibility, nor does there appear to be a relationship between the corrected degree of anisotropy with bulk magnetic susceptibility (Fig. 10). High susceptibilities do not correspond with higher degrees of anisotropy within this unit.

The magnetic foliation plane in the Power Line granodiorite is striking NW-SE to N-S fabric and is steeply dipping, consistent with field measurements. The western margin of the Power Line intrusive complex preserves a more NW-SE trending magnetic foliation, but becomes progressively more N-S oriented on the eastern margin. The magnetic lineation for the Power Line granodiorite is subvertical (Fig. 12). A slight N-S trend to the magnetic lineation is observed along the western marginal outcrops, whereas the easternmost outcrops yield a more vertical magnetic lineation with slight NW-SE trends.

4. Discussion

4.1 Emplacement of the Sahwave Range intrusive suite

In this section, we summarize the microstructures and magnetic fabrics in the Sahwave Range intrusive suite, starting with the emplacement of the granodiorite of Juniper Pass through the Sahwave granodiorite. We explicitly compare these fabrics to those in the Tuolumne intrusive suite in the east-central Sierra Nevada. We conclude that dextral strike-slip movement likely facilitated emplacement of the plutons of the Sahwave Range intrusive suite.

4.1.1 Synthesis of microstructural and magnetic fabrics

The E-W planar fabric is observable across all the granodiorite of Juniper Pass sites in the Sahwave Range. AMS orientation data reveal highly clustered K_3 maxima (pole to the plane of

magnetic foliation) that define an E-W-oriented, oblate planar fabric from the granodiorite of Juniper Pass, consistent with our field observations from the unit. The granodiorite of Juniper Pass however, yields neither an observable field lineation nor do AMS data reveal a consistent magnetic linear (e.g., K_1 maxima). We interpret the oblate magnetic ellipsoids, consistent planar fabric, and lack of a consistent lineation to result from flattening strains. The microstructures observed in granodiorite of Juniper Pass ranges from magmatic to high-temperature solid state. The spatial pattern of the fabric texture observed from thin sections of the granodiorite of Juniper Pass is limited. When paired with the P_j values, however, we observe that higher degrees of anisotropy (~1.20) correspond to sites with sub-solidus textures (Fig. 13). Thus, we interpret these higher P_j values to be a reliable indicator of high temperature solid state deformation within the unit. The mean P_j value for the sites in the granodiorite of Juniper Pass is 1.16, with the sites exhibiting magmatic fabrics having P_j values of ~1.0-1.13. These magmatic fabrics are observed predominately in sites from the northern outcrops of the granodiorite of Juniper Pass in the Sahwave Range. The granodiorite of Juniper Pass sites in the Nightingale Range show significant variability from the strong E-W fabric in the Sahwave Range. Prolate fabrics in the Nightingale Range are NW-SE trending and are more similar in orientation and texture to the Power Line intrusive complex (Fig. 13).

The sparse sampling of granodiorite of Bob Spring makes interpretations of the fabric pattern inherently speculative. Overall, the microstructures indicate magmatic deformation and P_j values are low despite having the highest mean susceptibilities. The granodiorite of Bob Spring also yields predominately prolate to triaxial shape ellipsoids indicative of constriction to plane strains. The more constructional strain pattern in the granodiorite of Bob Spring differs from the flattening strains observed in all other units. From map patterns, the granodiorite of

Bob Spring bulges into the granodiorite of Juniper Pass in the Nightingale Range; this pattern is likely a result of igneous intrusive processes rather than as a result of regional tectonics (Fig. 13). The AMS data support this intrusion, as the internal fabric pattern of the granodiorite of Bob Spring roughly parallels the proposed intrusive contact. Another intrusive bulge of occurs to the south, consistent with the younger Sahwave granodiorite intruding the older granodiorite of Bob Spring. In this location, fabric in the granodiorite of Bob Spring does not follow that contact but yields a steep N-S magnetic planar fabric. These lobate-shaped intrusive relations may explain why there is no consistent lineation in the granodiorite of Bob Spring.

The Sahwave granodiorite is the most densely sampled of all the Sahwave batholith units and transects from this unit yield the most compelling and complete fabric pattern. The contact between the granodiorite of Bob Spring and the Sahwave granodiorite on the western side is gradational and the boundary on Figure 5 was selected using magnetic susceptibility measurements, as the granodiorite of Bob Spring yields a higher average magnetic susceptibility than the Sahwave granodiorite. Bulk magnetic susceptibility in the Sahwave granodiorite varies slightly, with lower susceptibilities near the margin and higher susceptibilities towards the interior of the pluton. The AMS ellipsoid data for the Sahwave granodiorite shows constructional shapes (prolate shape ellipsoids) along the eastern margin, to progressively plane strains (triaxial) and then predominately flattening (oblate) in the interior of the unit. This pattern is mirrored along the western side, with prolate shape ellipsoids near the contact with the granodiorite of Bob Springs.

The AMS fabric orientation data from west to east across the Sahwave granodiorite reveals a magnetic fabric pattern that trends more E-W in the west and then rotates to nearly NNW-SSE within the interior of the unit and maintains this orientation through the eastern

margin (Fig. 13). The magnetic lineation trends NW-SE and plunges subhorizontal to both the NW and SE across the unit. P_j values are weaker along the margin (1.13) and increase towards the interior of the unit (1.2). A value of P_j of 1.20 and above appears to be a reliable indicator of the presence of solid-state deformation in the Sahwave granodiorite, with lower P_j values correlating with the magmatic textures (Fig. 13).

4.1.2 Comparison of the syntectonic Sahwave Range intrusive suite with simultaneous intrusions Sierra Nevada batholith

We use the microstructural and AMS data to constrain both the emplacement and deformation of the Sahwave Range intrusive suite. Constraining the regional geometry deformation within magmatic units is non-trivial, however, because of the diffuse nature of strain, the magmatic nature of most of the microstructures, and the lack of offset markers. To facilitate our interpretation, we compare the Sahwave Range intrusive suite to simultaneously crystallized plutons within the Sierra Nevada batholith, which contains nearly continuous exposures. As previously mentioned, there are striking similarities in composition and crystallization age between the nested Sahwave Range intrusive suite and the nested Tuolumne intrusive suite (Van Buer and Miller, 2010). New preliminary U-Pb on zircon LA-ICPMS dates further constrain the age of pluton crystallization for the three granodiorite units of the Sahwave Range intrusive suite and the Power Line intrusive complex. See the Appendix for a more detailed explanation of the zircon U-Pb geochronology methods and results (text and Supplementary Figure 1). Using U-Pb zircon dates as a means of comparison: 1) The granodiorite of Juniper Pass (92.7 ± 1.4 Ma; Van Buer and Miller, 2010) is equivalent to the tonalites of Glen Aulin and Kuna Crest (93.1 ± 0.1, 93.5 ± 0.7 Ma; Colman et al., 2004; Matzel et al., 2005); 2) The granodiorite of Bob Spring (92.8± 1.7 Ma; Van Buer and Miller, 2010) is

equivalent to the Half-Dome granodiorite (92.8 ± 0.1, 88.8 ± 0.8 Ma; Colman et al., 2004); and 3) The Sahwave granodiorite (88.5 ± 2 Ma; Van Buer and Miller, 2010) is equivalent to the Cathedral Peak granodiorite (88.1 ± 0.2 Ma; Colman et al., 2004). Although the bulk composition differs slight between the intrusive suites, the rocks are surprisingly similar in hand sample. The similarity of compositions and crystallization also apply to the Sonora Pass, Mono Pass, and Mt. Whitney intrusive suites in the eastern Sierra Nevada (Bateman, 1992).

AMS data are utilized to further interpret finite strain directions in each of the units where possible. AMS magnetic lineations from the Sahwave granodiorite plunge moderately to the SSE and NNW. These lineations are interpreted to reflect principal stretching directions and indicate oblique-slip shear sense within the unit. Additionally, the southeast-plunging lineations combined with dextral shear sense indicators observed near the eastern contact indicate that the pluton was moving upward and to the north, relative to the wall rock. This pattern is consistent with both upward ascent and emplacement of the pluton as well as northward horizontal displacement.

Similar AMS, microstructural, and field patterns are observed in the Tuolumne intrusive suite. Tikoff et al. (2005) document the presence of shallow-moderate southeast-plunging lineations along in the northeastern margin of the Tuolumne intrusive suite (also Tikoff and Greene, 1997). Further, Tikoff et al. (2005) demonstrate a change from magnetic foliations from NW-oriented near the contact to EW-oriented in the center of the Cathedral Peak granodiorite of the Tuolumne intrusive suite. This change in foliation orientation is also observed with field observations (Bateman, 1983). Another similarity is the presence of late stage, low temperature localized shear zones in the Sierra Nevada batholith. The movement is dextral in cases where the shear zones are parallel to contacts and sinistral in cases where they form at a high angle to it

(e.g., Martel et al., 1988; Burgman et al., 1994). The late-stage dextral shear parallel to the contact in the Sahwave granodiorite is consistent with this trend.

The fabrics and internal structure of the Sahwave Range and Tuolumne intrusive suites are not identical (Table 1). There is evidence for lobes of younger rock intruding into older rock (e.g., Memeti et al., 2010). Second, the granodiorite of Bob Springs is similar to the Half Dome granodiorite, including NNW-oriented fabrics and that the western contact of both units with the younger inward units (Sahwave, Cathedral Peak) are gradational. There are three problems with a direct comparison of these units, however: 1) There has not been a systematic AMS study of the Half Dome granodiorite; 2) The granodiorite of Bob Spring is so poorly exposed that larger-scale trends are inherently interpretational; and 3) The granodiorite of Juniper Pass has different fabric patterns relative the Kuna Crest granodiorite, although its composition and timing are equivalent in the Tuolumne intrusive suite. The E-W foliation trend in the granodiorite of Juniper Pass is only locally observed in the Kuna Crest granodiorite, in which the foliation mostly trends NNW. We attribute these minor variations to differences in igneous processes associated with pluton emplacement.

A significant limitation in the interpretation of the deformational history of the Sahwave Range intrusive suite is the lack of wallrocks, particularly on the east side of the intrusions. The equivalent wallrocks in the Sierra Nevada are often highly deformed and part of a series of dextral shear zone systems in the Sierra Crest shear zone system (e.g., Tikoff and Greene, 1997; Tikoff and St. Blanquat, 1997). These shear zones within the wallrocks have been recognized by many workers (e.g., Greene and Schweickert, 1995; Cao et al. 2015) and the timing of deformation is broadly consistent with the emplacement and cooling of the adjacent granites (e.g., Sharp et al., 2000). We postulate that sheared wallrocks were likely adjacent to the eastern

side of the Sahwave intrusive suite but were likely reactivated by a Miocene normal fault associated with Basin and Range extension. It is possible that a small shear zone, highly deformed shear zone along the eastern side of the Sahwave granodiorite and granodiorite of Bob Spring is part of a larger shear one and could be used to further constrain deformation within the Sahwave Range intrusive suite.

The timing of deformation – from both the intrusions and the wallrocks – are used to constrain the timing of deformation in the Sierra Nevada batholith (Table 1). In general, dextral transpressional deformation in the Sierra Nevada batholith appears to occur during the entire emplacement time of the Late Cretaceous intrusive suites. There is certainly dextral shearing that occurs on the NE margin of the Tuolumne intrusive suite (e.g., Cao et al., 2015), but the presence of shearing during the earlier (~92-88 Ma) phases of emplacement remains controversial. Bartley et al. (2005) document dextral motion during emplacement of the ~92 Ma Mt Lamarck granodiorite in the Mono Pass intrusive suite; the *en echelon* nature of the Mono Pass intrusive suite allows better resolution of the earlier phases of deformation. McNulty (1995) suggests that movement on the Bench Canyon shear zone was active at this time. The possible link with emplacement of the ~85 Ma (U-Pb date on zircon) Johnson granite porphyry with movement on the Bench Canyon (Titus et al., 2003). Sharp et al. (2000) data for $^{40}Ar/^{39}Ar$ closure on muscovite in Gem Lake shear zone, indicate that deformation ceased at ~80 Ma. The cessation of the shear zone is effectively dated by cross-cutting sinistral shear zones in the Mono Pass intrusive suite, which cooled through $^{40}Ar/^{39}Ar$ closure of muscovite at 79-75 Ma (Segall et al., 1990).

4.1.3 Tectonic-assisted, pull-apart syntectonic emplacement model for the Sahwave Range intrusive suite

The striking similarity of these two systems allows us to utilize the better-exposed and better-constrained intrusive suites in the Sierra Nevada batholith to interpret emplacement of Sahwave Range intrusive suite. We interpret the fabrics across all units of the Sahwave Range intrusive suite to suggest non-coaxial, dextral deformation across this zone occurred during magma emplacement from 94 Ma to 88 Ma. Further, this dextral shearing facilitated magma emplacement and is part of a larger shear zone system along the trend of the Late Cretaceous arc in western Nevada and eastern California.

Tikoff and St. Blanquat (1997) suggest that these large plutons in the eastern Sierra Nevada were emplaced into a shear zone system that created *en echelon* pull-apart zones (P-shear model). Although originally applied to the *en echelon* Mono Pass intrusive suite (e.g., Tikoff and Teyssier, 1992), it was subsequently extended to include the nested Tuolumne intrusive suite (e.g., Tikoff and St. Blanquat, 1997). These shear zones that were active in the Sierra Crest shear zone system indicate dextral transpressional kinematics (Tikoff and Greene, 1997). In this model, pluton emplacement occurs in dilatational jogs created by these shear zones, which allows the accumulation of such large plutons. In cases where magma supply outpaces shear zone movement, lobes or bulges are formed. This type of interaction between magmatism and shearing results in a complex thermal evolution where magma emplacement is facilitated by shear zones as conduits. However, the magma emplacement also results in softening of the crust, which facilitates greater deformation in these systems (Tommasi et al., 1994).

We interpret that the Sahwave Range intrusive suite was emplaced during dextral shearing. The granodiorite of Juniper Pass intruded the Jungo terrane and Power Line intrusive complex at 94 Ma associated with strike-slip movement. Sub-magmatic conditions persisted and the granodiorite of Bob Springs intruded and mixed with the granodiorite of Juniper Pass, but under evolving deformation conditions as simple shear localized into the weaker magmatic rocks. Magmatic fabrics indicate both upward and horizontal flow from 94-88 Ma. Younger simple shear deformation was experienced by the Sahwave granodiorite as deformation localized during and after the emplacement of this unit. We interpret the gradation clockwise rotation of fabrics across all units of the Sahwave batholith (E-W in the granodiorite of Juniper Pass to NW-SE in the Sahwave granodiorite) to result from non-coaxial, dextral deformation across this zone during magma emplacement. Moreover, the fabric rotation is both gradual (batholith scale) and discrete (individual pluton scale), and presumably reflects the syn-tectonic emplacement of the Sahwave Range intrusive suite.

We further interpret that the Sahwave Range intrusive suite was likely emplaced into a dilatational zone between two large-scale dextral shear zones. This emplacement model is largely based on the presence of shearing on the eastern side of the Sahwave granodiorite, and the striking similarity of fabrics patterns to those in the eastern side of the Tuolumne intrusive suite (Fig. 14). The large-scale shear zones are admittedly cryptic for the Sahwave Range intrusive suite, because of subsequent Basin and Range extension, including a major normal fault on the east sides of the intrusive suite where a suspected shear zone occurs. Because of the nature of the outcropping in the Sahwave and Nightingale Ranges, this model will necessarily remain speculative.

Regardless of the exact mechanism of emplacement, dextral deformation occurred along the axis of magmatism from northwest Nevada through the Sierra Nevada arc. The diffuse shearing in the Sahwave Range intrusive suite is likely a northward extension of the dextral Sierra Crest shear zone system within the Sierra Nevada mountains.

4.2 Deformation of the Power Line intrusive complex

4.2.1 Synthesis of solid-state fabrics in the Power Line intrusive complex

The Power Line intrusive complex contains a consistent NW-SE field foliation. The AMS data reveal a highly clustered K_3 maxima (pole to the plane of magnetic foliation) that is consistent with a NW-SE planar magnetic fabric. A steep lineation was measured at field locations when possible. The AMS data yield a linear magnetic fabric on the western margin of the pluton, as indicated by clustering of K_1 maxima plunging steeply to the south and southeast. The AMS sites along the eastern margin yield a steep, south plunging magnetic lineation; the western margin of the intrusive suite yields SE-oriented, moderately plunging magnetic lineations. These orientations show a loosely defined sigmoidal trajectory within the Power Line intrusive complex, which correlates with the observed shear indicators (e.g., feldspar sigma clasts) to suggest dextral shear movement in the syn- to late- magmatic state.

Oblate shape ellipsoids dominate in the Power Line intrusive complex sites along the eastern margin and correspond with higher P_j values (1.2-14). We interpret the oblate shape ellipsoids from the eastern margin as indicators of flattening strains. Triaxial to prolate shape ellipsoids are dominate along the western margin and yield lower P_j (~1.2) values. The prolate pattern may represent variation in the deformation conditions and/or result from the inclusion of paramagnetic minerals in the AMS signal as a result of fluid migration (see below).

In addition to the variations in the shape ellipsoid and corrected degree of anisotropy along the eastern vs. western margins, the bulk susceptibility is also variable. The western margin has a higher bulk susceptibility than the eastern margin. The nature of the biotite grains also differs; the biotite grains along the western margin are smaller and exhibit higher birefringence. This intensity of birefringence color in biotite generally increases with an increase in iron content. As the iron-rich paramagnetic phases are the ones carrying the AMS fabric, these fluids could affect the characteristics of the magnetic parameters even though the orientation of the fabric remains relatively uniform across the intrusive suite. This effect could explain with the higher K_m in this region. Further, the biotite grains on the western margin are also less planar and are more tabular in habit, which could contribute to the more prolate AMS shape ellipsoids along the western margin. The variation in grain shape affects the AMS signal, and thus could explain the double maxima shown in the K_m probability density for this unit (Fig. 10).

One possible interpretation for the difference in biotite shape and composition is the role of metamorphic fluids, with increased fluid mobility on the western contact. These fluids were possibly derived from the sedimentary rocks during deformation and metamorphism, which subsequently permeated through the margin of the intrusive suite and facilitated the recrystallization of internally undeformed biotite.

4.2.2 Kinematics of shearing within the Power Line intrusive complex and constraints on emplacement

Field fabric, AMS, and microstructural data reveal a pure shear dominated dextral transpressional structural pattern within the Power Line intrusive complex. The Power Line intrusive complex yields consistently subvertical NW-SE magnetic foliation and steep lineation.

The unit exhibits prolate to oblate AMS ellipsoids (L>S to S=L to S>L tectonites), although oblate magnetic fabrics dominate away from the western margin of the pluton. The steep foliation and vertical lineation, oblate AMS ellipsoids, and the presence of shear indicators perpendicular to lineation are all indicative of pure shear dominated transpression (e.g., Fossen and Tikoff, 1993). The dextral shear sense is given by the lineation-perpendicular shear sense indicators and the change of orientation of the foliation from the margin of the pluton into the interior.

The high- to low-temperature microstructures indicate that the deformation in the Power Line intrusive complex commenced immediately after or during solidification of the plutonic complex. Hence the deformation must have continued after ~106 Ma. There are two lines of evidence that support syn-magmatic shearing. First, the presence of sub-magmatic microstructures suggest that shearing must have occurred during or shortly after emplacement. Second, we interpret the S-SE plunging magnetic lineation from the Power Line intrusive complex to reflect the simple shear component of deformation. The S-SE plunging lineation, combined with dextral shear sense indicators along observed near the eastern and western contacts, indicate that the entire Power Line intrusive complex was flowing upward and to the north during deformation. This interpretation is consistent with the observation of strong wall rock fabrics that parallel the solid-state fabric preserved in the Power Line intrusive complex.

The field, microstructural, and AMS data – when combined with geochronology – constrain the timing of deformation in the Power Line intrusive complex. U-Pb zircon LA-ICPMS dates suggests a crystallization age of ~106 Ma for the Power Line intrusive complex. The solid-state fabrics – particularly the vertical lineation – are not present in the units of the 94-88 Ma Sahwave Range intrusive suite. Thus, it appears that pure shear dominated tranpression

did not occur during emplacement of the younger intrusive suite. Thus, the pure shear dominated transpression must have occurred between ~106 and 94 Ma.

4.2.3 Comparison with the western Idaho shear zone and a regional ~100 Ma deformation in the magmatic arcs of the western U.S.

The deformation preserved in the Power Line intrusive suite is similar in geometry, composition, age, and age progression to the western Idaho shear zone, in both the Owyhee segments (Benford et al., 2010) and the McCall segments (Giorgis et al., 2008) (Table 2; Fig. 15). The western Idaho shear zone exhibits solid state flattening fabrics that strike NS-020. In this shear zone, fabrics are defined by fine-grained ribboned quartz, biotite, and K-feldspar sigma clasts with tails. Dextral shear indicators are found on sub-horizontal planes in the western Idaho shear zones, perpendicular to the stretching lineation. The fabrics of the western Idaho shear zone are documented to record pure shear dominated dextral transpression (Giorgis and Tikoff, 2004; Giorgis et al., 2008; Michels et al., 2015; Braudy et al., 2017; Giorgis et al., 2017).

The Little Goose Creek complex of the McCall segment preserved the most developed planar and linear fabric elements, in a highly telescoped zone with a mean degree of shape preferred of porphyroclasts anisotropy of 1.64 (Giorgis et al., 2004). The Owyhee segment, south of the McCall segment, varies in orientation (~020), is wider (15 km), and yields a lower degree of anisotropy (1.097) with few shear indicators (Benford et al., 2010). The Power Line intrusive complex, which is located ~300 km south of the Owyhee segment (Fig. 15), yields a N-S to NW-SE fabric orientation, is ~ 8 km wide, and yields a 1.2 – 1.8 (P_j) degree of shape preferred anisotropy, with abundant shear indicators in the horizontal plane.

We hypothesize that the deformation recorded in the western Idaho shear zone is likely the same deformation recorded in the Power Line intrusive complex. The fabrics in the western

Idaho shear zone are N-NNW oriented and, if projected, would line up with the location of the Power Line intrusive complex. The region between the southern mapped extent of the western Idaho shear zone and the northern end of the Power Line intrusive complex is almost entirely covered by Neogene volcanic rocks, providing no opportunity to directly field check this correlation. However, the timing, kinematics, and location of the transpressional deformation in the western Idaho shear zone and the Power Line intrusive complex are identical and suggest that regional deformation is localized into the axis of active arc magmatism.

The formation of the western Idaho shear zone is attributed to the collision of the Insular terrane by Giorgis et al. (2008) and Tikoff et al. (2017). If so, the same causal mechanism could be attributed to the deformation in the Power Line intrusive complex. The fault reconstructions of the terranes of the Canadian Cordillera suggest that the southern end of the Insular terrane was located in northernmost California (Wyld et al., 2006) at ~100 Ma, located marginward of the Power Line intrusive complex. Consequently, we also attribute this regional deformation to the collision of the Insular superterrane. We note that the fault reconstructions of Wyld et al. (2006) are minimum offset reconstructions; paleomagnetic constraints place the Insular superterrane significantly south of this location (e.g., Enkin et al., 2006; Tikoff et al., 2022).

Dextral transpressional deformation also occurs in the Sierra Nevada batholith during 106-94 Ma deformation of the Power Line intrusive complex. Krueger and Yoshinobu (2018) document a major dextral transpressional deformation within the Sing Lake shear zone at ~100 Ma in the Sierra Nevada batholith (Table 2). More recently, Torres Andrade and Tikoff (2022) also documented dextral transpressional deformation in the Courtright shear zone at ~100 Ma. In both locations, these ~100 Ma shear zones are mostly obliterated by the abundant 95-85 Ma magmatism in the Sierra Nevada batholith (Fig. 16).

This pattern of deformation in the Sierra Nevada batholith is strikingly similar to deformation recorded in the Sahwave and Nightingale Ranges. In effect, we see two periods of dextral transpressional deformation: One at ~100-95 Ma and one at ~90-85 Ma. The ~100 Ma deformation – preserved in the central Sierra Nevada and the Power Line intrusive complex – occurs first. In both areas, this deformation is crosscut but younger magmatism. The second (~90-85 Ma) event is associated with voluminous magmatism in both places. The record of this deformation is more subtle, because it requires detailed fabric studies of the plutonic rocks.

There is a clear compositional and geochronological similarity that ties the plutonic rocks of northwestern Nevada to the Sierra Nevada. However, the ~100 Ma deformation in northwestern Nevada can be clearly tied to the deformation in the western Idaho shear zone. As such, the plutonic rocks of northwestern Nevada are the lynchpin in connecting transpression deformation in the Sierra Nevada and Idaho magmatic arcs.

A further implication of this study is that the ~100 Ma deformation in the Sierra Nevada batholith is also a result of the Insular terrane collision (Figure 17). The paleomagnetic data (e.g., Enkin et al., 2006) consistently indicate that the Insular terrane is located offshore California, as do recent models that involve tectonic reconstructions based on tomographic images of subducted slabs (tomotectonics; e.g., Sigloch et al., 2017; Clennet et al., 2020). As a result, a ~100 Ma dextral transpressional shear system would have been active from the northern Peninsular Range through the Idaho batholith, consistent with different models proposed by Hildebrand and Whalen (2021a,b; westward subduction then collision) and Tikoff et al. (2022; eastward subduction then collision). Regardless of polarity, the collision would also explain the long-standing problem of the cessation of arc magmatism in both the Sierra Nevada and Idaho magmatic arcs at ~85 Ma (e.g., Bateman, 1992; Gaschnig et al., 2011). Effectively, the collision

caused the cessation of magmatism, and subduction moved westward of the Insular terrane, which contains a Late Cretaceous-Paleogene magmatic arc (e.g., Maxson and Tikoff, 1995). The time-lag between 100 Ma and 85 Ma effectively marks the time necessary to complete subduction of the downgoing plate. While these models are speculative, they do emphasize that there are regional patterns of arc deformation (see Tikoff et al., 2022). The plutons of northwestern Nevada provide critical information about the arc systems and overall tectonics of the western United States.

5. Conclusions

1. The granodiorite of Juniper Pass, the granodiorite of Bob Spring, and the Sahwave granodiorite – that constitute the Sahwave Range intrusive suite – record dextral transpression during batholith emplacement between 94-88 Ma. Strain is recorded by: 1) Right-lateral rotation of field fabrics; and 2) Magmatic to high temperature solid state microstructures.
2. Three different data sets – field fabrics, AMS data, and microstructural analysis – were used to characterize the fabrics preserved in the Sahwave Range intrusive suite. Aspects of all three methods support the interpretation that dextral transpression occurred during pluton emplacement. Specifically, in the Sahwave granodiorite, a dextral shear zone occurs on the eastern edge of the pluton. Emplacement of the pluton was likely facilitated by this shearing.
3. The composition, geochronology, and fabric patterns observed in the Sahwave Range intrusive suite are similar to those to the Tuolumne intrusive suite in the eastern Sierra Nevada batholith. The dextral shearing in the Sahwave Range intrusive suite is synchronous with dextral

shearing in the Cascade Lake shear zone in the Tuolumne intrusive suite. This similarity suggests a through-going dextral shear zone along the trend of active magmatism in the Sierra Nevada batholith. These similarities exist despite the observation that the Sahwave Range intrusive suite intrudes into oceanic terranes and the Tuolumne intrusive suite intrudes Precambrian North America.

4. The Power Line intrusive complex records ~100 Ma solid state deformation. Microstructural analyses of this unit suggest a history of both high- to low-temperature deformation, indicating syn- to post-emplacement deformation of the Power Line intrusive complex. Field fabrics, AMS, and microstructure all support pure shear dominated dextral transpression kinematics. Deformation in the Power Line intrusive complex must have ceased prior to ~94 Ma. Finally, this deformation is consistent with transpressional deformation in both the western Idaho shear zone and the Sierra Nevada batholith at this time, indicating a regional deformation that was focused along the trend of the magmatic arc.

6. Figure Captions

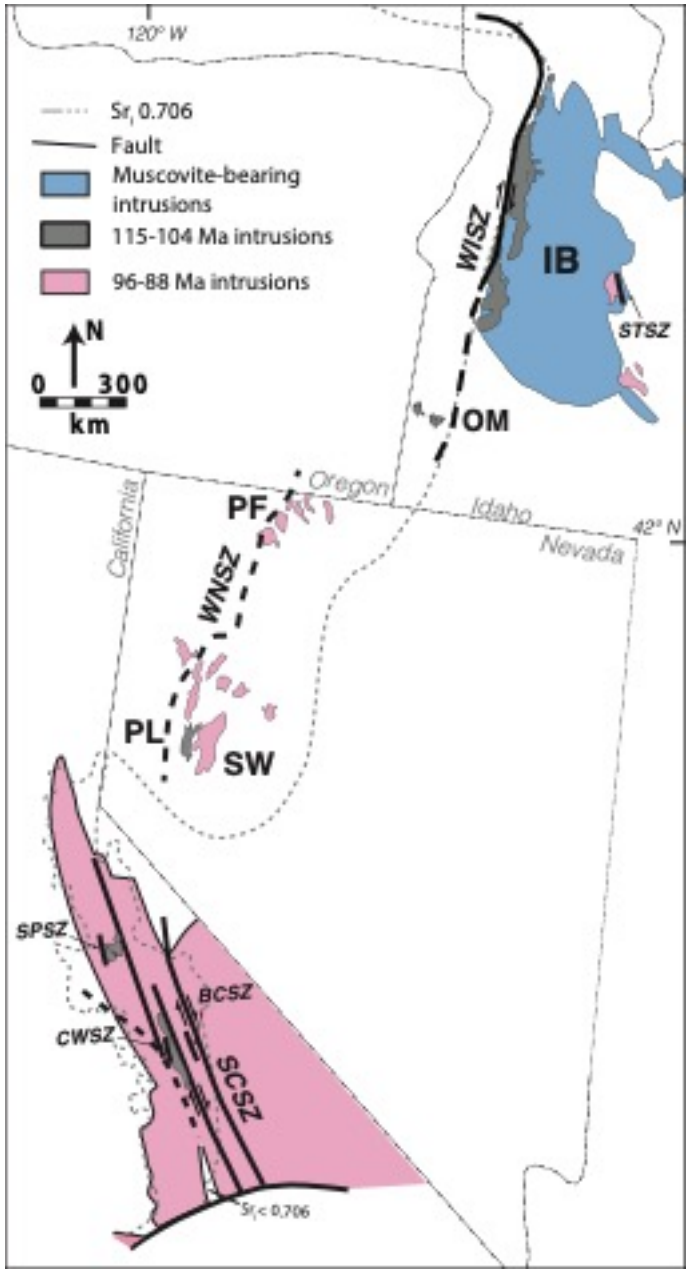

Figure 1. Geologic map of the central North American Cordillera, including $Sr_i = 0.706$ line, shear zone systems, and different magmatic events. Intrusive centers: IB – Idaho batholith, OM – Owyhee Mountains; PF – Pine Forest Range; PL – Power Line intrusive complex; and the SW – Sahwave Range intrusive suite. Shear zones include – the western Idaho shear zone (WISZ); the Sierra Crest shear zone (SCSZ); the Sing Peak shear zone (SPSZ); the Courtright-

Wishon shear zone (CWSZ); Bench Canyon shear zone (BCSZ); and Sawtooth shear zone (STSZ).

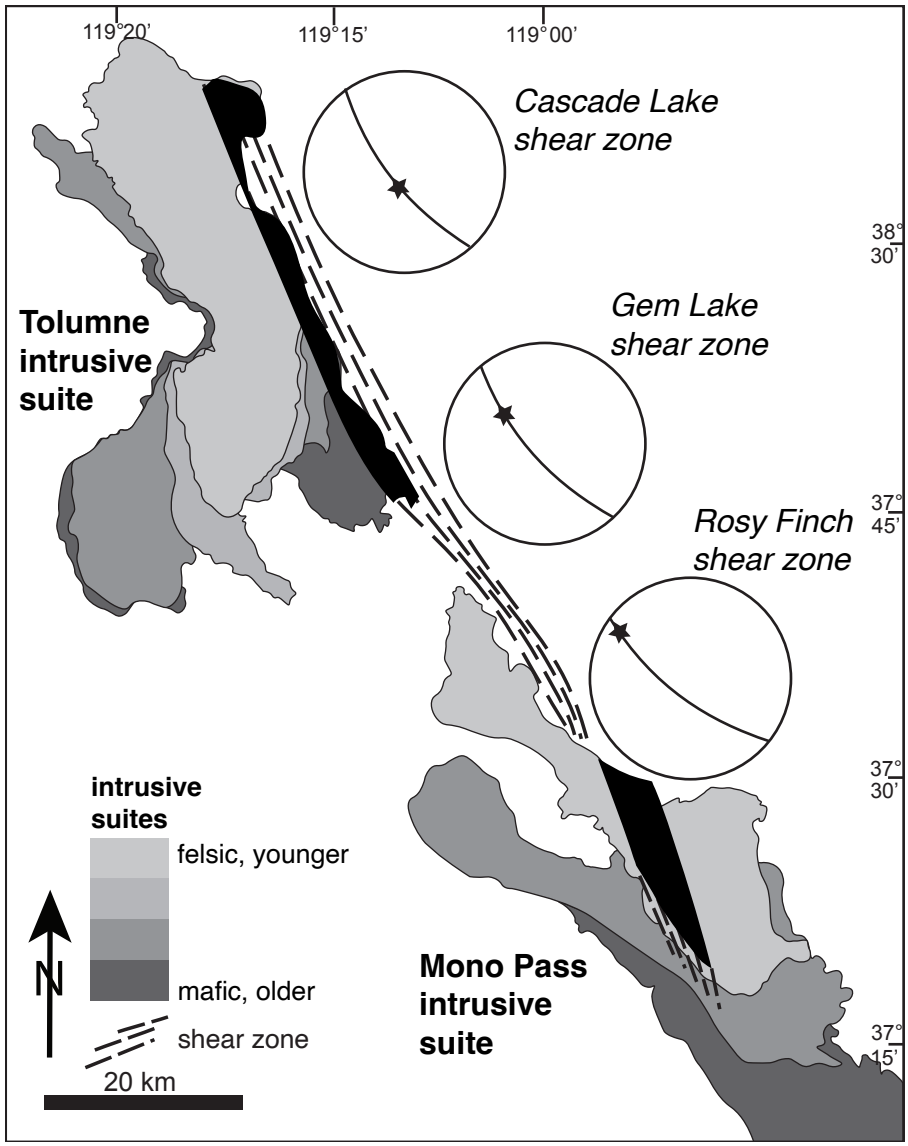

Figure 2. Summary figure showing the nested (dark grey to light grey denoting composition) Tuolumne intrusive suite and the Mono Pass intrusive suite including the summarized trend of the shear zone segments within these units is highlighted in black (dashed lines show inferred extent where not exposed). Lower hemisphere, equal area nets summarize field fabric orientations, including the mean strike and dip of the mineral foliation and the lineation direction (a star) in each of the shear zone segments. Map modified from Titus et al. (2005).

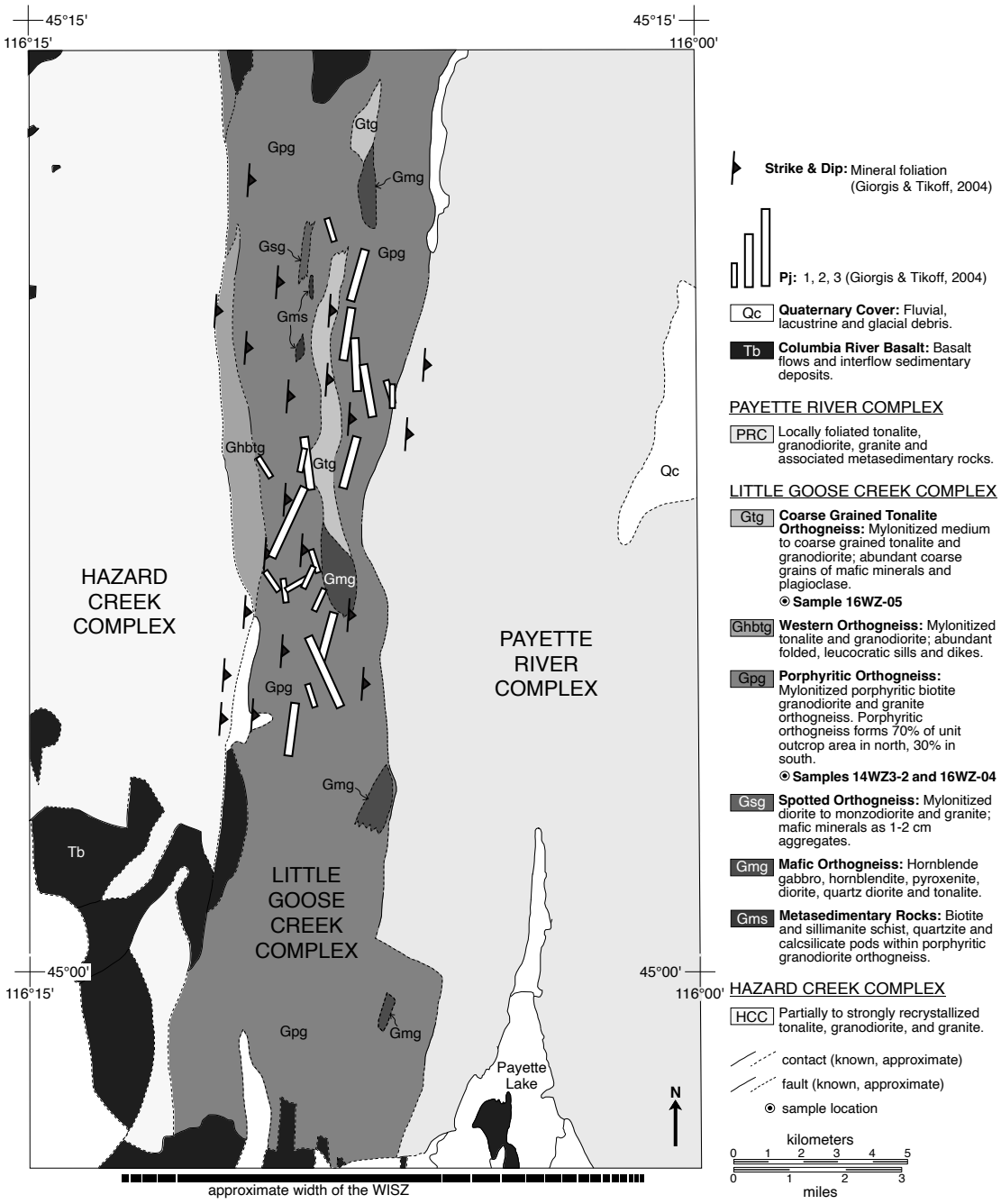

Figure 3. Simplified geologic map of the magmatic units deformed by the western Idaho shear zone along the western margin of the Idaho batholith. This map includes anisotropy data from the Little Goose Creek complex as well as compiled field fabric data from Giorgis & Tikoff (2004).

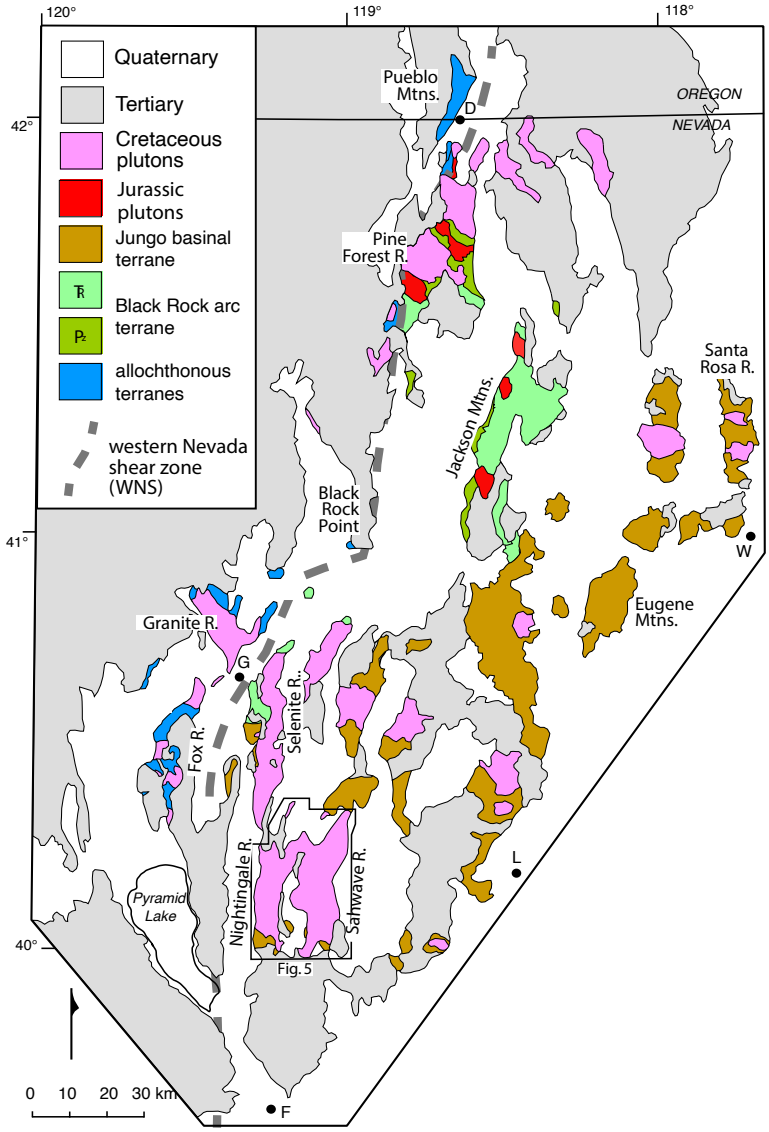

Figure 4. Simplified geologic map showing the location of intrusive units in NW central Nevada and the position of the western Nevada shear zone (WNS)(Wyld and Wright, 2001). Towns are Denio (D), Fernley (F), Gerlach (G), Lovelock (L), and Winnemucca (W). WNS drawn to show general location without obscuring geologic units (Stewart and Carlson, 1976; Wyld, 1996, 2002, 2007; Quinn et al. 1997; Wolak, 2001).

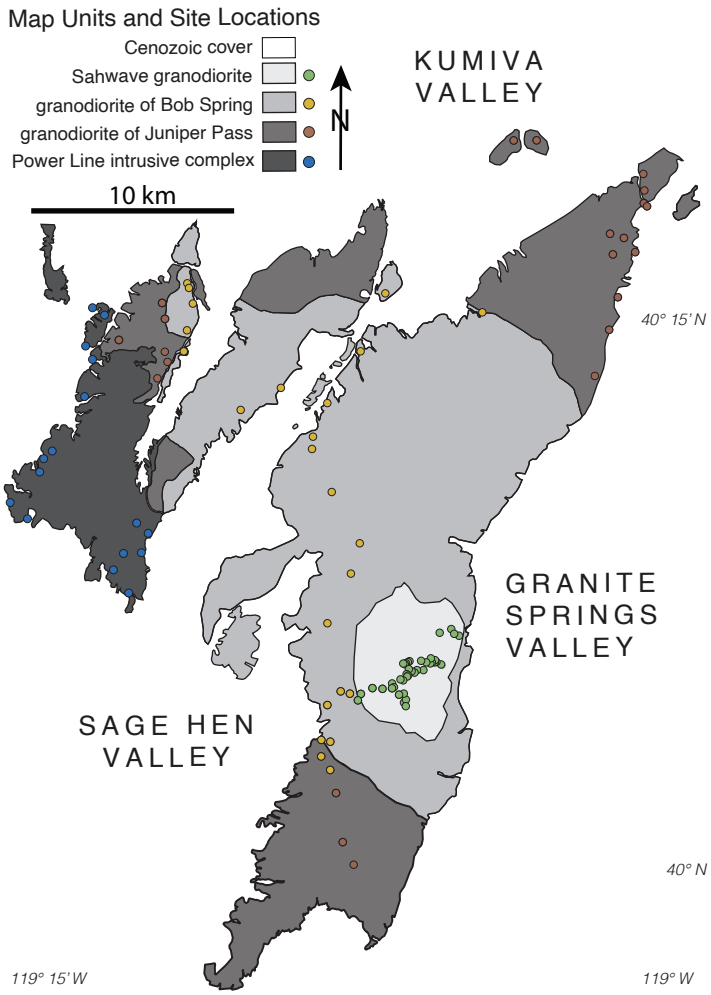

Figure 5. Simplified geologic map of the Sahwave and Nightingale Ranges showing the Cretaceous units of study in this area. Dots on the map denote field sites associated with each of the units.

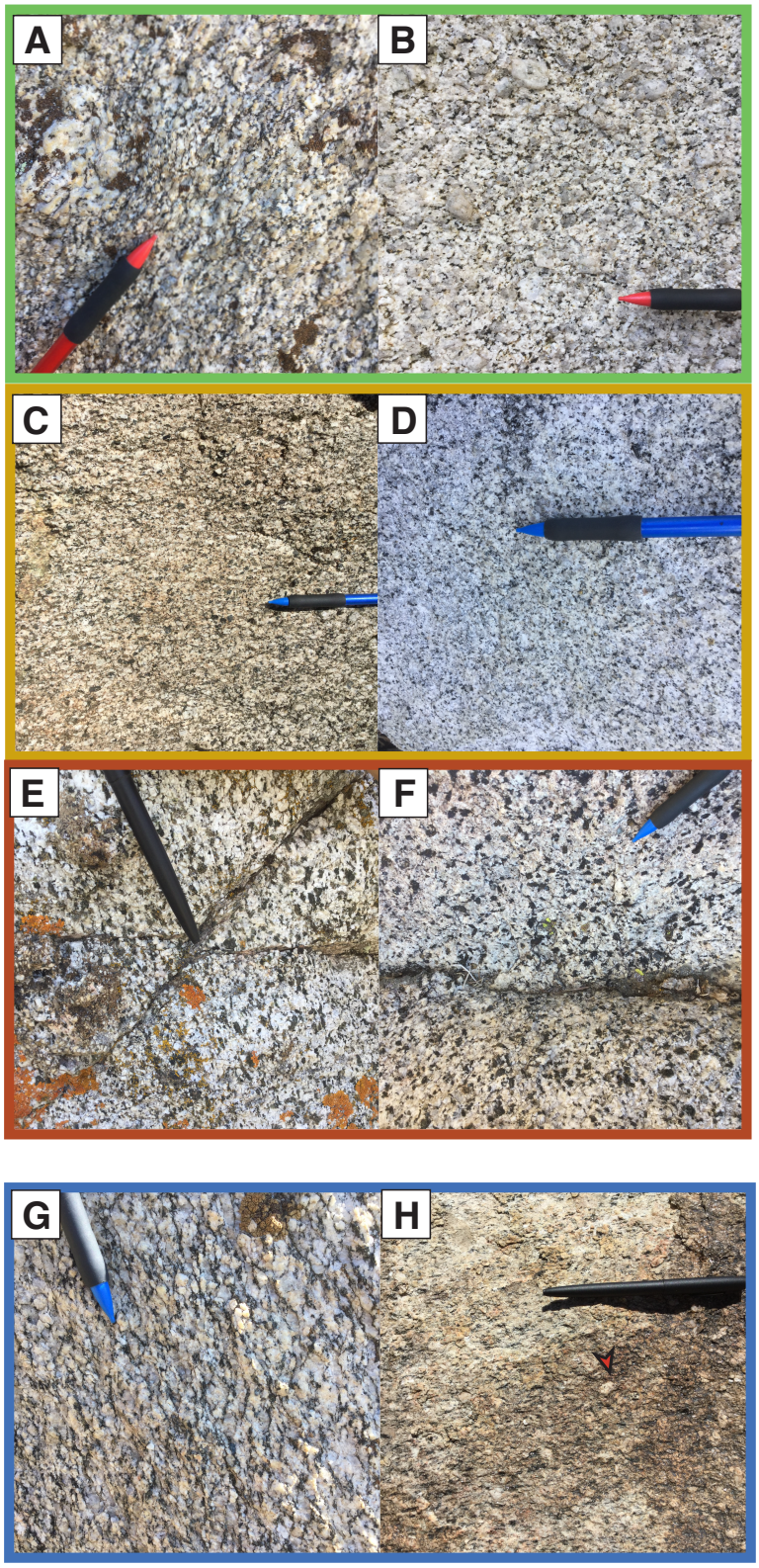
A
B
C
D
E
F
G
H

Figure 6. Field photographs of the observed fabrics in the Sahwave granodiorite (green), the granodiorite of Bob Spring (yellow), the granodiorite of Juniper Pass (red), and the Power Line intrusive unit (blue). A) A strong submagmatic fabric is preserved in the Sahwave granodiorite as indicated by the alignment of mafic minerals, elongate quartz parallel to the foliation and wrapping of potassium feldspar megacrysts. B) An example of the weak magmatic fabric also observed within the Sahwave granodiorite. The mafic minerals are poorly aligned and do not wrap around potassium feldspar phenocrysts. C) A site from the granodiorite of Bob Spring that exhibited a measurable alignment of biotite. D) Typical sites from the granodiorite of Bob Spring exhibit no observable mineral fabric within an equigranular matrix. E) The Power Line intrusive complex exhibits a measurable field lineation defined by mafic domains, ribboned quartz, and aligned plagioclase porphyroclasts (pencil points parallel to the plunge. F) In the horizonal plane plagioclase sigma clasts exhibit dextral shear sense.

Figure 7. Simplified geologic map, hand-sample, and photomicrograph from 19SW50.

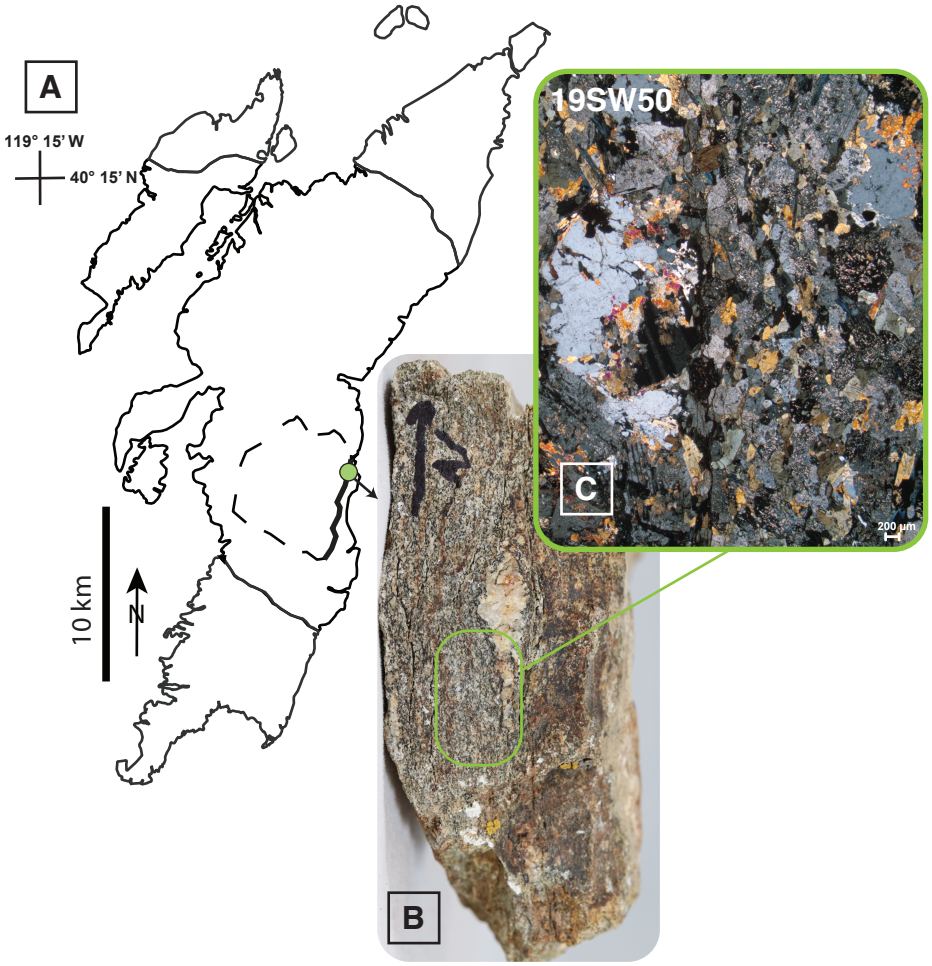

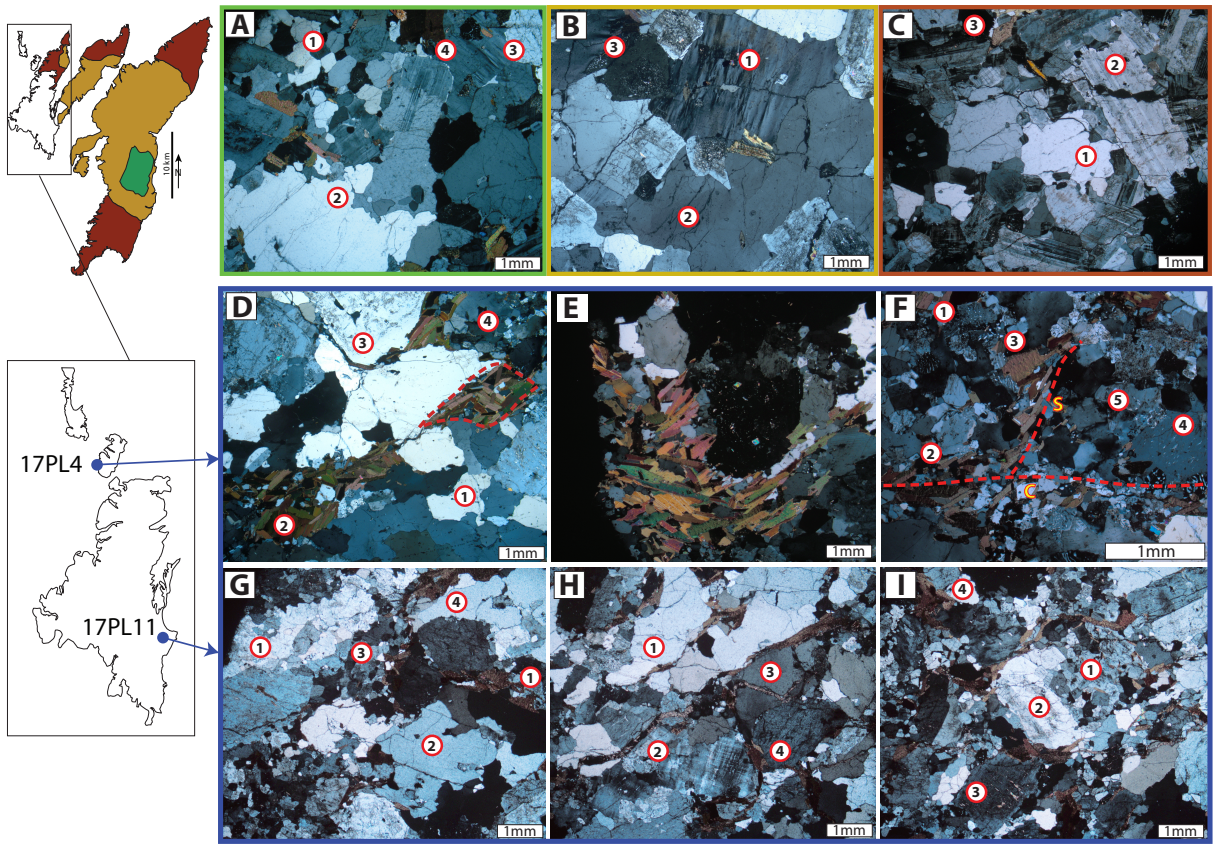

Figure 8. Photomicrographs A-C show representative microstructures for all three units of the Sahwave Range intrusive suite. A) XPL photomicrograph of the Sahwave granodiorite: 1) Domains of smaller quartz grains exhibit a polygonal texture; 2) Large quartz grains show cuspate-lobate grain boundaries and chessboard subgrains indicative of high-temperature deformation (>500-600 °C); 3) Kinked potassium feldspar grain; and 4) A thin film of alkali feldspar rims many plagioclase laths, which is interpreted as evidence for melt presence. Alkali feldspar rim shows cuspate lobate margins around a tabular plagioclase grain. B) XPL photomicrograph of the granodiorite of Bob Springs. Thin section displays a coarse-grained matrix and: 1) Kinked potassium feldspar; 2) Checkerboard extinction in quartz grains; 3) Myrmektic texture nucleating along the margins of potassium feldspar. C) XPL photomicrograph of the granodiorite of Juniper Pass contains euhedral magmatic grains of titanite, plagioclase, potassium feldspar, and quartz. Microstructures include: 1) Bulging recrystallization of quartz grains; 2) Abundant crack seal features in plagioclase grains; and 3) Partially recrystallized magmatic titanite in a recrystallized feldspar domain that shows grain size reduction.

Photomicrographs D-E show the spectrum of representative microstructures for rocks belonging to the Power Line intrusive complex. The location of 17PL4 (D-F) is from the western margin and the location of 17PL11 (G-I) is more towards the interior and eastern region of the unit. D-F exhibit a high temperature solid-state fabric defined by recrystallized quartz ribbons and rounded, partially recrystallized feldspars (A3/A4), and fully recrystallized biotite (A2). Recrystallized quartz grains are large with amoeboidal to polygonal grain boundaries (A1). Large, recrystallized biotite exhibit kinking, and smaller recrystallized biotite show book sliding textures indicating dextral shear (B2/B3). Feldspar is also finely recrystallized on sides of phenocrysts that are aligned with lineation (B4). Recrystallized biotite domains also exhibit a higher birefringence, indicative of higher iron content. G-I exhibit near-solidus submagmatic fabric defined by polyphase aggregates of recrystallized quartz and feldspar (E3/1) of large grain size and amoeboidal grain boundaries (E2). Some quartz and feldspar grains are more finely recrystallized on the sides of phenocrysts aligned with lineation (G1/3). Feldspars that have fractures infilled with biotite and quartz that provide evidence for an earlier submagmatic history (F3). Plagioclase and alkali feldspar with tartan twinning are fully recrystallized along with quartz (F4/2) and myrmekite texture occurs adjacent to plagioclase feldspar. The Power Line intrusive complex is absent of observable oxides.

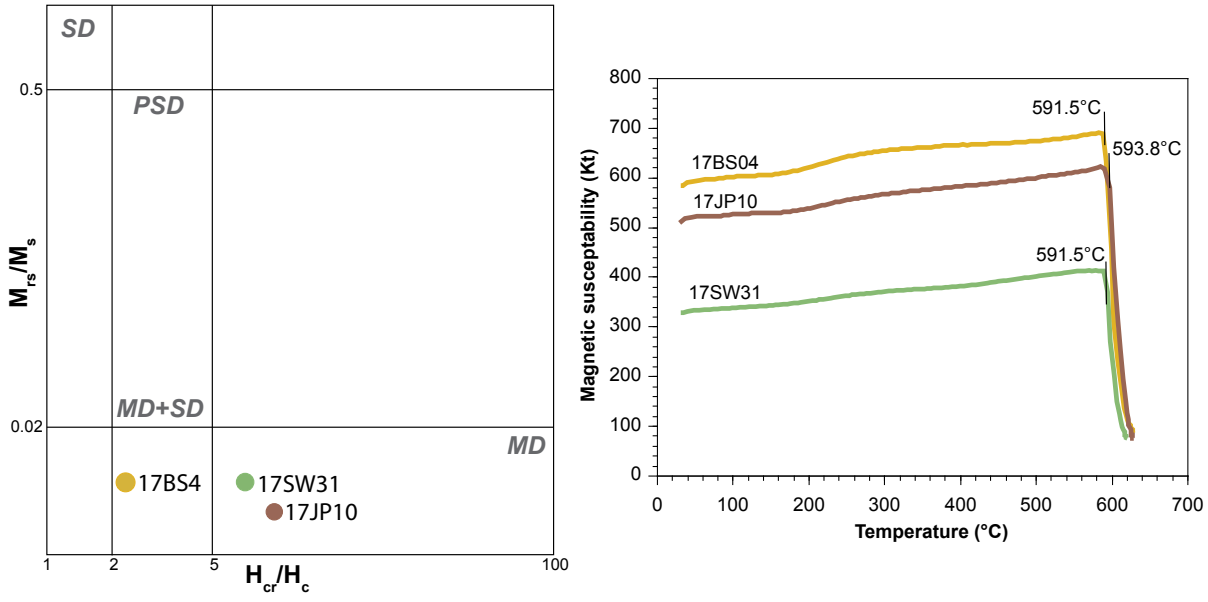

Figure 9. Day Plot and temperature susceptibility plot of representative samples from each of the three units from the Sahwave Range intrusive suite.

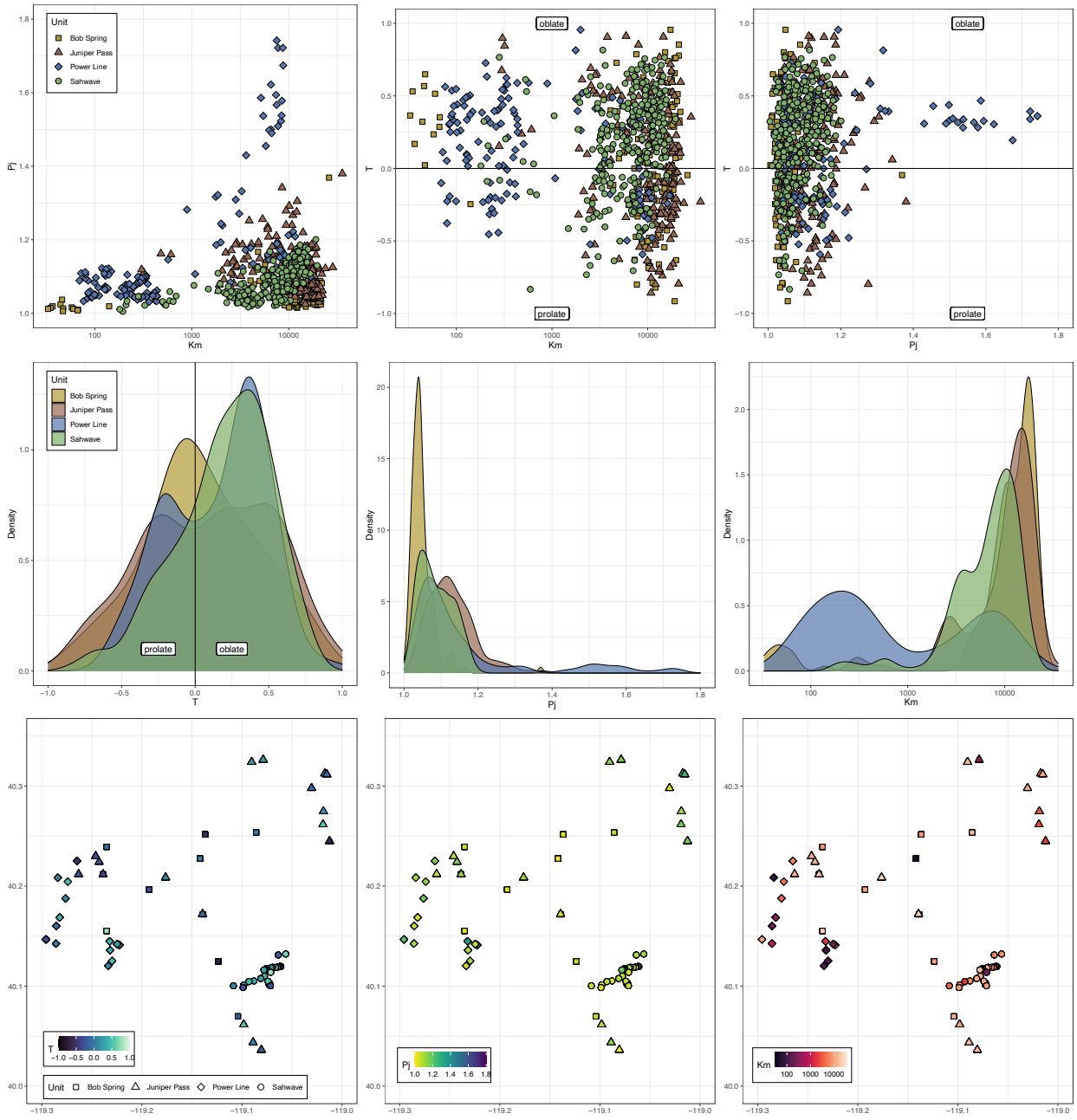

Figure 10. A summary of AMS parameter results. For A-C, grey points are individual core specimens. A) Bulk susceptibility versus anisotropy degree Pj shows that the majority of the Sahwave Range intrusive suite units with higher susceptibility samples have a clustered low range of anisotropies. Samples from the Power Line intrusive complex yields a different pattern. Low and high susceptibility samples show predominately lower degree Pj with several sites with higher susceptibilities yielding higher Pj values. B) Bulk susceptibility versus shape

parameter T shows do not show a clear pattern other than populations from the Power Line intrusive complex are distinct from the highly cluster units of the Sahwave Range intrusive suite. C) Anisotropy degree versus shape parameter T shows that there is no strong dependency of shape on anisotropy degree. D) Probability density function plot of shape parameter T, plot of shape anisotropy colored by unit. All units have somewhat similar maxima. The granodiorite of Juniper Pass has a larger spread than the other two units of the Sahwave Range intrusive suite and tends towards plane strain shape. The granodiorite of Bob Spring yields a predominately prolate maxima while the Sahwave granodiorite yields am oblate maxima. The Power Line intrusive complex yields a bimodal pattern with a smaller maxima in the prolate field and large maxima in the oblate field. E) Probability density function plot of shape anisotropy Pj colored by unit. Sahwave Range units have similar maxima with the granodiorite of Bob Spring yielding the least amount of anisotropy. The Power Line intrusive complex yields a larger spread than the rocks of the Sahwave Range intrusive suite. F) Probability density function plot of bulk susceptibility, colored by unit. G) Shape parameter T. Blue colors represent prolate ellipsoids, teal represents plane strain ellipsoids, and white/green indicate prolate ellipsoids. H) Anisotropy parameter Pj. Yellow color represents low anisotropy, purple color indicates high anisotropy. I) Mean susceptibility. Dark reds indicate low susceptibilities in the paramagnetic field, red color indicates high susceptibility in the ferromagnetic field. The scale is log (bulk susceptibility).

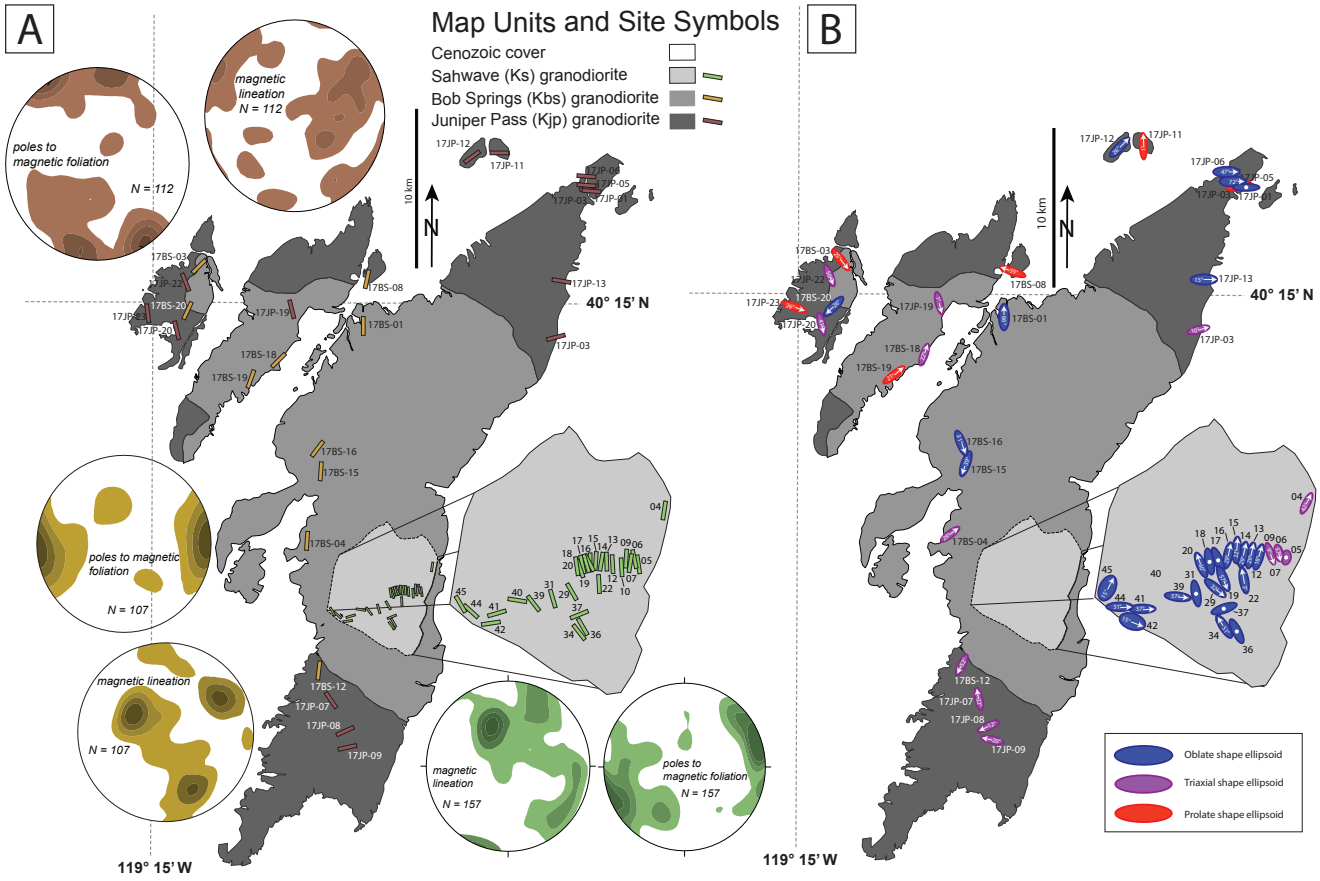

Figure 11. Summary of spatial distribution of interpreted foliation (A) and lineation (B) from mean AMS ellipsoids for the Sahwave Range intrusive suite. Equal area projections of poles to foliation and lineation are plotted with shaded Kamb contours colored according to unit. Kamb contours are σ = 3, 6, 9, 12, 15, and 18.

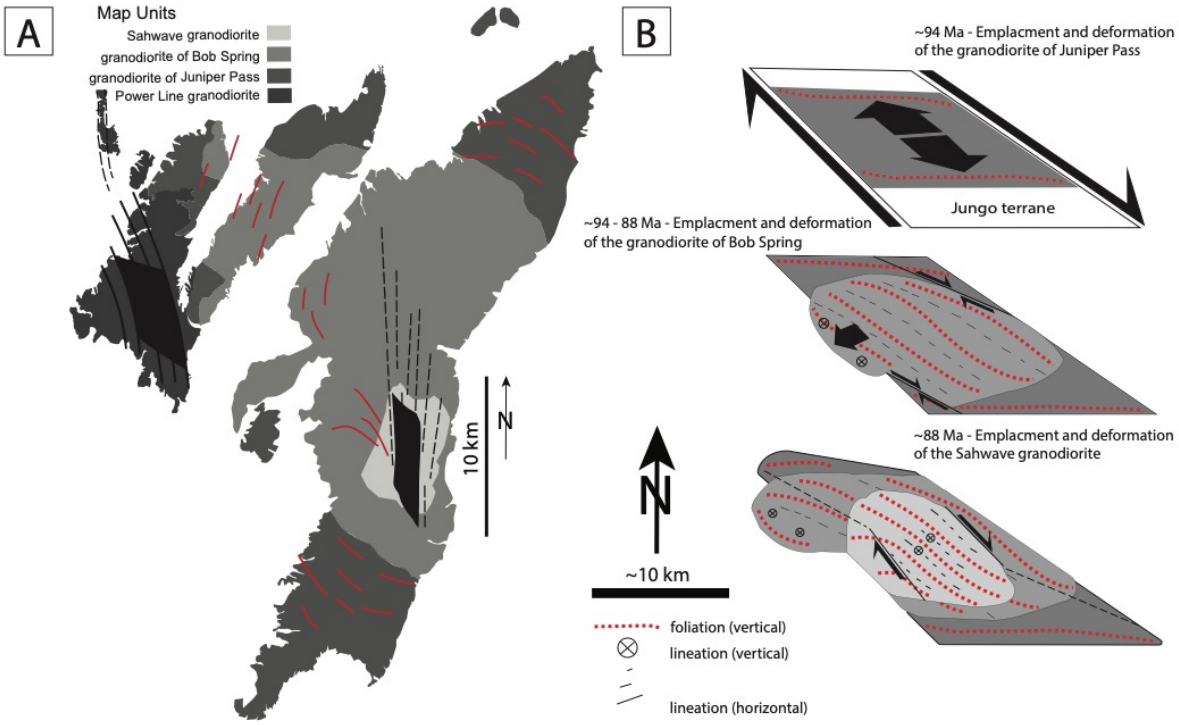

Figure 12. A) Summary illustration of the internal structure of the Sahwave Range intrusive suite and the Power Line intrusive complex, interpreted from AMS foliations and lineations. Red lines indicate magmatic textures and black lines indicate solid-state fabric textures. B) A three-step emplacement evolution of the Sahwave Range intrusive suite. See text for explanation.

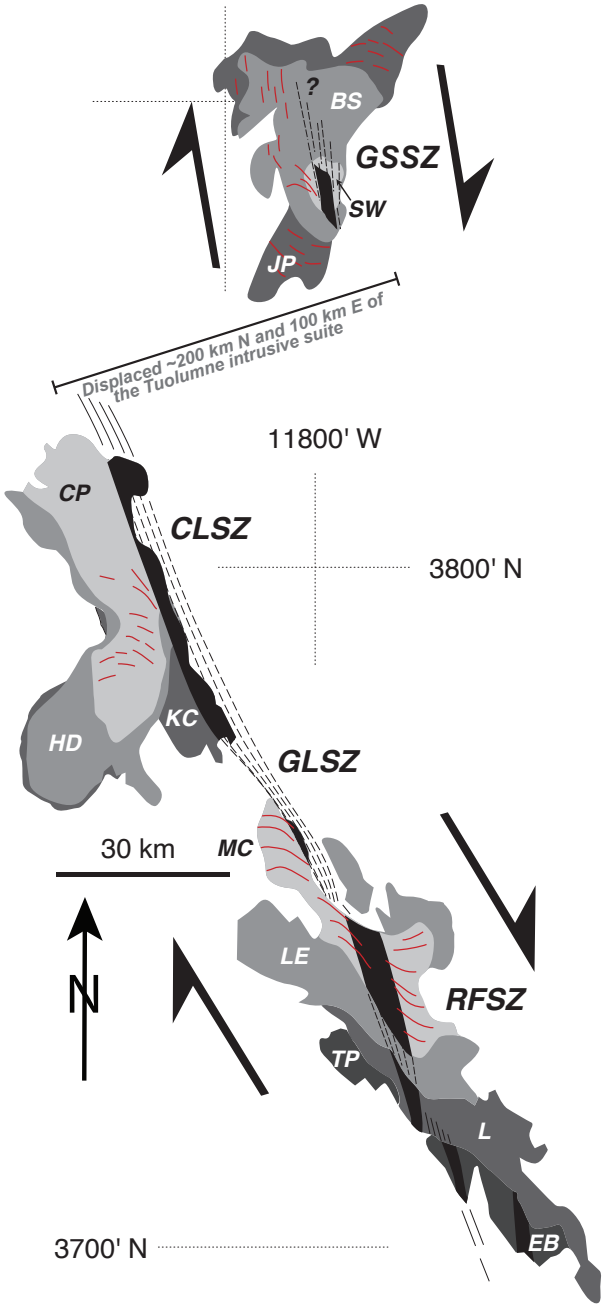

Figure 13. Dextral shearing along the Sierra Crest shear zone system, including the Sahwave Range, Tuolumne, and Mono Pass intrusive suites. Plutons include SW, Sahwave, BS Bob Spring, JP, Juniper Pass, CP, Cathedral Peak; HD, Half Dome; KC, Kuna Crest; RVG, Round Valley Peak; MC, Mono Creek; LE, Lake Edison; L, Lamarck; TP, Turret Peak; EB, Evolution Basin. Shear zones include GSSZ, Granite Springs, CLSZ, Cascade Lake; GLSZ, Gem Lake; and RFSZ, Rosy Finch.

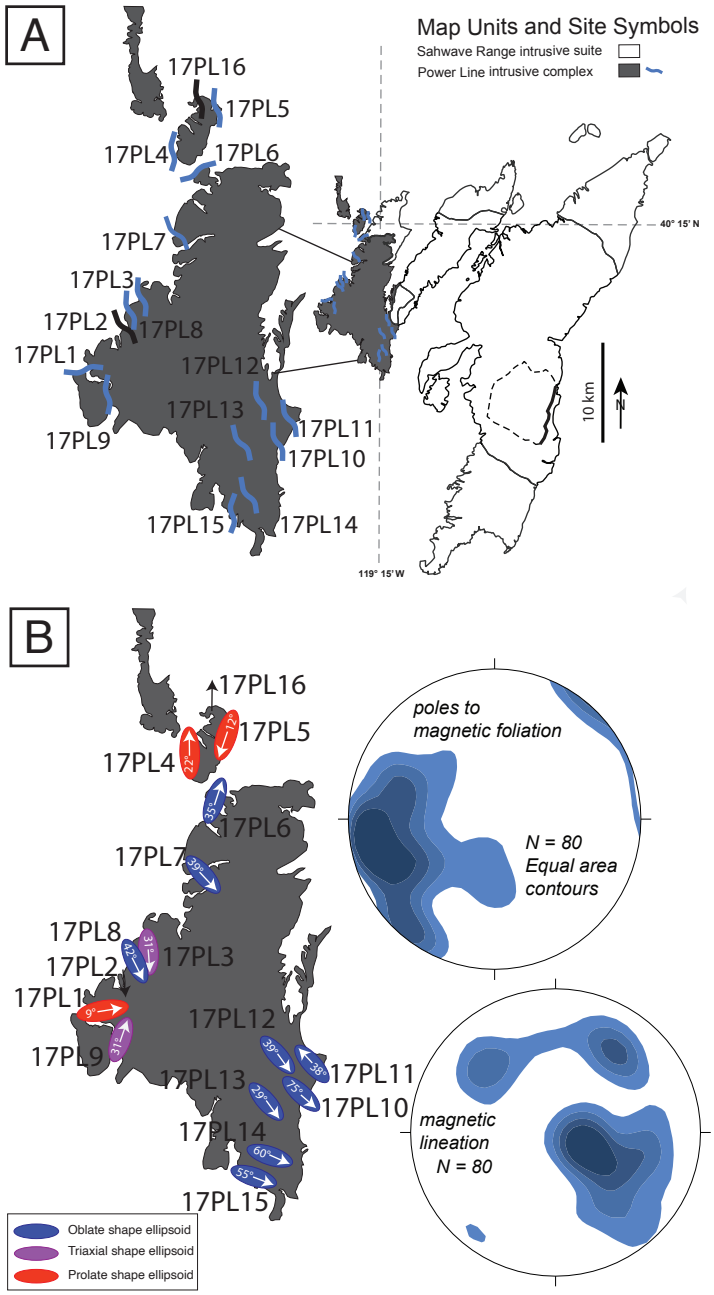

Figure 14. Summary of spatial distribution of interpreted foliation (A) and lineation (B) from mean AMS ellipsoids at each site from the Power Line intrusive complex. Equal area projections of poles to foliation and lineation are plotted with shaded Kamb contours. Kamb contours are σ = 3, 6, 9, 12, 15,and 18. The western margin reveal a steeply dipping, north–south foliation, with lineations that plunge steeply toward the south. The eastern margin yields a more northwest-southeast steeply dipping foliation and lineations that plunge moderately to steeply to the southeast.

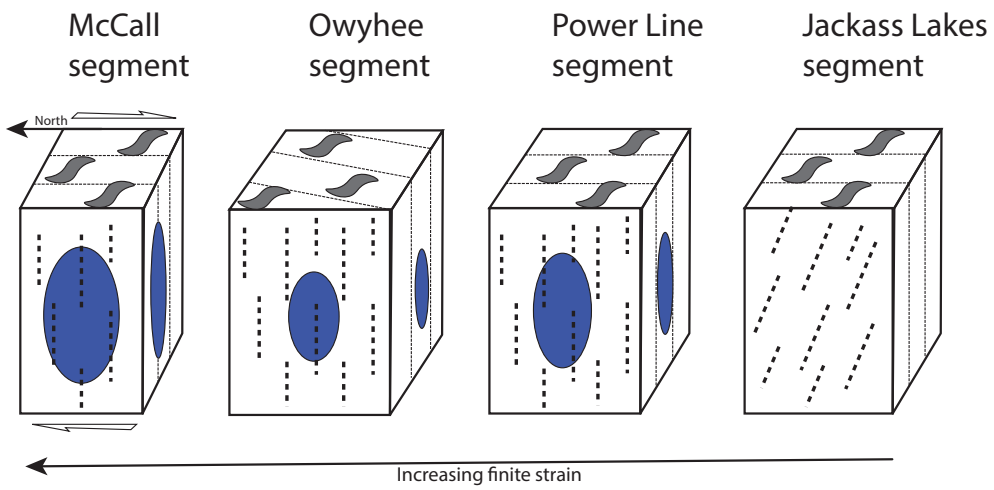

Figure 15. Cartoon block diagrams of the different segments of 100 Ma deformation from Idaho, Nevada, and California. Dashed lines represent lineation, solid lines represent foliation. Dextral shear indicators are observed in the horizontal plane in all segments. The blue ellipse represents the magnitude of anisotropy recorded in the segments, except for the Jackass Lakes segment which does not have anisotropy data.

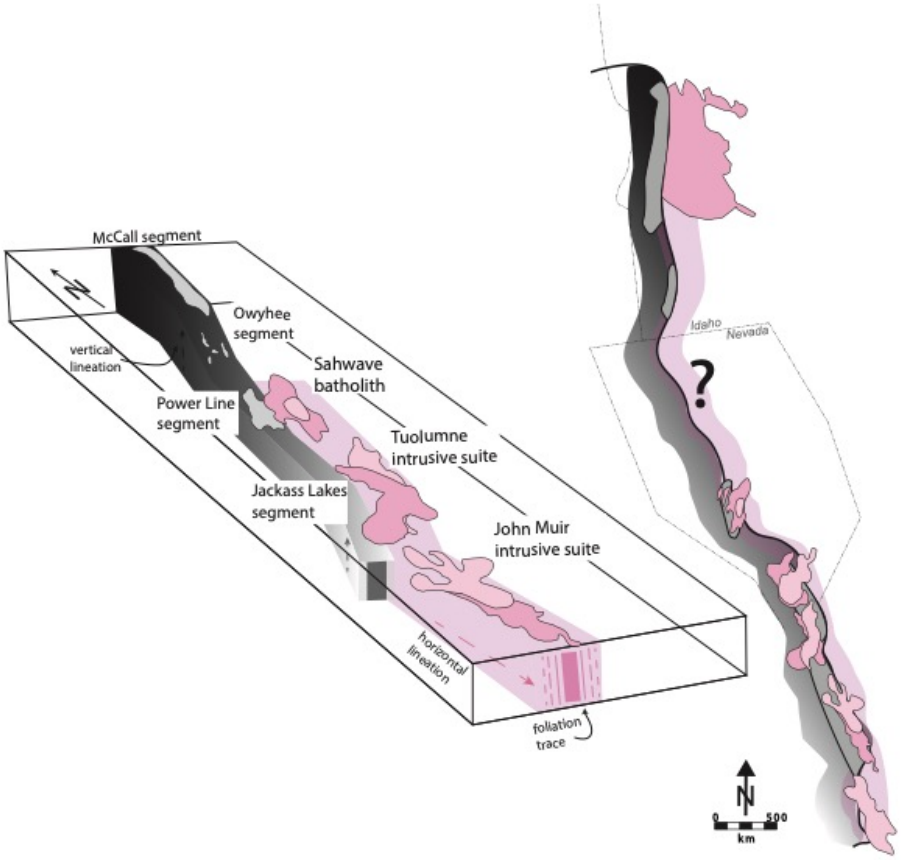

Figure 16. Generalized reconstructed geologic map of the Cretaceous for the central section of the North America Cordillera. Shaded grey to black region represents mid–Cretaceous deformation along the continental margin with finite strain increasing to the north as indicated by the darker shading. Light grey units are representative of the scarce plutons with evidence for pure shear dominated transpression. The pink regions are those associated with a more distributed simple shear dominated transpression associated with the Late Cretaceous Sierra Nevada arc. A three-dimensional sketch shows the regional variations in transpression of the two systems including the main McCall segment of the WISZ, the Owyhee segment of the WISZ, and the Power Line deformation, but also extending further south to the western side of the Sierra Nevada batholith with the Jackass Lakes segment. The pink region to the east illustrates the simple shear dominated transpression associated with the Sierra Crest shear zone and the northward extent into Nevada. Note that width of shear zones is not to scale.

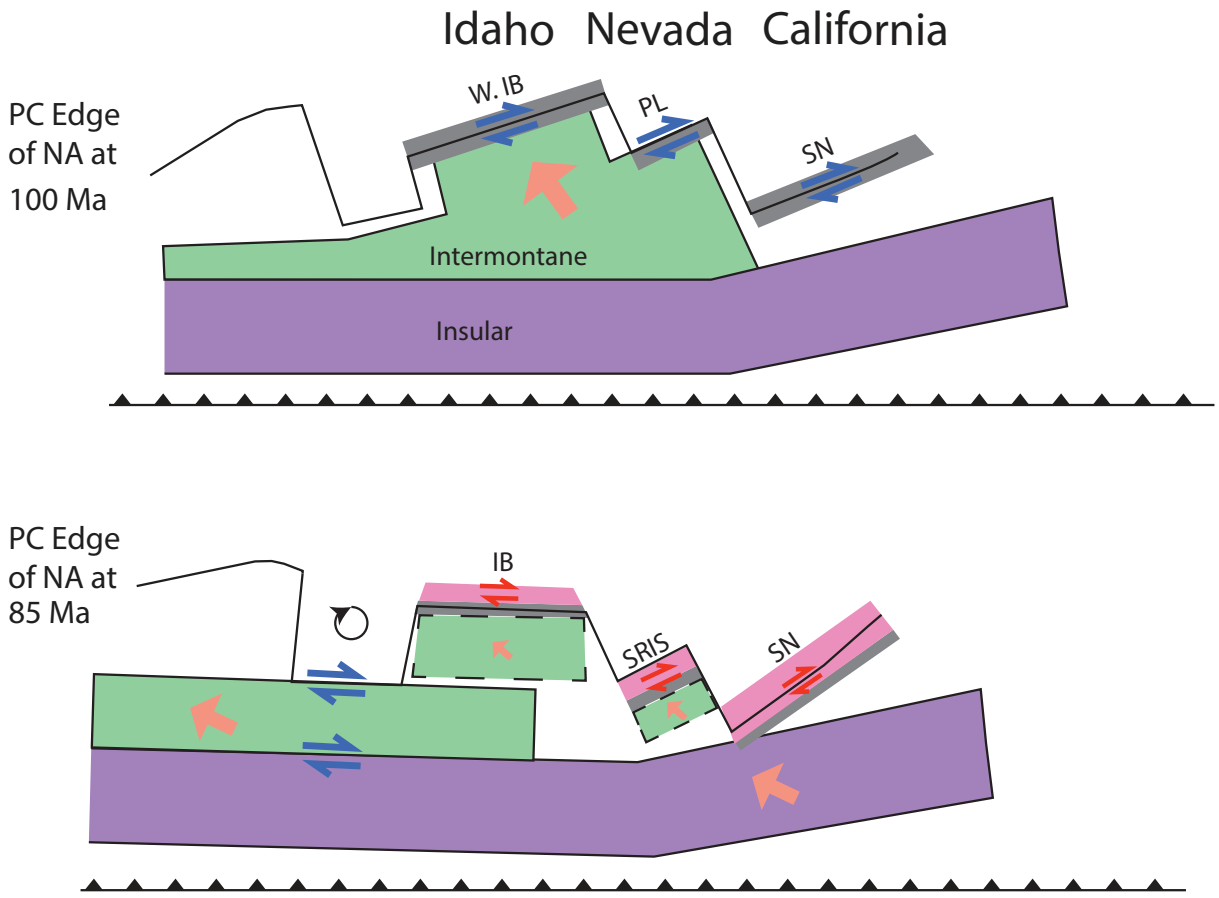

Figure 17. Generalized reconstructed geologic map illustrating the timeline for Cretaceous magma emplacement and deformation at 100 and 88 Ma for the central section of the North America Cordillera. Shaded grey boxes represent the emplacement of mid–Cretaceous granites and the deformation preserved in those segments along the continental margin as a result of Intermontane terrane collision. Blue shear arrows indicate pure shear dominated transpression. The pink regions are those associated with a more distributed simple shear dominated transpression (red shear arrows) associated with the Late Cretaceous arc magmatism as the Intermontane and Insular terranes move north along the margin. Black rotational arrow demonstrates the observed 20° of clockwise rotation of the Idaho promontory.

TABLE 1. COMPARISON SUMMARY OF LATE CRETACEOUS FABRICS AND MICROSTRUCTURES FROM THE CENTRAL SIERRA NEVADA AND SAHWAVE RANGE

Unit name	Age (Ma)	Shear Zone	Foliation	Lineation	Microstructures	Interpreted strain field	Reference
Toulomne Intrusive Suite							
Cathedral Peak granodiorite	86	*Cascade Lake*	Steep NW	moderate to steeply plunging	S-C fabrics	Dextral transpression	Tikoff et al., 2005
Johnson Pass prophyry	85	*Cascade Lake*				Dextral transpression	Titus et al., 2010
Half Dome granodiorite	88-89	*Cascade Lake/Gem Lake?*					
Kuna Crest granodiorite	90-91	*Gem Lake*	Steep NW	steepy to moderatly N plunging	S-C fabrics	Dextral transpression	Greene and Schweickert, 1995; Tikoff and Greene, 1997
John Muir Intrusive Suite							
Mono Creek granodiorite	88	*Rosy Finch*	steep NNW	moderatly shallowly N plunging	hypersolidus-subsolidus foliations, S-C fabrics	Wrench dominated dextral transpression	Tikoff and Teyssier, 1992; de Saint Blanquat and Tikoff, 1998; Tikoff and de Saint Blanquat
Silver Pass porphyry	84	*Rosy Finch*			hypersolidus-subsolidus foliations, S-C fabrics	Wrench dominated dextral transpression	Titus et al., 2010
Sahwave Range intrusive suite							
Sahwave granodiorite	88	*?*	Steep NNW	steepy to moderatly N plunging	magmatic to subsolidus fabrics	Wrench dominated dextral transpression	This study; Van Buer and Miller 2010
granodiorite of Bob Spring	94	*?*	Steep NNW	steepy to moderatly N plunging	magmatic to subsolidus fabrics	Wrench dominated dextral transpression	This study; Van Buer and Miller 2010
granodiorite of Juniper Pass	94	*?*	Steep E-W	No lineation	magmatic to subsolidus fabrics	Wrench dominated dextral transpression/ contractional	This study; Van Buer and Miller 2010

TABLE 2. COMPARISON SUMMARY OF CRETACEOUS FABRICS AND MICROSTRUCTURES FROM THE CENTRAL SIERRA NEVADA, THE NIGHTINGALE RANGE, AND THE WESTERN IDAHO SHEAR ZONE

Unit name	Deformation Age (Ma)	Shear Zone	Foliation	Lineation	Microstructures	Interpreted strain field	Reference
Sierra Nevada Batholith							
Jackass Lakes granodiorite	98	*Sing Lake*	Steep NW	moderate, north-plunging	from near-solidus to subsolidus deformation mechanisms	Dextral transpression	Krueger, 2005; Krueger and Yoshinobu, 2018
Dinkey Creek pluton	102	*Courtright-Wishon*	Steep NW	?	mylonitic and ultramylonitic fabrics superimposed on a magmatic foliation	contractional deformation	Tobisch et al., 1995
Shart Hair Creek pluton	Pre-90	*Courtright-Wishon*	Steep NW	?	mylonitic and ultramylonitic fabrics superimposed on a magmatic foliation	contractional deformation	Tobisch et al., 1996
Lost Peak pluton	Pre 90	*Courtright-Wishon*	Steep NW	?	mylonitic and ultramylonitic fabrics superimposed on a magmatic foliation	contractional deformation	Tobisch et al., 1997
Nighingale Range							
Power Line intrusive complex	104-96	*?*	Steep NW-SE, Steep N-S	steeply to moderatly N plunging	hypersolidus-subsolidus foliations, S-C fabrics	Pure shear, dextral transpression	This study; Van Buer and Miller 2010
Idaho Batholith							
Crevice pluton	104; 98-96	*western Idaho (McCall segment)*	N-S and dips steeply to the east	vertical - steeply N plunging	hypersolidus-subsolidus foliations, S-C fabrics	Pure shear, dextral transpression	Gray et al., 2012; Braudy et al., 2017
Hazard Creek Complex	98-96	*western Idaho (McCall segment)*	N-S and dips steeply to the east	vertical - steeply N plunging	hypersolidus-subsolidus foliations, S-C fabrics	Pure shear, dextral transpression	Harrigan, 2022: Giorgis et al., 2008
Little Goose Creek Complex	98-97	*western Idaho (McCall segment)*	N-S and dips steeply to the east	vertical - steeply N plunging	hypersolidus-subsolidus foliations, S-C fabrics	Pure shear, dextral transpression	Harrigan, 2022: Giorgis et al., 2009
Payette River Tonalite	98-98	*western Idaho (McCall segment)*	N-S and dips steeply to the east	vertical - steeply N-S plunging	hypersolidus-subsolidus foliations, S-C fabrics	Pure shear, dextral transpression	Harrigan, 2022: Giorgis et al., 2010
Owyhee Mountains	?	*western Idaho (Owyhee segment)*	NE, dips steeply to the east	vertical - steeply N plunging	hypersolidus-subsolidus foliations, S-C fabrics	Pure shear, dextral transpression	Benford et al., 2010
Sawtooth metamorphic complex	95-92	*western Idaho*	Steep N-S	?	solid-state fabrics	Pure shear, dextral transpression	Ma et al., 2017

7. References

Armstrong, R.L., 1988, Mesozoic and Early Cenozoic magmatic evolution of the Canadian Cordillera, in Clark, S.P., Jr., Burchfiel, B.C., and Suppe, J., Processes in Continental Lithospheric Deformation: Geological Society of America Special Paper 218, p. 55–92, https://doi.org/10.1130/SPE218-p55.

Ague, J.J., and Brimhall, G.H., 1988, Regional variations in bulk chemistry, mineralogy, and the compositions of mafic and accessory minerals in the batholiths of California: Geological Society of America Bulletin, v. 100, p. 912–927, https://doi.org/10.1130/0016- 7606(1988)1002.3.CO;2.

Andronicos, C.L., Hollister, L.S., Davidson, C. and Chardon, D., 1999, Kinematics and tectonic significance of transpressive structures within the Coast plutonic complex, British Columbia: Journal of Structural Geology, v. 21, p. 229-243.

Atwater, T., and Stock, J., 1998, Pacific–North America plate tectonics of the Neogene southwestern United States; an update, in Ernst, W.G., and Nelson, C.A., eds., Integrated Earth and Environmental Evolution of the Southwestern United States: The Clarence A. Hall, Jr. Volume: Columbia, Maryland, Bellwether Publishing, p. 375–402, https://doi.org/ 10.1080/00206819809465216.

Bateman, P.C., 1992, Plutonism in the Central Part of the Sierra Nevada Batholith, California: U.S. Geological Survey Professional Paper 1483, https://doi.org/10.3133/pp1483, scale: 1:250,000.

Benford, B., Crowley, J., Schmitz, M., Northrup, C.J. and Tikoff, B., 2010. Mesozoic magmatism and deformation in the northern Owyhee Mountains, Idaho: Implications for along-zone variations for the western Idaho shear zone. Lithosphere, 2(2), pp.93-118.

Bouchez, J.L., Delas, C., Gleizes, G., N´ed´elec, A., Cuney, M., 1992. Submagmatic microfractures in granites. Geology 20 (1), 35. https://doi.org/10.1130/0091-7613 (1992)0202.3.CO;2.

Bouchez, J.L., Gleizes, G., Djouadi, T., and Rochette, P., 1990. Microstructure and magnetic susceptibility applied to emplacement kinematics of granites: The example of the foix pluton (French Pyrenees): Tectonophysics, v. 184, p. 157–171. https://doi.org/10.1016/0040-1951(90)90051-9

Bouchez, J.L., 1997. Granite is Never Isotropic: An Introduction to AMS Studies of Granitic Rocks. In Granite: From Segregation of Melt to Emplacement Fabrics. Petrology and Structural Geology (Vol. 8). Springer.

Braudy, N., Gaschnig, R.M., Wilford, D., Vervoort, J.D., Nelson, C.L., Davidson, C., Kahn, M.J., and Tikoff, B., 2017, Timing and deformation conditions of the western Idaho shear zone,

West Mountain, west-central Idaho: Lithosphere, v. 9, no. 2, p. 157–183, https://doi.org/10.1130/L519.1.

Bürgman, R., and Pollard D., 1994**, Strain accommodated about strike-slip fault discontinuities in granitic rock under brittle-to-ductile conditions**: J. Struct. Geol., v. 16, p. 1655-1674.

Busby, C., 2022, The Guerrero-Alisitos-Vizcaino superterrane of western Mexico and its ties to the Mexican continental margin (Gondwana and SW Laurentia), in Whitmeyer, S.J., Williams, M.L., Kellett, D.A., and Tikoff, B., eds., Laurentia: Turning Points in the Evolution of a Continent: Geological Society of America Memoir 220, https://doi.org/10.1130/2022.1220(XX).

Busby-Spera, C.J., and Saleeby, J.B., 1990, Intra-arc strike-slip fault exposed at batholithic levels in the southern Sierra Nevada, California: Geology, v. 18, p. 255–259, https://doi.org/10.1130/0091-7613(1990)018<0255:IASSFE>2.3.CO;2.

Cao, W., Paterson, S., Memeti, V., Mundil, R., Anderson, J.L., and Schmidt, K., 2015, Tracking paleodeformation fields in the Mesozoic central Sierra Nevada arc: Implications for intra-arc cyclic deformation and arc tempos: Lithosphere, v. 7, p. 296–320, https://doi.org/10.1130/L389.1.

Chen, J.H., and Moore, J.G., 1982, Uranium-lead isotopic ages from the Sierra Nevada Batholith, California: Journal of Geophysical Research, v. 87, p. 4761–4784, https://doi.org/10.1029/JB087iB06p04761.

Clennett, E.J., Sigloch, K., Mihalynuk, M.G., Seton, M., Henderson, M.A., Hosseini, K., Mohammadzaheri, A., Johnston, S.T., and Müller, R.D., 2020, A quantitative tomotectonic plate reconstruction of western North America and the eastern Pacific Basin: Geochemistry, Geophysics, Geosystems, v. 21, e2020GC009117, https://doi.org/10.1029/2020GC009117.

Coleman, D.S., Gray, W., and Glazner, A.F., 2004, Rethinking the emplacement and evolution of zoned plutons: Geochronologic evidence for incremental assembly of the Tuolumne Intrusive Suite, California: Geology, v. 32, p. 433–436, https://doi.org/10.1130/G20220.1.

Coleman, D.S., and Glazner, A.F., 1997, The Sierra Crest magmatic event: Rapid formation of juvenile crust during the Late Cretaceous in California: International Geology Review, v. 39, p. 768–787, https://doi.org/10.1080/00206819709465302.

Criss, R.E., and Fleck, R.J., 1987, Petrogenesis, geochronology, and hydrothermal systems of the northern Idaho batholith and adjacent areas based on 18O/16O, D/H, $^{87}Sr/^{86}Sr$, K-Ar, and $^{40}Ar/^{39}Ar$ studies, *in* Vallier, T.L. and Brooks, H.C. eds., Geology of the Blue Mountains region of Oregon, Idaho, and Washington: The Idaho batholith and its border zone, U.S. Geological Survey Professional Paper 1436, p. 95–138.

De Saint Blanquat, M., Tikoff, B., Teyssier, C., and Vigneresse, J.-L., 1998, Transpressional kinematics and magmatic arcs, in Holdsworth, R.E., Strachan, R.A., and Dewey, J.F., eds.,

Continental Transpressional and Transtensional Tectonics: Geological Society, London, Special Publication 135, p. 327–340, https://doi.org/10.1144/GSL.SP.1998.135.01.21

Dickinson, W.R., 2004, Evolution of the North American Cordillera: Annual Review of Earth and Planetary Sciences, v. 32, p. 13–45, https://doi.org/10.1146/annurev.earth.32.101802.120257.

Dickinson, W.R., 2008, Accretionary Mesozoic–Cenozoic expansion of the Cordilleran continental margin in California and adjacent Oregon: Geosphere, v. 4, p. 329–353, https://doi.org/10.1130/GES00105.1.

Ducea, M.N., 2001, The California arc: Thick granitic batholiths, eclogitic residues, lithospheric-scale thrusting and magmatic flare-ups: GSA Today, v. 11, p. 4–10, https://doi.org/10.1130/1052-5173(2001)011<0004:TCATGB>2.0.CO;2.

Enkin, R.J., 2006, Paleomagnetism and the case for Baja British Columbia, in Haggart, J.W., Enkin, R.J., and Monger, J.W.H., eds., Paleogeography of the North American Cordillera: Evidence For and Against Large-Scale Displacements: Geological Association of Canada Special Paper 46, p. 233–254.

Everden, J.F., and Kistler, R.W., 1970, Chronology of Emplacement of Mesozoic Batholith Complexes in California and Western Nevada: U.S. Geological Survey Professional Paper 623, 42 p. + 2 pls.

Fleck, R.J., and Criss, R.E., 1985, Strontium and oxygen isotopic variations in Mesozoic and Tertiary plutons of central Idaho: Contributions to Mineralogy and Petrology, v. 90, p. 291–308, doi:10.1007/BF00378269.

Fossen, H., and Tikoff, B., 1993, The deformation matrix for simultaneous simple shearing, pure shearing and volume change, and its application to transpression-transtension tectonics: Journal of Structural Geology, v. 15, p. 413–422, https://doi.org/10.1016/0191- 8141(93)90137-Y.

Gaschnig, R.M., Vervoort, J.D., Lewis, R.S., and McClelland, W.C., 2010, Migrating magmatism in the northern US Cordillera: In situ U-Pb geochronology of the Idaho batholith: Contributions to Mineralogy and Petrology, v. 159, p. 863–883, doi:10.1007/s00410–009–0459–5.

Gaschnig, R.M., Vervoort, J.D., Lewis, R.S., and Tikoff, B., 2011, Isotopic evolution of the Idaho batholith and Challis intrusive province, northern U.S. Cordillera: Journal of Petrology, v. 52, p. 2397–2429, https://doi.org/10.1093/petrology/egr050.

Gaschnig, R.M., Vervoort, J.D., Tikoff, B., and Lewis, R.S., 2017, Construction and preservation of batholiths in the northern U.S. Cordillera: Lithosphere, v. 9, p. 315–324, https://doi.org/10.1130/L497.1.

Giorgis, S., McClelland, W., Fayon, A., Singer, B.S., and Tikoff, B., 2008, Timing of deformation and exhumation in the western Idaho shear zone, McCall, Idaho: Geological Society of America Bulletin, v. 120, no. 9–10, p. 1119–1133, https://doi.org/10.1130/B26291.1.

Giorgis, S., Tikoff, B., and McClelland, W.C., 2005, Missing Idaho arc: Transpressional modification of the $^{87}Sr/^{86}Sr$ transition on the western edge of the Idaho batholith: Geology, v. 33, p. 469-472, https://doi.org/10.1130/g20911.1.

Glazner, A.F., Bartley, J.M. and Carl, B.S., 1999, Oblique opening and noncoaxial emplacement of the Jurassic Independence dike swarm, California: Journal of Structural Geology, v. 21, p. 1275-1283.

Greene, D.C., 1995, Stratigraphy, structure and tectonic significance of the northern Ritter Range Pendant, eastern Sierra Nevada, California [Ph.D. thesis]: Reno, Nevada, USA, University of Nevada.

Greene, D.C., and Schweickert, R.A., 1995, The Gem Lake shear zone; Cretaceous dextral transpression in the northern Ritter Range pendant, eastern Sierra Nevada, California: Tectonics, v. 14, p. 945–961, https://doi.org/10.1029/95TC01509.

Harrigan, C.O., Trevino, S.F., Schmitz, M.D., and Tikoff, B., 2021, Titanite petrochronology dates shear zone initiation to between 99 and 96 Ma in the Western Idaho shear zone: Geological Society of America Abstracts with Programs, v. 53, no. 6, paper 127-5, https://doi.org/10.1130/abs/2021AM-369987.

Hildebrand, R.S., and Whalen, J.B., 2021a, The mid-Cretaceous Peninsular Ranges orogeny: A new slant on Cordilleran tectonics? I: Mexico to Nevada: Canadian Journal of Earth Sciences, v. 58, no. 8, p. 670–696, https://doi.org/10.1139/cjes-2020-0154.

Hildebrand, R.S., and Whalen, J.B., 2021b, The mid-Cretaceous Peninsular Ranges orogeny: A new slant on Cordilleran tectonics? II: Northern United States and Canada: Canadian Journal of Earth Sciences, v. 58, no. 8, p. 697–719, https://doi.org/10.1139/cjes-2021-0006.

Hirt, W. H., 2007, Petrology of the Mount Whitney Intrusive Suite, eastern Sierra Nevada, California: Implications for the emplacement and differentiation of composite felsic intrusions. Geological Society of America Bulletin, 119, 1185–1200.

Hrouda, F., 2010, Modelling relationship between bulk susceptibility and AMS in rocks consisting of two magnetic fractions represented by ferromagnetic and paramagnetic minerals - Implications for understanding magnetic fabrics in deformed rocks: Journal of the Geological Society of India, v. 75(1), p. 254–266

Hrouda, F., 2004, Problems in interpreting AMS parameters in diamagnetic rocks: Geological Society Special Publication, v. 238, p. 49–59

Hrouda, F., and Kahan, S., 1991, The magnetic fabric relationship between sedimentary and basement nappes in the High Tatra Mountains, N. Slovakia: Journal of Structural Geology, v. 13, i. 4, p. 431-442, ISSN 0191-8141, https://doi.org/10.1016/0191-8141(91)90016-C.

Hrouda, F., 1982, Magnetic anisotropy of rocks and its application in geology and geophysics. Geophysical Surveys, v. 5, p. 37–82. https://doi.org/10.1007/BF01450244

Hrouda, F. 1986, The effect of quartz on the magnetic anisotropy of quartzite. Studia Geophysica et Geodetica, v. 30, p. 39-45.

John, D. A., and Robinson, A. C., 1982, Granitic Rocks in the Triassic-Jurassic Magmatic Arc of Western Nevada and Eastern California. U.S. Geological Survey Professional Paper P1375.

Kistler, R.W., Chappell, B.W., Peck, D.L., and Bateman, P.C., 1986, Isotopic variation in the Tuolumne intrusive suite, central Sierra Nevada, California: Contributions to Mineralogy and Petrology, v. 94, p. 205–220, https://doi.org/10.1007/BF00592937.

Kistler, R.W., 1990, Two different lithosphere types in the Sierra Nevada, California, in Anderson, J.L., ed., The Nature and Origin of Cordilleran Magmatism: Geological Society of America Memoir 174, p. 271–282, https://doi.org/10.1130/MEM174-p271.

Krueger, R.J., and Yoshinobu, A., 2018, Structures in the Jackass Lakes pluton–host-rock system, central Sierra Nevada, California, and inferred mid-Cretaceous Farallon–North America plate kinematics: Geological Society of America Bulletin, v. 130, p. 1940–1958, https://doi.org/10.1130/B31992.1.

Kuntz, M.A., 2007, The Idaho Batholith near McCall, Idaho—Field Relations, Petrology, Major-Element Chemistry, Emplacement History, and Magma Genesis, *in* Kuntz, M.A. and Snee, L.W. eds., Geological Studies of the Salmon River Suture Zone and Adjoining Areas, West-Central Idaho and Eastern Oregon, p. 123–161.

Lackey, J.S., Cecil, M.R., Windham, C.J., Frazer, R.E., Bindeman, I.N., and Gehrels, G.E., 2012, The Fine Gold intrusive suite: The roles of basement terranes and magma source development in the Early Cretaceous Sierra Nevada batholith: Geosphere, v. 8, p. 292–313, https://doi.org/10.1130/GES00745.1.

Leopold, M.B., 2016, Structure, construction, and emplacement of the Late Cretaceous Sonora Pass intrusive suite: Central Sierra Nevada batholith, California [M.S. thesis]: San José, California, San José State University, 100 p.

Lewis, R.S., Kiilsgaard, T.H., Bennett, E.H., and Hall, W.E., 1987, Lithologic and chemical characteristics of the central and southeastern part of the southern lobe of the Idaho Batholith, *in* Vallier, T.L. and Brooks, H.C. eds., Geology of the Blue Mountains region of Oregon, Idaho,

and Washington; the Idaho batholith and its border zone, U.S. Geological Survey Professional Paper 1436, p. 171–196.

Lund, K., and Snee, L.W., 1988, Metamorphism, structural development, and age of the continent-island arc juncture in west-central Idaho, *in* Ernst, W.G. ed., Metamorphism and Crustal Evolution of the Western United States, Englewood Cliffs, NJ, Prentice-Hall, Rubey, v. 7, p. 296–331.

Lupe, R., and Silberling, N.J., 1985, Genetic relationship between lower Mesozoic continental strata of the Colorado Plateau and marine strata of the western Great Basin: Significance for accretionary history of Cordilleran lithotectonic terranes, in Howell, D.G., ed., Tectonostratigraphic Terranes of the Circum-Pacific Region: Circum-Pacific Council for Energy and Mineral Resources, Earth Science Series, no. 1, p. 263–271.

Ma, C., Foster, D.A., Mueller, P.A., and Dutrow, B.L., 2017, Magma-facilitated transpressional strain partitioning within the Sawtooth metamorphic complex, Idaho: A zone accommodating Cretaceous orogen-parallel translation in the Idaho batholith: Tectonics, v. 36, p. 444–465, https://doi.org/10.1002/2016tc004264.

Manduca, C.A., Kuntz, M.A., and Silver, L.T., 1993, Emplacement and deformation history of the western margin of the Idaho batholith near McCall, Idaho: Influence of a major terrane boundary: Geological Society of America Bulletin, v. 105, p. 749–765.

Manduca, C.A., Silver, L.T., and Taylor, H.P., 1992, $^{87}Sr/^{86}Sr$ and $^{18}O/^{16}O$ isotopic systematics and geochemistry of granitoid plutons across a steeply-dipping boundary between contrasting lithospheric blocks in western Idaho: Contributions to Mineralogy and Petrology, v. 109, p. 355–372, https://doi.org/10.1007/bf00283324.

Manduca, C.A., 1988, Geology and geochemistry of the oceanic arc-continent boundary in the western Idaho Batholith near McCall [Ph.D. thesis]: California Institute of Technology, 272 p.

Martel, S. J., Pollard, D. D. & Segall, P. 1988. Development of simple strike-slip fault zones, Mount Abbot quadrangle, Sierra Nevada, California. Bull. geol. Soc. Am. 100, 1451-1465.

Matthews, K.J., Seton, M., and Müller, R.D., 2012, A global-scale plate reorganization event at 105–100 Ma: Earth and Planetary Science Letters, v. 355–356, p. 283–298, https://doi.org/10.1016/j.epsl.2012.08.023.

Maxson, J., and Tikoff, B., 1996, A hit-and-run model for the Laramide orogeny, western United States: Geology, v. 24, p. 968–972, https://doi.org/10.1130/0091- 7613(1996)0242.3.CO;2.

Memeti, V., Paterson, S., Matzel, J., Mundil, R., and Okaya, D., 2010, Magmatic lobes as "snapshots" of magma chamber growth and evolution in large, composite batholiths: An example from the Tuolumne intrusion, Sierra Nevada, California: Bulletin of the Geological Society of America, v. 122, p. 1912–1931, https://doi.org/10.1130/B30004.1.

McClelland, W.C., Tikoff, B., and Manduca, C.A., 2000, Two-phase evolution of accretionary margins: Examples from the North American Cordillera: Tectonophysics, v. 326, p. 37–55, https://doi.org/10.1016/S0040-1951(00)00145-1.

McNulty, B.A., 1995, Shear zone development during magmatic arc construction: The Bench Canyon shear zone, central Sierra Nevada, California: Geological Society of America Bulletin, v. 107, p. 1094–1107, https://doi.org/10.1130/0016- 7606(1995)1072.3.CO;2.

McNulty, B.A., Tobisch, O.T., Cruden, A.R., and Gilder, S., 2000, Multistage emplacement of the Mount Givens Pluton, central Sierra Nevada Batholith, California: Geological Society of America Bulletin, v. 112, p. 119-135.

McQuarrie, N., and Wernicke, B.P., 2005, An animated tectonic reconstruction of southwestern North America since 36 Ma: Geosphere, v. 1, p. 147–172, https://doi.org/10.1130/GES00016.1.

Michels, Z.D., Kruckenberg, S.C., Davis, J.R., and Tikoff, B., 2015, Determining vorticity axes from grain-scale dispersion of crystallographic orientations: Geology, v. 43, p. 803–806, https://doi.org/10.1130/g36868.1.

Nadin, E.S., 2007, Structure and History of the Kern Canyon Fault System, Southern Sierra Nevada, California [Ph.D. thesis]: Pasadena, California Institute of Technology, 297 p.

Oldow, J.S., 1984, Evolution of a Late Mesozoic back-arc fold and thrust belt, Northwestern Great Basin, U.S.A.: Tectonophysics, v. 102, p. 245–274, https://doi.org/10.1016/0040-1951(84)90016-7.

Pryer, L.L., Robin, P.-Y.F., 1995, Retrograde metamorphic reactions in deforming granites and the origin of flame perthite: Journal of Metamorphic Geology, v. 14, p. 645–658.

Pryer, L.L., Robin, P.-Y.F., 1996. Differential stress control on the growth and orientation of flame perthite: a palaeostress-direction indicator: Journal of Structural Geology, v. 18, p. 1151–1166.

Quinn, M.J., Wright, J.E., and Wyld, S.J., 1997, Happy Creek igneous complex and tectonic evolution of the early Mesozoic arc in the Jackson Mountains, northwest Nevada: Geological Society of America Bulletin, v. 109, p. 461–482, https://doi.org/10.1130/0016-7606(1997)1092.3.CO;2.

Rochette, P., 1987, Magnetic susceptibility of the rock matrix related to magnetic fabric studies: Journal of Structural Geology, v. 9., p. 1015-1020.

Saleeby, J. B., 1981, Ocean floor accretion and volcanoplutonic arc evolution of the Mesozoic Sierra Nevada, California, in Ernst W.G., ed. In Geotectonic Development of California: Rubey Vol. 1, p. 132–181, Prentice-Hall, New York.

Saleeby, J.B., and Dunne, G., 2015, Temporal and tectonic relations of early Mesozoic arc magmatism, southern Sierra Nevada, California, in Anderson, T.H., Didenko, A.N., Johnson, C.L., Khanchuk, A.I., and MacDonald, J.H.Jr,, eds., Late Jurassic Margin of Laurasia—A Record of Faulting Accommodating Plate Rotation: Geological Society of America Special Paper 513, p. 223–268, doi:10.1130/2015.2513(05).

Schmidt, K.L., and Paterson, S.R., 2002, A doubly vergent, fan structure in the Peninsular Ranges batholith: Transpression or complex flow along a crustal-scale discontinuity?: Tectonics, v. 21, 1050, https://doi.org/10.1029/2001TC001353.

Segall, P., McKee, E.H., Martel, S.J., and Turrin, B.D., 1990, Late Cretaceous age of fractures in the Sierra Nevada batholith, California: Geology, v. 18, p. 1248–1251.

Sharp, W.D., Tobisch, O.T., and Renne, P.R., 2000, Development of Cretaceous transpressional cleavage synchronous with batholith emplacement, central Sierra Nevada, California: Geological Society of America Bulletin, v. 112, p. 1059–1066, doi: 10.1130/0016- 7606(2000)1122.3.CO;2.

Sigloch, K., and Mihalynuk, M.G., 2017, Mantle and geological evidence for a Late Jurassic−Cretaceous suture spanning North America: Geological Society of America Bulletin, v. 129, p. 1489–1520, https://doi.org/10.1130/B31529.1.

Silberling, N.J., Jones, D.L., Blake, M.C., Jr., and Howell, D.G., 1987, Lithotectonic Terrane Map of the Western Conterminous United States: U.S. Geological Survey Miscellaneous Field Studies Map 1874-C, scale 1:2,500,000, 20-p. pamphlet and map.

Snow, C.A., and Scherer, H., 2006, Terranes of the Western Sierra Nevada Foothills Metamorphic Belt, California: A Critical Review, International Geology Review, v. 48:1, p. 46-62, DOI: 10.2747/0020-6814.48.1.46.

Stevens, C.H., and Greene, D.C., 1999, Stratigraphy, depositional history, and tectonic evolution of Paleozoic continental-margin rocks in roof pendants of the eastern Sierra Nevada, California: Geological Society of America Bulletin, v. 111, p. 919–933, doi: 10.1130/0016-7606(1999)1112.3.CO;2.

Taubeneck, W.H., 1971, Idaho Batholith and Its Southern Extension: Geological Society of America Bulletin, v. 82, p. 1899–1928, https://doi.org/10.1130/0016-7606(1971)82[1899:ibaise]2.0.co;2.

Tikoff, B., Davis, M.R., Teyssier, C., de St. Blanquat, M., Habert, G., and Morgan, S., 2005, Fabric studies within the Cascade Lake shear zone, Sierra Nevada, California: Tectonophysics, v. 400, p. 209–226, https://doi.org/10.1016/j.tecto.2005.03.003.

Tikoff, B., Kelso, P., Manduca, C., Markley, M.J., and Gillaspy, J., 2001, Lithospheric and crustal reactivation of an ancient plate boundary: The assembly and disassembly of the Salmon

River suture zone, Idaho, USA, in Holdsworth, R.E., Strachan, R.A., Magloughlin, J.F., and Knipe, R.J., eds., The Nature and Tectonic Significance of Fault Zone Weakening: Geological Society, London, Special Publication 186, p. 213–231, https://doi.org/10.1144/GSL.SP.2001.186.01.13.

Tikoff, B., and de Saint Blanquat, M., 1997, Transpressional shearing and strike-slip partitioning in the Late Cretaceous Sierra Nevada magmatic arc, California: Tectonics, v. 16, no. 3, p. 442–459, https://doi.org/10.1029/97TC00720.

Tikoff, B., and Greene, D., 1997, Stretching lineations in transpressional shear zones: An example from the Sierra Nevada batholith, California: Journal of Structural Geology, v. 19, p. 29–39, https://doi.org/10.1016/S0191-8141(96)00056-9.

Tikoff, B., & Teyssier, C., 1994, Strain and fabric analyses based on porphyroclast interaction: Journal of Structural Geology, v. 16, p. 477–491.

Tikoff, B., and Fossen, H., 1993, Simultaneous pure and simple shear: the unified deformation matrix: Tectonophysics, v. 217, p. 267 – 283.

Tikoff, B., and Teyssier, C., 1992, Crustal-scale, en echelon "P-shear" tensional bridges: A possible solution to the batholithic room problem: Geology, v. 20, p. 927–930, https://doi.org/10.1130/0091-7613(1992)020<0927:CSEEPS>2.3.CO;2.

Tikoff, B., Teyssier, C., and St. Blanquat, M., 1998, Nucleation, growth and structural development of mylonitic shear zones in granitic rocks: discussion and reply: Journal of Structural Geology, v. 20, p. 1795-1799, doi: 10.1016/S0191-8141(98)00086-8.

Tikoff, B., Housen, B.A., Maxson, J.A., Nelson, E.M., Trevino, S., Shipley, T.F., 2022, Hit- and-run model for Cretaceous–Paleogene tectonism along the western margin of Laurentia, *in* Whitmeyer, S.J., Williams, M.L., Kellett, D.A., Tikoff, B., eds., Laurentia: Turning Points in the Evolution of a Continent: Geological Society of America Memoir 220. https://doi.org/10.1130/2022.1220(32).

Titus, S.J., Clark, R., Tikoff, B., 2005. Geologic and geophysical investigation of two finegrained granites, Sierra Nevada Batholith, California: evidence for structural controls on emplacement and volcanism: Geological Society of America Bulletin, v. 117, p. 1256-1271. https://doi.org/ 10.1130/B25689.1.

Tobisch, O. T., Saleeby, J.B., Renne, P.R., McNulty, B., and Wong, T., 1995, Variations in deformation fields during development of a large-volume magmatic arc, central Sierra Nevada, California. Geological Society of America Bulletin, v. 107, p. 148-166.

Tommasi, A., Vauchez, A., Fernandes, L.A.D., and. Porcher, C.C., 1994, Magma-assisted strain localization in an orogen-parallel transcurrent shear zone of southern Brazil: Tectonics, v. 13, p. 421-437

Torres Andrade, E., and Tikoff, B,, 2022. Microstructural evidence of kinematics in the mid-Cretaceous Courtright-Wishon Shear Zone, Central Sierra Nevada Batholith, California: Geological Society of America Cordillera Meeting Abstracts with Programs, v. 54, no. 2, p. 34.

Trevino, S.F., Tikoff, B., Van Buer, N., Wyld, S.J., and McLachlan, H., 2021, Exploring the emplacement of Cretaceous arc granites and dextral shear zones in northwestern Nevada, USA, using the StraboSpot data system, in Florsheim, J., Koeberl, C., McKay, M.P., and Riggs, N., and., Field Excursions from the 2021 GSA Section Meetings: Geological Society of America Field Guide 61, p. 1–31, https://doi.org/10.1130/2021.0061(10).

Van Buer, N.J., and Miller, E.L., 2010, Sahwave batholith, NW Nevada: Cretaceous arc flare-up in a basinal terrane: Lithosphere, v. 2, p. 423–446, https://doi.org/10.1130/L105.1.

Wernicke, B., and Snow, J.K., 1998, Cenozoic tectonism in the central Basin and Range: Motion of the Sierran–Great Valley block: International Geology Review, v. 40, p. 403–410, https://doi.org/10.1080/00206819809465217.

Wesnousky, S.G., Barron, A.D., Briggs, R.W., Caskey, S.J., Kumar, S., and Owen, L., 2005, Paleoseismic transect across the northern Great Basin: Journal of Geophysical Research, v. 110, B05408, https://doi.org/10.1029/2004JB003283.

Wolf, D.E., Andronicos, C.L., Vervoort, J.D., Mansfield, M.R., and Chardon, D., 2010, Application of Lu–Hf garnet dating to unravel the relationships between deformation, metamorphism and plutonism: An example from the Prince Rupert area, British Columbia: Tectonophysics, v. 485, p. 62-77, https://doi.org/10.1016/j.tecto.2009.11.020.

Wood, D.J., and Saleeby, J.B., 1998, Late Cretaceous–Paleocene extensional collapse and disaggregation of the southernmost Sierra Nevada batholith: International Geology Review, v. 39, p. 973–1009.

Wyld, S.J., 1990, Paleozoic and Mesozoic rocks of the Pine Forest Range, northwest Nevada, and their relation to volcanic arc assemblages of the western U.S. Cordillera, in Harwood, D.S., and Miller, M.M., eds., Late Paleozoic and Early Mesozoic Paleogeographic Relations: Klamath Mountains, Sierra Nevada, and Related Rocks: Geological Society of America Special Paper 255, p. 219–237, https://doi.org/10.1130/SPE255-p219.

Wyld, S.J., 1996, Early Jurassic deformation in the Pine Forest Range, northwest Nevada, and implications for Cordilleran tectonics: Tectonics, v. 15, p. 566–583, https://doi.org/10.1029/95TC03693.

Wyld, S.J., 2000, Triassic evolution of the arc and backarc of northwest Nevada, and evidence for extensional tectonism, in Soreghan, M.J., and Gehrels G.E., eds., Paleozoic and Triassic

Paleogeography and Tectonic Evolution of Western Nevada and Northern California: Geological Society of America Special Paper 347, p. 185–208, https://doi.org/10.1130/0-8137-2347-7.185.

Wyld, S.J., and Wright, J.E., 2001, New evidence for Cretaceous strike-slip faulting in the United States Cordillera and implications for terrane-displacement, deformation patterns, and plutonism: American Journal of Science, v. 301, p. 150–181, https://doi.org/10.2475/ajs.301.2.150.

Wyld, S.J., 2002, Structural evolution of a Mesozoic back-arc fold-thrust belt in the U.S. Cordillera; new evidence from northern Nevada: Geological Society of America Bulletin, v. 114, p. 1452–1468, https://doi.org/10.1130/0016-7606(2002)114<1452:SEOAMB>2.0.CO;2.

Wyld, S.J., Wright, J.E., Kinsella, M.E., and Warren, M.B., 2007, Identification of a distinct terrane in the Cordillera that is offset along the Early Cretaceous dextral MSNI fault system: Geological Society of America Abstracts with Programs, v. 39, no. 4, p. 81.

Wyld, S.J., and Wright, J.E., 2019, Allochthonous Paleozoic–Jurassic terranes of NW Nevada and SE Oregon displaced dextrally from the southwest Cordillera in the Early Cretaceous. Where is their homeland?: Geological Society of America Abstracts with Programs, v. 50, no. 5, https://doi.org/10.1130/abs/2018RM-313792.</jrn>

Zen, E., and Hammarstrom, J.M., 1984, Magmatic epidote and its petrologic significance: Geology, v. 12, p. 515–518.

Appendix

U-Pb Geochronology

Methods

We dated five zircon samples to constrain the ages of pluton crystallization for the three granodiorite units of the Sahwave Range intrusive suite and the Power Line intrusive complex. The five samples were collected following an EW transect and were then separated, mounted, and imaged using cathodoluminescence. We then selected >250 spots for LA-ICPMS. Zircon chemistry and U-Pb dates were measured LA-ICPMS using a ThermoElectron X-Series II quadrupole ICPMS and New Wave Research UP-213 Nd:YAG UV (213 nm) laser ablation system at Boise State University. In-house analytical protocols, standard materials, and data reduction software were used for acquisition and calibration of U-Pb dates and a suite of high field strength element and rare earth elements. Zircon grains were ablated with a laser spot of 25 μm wide (fluence: 5 J/cm^2; pulse rates:10 Hz; analysis time: 45 s) that excavated a ~25 μm deep pit. Background count rates were obtained prior to each analysis and subtracted from the raw count rate. Data from ablation pits that intersected glass or mineral inclusions were identified based on Ti and P signal excursions and were not utilized in the analyses. If the U-Pb ratios appear to have been unaffected by the inclusions, the U-Pb dates were considered valid. For U-Pb and $^{207}Pb/^{206}Pb$ dates, instrumental fractionation of the background-subtracted ratios were corrected and dates calibrated with respect to zircon standards and reference materials. The geochronologic methods for this study are full described in Macdonald et al. (2018).

Results

Laser ablation-inductively coupled plasma-mass spectroscopy (LA-ICP-MS) yielded a U-Pb zircon age of ca. 88 Ma from two samples (17SW-20, 17SW-40). Zircon grains from the Sahwave granodiorite display significant oscillatory and sector zoning and many grains contain inherited cores (Supplementary Fig. 1B). Probability density plots show a narrow distribution of ages for zircon from the two Sahwave granodiorite samples, which overlap significantly and both yield maxima at 87 Ma (Supplementary Fig. 1A).

Zircons from the granodiorite of Bob Spring are similar to those of the Sahwave granodiorite in that they display significant oscillatory zoning and sector zoning and abundant inherited cores. LA-ICP-MS zircon ages of the granodiorite of Bob Spring (17BS-1) suggest a crystallization age of ca. 95 Ma (Supplementary Fig. 1A). The U-Pb zircon ages (SHRIMP and LA-ICP-MS) suggest that the Juniper Pass granodiorite was emplaced synchronously or even after the granodiorite of Bob Spring (94.7 Ma). LA-ICP-MS zircon ages from the granodiorite of Juniper Pass (17JP-7) indicate that this unit is slightly younger than the granodiorite of Bob Spring, with a crystallization age of ca. 93.5 Ma (Supplementary Fig. 1A). Probability density plots show a slightly larger distribution of ages for zircon and the two curves overlap significantly from the granodiorite of Bob Spring and the granodiorite of Juniper Pass samples. However, the uncertainties for these new ages are still large, and high-resolution U-Pb geochronology is needed to resolve the emplacement history of these units. (Supplementary Fig. 1A).

LA-ICP-MS analyses were conducted on zircon separates from 17PL-3, yielding a U-Pb zircon age of 106 Ma. Zircons from the Power Line intrusive complex are visibly distinct from the highly zoned zircons of the Sahwave units, with very little zoning, and large zircon crystals showing some possible metamorphic rims (Supplementary Fig. 1B). Probability density plots

show a slightly broader distribution of ages for zircon from the Power Line intrusive complex samples. Older ages could be indicative of inheritance, whereas the small peak of younger ages at ~94 Ma could be a result of metamorphism (Supplementary Fig. 1A).

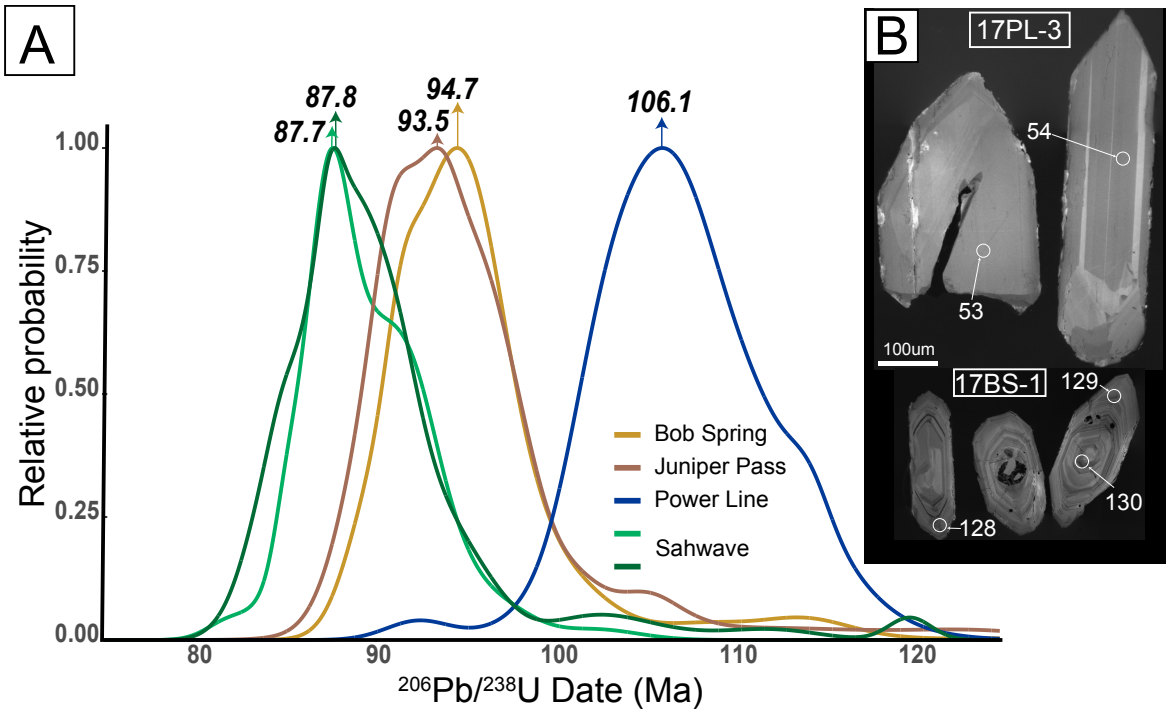

Supplementary Figure 1. (A) U-Pb zircon ages from in situ laser ablation-inductively coupled plasma-mass spectroscopy (LA-ICP-MS). (B) Cathodoluminescence images of representative zircons from the Power Line intrusive complex and the Granodiorite of Bob Spring. White numbers indicate the spot locations; circles represent the spot size. All units from the Sahwave Range intrusive suite contain zircon with magmatic oscillatory zoning. Zircon from the Power Line intrusive complex display less oscillatory zoning, with some grains showing metamorphic rims.

Supplementary Table S1.

COMPILED ANISOTROPY OF MAGNETIC SUSCEPTIBILITY DATA FROM THE SAHWAVE AND NIGHTINGALE RANGES

Name	UNIT	Km	Pj	T	LOCATION X	LOCATION Y	K3dec	K3inc	K1dec	K1inc
17BS-01_A1	Bob Spring	18451.98	1.041	0.34	40.22753	-119.14187	90.9	9.2	209.9	71.6
17BS-01_A2	Bob Spring	19147.37	1.048	0.117	40.22753	-119.14187	104.1	2.1	8.1	70.5
17BS-01_A3	Bob Spring	15044.6	1.03	-0.221	40.22753	-119.14187	253.1	5.6	9	77.4
17BS-01_B1	Bob Spring	19506.08	1.052	0.359	40.22753	-119.14187	243.7	11.8	357.8	62.9
17BS-01_B2	Bob Spring	17750.73	1.05	0.336	40.22753	-119.14187	266.2	4.9	356.6	4.1
17BS-01_B3	Bob Spring	19199.06	1.062	0.347	40.22753	-119.14187	272.2	20	167.1	35.5
17BS-01_C1	Bob Spring	17258.21	1.033	0.289	40.22753	-119.14187	86.7	2.7	188	76.5
17BS-01_C2	Bob Spring	17323.06	1.048	0.956	40.22753	-119.14187	91.7	13.1	201.9	55.9
17BS-01_C3	Bob Spring	17607.3	1.034	0.532	40.22753	-119.14187	254.9	5.9	346.1	12
17BS-01_C4	Bob Spring	16089.23	1.038	-0.038	40.22753	-119.14187	256.9	7.3	348.5	12.1
17BS-01_D1	Bob Spring	21468.09	1.046	0.331	40.22753	-119.14187	98.9	9.4	4.7	23.8
17BS-01_D2	Bob Spring	16105.39	1.043	-0.114	40.22753	-119.14187	91	10.3	319.7	74.6
17BS-01_D3	Bob Spring	16163.67	1.073	0.591	40.22753	-119.14187	93.9	2.5	189.3	64.9
17BS-01_D4	Bob Spring	18918.19	1.042	-0.087	40.22753	-119.14187	258.8	3.3	154.7	76.5
17BS-01_E1	Bob Spring	16286.63	1.07	0.741	40.22753	-119.14187	266	25.1	150.6	42.5
17BS-01_E2	Bob Spring	18553.06	1.043	-0.148	40.22753	-119.14187	271	16.8	11.5	31.2
17BS-01_F1	Bob Spring	14552.84	1.053	-0.098	40.22753	-119.14187	55	25.1	247.2	64.4
17BS-01_F2	Bob Spring	14943.89	1.043	-0.544	40.22753	-119.14187	139.9	51.4	321	38.6
17BS-01_F3	Bob Spring	19141	1.066	0.444	40.22753	-119.14187	64.7	27.4	159.5	9.1
17BS-01_G1	Bob Spring	19219.04	1.038	0.656	40.22753	-119.14187	246.5	15.3	125.5	62.1
17BS-01_G2	Bob Spring	17670.34	1.036	0.664	40.22753	-119.14187	219.1	36	99.7	34
17BS-01_G3	Bob Spring	21207.4	1.088	0.853	40.22753	-119.14187	94.9	2	185.2	9.2
17BS-01_G4	Bob Spring	19762.96	1.033	0.073	40.22753	-119.14187	258.8	9.6	32.2	76.2
17BS-01_G5	Bob Spring	17355.9	1.031	0.521	40.22753	-119.14187	255.6	12.3	347.5	8.6
17BS-01_G6	Bob Spring	19835.22	1.022	-0.632	40.22753	-119.14187	95.3	35	207.7	28.5
17BS-01_H1	Bob Spring	17899	1.03	0.608	40.22753	-119.14187	65.7	12.6	171.3	50.1
17BS-01_H2	Bob Spring	18014.48	1.06	-0.048	40.22753	-119.14187	204.9	12.9	311.8	51.7
17BS-03_A	Bob Spring	7958.294	1.038	0.202	40.23924	-119.23522	344.4	62.8	142.7	25.5
17BS-03_B	Bob Spring	7692.581	1.044	-0.142	40.23924	-119.23522	19.7	54.8	146.2	22.7
17BS-03_C	Bob Spring	6332.384	1.042	-0.252	40.23924	-119.23522	56.7	38.6	171.3	27.5
17BS-03_D	Bob Spring	7318.883	1.048	-0.224	40.23924	-119.23522	41	43.7	157	24.6
17BS-03_E1	Bob Spring	7712.646	1.04	-0.8	40.23924	-119.23522	277.2	45.8	170.6	15.5
17BS-03_E2	Bob Spring	7298.934	1.039	-0.63	40.23924	-119.23522	271.7	51.3	158.9	17.3
17BS-03_F1	Bob Spring	7856.4	1.055	-0.331	40.23924	-119.23522	289	55.6	154.4	25.6
17BS-03_F2	Bob Spring	8042.933	1.063	-0.126	40.23924	-119.23522	342.3	56.9	150.9	32.6

17BS-03_G1	Bob Spring	8244.609	1.072	0.104	40.23924	-119.23522	342.5	59.6	139	28.3
17BS-03_H	Bob Spring	8065.124	1.056	-0.087	40.23924	-119.23522	320.7	69.3	159.1	19.7
17BS-04_A1	Bob Spring	16791.35	1.031	-0.146	40.12474	-119.12361	347	56.6	91.1	9.1
17BS-04_A2	Bob Spring	16050.89	1.144	-0.338	40.12474	-119.12361	298.3	44.1	159.6	37.8
17BS-04_A3	Bob Spring	15086.69	1.06	-0.409	40.12474	-119.12361	183.2	47.6	59.8	26.7
17BS-04_B1	Bob Spring	19153.04	1.054	-0.915	40.12474	-119.12361	347.4	27	153.8	62.3
17BS-04_B2	Bob Spring	19090.05	1.047	0.36	40.12474	-119.12361	91.9	4.3	305	84.9
17BS-04_B3	Bob Spring	18760.43	1.026	-0.211	40.12474	-119.12361	275.7	15.3	156.9	60.5
17BS-04_C1	Bob Spring	17115.77	1.11	0.439	40.12474	-119.12361	312.7	40.8	189.6	32.4
17BS-04_C2	Bob Spring	14910.82	1.037	-0.086	40.12474	-119.12361	328	34.4	110.5	49.3
17BS-04_C3	Bob Spring	18747.9	1.023	-0.322	40.12474	-119.12361	245	23.7	35.2	63.1
17BS-04_C4	Bob Spring	17926.72	1.025	0.024	40.12474	-119.12361	196.1	54.1	49.7	31.1
17BS-04_D1	Bob Spring	17297.54	1.033	0.615	40.12474	-119.12361	152.2	16	246.4	14.2
17BS-04_D2	Bob Spring	15044.52	1.058	0.178	40.12474	-119.12361	147.8	46.2	27	26.1
17BS-04_D3	Bob Spring	26032.81	1.369	-0.046	40.12474	-119.12361	250.9	65.3	55.1	23.9
17BS-04_D4	Bob Spring	18138.72	1.056	0.423	40.12474	-119.12361	271.7	45.9	19.2	16.2
17BS-04_E1	Bob Spring	15230.48	1.043	0.801	40.12474	-119.12361	133.9	65.3	349.8	20.5
17BS-04_F1	Bob Spring	9928.43	1.019	-0.136	40.12474	-119.12361	153.1	33.9	59	6.2
17BS-04_F2	Bob Spring	10344.84	1.02	-0.087	40.12474	-119.12361	266	41.3	37.7	37.1
17BS-04_F3	Bob Spring	12526.91	1.022	-0.392	40.12474	-119.12361	262.9	20	139.8	56.3
17BS-04_G1	Bob Spring	7523.125	1.04	-0.471	40.12474	-119.12361	268	26.3	121.2	59.4
17BS-04_G2	Bob Spring	12192.67	1.015	0.016	40.12474	-119.12361	130.2	0.1	220.3	52.9
17BS-04_G3	Bob Spring	13090.88	1.035	-0.661	40.12474	-119.12361	266.5	21.3	156.8	40.8
17BS-04_H1	Bob Spring	10174.65	1.077	-0.645	40.12474	-119.12361	14.4	53.4	280.4	3
17BS-08_A1	Bob Spring	11450.38	1.027	-0.04	40.25168	-119.1367	68.7	23.2	310	48.3
17BS-08_A2	Bob Spring	9826.765	1.037	-0.037	40.25168	-119.1367	113.6	35.5	307.2	53.7
17BS-08_A3	Bob Spring	7033.986	1.049	-0.08	40.25168	-119.1367	127.6	29.7	291.3	59.3
17BS-08_B1	Bob Spring	7935.371	1.036	-0.308	40.25168	-119.1367	94.8	21.6	290.1	67.7
17BS-08_B2	Bob Spring	7258.922	1.061	0	40.25168	-119.1367	111.5	19.1	306.2	70.3
17BS-08_C1	Bob Spring	9611.88	1.035	-0.281	40.25168	-119.1367	123.2	31.3	287.7	57.7
17BS-08_C2	Bob Spring	9928.575	1.026	0.033	40.25168	-119.1367	128	24.9	314.5	64.9
17BS-08_C3	Bob Spring	10397.55	1.032	-0.289	40.25168	-119.1367	145.5	37	279.3	42.6
17BS-08_C4	Bob Spring	11235.89	1.039	-0.789	40.25168	-119.1367	157	29.7	295.1	52.5
17BS-08_D1	Bob Spring	12083.29	1.033	-0.821	40.25168	-119.1367	99.9	36.9	282.7	53
17BS-08_D2	Bob Spring	11968.26	1.018	0.557	40.25168	-119.1367	147.6	47.8	339.3	41.6
17BS-08_D3	Bob Spring	10495.47	1.041	0.091	40.25168	-119.1367	104.4	23.9	336.5	54.3
17BS-08_E1	Bob Spring	9559.688	1.027	-0.209	40.25168	-119.1367	151	20.9	280.7	59.1
17BS-08_E2	Bob Spring	10352.71	1.049	-0.11	40.25168	-119.1367	36.4	33.6	268.3	43
17BS-08_E3	Bob Spring	11245.62	1.02	-0.347	40.25168	-119.1367	76.1	28	309.1	48.5

17BS-08_E4	Bob Spring	9496.321	1.03	-0.331	40.25168	-119.1367	107.3	35.4	280	54.4
17BS-08_F1	Bob Spring	10343.3	1.033	-0.478	40.25168	-119.1367	169.6	20.2	285.4	49.8
17BS-08_F2	Bob Spring	10978.14	1.024	0.171	40.25168	-119.1367	70.1	5.8	330.7	58.2
17BS-08_F3	Bob Spring	10863.1	1.025	0.192	40.25168	-119.1367	95	13	232.2	72.5
17BS-08_F4	Bob Spring	10648.99	1.033	-0.674	40.25168	-119.1367	169.2	29.9	310.7	53.7
17BS-08_F5	Bob Spring	10645.41	1.026	-0.28	40.25168	-119.1367	74.7	27.7	301.6	52.4
17BS-08_G1	Bob Spring	12021.85	1.041	-0.053	40.25168	-119.1367	102.3	36.8	306.1	50.7
17BS-08_G2	Bob Spring	9465.835	1.026	-0.54	40.25168	-119.1367	128.3	27	270.2	57
17BS-08_G4	Bob Spring	9339.287	1.023	0.043	40.25168	-119.1367	79.9	26.1	309.2	53.1
17BS-08_H1	Bob Spring	8663.058	1.039	-0.508	40.25168	-119.1367	115.4	15.7	292.8	74.3
17BS-12_A	Bob Spring	9043.276	1.022	0.628	40.06974	-119.10403	129	20.4	231.8	30.7
17BS-12_B	Bob Spring	7620.73	1.062	0.787	40.06974	-119.10403	144.4	10.7	259.1	65.7
17BS-12_C	Bob Spring	10378.98	1.024	0.547	40.06974	-119.10403	242.2	4.4	333	9.5
17BS-12_D	Bob Spring	11035.16	1.043	-0.17	40.06974	-119.10403	242.1	21.9	128.5	44.9
17BS-12_E	Bob Spring	10203.04	1.047	-0.686	40.06974	-119.10403	106.2	7	202.6	42.4
17BS-12_F	Bob Spring	9285.063	1.043	0.083	40.06974	-119.10403	51	44.5	199.2	40.9
17BS-12_G1	Bob Spring	10818.97	1.032	0.446	40.06974	-119.10403	262.1	5.5	354.2	21
17BS-12_G2	Bob Spring	10073.83	1.016	0.242	40.06974	-119.10403	90.9	39.4	352.7	9.9
17BS-12_H	Bob Spring	12557.03	1.056	-0.223	40.06974	-119.10403	119	19	225.1	38.9
17BS-15_A	Bob Spring	20264	1.045	0.464	40.1552	-119.23522	116.8	52.6	216.5	7.3
17BS-15_B	Bob Spring	15735.64	1.027	-0.083	40.1552	-119.23522	103.7	24.2	238.9	57.6
17BS-15_C1	Bob Spring	20491.68	1.037	0.095	40.1552	-119.23522	11.4	45.2	185.5	44.7
17BS-15_C2	Bob Spring	17392.53	1.064	-0.191	40.1552	-119.23522	89.1	19.8	307	65.5
17BS-15_D1	Bob Spring	18893.54	1.087	0.288	40.1552	-119.23522	300.3	34.6	195.3	20.5
17BS-15_D2	Bob Spring	15963.93	1.062	0.177	40.1552	-119.23522	94.8	27.6	194.1	17.2
17BS-15_E	Bob Spring	20556.64	1.047	0.512	40.1552	-119.23522	84.1	31	180.4	10.4
17BS-15_F	Bob Spring	19080.33	1.05	0.163	40.1552	-119.23522	240.6	25.3	91.5	61.1
17BS-15_G1	Bob Spring	21391.63	1.083	0.117	40.1552	-119.23522	106.4	22.3	266.9	66.5
17BS-15_H	Bob Spring	19091.44	1.047	0.759	40.1552	-119.23522	97.6	19	196.1	23.1
17BS-15_I	Bob Spring	21173.96	1.048	0.778	40.1552	-119.23522	110.8	31.1	241.3	47.1
17BS-16_A1	Bob Spring	18003.87	1.03	-0.024	40.17182	-119.13883	3.5	41.7	132.2	35.1
17BS-16_A2	Bob Spring	17439.87	1.038	-0.014	40.17182	-119.13883	353.7	51.5	97.8	11
17BS-16_B	Bob Spring	14979.71	1.018	0.114	40.17182	-119.13883	73.6	49	186	18.4
17BS-16_C	Bob Spring	21444.02	1.024	0.08	40.17182	-119.13883	340.3	23.4	104.5	52.3
17BS-16_D1	Bob Spring	14423.03	1.027	0.077	40.17182	-119.13883	237.6	44.5	11.3	35.1
17BS-16_D2	Bob Spring	14501.83	1.04	0.214	40.17182	-119.13883	272	32.3	6.6	7.2
17BS-16_E	Bob Spring	19648	1.049	0.762	40.17182	-119.13883	276.4	56.4	120.9	31.2
17BS-16_F	Bob Spring	17997.27	1.04	0.104	40.17182	-119.13883	351.8	52.7	152.7	35.8
17BS-16_G	Bob Spring	21922.57	1.082	0.39	40.17182	-119.13883	356.6	41.8	92.6	6.7

17BS-18_A	Bob Spring	18754.33	1.079	-0.083	40.2536	-119.08576	199.2	48.9	23	41
17BS-18_B1	Bob Spring	18167.38	1.081	0.299	40.2536	-119.08576	139.3	60.6	14.2	18
17BS-18_C	Bob Spring	18151.65	1.073	-0.047	40.2536	-119.08576	127.2	52.6	15.6	15.7
17BS-18_D	Bob Spring	19214.7	1.074	0.125	40.2536	-119.08576	122.6	43.3	20.2	12.9
17BS-18_E	Bob Spring	19520.15	1.076	0.071	40.2536	-119.08576	202.1	57.4	36.6	31.8
17BS-18_F	Bob Spring	18957.16	1.071	-0.074	40.2536	-119.08576	136.4	45.7	36.1	9.9
17BS-18_G	Bob Spring	16774.01	1.074	-0.023	40.2536	-119.08576	160.8	60.8	33.6	18.7
17BS-19_A1	Bob Spring	12734.71	1.035	-0.056	40.19655	-119.19272	149.5	5.8	58.1	13.3
17BS-19_A2	Bob Spring	11569.43	1.03	0.024	40.19655	-119.19272	324.6	7.6	60.2	36.3
17BS-19_A3	Bob Spring	10051.86	1.047	-0.501	40.19655	-119.19272	333.7	3.7	64.4	10.6
17BS-19_B1	Bob Spring	13670.82	1.03	-0.475	40.19655	-119.19272	336.3	18.9	70.6	12.4
17BS-19_C	Bob Spring	12914.19	1.057	-0.456	40.19655	-119.19272	315.7	40.3	63.3	19.5
17BS-19_D1	Bob Spring	17722.6	1.044	-0.109	40.19655	-119.19272	305.2	25.7	56.7	37.3
17BS-19_E1	Bob Spring	14277.33	1.056	-0.162	40.19655	-119.19272	324.5	30	73.9	30
17BS-19_F	Bob Spring	16405.98	1.051	-0.171	40.19655	-119.19272	305.9	36.1	59.2	28.6
17BS-19_G1	Bob Spring	15894.68	1.042	-0.427	40.19655	-119.19272	313.5	19.2	59.9	39
17BS-19_G2	Bob Spring	15002.93	1.044	-0.139	40.19655	-119.19272	310.3	23.3	55.9	32
17BS-19_H	Bob Spring	17280.65	1.044	-0.192	40.19655	-119.19272	303.8	39.8	61.8	29.4
17BS-19_I1	Bob Spring	11641.28	1.037	-0.206	40.19655	-119.19272	304.1	25.5	43.9	19.5
17BS-19_I2	Bob Spring	10095.39	1.045	-0.288	40.19655	-119.19272	118.4	5.6	209.2	8.2
17BS-1B_A1	Bob Spring	45.99542	1.037	0.568	40.22753	-119.14187	198.1	4.2	292.5	46.6
17BS-1B_A2	Bob Spring	36.73918	1.019	0.169	40.22753	-119.14187	24.6	0.6	294	44.3
17BS-1B_B2	Bob Spring	140.5524	1.019	-0.246	40.22753	-119.14187	195.6	12.4	329.4	72.4
17BS-1B_C3	Bob Spring	57.83371	1.016	0.235	40.22753	-119.14187	331.9	25.4	132.5	63.2
17BS-1B_D1	Bob Spring	34.92197	1.015	0.531	40.22753	-119.14187	322.2	39.4	129	49.9
17BS-1B_D2	Bob Spring	32.93632	1.012	0.365	40.22753	-119.14187	294.9	33.3	179.4	33.3
17BS-1B_D3	Bob Spring	44.26745	1.024	0.322	40.22753	-119.14187	250.4	56.8	54.1	32.1
17BS-1B_E	Bob Spring	60.01459	1.012	0.515	40.22753	-119.14187	317.3	15.9	199.3	58.8
17BS-1B_E2	Bob Spring	67.13338	1.01	0.353	40.22753	-119.14187	314.3	8.1	46.7	16.2
17BS-1B_E3	Bob Spring	66.57249	1.008	0.287	40.22753	-119.14187	150.7	1.5	58	61.8
17BS-1B_F2	Bob Spring	47.23462	1.013	0.649	40.22753	-119.14187	138	19.5	342.7	68.7
17BS-1B_F3	Bob Spring	46.9333	1.006	0.022	40.22753	-119.14187	188.6	19.4	57.2	61.9
17BS-20_A	Bob Spring	4731.007	1.128	0.728	40.21176	-119.23869	337.4	13.6	244.7	11
17BS-20_B	Bob Spring	4754.894	1.119	0.263	40.21176	-119.23869	7.8	16.4	110.6	37
17BS-20_C	Bob Spring	4095.804	1.131	0.399	40.21176	-119.23869	154.9	1.5	254.3	80.8
17BS-20_E2	Bob Spring	5697.874	1.132	0.11	40.21176	-119.23869	326.2	4.8	232.3	39.1
17BS-20_F1	Bob Spring	4372.625	1.079	-0.114	40.21176	-119.23869	4.7	53.1	232.6	26.7
17BS-20_G1	Bob Spring	5002.876	1.088	0.069	40.21176	-119.23869	288.3	49	27.1	7.6
17BS-20_G2	Bob Spring	6045.81	1.082	0.253	40.21176	-119.23869	329.5	67.2	142.5	22.7

17BS-20_H1	Bob Spring	4032.595	1.089	-0.119	40.21176	-119.23869	59.4	38.8	203.3	45.2
17BS-20_H2	Bob Spring	5516.872	1.12	0.227	40.21176	-119.23869	163.7	10.7	256.2	13.1
17BS-20_I	Bob Spring	4827.69	1.167	0.393	40.21176	-119.23869	328.2	8.2	236.3	13.1
17JP_19_B	Juniper Pass	15682.27	1.091	0.006	40.20854	-119.17626	263.7	30.3	169.8	6.8
17JP-01_A	Juniper Pass	3446.733	1.146	0.507	40.31255	-119.01728	41	23.1	214.7	66.7
17JP-01_C	Juniper Pass	2331.232	1.135	0.098	40.31255	-119.01728	10.4	13	154.4	74.1
17JP-01_D1	Juniper Pass	4833.845	1.187	0.535	40.31255	-119.01728	192.6	4.5	312.7	81
17JP-01_D2	Juniper Pass	6046.77	1.235	0.243	40.31255	-119.01728	189	2.3	299.3	83.3
17JP-01_E1	Juniper Pass	6179.852	1.208	0.119	40.31255	-119.01728	200	15.8	55.3	70.8
17JP-01_F	Juniper Pass	4261.931	1.112	0.528	40.31255	-119.01728	172.1	16.6	14.9	72
17JP-01_G	Juniper Pass	6077.869	1.229	0.176	40.31255	-119.01728	338	29.8	139.9	58.9
17JP-03_A1	Juniper Pass	2902.428	1.192	0.514	40.24493	-119.01244	329.4	41.4	85.4	26.5
17JP-03_A2	Juniper Pass	2711.362	1.081	-0.291	40.24493	-119.01244	309.9	47.4	116.2	41.8
17JP-03_B	Juniper Pass	2523.156	1.071	-0.291	40.24493	-119.01244	276.6	34.2	126.2	52
17JP-03_C	Juniper Pass	4126.559	1.188	0.056	40.24493	-119.01244	33.7	69.4	301.4	0.9
17JP-03_D1	Juniper Pass	2143.482	1.092	-0.159	40.24493	-119.01244	33	63.7	297.7	2.6
17JP-03_D2	Juniper Pass	2706.379	1.146	-0.204	40.24493	-119.01244	33.6	41.3	296.2	8.4
17JP-03_D3	Juniper Pass	2788.811	1.125	-0.525	40.24493	-119.01244	0.5	76.8	95.6	1.2
17JP-03_E1	Juniper Pass	2057.924	1.116	0.612	40.24493	-119.01244	341.1	6.7	73.9	23.2
17JP-03_E2	Juniper Pass	1891.48	1.061	-0.32	40.24493	-119.01244	168.7	11.6	70.7	34.3
17JP-03_F1	Juniper Pass	2700.604	1.103	0.536	40.24493	-119.01244	146.2	2	56	6
17JP-03_F2	Juniper Pass	2653.61	1.14	-0.127	40.24493	-119.01244	327	1.4	57.2	6.9
17JP-03_G	Juniper Pass	1921.264	1.078	0.136	40.24493	-119.01244	139.5	9.8	39	46.5
17JP-03_H	Juniper Pass	2242.501	1.165	-0.601	40.24493	-119.01244	161.6	35.3	340.4	54.7
17JP-05_A	Juniper Pass	7373.938	1.154	0.287	40.3117	-119.01527	200	18.1	71.4	62.3
17JP-05_D1	Juniper Pass	8015.234	1.186	0.852	40.3117	-119.01527	189.8	9.3	280.5	3.8
17JP-05_F	Juniper Pass	8512.729	1.342	0.06	40.3117	-119.01527	193.9	13.4	31.2	76
17JP-05_G	Juniper Pass	8586.613	1.157	0.562	40.3117	-119.01527	182.2	1.3	330.8	88.5
17JP-05_I	Juniper Pass	10091.45	1.292	0.325	40.3117	-119.01527	194	1	100.9	72.7
17JP-06_A	Juniper Pass	10784.94	1.24	0.517	40.3117	-119.01522	359.3	14.2	106.4	49.3
17JP-06_D1	Juniper Pass	12231.88	1.305	0.356	40.3117	-119.01522	356.4	16.9	121.3	62.1
17JP-06_D2	Juniper Pass	9382.468	1.279	0.599	40.3117	-119.01522	11.4	19.4	130.1	53.8
17JP-06_E	Juniper Pass	9384.021	1.24	0.261	40.3117	-119.01522	95.4	20.8	236.7	64.1
17JP-06_F	Juniper Pass	6171.771	1.16	0.2	40.3117	-119.01522	14.9	12.4	118.2	46.2
17JP-06_G	Juniper Pass	4866.748	1.193	0.298	40.3117	-119.01522	7.4	13.3	122.9	61.2
17JP-06_H	Juniper Pass	5370.529	1.256	0.497	40.3117	-119.01522	19.2	15.5	118.2	29.2
17JP-06_I	Juniper Pass	8035.685	1.183	0.497	40.3117	-119.01522	192.5	19.8	283.3	2.2
17JP-06_J	Juniper Pass	11024	1.267	-0.134	40.3117	-119.01522	182.1	50.4	75.9	13
17JP-07_A1	Juniper Pass	13993.09	1.056	0.213	40.06158	-119.09826	231.6	23.1	325.1	8.1

17JP-07_A2	Juniper Pass	14233.15	1.083	-0.391	40.06158	-119.09826	137.7	67	349.4	19.8
17JP-07_B1	Juniper Pass	20438.82	1.076	0.107	40.06158	-119.09826	85.7	54.9	191.7	11
17JP-07_C1	Juniper Pass	14023.54	1.22	-0.273	40.06158	-119.09826	227.7	58.3	57.5	31.3
17JP-07_C2	Juniper Pass	13264.7	1.078	0.174	40.06158	-119.09826	228.2	7.8	321.9	25.6
17JP-07_D1	Juniper Pass	16143.84	1.046	-0.264	40.06158	-119.09826	9.2	62.5	149.5	21.8
17JP-07_D2	Juniper Pass	13312.09	1.07	0.766	40.06158	-119.09826	128.4	50.8	280	35.6
17JP-07_E1	Juniper Pass	16530.07	1.046	0.371	40.06158	-119.09826	288.5	12	187.4	42.1
17JP-07_E2	Juniper Pass	15522.04	1.105	0.445	40.06158	-119.09826	268.8	42.1	130.9	39.3
17JP-07_F1	Juniper Pass	11350.45	1.078	0.588	40.06158	-119.09826	232.6	42.8	51.6	47.2
17JP-07_F2	Juniper Pass	14326.17	1.035	0.596	40.06158	-119.09826	208.7	31.9	16.6	57.5
17JP-07_G	Juniper Pass	19400.92	1.081	-0.322	40.06158	-119.09826	244.3	20.3	347.4	31.4
17JP-07_H	Juniper Pass	16558.1	1.08	-0.172	40.06158	-119.09826	214.1	42.9	340.2	32.4
17JP-07_I	Juniper Pass	10997.45	1.079	0.528	40.06158	-119.09826	332.3	43.8	203.3	33.3
17JP-08_A1	Juniper Pass	15007.64	1.11	-0.225	40.04372	-119.08884	269.9	61.9	68.2	26.4
17JP-08_A2	Juniper Pass	20201.94	1.124	-0.279	40.04372	-119.08884	282.4	62.3	80.9	26
17JP-08_C1	Juniper Pass	17548.32	1.097	0.135	40.04372	-119.08884	144.2	16.3	252.1	46.5
17JP-08_D1	Juniper Pass	12992.33	1.06	0.497	40.04372	-119.08884	136	15.9	256.5	60.8
17JP-08_D2	Juniper Pass	13163.96	1.057	-0.319	40.04372	-119.08884	340	12.2	233.4	52.9
17JP-08_F	Juniper Pass	14223.33	1.147	-0.739	40.04372	-119.08884	117.9	23.7	220.7	26.6
17JP-08_G2	Juniper Pass	9843.422	1.07	-0.17	40.04372	-119.08884	148.6	16.4	253.8	41.6
17JP-08_H	Juniper Pass	10406.51	1.045	0.696	40.04372	-119.08884	323.3	15.2	70.9	48.1
17JP-08_I	Juniper Pass	16142.26	1.123	0.116	40.04372	-119.08884	318	10.2	223.7	22.6
17JP-09_A1	Juniper Pass	16714.25	1.11	0.015	40.03624	-119.08058	244.3	58.2	58.7	31.7
17JP-09_A2	Juniper Pass	17777.53	1.113	0.671	40.03624	-119.08058	195.9	47.9	340.1	36.2
17JP-09_B	Juniper Pass	16968.81	1.123	-0.307	40.03624	-119.08058	166.4	50	333.7	39.3
17JP-09_C	Juniper Pass	14250.56	1.03	0.168	40.03624	-119.08058	166.5	63.1	306.2	21.1
17JP-09_D	Juniper Pass	17304.25	1.055	-0.395	40.03624	-119.08058	144.7	60.8	274.1	19.5
17JP-09_E2	Juniper Pass	17989.85	1.072	0.595	40.03624	-119.08058	32.2	59.4	228.9	29.5
17JP-09_F	Juniper Pass	15299.57	1.113	0.247	40.03624	-119.08058	161.2	43.2	281.9	28.5
17JP-09_H	Juniper Pass	21060.76	1.119	-0.795	40.03624	-119.08058	187.2	21.1	286.1	21.7
17JP-09_I2	Juniper Pass	14818.94	1.025	-0.195	40.03624	-119.08058	196.5	25	68.3	53
17JP-10_A	Juniper Pass	18231.97	1.057	-0.307	40.17198	-119.13931	148.8	80.8	297.4	7.9
17JP-10_B	Juniper Pass	20463.32	1.031	-0.226	40.17198	-119.13931	340.4	66.6	148	22.9
17JP-10_C	Juniper Pass	21095.17	1.04	0.151	40.17198	-119.13931	12.9	76.9	154.6	10.4
17JP-10_E	Juniper Pass	22199.21	1.049	-0.094	40.17198	-119.13931	162.1	70.7	314.4	17.2
17JP-10_F1	Juniper Pass	18029.38	1.067	0.114	40.17198	-119.13931	192.6	69.3	296.9	5.3
17JP-10_F2	Juniper Pass	19371.33	1.042	-0.035	40.17198	-119.13931	199.3	43	105.8	3.7
17JP-10_G	Juniper Pass	18403.36	1.044	-0.658	40.17198	-119.13931	305.2	67.4	134.3	22.3
17JP-10_H	Juniper Pass	22118.12	1.062	0.595	40.17198	-119.13931	167.6	73.3	53.9	6.9

17JP-10_I	Juniper Pass	28400.68	1.125	0.355	40.17198	-119.13931	82.7	87.9	256	2.1
17JP-10_J	Juniper Pass	20451.54	1.047	-0.026	40.17198	-119.13931	159.9	71.2	254.3	1.5
17JP-11_AA	Juniper Pass	12131.19	1.131	-0.48	40.32627	-119.0788	283.3	38.8	182.1	13.7
17JP-11_AB	Juniper Pass	13086.28	1.117	-0.712	40.32627	-119.0788	292.1	45.4	191.1	10.6
17JP-11_AC	Juniper Pass	10328.24	1.115	-0.555	40.32627	-119.0788	100.3	66.3	207.8	7.5
17JP-11_AD	Juniper Pass	10849.77	1.099	-0.754	40.32627	-119.0788	129.6	27.1	21	32
17JP-11_AE	Juniper Pass	12050.52	1.276	-0.798	40.32627	-119.0788	273.2	77.8	14.1	2.3
17JP-11_AF	Juniper Pass	11955.75	1.133	-0.501	40.32627	-119.0788	243.8	78.6	28.4	9.4
17JP-11_AG	Juniper Pass	11071.61	1.104	-0.694	40.32627	-119.0788	312.7	68.4	198	9.4
17JP-11_AH	Juniper Pass	10825.34	1.108	-0.858	40.32627	-119.0788	265.7	77.4	10.6	3.3
17JP-11_AI1	Juniper Pass	9842.907	1.129	-0.213	40.32627	-119.0788	105.1	20.6	199.2	10.8
17JP-11_AI2	Juniper Pass	9932.652	1.109	-0.637	40.32627	-119.0788	133	56.4	14.5	17.5
17JP-11_BA1	Juniper Pass	319.2728	1.111	0.844	40.32627	-119.0788	194.8	53.8	31.1	35.1
17JP-11_BA2	Juniper Pass	303.6537	1.119	0.898	40.32627	-119.0788	188.9	49	41.1	36.4
17JP-11_BD	Juniper Pass	298.3719	1.093	0.676	40.32627	-119.0788	171.4	56	69.6	7.9
17JP-11_BF	Juniper Pass	280.1156	1.088	0.153	40.32627	-119.0788	191.5	20.3	88.8	30.6
17JP-11_BG1	Juniper Pass	610.0256	1.16	0.268	40.32627	-119.0788	146.3	20.8	53.8	6.4
17JP-11_H	Juniper Pass	480.6517	1.162	0.239	40.32627	-119.0788	134.3	39.6	228.4	5
17JP-12_A	Juniper Pass	10566.3	1.105	0.209	40.32406	-119.09029	325.5	12.3	71.3	51.3
17JP-12_B1	Juniper Pass	13823.19	1.144	0.612	40.32406	-119.09029	151.3	1.9	59.3	46.3
17JP-12_B2	Juniper Pass	15552.11	1.183	0.194	40.32406	-119.09029	327.2	8.5	62.5	31.5
17JP-12_C	Juniper Pass	11488.68	1.117	0.33	40.32406	-119.09029	149.4	5.9	57.8	15.1
17JP-12_D2	Juniper Pass	13438.45	1.135	0.374	40.32406	-119.09029	144.2	4.7	52.9	15
17JP-12_E1	Juniper Pass	13742.52	1.122	0.26	40.32406	-119.09029	153.1	10.6	51.3	47.5
17JP-12_E2	Juniper Pass	10586.4	1.117	0.469	40.32406	-119.09029	334.7	0.4	65.4	59.2
17JP-12_F1	Juniper Pass	16334.97	1.179	0.397	40.32406	-119.09029	144.9	3.9	53	26.3
17JP-12_F2	Juniper Pass	15541.38	1.143	0.105	40.32406	-119.09029	146.8	1.6	56.4	14.4
17JP-12_G	Juniper Pass	15584.99	1.154	0.45	40.32406	-119.09029	150.3	23.1	54.2	13.9
17JP-12_H	Juniper Pass	9667.354	1.099	-0.027	40.32406	-119.09029	148.6	16.8	50.2	25.9
17JP-12_I	Juniper Pass	15404.86	1.14	0.219	40.32406	-119.09029	143.1	24.5	44.4	18.4
17JP-13_A	Juniper Pass	2925.564	1.129	0.653	40.27471	-119.01862	9.5	9.3	113.3	55.7
17JP-13_C	Juniper Pass	2537.048	1.109	0.691	40.27471	-119.01862	187.3	0.3	93.1	85.6
17JP-13_D	Juniper Pass	2823.713	1.187	0.642	40.27471	-119.01862	9	3.5	278.2	13.5
17JP-13_E	Juniper Pass	3331.252	1.187	-0.003	40.27471	-119.01862	186.2	25.3	346.2	63.3
17JP-13_F1	Juniper Pass	3907.795	1.252	0.484	40.27471	-119.01862	194.8	43.5	58.5	37.3
17JP-13_F2	Juniper Pass	3787.876	1.154	0.905	40.27471	-119.01862	197.3	37.8	102.7	6
17JP-13_H	Juniper Pass	3203.252	1.101	0.213	40.27471	-119.01862	197.9	16.7	294.7	21.4
17JP-14_A2	Juniper Pass	7606.76	1.195	0.324	40.26164	-119.01897	156	18.1	58	23
17JP-14_B	Juniper Pass	6736.363	1.181	0.52	40.26164	-119.01897	155.5	23.8	57.1	18.4

17JP-14_C2	Juniper Pass	8949.642	1.163	0.723	40.26164	-119.01897	155.8	31.4	43	32.5
17JP-14_D1	Juniper Pass	7458.615	1.21	0.643	40.26164	-119.01897	149.2	23	58.9	0.6
17JP-14_E1	Juniper Pass	6720.896	1.161	0.34	40.26164	-119.01897	156.6	42.8	35.7	28.9
17JP-14_F2	Juniper Pass	6426.317	1.15	0.622	40.26164	-119.01897	145.5	34.2	44.4	15.8
17JP-14_H2	Juniper Pass	2554.428	1.171	0.57	40.26164	-119.01897	165.7	24.6	51.7	41.7
17JP-17_A1	Juniper Pass	18193.81	1.176	0.524	40.29792	-119.03041	128	42.2	30.1	8.7
17JP-17_A2	Juniper Pass	15149.67	1.137	0.456	40.29792	-119.03041	60.4	9.1	163.4	54.7
17JP-17_B	Juniper Pass	12606.73	1.173	0.436	40.29792	-119.03041	345.5	28.8	152	60.5
17JP-17_C	Juniper Pass	14591.87	1.182	0.907	40.29792	-119.03041	2	28.3	139	53.7
17JP-17_D	Juniper Pass	16842.13	1.18	0.207	40.29792	-119.03041	54.6	17.1	262.2	70.8
17JP-17A_A	Juniper Pass	19029.56	1.063	-0.252	40.29792	-119.03041	222.5	3.7	323.8	72.1
17JP-17A_B	Juniper Pass	21174.6	1.072	0.315	40.29792	-119.03041	175.5	2.9	274.3	71.8
17JP-17A_C	Juniper Pass	18657.97	1.07	-0.095	40.29792	-119.03041	61.5	3.3	283.9	85.6
17JP-17A_D1	Juniper Pass	19671.6	1.066	-0.209	40.29792	-119.03041	63.7	11.1	310.9	63.1
17JP-17A_D2	Juniper Pass	11599.06	1.045	-0.129	40.29792	-119.03041	46.6	5.3	292.4	77.2
17JP-19_A1	Juniper Pass	14886.35	1.061	-0.099	40.20854	-119.17626	228.3	36.5	320.5	2.9
17JP-19_A2	Juniper Pass	18170.38	1.078	0.017	40.20854	-119.17626	220.5	21.3	129.8	1.8
17JP-19_C	Juniper Pass	17617.03	1.087	-0.349	40.20854	-119.17626	235.5	24.8	328.1	5.6
17JP-19_D	Juniper Pass	17213.7	1.101	-0.393	40.20854	-119.17626	239.9	25.2	139.3	21.4
17JP-19_E	Juniper Pass	18350.53	1.1	-0.107	40.20854	-119.17626	227.6	27.3	321.9	8.2
17JP-19_F	Juniper Pass	15262.03	1.045	-0.315	40.20854	-119.17626	224.7	45.4	127	7.5
17JP-19_G	Juniper Pass	17254.6	1.078	0.718	40.20854	-119.17626	257	23.2	350.4	7.8
17JP-19_H	Juniper Pass	19885.84	1.124	0.228	40.20854	-119.17626	236.1	25.7	338.4	24
17JP-19_I	Juniper Pass	21926.56	1.107	0.106	40.20854	-119.17626	246.6	27.2	154.3	4.4
17JP-20_A1	Juniper Pass	35652.17	1.38	-0.23	40.21176	-119.23869	41	25.8	165.8	49.8
17JP-20_A2	Juniper Pass	15503.95	1.106	0.442	40.21176	-119.23869	86.8	28.5	186.1	16.6
17JP-20_B	Juniper Pass	13322.42	1.067	-0.696	40.21176	-119.23869	347.4	19.3	100.5	48.1
17JP-20_C	Juniper Pass	15540.09	1.153	-0.183	40.21176	-119.23869	56.3	65.3	230.7	24.6
17JP-20_D	Juniper Pass	11135.43	1.103	0.469	40.21176	-119.23869	51.4	33.7	195.1	50.4
17JP-20_F1	Juniper Pass	18270.76	1.101	0.155	40.21176	-119.23869	49.1	63.1	220.4	26.6
17JP-20_F2	Juniper Pass	13526.4	1.126	0.637	40.21176	-119.23869	97.6	43.5	226.5	33.5
17JP-20_G	Juniper Pass	17221.39	1.137	-0.682	40.21176	-119.23869	59	53	201.5	30.8
17JP-20_H	Juniper Pass	17617.03	1.122	-0.337	40.21176	-119.23869	65.9	51.8	248.6	38.1
17JP-21_C	Juniper Pass	11418.68	1.162	-0.214	40.22417	-119.24273	231.8	14.5	138.6	12.2
17JP-21_D	Juniper Pass	9680.976	1.084	-0.115	40.22417	-119.24273	89.6	67.6	291.1	21
17JP-21_E	Juniper Pass	11647.03	1.148	-0.335	40.22417	-119.24273	163.8	70.9	304.2	15
17JP-21_H	Juniper Pass	12957.89	1.182	-0.099	40.22417	-119.24273	168.7	32.8	262.8	6.4
17JP-21_J	Juniper Pass	11991.13	1.166	-0.528	40.22417	-119.24273	185.1	48.3	327.9	35.4
17JP-21_K	Juniper Pass	13657.6	1.155	-0.312	40.22417	-119.24273	68.7	15.6	304.6	63.5

17JP-22_A1	Juniper Pass	7096.498	1.061	0.467	40.2299	-119.24613	350.3	37.4	145.2	49.8
17JP-22_A2	Juniper Pass	5917.59	1.145	-0.337	40.2299	-119.24613	39.4	37.8	172.6	41.4
17JP-22_B1	Juniper Pass	13064.06	1.086	-0.425	40.2299	-119.24613	126.8	4.1	33.3	40.9
17JP-22_B2	Juniper Pass	8990.197	1.118	0.397	40.2299	-119.24613	49.6	37.7	235.8	52.2
17JP-22_C1	Juniper Pass	18669.79	1.177	-0.455	40.2299	-119.24613	297.7	23.6	140	64.7
17JP-22_C2	Juniper Pass	10657.87	1.18	-0.111	40.2299	-119.24613	275.9	19.5	175.2	27.7
17JP-22_D1	Juniper Pass	11593.8	1.144	0.123	40.2299	-119.24613	222.7	17.7	73.4	69.6
17JP-22_E1	Juniper Pass	5946.062	1.112	0.912	40.2299	-119.24613	44.7	24.9	147.4	25.3
17JP-22_E2	Juniper Pass	5013.868	1.149	-0.626	40.2299	-119.24613	240.7	5.3	144.4	49.7
17JP-22_F1	Juniper Pass	10583.04	1.07	0.473	40.2299	-119.24613	41.9	11.6	191.3	76.6
17JP-22_G1	Juniper Pass	8222.938	1.129	-0.542	40.2299	-119.24613	204.2	0.1	114.1	58.7
17JP-22_G2	Juniper Pass	11327.78	1.075	-0.295	40.2299	-119.24613	18.5	12.6	283.2	22.8
17JP-23_A	Juniper Pass	13438.74	1.114	0.677	40.21189	-119.26315	219.4	58.5	122.9	4
17JP-23_C1	Juniper Pass	17601.4	1.118	0.002	40.21189	-119.26315	236.9	49	99.5	32.6
17JP-23_C2	Juniper Pass	19151.59	1.18	0.135	40.21189	-119.26315	228.7	45.3	97.7	33
17JP-23_D2	Juniper Pass	17247.63	1.187	-0.488	40.21189	-119.26315	243.8	49.1	77	40.2
17JP-23_F2	Juniper Pass	12142.1	1.145	-0.384	40.21189	-119.26315	300.2	66	151.7	20.8
17JP-23_H1	Juniper Pass	19030.29	1.159	0.5	40.21189	-119.26315	221.1	59.9	331.8	11.6
17JP-23_H2	Juniper Pass	23883.01	1.122	-0.239	40.21189	-119.26315	305.1	58.9	79.5	22.9
17JP-23_I	Juniper Pass	11518.61	1.066	-0.272	40.21189	-119.26315	198.6	43.8	88.2	20
17PL-01_A1	Power Line	10343.86	1.144	-0.167	40.14671	-119.29575	157.7	53.8	256.3	6.3
17PL-01_B1	Power Line	8122.419	1.153	0	40.14671	-119.29575	189.7	58.3	88.8	6.7
17PL-01_B2	Power Line	8887.603	1.147	-0.055	40.14671	-119.29575	178	44.9	81.6	6.4
17PL-01_C1	Power Line	16115.68	1.152	-0.242	40.14671	-119.29575	191.3	52.4	84.3	12.7
17PL-01_C2	Power Line	16869.5	1.099	-0.187	40.14671	-119.29575	186.7	48.8	86.9	8.5
17PL-01_C3	Power Line	8384.946	1.15	-0.247	40.14671	-119.29575	175.1	59.8	80	2.9
17PL-01_D1	Power Line	11104.42	1.222	-0.478	40.14671	-119.29575	186.3	41.2	87.7	9.7
17PL-01_D2	Power Line	10064.52	1.153	-0.348	40.14671	-119.29575	194.3	64	86.7	8.4
17PL-01_E1	Power Line	8828.177	1.143	-0.592	40.14671	-119.29575	190.8	60.7	85.8	8.3
17PL-01_E2	Power Line	8479.643	1.169	-0.482	40.14671	-119.29575	182.1	69.6	77.2	5.5
17PL-01_E3	Power Line	8306.032	1.163	-0.218	40.14671	-119.29575	199	66.6	86.1	9.6
17PL-01_F	Power Line	11639.9	1.209	0.171	40.14671	-119.29575	155.6	42.1	267.1	22.1
17PL-01_G	Power Line	8177.146	1.172	-0.147	40.14671	-119.29575	178	52.6	82.3	4.4
17PL-01_H1	Power Line	9136.397	1.158	-0.322	40.14671	-119.29575	162.6	42.6	262.3	10.4
17PL-01_H2	Power Line	8076.281	1.152	0.061	40.14671	-119.29575	169.6	57.2	266.4	4.4
17PL-01_I1	Power Line	7554.279	1.189	-0.262	40.14671	-119.29575	191.6	59.8	92.7	5.1
17PL-01_I2	Power Line	9922.159	1.212	-0.303	40.14671	-119.29575	179	54.2	77.2	8.4
17PL-03_A1	Power Line	362.7666	1.031	-0.097	40.16859	-119.2821	266	22	157.3	38.4
17PL-03_B	Power Line	418.9895	1.035	-0.193	40.16859	-119.2821	262.5	13.6	168	18

17PL-03_C1	Power Line	504.1487	1.029	0.169	40.16859	-119.2821	270.5	28.7	165.9	24.7
17PL-03_C2	Power Line	433.1595	1.033	0.589	40.16859	-119.2821	265.4	26.7	158.9	29.3
17PL-03_D1	Power Line	410.4503	1.048	-0.106	40.16859	-119.2821	86.3	0.6	176.9	45.6
17PL-03_D2	Power Line	437.0313	1.062	0.297	40.16859	-119.2821	74	12	174.7	41.1
17PL-03_E2	Power Line	393.9849	1.051	0.076	40.16859	-119.2821	86.3	5.6	179.2	27.2
17PL-03_F1	Power Line	405.856	1.055	0.379	40.16859	-119.2821	86.5	11.5	185.2	36.6
17PL-03_F2	Power Line	414.4946	1.056	0.128	40.16859	-119.2821	89.4	11.1	189.3	41.2
17PL-03_G1	Power Line	437.4862	1.046	0.25	40.16859	-119.2821	281	24.2	172.3	35.5
17PL-03_G2	Power Line	434.4479	1.047	0.341	40.16859	-119.2821	282.6	23.8	167	44.4
17PL-03_H1	Power Line	396.7832	1.048	0.403	40.16859	-119.2821	273.2	29.1	4.9	3.1
17PL-04_A1	Power Line	99.24356	1.084	-0.226	40.2084	-119.28393	141	60.5	1.8	23.2
17PL-04_B2	Power Line	69.53319	1.089	-0.101	40.2084	-119.28393	147.8	58.1	14.7	23
17PL-04_C	Power Line	85.37498	1.089	-0.193	40.2084	-119.28393	245.1	51.8	358	17
17PL-04_D1	Power Line	80.00133	1.095	-0.378	40.2084	-119.28393	144.4	57.1	15.4	22.2
17PL-04_D2	Power Line	80.35483	1.106	-0.226	40.2084	-119.28393	153	65.8	11.2	19.5
17PL-04_E	Power Line	72.15263	1.109	0.112	40.2084	-119.28393	165.8	60.5	23.1	24.2
17PL-04_H	Power Line	79.59823	1.112	0.053	40.2084	-119.28393	168.6	62.5	20.3	23.9
17PL-05_A	Power Line	9113.487	1.065	-0.425	40.22517	-119.26485	174.9	73.1	31	13.8
17PL-05_B	Power Line	10977.57	1.123	-0.202	40.22517	-119.26485	76	68	209.6	15.5
17PL-05_D	Power Line	9366.06	1.111	-0.416	40.22517	-119.26485	13.7	65.3	235	19.1
17PL-05_E1	Power Line	8133.623	1.074	-0.177	40.22517	-119.26485	358	77.9	217.3	9.4
17PL-05_E2	Power Line	8116.032	1.094	-0.261	40.22517	-119.26485	101.2	73.3	220.9	8.4
17PL-05_F	Power Line	2505.389	1.084	-0.523	40.22517	-119.26485	2.7	5	258.6	70.3
17PL-05_I1	Power Line	6236.13	1.146	-0.225	40.22517	-119.26485	53.4	13.7	321.2	9.1
17PL-05_J	Power Line	7427.674	1.126	-0.196	40.22517	-119.26485	218.2	21	331.6	45.9
17PL-05_K	Power Line	6078.832	1.16	-0.497	40.22517	-119.26485	192.7	18.6	41.1	69.1
17PL-06_A1	Power Line	4054.826	1.178	-0.178	40.20446	-119.27394	173.2	47.9	14	40.2
17PL-06_A2	Power Line	3342.899	1.124	0.031	40.20446	-119.27394	165.5	47.3	45.2	25
17PL-06_B	Power Line	1767.194	1.317	0.814	40.20446	-119.27394	176.9	69.6	18.1	19.1
17PL-06_E	Power Line	4294.198	1.135	0.489	40.20446	-119.27394	183.2	43.8	44	38.3
17PL-07_B	Power Line	1987.939	1.193	0.956	40.18771	-119.27627	237.1	33	114.3	39.8
17PL-07_C	Power Line	3080.534	1.271	-0.005	40.18771	-119.27627	227	53.3	69.1	34.6
17PL-07_D	Power Line	1782.542	1.186	0.478	40.18771	-119.27627	236.1	75.7	139.9	1.6
17PL-07_E	Power Line	2839.498	1.309	0.413	40.18771	-119.27627	225.7	67.3	119.3	6.8
17PL-07_F	Power Line	3632.891	1.43	0.309	40.18771	-119.27627	183.5	59.8	80	7.7
17PL-07_G	Power Line	3270.678	1.332	0.393	40.18771	-119.27627	206.5	54.1	104.4	8.6
17PL-07_H	Power Line	3577.321	1.172	0.063	40.18771	-119.27627	257.4	31.2	144.3	32.8
17PL-08_B	Power Line	189.8399	1.069	-0.232	40.1601	-119.28551	90.1	16	196.9	45.2
17PL-08_C	Power Line	208.5093	1.078	0.073	40.1601	-119.28551	258	7.4	159.9	47.2

17PL-08_D	Power Line	227.677	1.073	-0.198	40.1601	-119.28551	242.5	3.1	150.3	34.6
17PL-08_E	Power Line	218.6738	1.077	-0.454	40.1601	-119.28551	245.8	13.9	142	43.9
17PL-08_F	Power Line	235.9315	1.062	-0.278	40.1601	-119.28551	52.5	30.3	276	51.1
17PL-08_G	Power Line	222.4881	1.067	-0.316	40.1601	-119.28551	63	25.2	294.9	52.7
17PL-08_H	Power Line	225.9427	1.063	-0.099	40.1601	-119.28551	236.5	10.4	134.5	48.6
17PL-09_A	Power Line	274.9508	1.037	-0.443	40.14252	-119.28575	288.6	12.7	24	22.4
17PL-09_B1	Power Line	248.0758	1.046	-0.308	40.14252	-119.28575	289.8	19	31.5	30.6
17PL-09_B2	Power Line	255.4528	1.045	-0.202	40.14252	-119.28575	276.9	36.3	35.5	33.1
17PL-09_C	Power Line	337.1024	1.045	-0.175	40.14252	-119.28575	288.6	30.8	41.3	33
17PL-09_D	Power Line	297.2321	1.041	-0.22	40.14252	-119.28575	287.2	34.2	37.5	27
17PL-09_E	Power Line	344.7009	1.056	0.213	40.14252	-119.28575	282.7	37.8	42.1	32.3
17PL-09_F	Power Line	339.5753	1.045	-0.009	40.14252	-119.28575	277.2	32.6	30	31.2
17PL-09_G	Power Line	309.3916	1.045	0.02	40.14252	-119.28575	290.8	32.2	47.2	35.2
17PL-09_H	Power Line	1081.457	1.107	-0.068	40.14252	-119.28575	289	15.4	29.5	33.6
17PL-10_A1	Power Line	7512.789	1.742	0.361	40.14108	-119.22257	264.1	10.8	92.3	79.1
17PL-10_A2	Power Line	5801.666	1.455	0.43	40.14108	-119.22257	264.7	6.8	105.9	82.7
17PL-10_B1	Power Line	8321.521	1.523	0.316	40.14108	-119.22257	261	11.5	112.9	76.6
17PL-10_B2	Power Line	6551.954	1.622	0.305	40.14108	-119.22257	266.7	11.3	118.4	76.8
17PL-10_C	Power Line	7760.935	1.722	0.34	40.14108	-119.22257	260.8	12.1	87	77.8
17PL-10_D1	Power Line	6552.162	1.5	0.331	40.14108	-119.22257	268.9	13.6	107.7	75.7
17PL-10_D2	Power Line	7733.532	1.509	0.344	40.14108	-119.22257	258.6	13.3	116.5	73.3
17PL-10_D3	Power Line	8764.866	1.674	0.194	40.14108	-119.22257	262.9	14.9	106.1	73.9
17PL-10_E1	Power Line	7385.679	1.594	0.327	40.14108	-119.22257	265.7	11.6	95	78.3
17PL-10_F1	Power Line	6274.728	1.498	0.438	40.14108	-119.22257	271.2	19.8	115.7	68.4
17PL-10_F2	Power Line	5162.656	1.586	0.467	40.14108	-119.22257	264.5	11.2	140.4	70.6
17PL-10_G1	Power Line	7489.247	1.567	0.317	40.14108	-119.22257	254	17.3	130.1	60.8
17PL-10_G2	Power Line	8691.1	1.722	0.393	40.14108	-119.22257	255.6	19.5	132.7	57
17PL-10_H1	Power Line	8507.067	1.578	0.282	40.14108	-119.22257	261.9	16.4	116.7	70.3
17PL-10_H2	Power Line	8424.551	1.538	0.338	40.14108	-119.22257	263.8	19.2	78.1	70.7
17PL-10_I1	Power Line	5457.005	1.537	0.281	40.14108	-119.22257	254.1	14.2	131.4	64.9
17PL-10_I2	Power Line	6667.028	1.49	0.309	40.14108	-119.22257	262.1	18.1	128.5	64.7
17PL-11_A	Power Line	295.5786	1.084	0.479	40.142	-119.22456	219.8	5.6	314.6	40.1
17PL-11_B	Power Line	278.1781	1.099	0.017	40.142	-119.22456	36.9	3	182.5	86.4
17PL-11_C	Power Line	334.0031	1.095	0.577	40.142	-119.22456	234.4	27.3	348.8	38.7
17PL-11_D1	Power Line	340.2776	1.102	0.579	40.142	-119.22456	222.5	7.6	316.6	28.2
17PL-11_D2	Power Line	333.9925	1.099	0.625	40.142	-119.22456	214.1	8.4	310.3	36.3
17PL-11_E	Power Line	317.6603	1.097	0.536	40.142	-119.22456	230.5	17.2	331.7	32.2
17PL-11_F	Power Line	305.2758	1.088	0.438	40.142	-119.22456	39.9	1.5	309.1	26
17PL-11_G	Power Line	303.0289	1.095	0.543	40.142	-119.22456	210.4	1.9	301.9	37.9

17PL-11_H1	Power Line	275.1039	1.08	0.405	40.142	-119.22456	216.5	10.3	316.6	43.8
17PL-11_H2	Power Line	292.7048	1.084	0.309	40.142	-119.22456	221.1	11.7	319.8	36.2
17PL-11_I1	Power Line	267.5283	1.08	0.4	40.142	-119.22456	216.4	7.9	310.9	29.3
17PL-11_I2	Power Line	260.2972	1.075	0.287	40.142	-119.22456	217.9	3.5	309.8	28.1
17PL-12_A1	Power Line	2069.025	1.239	0.519	40.14478	-119.23215	290.9	60.4	110	29.6
17PL-12_A2	Power Line	2005.17	1.244	0.263	40.14478	-119.23215	289.1	64.1	113.6	25.8
17PL-12_B	Power Line	232.893	1.052	0.121	40.14478	-119.23215	261.1	38.2	137.3	35.2
17PL-12_C1	Power Line	210.5058	1.055	0.341	40.14478	-119.23215	243.6	39.6	142.4	13.3
17PL-12_C2	Power Line	169.9455	1.052	0.183	40.14478	-119.23215	238.2	43.4	128.2	19.8
17PL-12_D1	Power Line	208.8072	1.048	0.633	40.14478	-119.23215	246.3	25.2	135.6	37
17PL-12_D2	Power Line	202.3116	1.064	0.727	40.14478	-119.23215	244.1	25	352.9	34.6
17PL-12_D3	Power Line	570.1846	1.146	0.59	40.14478	-119.23215	253.2	42.1	143.8	20.1
17PL-12_E1	Power Line	249.6314	1.073	0.395	40.14478	-119.23215	239.1	26.1	140.4	17.2
17PL-12_E2	Power Line	351.7185	1.08	0.484	40.14478	-119.23215	254.9	29.2	3.2	29.4
17PL-12_F1	Power Line	185.2304	1.046	0.385	40.14478	-119.23215	242.1	48.2	102.8	34.1
17PL-12_F2	Power Line	216.4034	1.105	-0.218	40.14478	-119.23215	253.3	50.8	103	35.3
17PL-12_G	Power Line	227.5291	1.08	0.313	40.14478	-119.23215	316.5	46.5	167.8	39
17PL-12_H1	Power Line	893.5042	1.282	0.585	40.14478	-119.23215	279.6	40.9	108.9	48.7
17PL-12_H2	Power Line	1856.342	1.322	0.396	40.14478	-119.23215	270.7	36.4	119.4	49.9
17PL-13_A	Power Line	76.53304	1.033	0.563	40.13596	-119.23166	221.9	22	108.8	44.2
17PL-13_B1	Power Line	84.24859	1.041	0.303	40.13596	-119.23166	238.1	27	123	39.8
17PL-13_B2	Power Line	86.40188	1.052	0.251	40.13596	-119.23166	227.1	31.2	106.1	40.3
17PL-13_C	Power Line	92.39664	1.043	0.334	40.13596	-119.23166	236.7	37.6	88.9	47.7
17PL-13_D1	Power Line	102.3074	1.049	0.441	40.13596	-119.23166	244	27	106	55.6
17PL-13_D2	Power Line	88.3972	1.053	0.357	40.13596	-119.23166	239.2	29.4	116.5	43.8
17PL-13_E1	Power Line	90.45369	1.048	0.376	40.13596	-119.23166	234.7	29.3	119.6	37.1
17PL-13_E2	Power Line	110.6912	1.048	0.261	40.13596	-119.23166	227.3	26.9	114.8	36.9
17PL-13_F1	Power Line	100.9585	1.051	0.248	40.13596	-119.23166	235.8	22.3	131.4	31.2
17PL-13_F2	Power Line	89.79913	1.06	0.537	40.13596	-119.23166	243.3	26.6	133.7	33.9
17PL-13_G	Power Line	93.93742	1.044	0.43	40.13596	-119.23166	241.8	26.5	121.6	45.3
17PL-13_H	Power Line	85.59188	1.056	0.309	40.13596	-119.23166	15.2	17.5	109.2	12.5
17PL-13_I1	Power Line	99.30115	1.051	0.547	40.13596	-119.23166	221.4	28.7	121.6	17.4
17PL-13_I2	Power Line	102.5669	1.097	0.315	40.13596	-119.23166	214.2	30.8	111.1	20.8
17PL-14_A	Power Line	121.2309	1.119	0.432	40.12524	-119.22968	237.5	44.2	86.2	42
17PL-14_C	Power Line	147.4142	1.114	0.391	40.12524	-119.22968	243.2	6.9	135.6	68.2
17PL-14_D1	Power Line	118.3564	1.123	0.471	40.12524	-119.22968	239.7	28.3	73.6	61
17PL-14_D2	Power Line	138.9657	1.122	0.504	40.12524	-119.22968	239	29.2	86.1	57.9
17PL-14_E	Power Line	130.6071	1.12	0.494	40.12524	-119.22968	227.4	44.3	91.5	36.3
17PL-14_F	Power Line	128.9219	1.102	0.335	40.12524	-119.22968	191.4	54.6	72.5	19

17PL-14_H	Power Line	139.3505	1.105	0.37	40.12524	-119.22968	229.9	14.8	119.9	52.2
17PL-14_I	Power Line	125.1761	1.108	0.488	40.12524	-119.22968	253.3	27.4	114.5	55.4
17PL-15_A	Power Line	108.7987	1.07	0.143	40.12032	-119.23368	317.4	47.8	99.1	35.5
17PL-15_B	Power Line	132.1752	1.064	0.016	40.12032	-119.23368	322.7	47.7	89	28.3
17PL-15_E	Power Line	128.0424	1.073	0.098	40.12032	-119.23368	292.7	43.4	131.9	45
17PL-15_F	Power Line	129.5183	1.07	0.091	40.12032	-119.23368	278.1	46.6	114.2	42.2
17PL-15_H1	Power Line	135.7878	1.068	0.071	40.12032	-119.23368	294.2	30.3	109.2	59.6
17PL-15_H2	Power Line	126.5631	1.065	0.055	40.12032	-119.23368	294.8	28.4	116.3	61.6
17SW_20_H1	Sahwave	12470.43	1.118	0.548	40.11618	-119.07804	96.4	14.4	353.3	41.4
17SW_20_H2	Sahwave	11529.11	1.17	0.37	40.11618	-119.07804	89.7	11.9	355.6	18.9
17SW_20_H3	Sahwave	9295.123	1.132	0.675	40.11618	-119.07804	91.4	14.3	353.1	29.6
17SW_39_G	Sahwave	7002.965	1.06	0.36	40.10519	-119.08795	203.2	53.1	91.7	15.4
17SW-04_B	Sahwave	1053.545	1.076	0.363	40.13213	-119.05626	109.7	5.3	19.2	5.1
17SW-04_C	Sahwave	690.0622	1.047	-0.182	40.13213	-119.05626	263.2	37	35.1	41.5
17SW-04_D1	Sahwave	529.183	1.023	0.613	40.13213	-119.05626	70.8	3.1	336.7	52.8
17SW-04_D2	Sahwave	499.2522	1.032	0.048	40.13213	-119.05626	128	40.2	325.7	48.4
17SW-04_F!	Sahwave	593.6982	1.059	-0.833	40.13213	-119.05626	149.6	12.8	307.6	76.2
17SW-04_F!	Sahwave	591.5352	1.034	-0.161	40.13213	-119.05626	314.7	2.4	47.5	49.3
17SW-04_G	Sahwave	7221.816	1.095	0.587	40.13213	-119.05626	268.7	19.2	18.6	44.4
17SW-04_H1	Sahwave	7834.792	1.092	-0.095	40.13213	-119.05626	122.5	18.8	19.6	33.3
17SW-04_H2	Sahwave	7221.901	1.12	0.635	40.13213	-119.05626	117.6	17.3	26.6	3.1
17SW-05_A1	Sahwave	3139.676	1.036	0.144	40.11961	-119.0611	254.7	13.8	13.7	63.1
17SW-05_B1	Sahwave	3534.759	1.047	0.107	40.11961	-119.0611	83.2	16.6	214.8	65.8
17SW-05_B2	Sahwave	3173.747	1.047	-0.329	40.11961	-119.0611	89.6	22	215.9	55.6
17SW-05_C1	Sahwave	3537.232	1.057	0.033	40.11961	-119.0611	61.7	12.6	291.1	71
17SW-05_D1	Sahwave	3561.96	1.049	0.095	40.11961	-119.0611	242.7	5.3	104.9	82.8
17SW-05_E1	Sahwave	3983.067	1.053	0.264	40.11961	-119.0611	90.7	12.3	186.8	25.9
17SW-05_F2	Sahwave	3327.181	1.037	0.381	40.11961	-119.0611	94.2	20.3	328	57.9
17SW-05_G	Sahwave	3916.427	1.029	0.563	40.11961	-119.0611	29.5	25.8	159.9	53.3
17SW-05_I1	Sahwave	2685.768	1.043	-0.337	40.11961	-119.0611	200.8	12.1	75.2	69.7
17SW-05_K	Sahwave	3639.506	1.058	-0.044	40.11961	-119.0611	87.8	6.4	337.6	71.9
17SW-05_M1	Sahwave	3327.544	1.028	-0.043	40.11961	-119.0611	45.6	5.6	304.9	61.9
17SW-05_N	Sahwave	3582.762	1.035	-0.403	40.11961	-119.0611	79.6	28.5	274.5	60.7
17SW-06_A	Sahwave	2923.559	1.028	-0.091	40.11985	-119.06166	276.6	8.6	43.2	75.8
17SW-06_B	Sahwave	2638.592	1.042	-0.243	40.11985	-119.06166	56.9	26.8	169.9	37.7
17SW-06_C	Sahwave	3039.606	1.049	-0.608	40.11985	-119.06166	271.3	14.5	159.6	55.2
17SW-06_D	Sahwave	3285.132	1.047	0.263	40.11985	-119.06166	240.5	26.6	117	47.8
17SW-06_E	Sahwave	2419.515	1.046	-0.35	40.11985	-119.06166	256.8	24.7	135.6	48.4
17SW-06_F	Sahwave	3172.455	1.035	0.007	40.11985	-119.06166	256	32.6	127.4	44.2

17SW-06_G	Sahwave	642.8112	1.032	0.031	40.11985	-119.06166	191.9	7.2	322.1	78.9
17SW-06_H1	Sahwave	3832.573	1.021	0.041	40.11985	-119.06166	263.7	45.2	150.4	21.5
17SW-06_H2	Sahwave	4349.795	1.044	-0.152	40.11985	-119.06166	234.1	17.5	140.4	11.5
17SW-06_I	Sahwave	3198.197	1.049	0.225	40.11985	-119.06166	231.1	28.9	133.3	13.7
17SW-06_J1	Sahwave	2332.918	1.063	-0.221	40.11985	-119.06166	44.5	6	170.9	80
17SW-06_J2	Sahwave	2164	1.056	-0.418	40.11985	-119.06166	84.5	7.7	264	82.3
17SW-07_A2	Sahwave	4075.898	1.069	-0.103	40.11956	-119.0624	283.9	11.4	191.9	9.8
17SW-07_B	Sahwave	2501.844	1.046	-0.669	40.11956	-119.0624	288.4	11.5	23.1	21.8
17SW-07_C1	Sahwave	5557.341	1.061	0.219	40.11956	-119.0624	61.5	72.3	326.8	1.5
17SW-07_C2	Sahwave	5118.609	1.045	-0.501	40.11956	-119.0624	41.4	76.7	149.5	4.2
17SW-07_E	Sahwave	4459.587	1.042	-0.637	40.11956	-119.0624	230.2	24	53.4	66
17SW-07_J	Sahwave	5505.525	1.053	-0.127	40.11956	-119.0624	332.3	51.3	133.6	37.2
17SW-09_B	Sahwave	7647.197	1.079	0.289	40.11925	-119.06384	257	70.7	106.6	16.9
17SW-09_C	Sahwave	6962.878	1.049	-0.163	40.11925	-119.06384	259.3	85.1	127.8	3.2
17SW-09_D	Sahwave	7322.194	1.051	-0.103	40.11925	-119.06384	255.1	65.8	135	12.7
17SW-09_E	Sahwave	7267.19	1.066	0.145	40.11925	-119.06384	247.4	56.4	133.2	15.2
17SW-09_F	Sahwave	8161.216	1.084	0.039	40.11925	-119.06384	224	80.9	117.6	2.6
17SW-09_G	Sahwave	7808.322	1.067	0.682	40.11925	-119.06384	14.3	68	267	6.8
17SW-09_H	Sahwave	6956.143	1.078	0.39	40.11925	-119.06384	238.8	75.1	138.6	2.7
17SW-09_I	Sahwave	7889.848	1.064	0.129	40.11925	-119.06384	252.2	77.1	124.5	8
17SW-09_J	Sahwave	8402.964	1.123	0.599	40.11925	-119.06384	272.2	76.4	16.2	3.3
17SW-09_K	Sahwave	7959.14	1.067	-0.405	40.11925	-119.06384	265.8	63.8	139.3	16.3
17SW-10_A2	Sahwave	8327.694	1.052	-0.445	40.11875	-119.06453	260.2	52	39.3	30.5
17SW-10_F1	Sahwave	3262.127	1.044	0.122	40.11875	-119.06453	279.7	25.8	17.8	16.2
17SW-10_G1	Sahwave	9493.483	1.062	-0.407	40.11875	-119.06453	314.1	36.3	64.9	25.8
17SW-10_I1	Sahwave	5239.917	1.033	-0.185	40.11875	-119.06453	230.9	37.6	131	12.7
17SW-12_A1	Sahwave	5441.652	1.076	0.431	40.11876	-119.06667	287.8	45.4	19.7	1.9
17SW-12_C1	Sahwave	4017.592	1.069	0.041	40.11876	-119.06667	315.3	28.2	47.7	4.5
17SW-12_C2	Sahwave	6602.514	1.105	0.323	40.11876	-119.06667	298.9	48.9	58.6	23.3
17SW-12_D1	Sahwave	6931.648	1.094	0.543	40.11876	-119.06667	306.8	5.5	216.3	4.9
17SW-12_E2	Sahwave	6934.596	1.07	-0.315	40.11876	-119.06667	290.4	50.3	43.4	17.9
17SW-12_I1	Sahwave	6152.773	1.1	0.413	40.11876	-119.06667	275.9	28.4	21.1	26
17SW-12_J1	Sahwave	5613.541	1.091	0.427	40.11876	-119.06667	282.6	57.1	29.7	10.8
17SW-12_J2	Sahwave	5438.861	1.097	0.298	40.11876	-119.06667	283.2	46	71.9	39.5
17SW-12_K1	Sahwave	6951.89	1.1	0.107	40.11876	-119.06667	273.5	38.7	26.2	25.8
17SW-12_K2	Sahwave	6072.135	1.08	0.652	40.11876	-119.06667	296.3	59.3	205.2	0.7
17SW-13_A	Sahwave	15011.48	1.177	0.765	40.11888	-119.06945	119	11.4	25.9	15
17SW-13_C	Sahwave	5429.374	1.072	-0.061	40.11888	-119.06945	66.8	15.4	333.5	11.7
17SW-13_D	Sahwave	8047.473	1.083	0.369	40.11888	-119.06945	290	39.1	198.7	1.7

17SW-13_E	Sahwave	8112.28	1.042	-0.468	40.11888	-119.06945	27.9	45.6	154.4	30.2
17SW-13_F	Sahwave	12553.31	1.179	0.469	40.11888	-119.06945	73.4	9.8	323	63.5
17SW-13_G	Sahwave	10375.69	1.035	-0.044	40.11888	-119.06945	56.1	7.7	319.3	41.2
17SW-13_H	Sahwave	11692.77	1.111	0.356	40.11888	-119.06945	356.2	22.7	90.4	9.9
17SW-14_D1	Sahwave	3951.276	1.038	-0.287	40.11765	-119.0752	14.8	42.3	134.9	28.8
17SW-14_G1	Sahwave	15354.05	1.136	0.31	40.11835	-119.07101	288.7	15.6	23.7	17.3
17SW-14_G2	Sahwave	14261.96	1.142	0.441	40.11835	-119.07101	282.9	16.6	18.4	17.7
17SW-14_H2	Sahwave	11484.71	1.128	0.022	40.11835	-119.07101	127.7	32.9	346.6	50.3
17SW-14_J	Sahwave	13161.27	1.143	0.328	40.11835	-119.07101	294.7	10.9	33.1	37.2
17SW-14_K1	Sahwave	11500.21	1.115	0.44	40.11835	-119.07101	134.9	17.9	33.7	31.1
17SW-14_K2	Sahwave	11726.44	1.095	0.147	40.11835	-119.07101	126.6	11.4	33.9	13
17SW-15_B	Sahwave	5874.651	1.078	0.148	40.13118	-119.06364	299	4.4	31.5	30.5
17SW-15_C1	Sahwave	4784.771	1.125	-0.209	40.13118	-119.06364	280.2	12	23.7	47.8
17SW-15_C2	Sahwave	5459.684	1.117	0.159	40.13118	-119.06364	108.8	2.7	17.3	28.5
17SW-15_D	Sahwave	5722.063	1.077	-0.116	40.13118	-119.06364	293.2	12.2	28.9	24.9
17SW-15_E	Sahwave	6766.036	1.119	-0.29	40.13118	-119.06364	112.3	13.4	20.1	9.4
17SW-15_F	Sahwave	6919.858	1.143	-0.184	40.13118	-119.06364	295.1	5.7	26.9	17.5
17SW-15_G1	Sahwave	6383.918	1.168	-0.249	40.13118	-119.06364	118.2	15.9	21.7	21.8
17SW-15_G2	Sahwave	6283.251	1.098	0.133	40.13118	-119.06364	289.4	11.7	92.2	77.7
17SW-15_H1	Sahwave	6446.067	1.093	0.199	40.13118	-119.06364	125	12.6	31.8	14.1
17SW-15_H2	Sahwave	7051.043	1.093	-0.705	40.13118	-119.06364	277.2	22.9	15.2	18
17SW-15_I	Sahwave	6623.552	1.102	-0.081	40.13118	-119.06364	109.6	37.3	7.7	15.1
17SW-15_J	Sahwave	6207.591	1.104	-0.215	40.13118	-119.06364	109.8	7.7	18.1	12.4
17SW-16_A1	Sahwave	4021.266	1.067	0.371	40.11765	-119.0752	47.7	18.8	147	25.4
17SW-16_A2	Sahwave	3601.186	1.058	0.71	40.11765	-119.0752	53.1	30.9	311.5	18.5
17SW-16_A3	Sahwave	4217.875	1.07	0.129	40.11765	-119.0752	41.5	31.1	154.4	32.9
17SW-16_B	Sahwave	4250.984	1.042	-0.064	40.11765	-119.0752	38.5	43.1	145.8	17.7
17SW-16_C2	Sahwave	4546.189	1.036	0.394	40.11765	-119.0752	226.7	16.1	129.2	24.4
17SW-16_C3	Sahwave	5146.063	1.05	0.243	40.11765	-119.0752	236	9.7	143.4	14.8
17SW-16_E1	Sahwave	2835.77	1.056	-0.064	40.11765	-119.0752	30.6	18	141.9	48.2
17SW-16_F1	Sahwave	3967.808	1.035	0.042	40.11765	-119.0752	235.6	51.4	139.7	4.7
17SW-16_F2	Sahwave	2939.881	1.06	-0.309	40.11765	-119.0752	231.5	32.3	127.7	20.7
17SW-16_G1	Sahwave	3002.568	1.035	0.448	40.11765	-119.0752	270	17.1	0	0
17SW-16_H1	Sahwave	3280.83	1.032	0.238	40.11765	-119.0752	240.6	18.6	335.1	13.1
17SW-16_H4	Sahwave	2293.116	1.029	-0.733	40.11765	-119.0752	8.3	34.4	143.2	45.9
17SW-17_A1	Sahwave	14170.28	1.157	0.5	40.11713	-119.0759	250.6	32.3	68.8	57.7
17SW-17_A2	Sahwave	15841.32	1.153	-0.066	40.11713	-119.0759	287.4	35.3	76.6	50.5
17SW-17_B	Sahwave	14087.72	1.139	0.524	40.11713	-119.0759	242.1	10.1	12.5	74.6
17SW-17_C1	Sahwave	6046.227	1.102	0.191	40.11713	-119.0759	63.5	9.4	209.1	78.7

17SW-17_C2	Sahwave	9733.514	1.069	0.699	40.11713	-119.0759	48.8	15.9	163.8	56
17SW-17_C3	Sahwave	9454.284	1.096	0.118	40.11713	-119.0759	232.8	6.1	130.1	64.3
17SW-17_C4	Sahwave	9239.771	1.142	0.446	40.11713	-119.0759	66.2	9.9	214.6	78.4
17SW-17_D1	Sahwave	10929.64	1.117	0.484	40.11713	-119.0759	245.7	15.2	24.6	70.2
17SW-17_D2	Sahwave	14012.1	1.141	0.071	40.11713	-119.0759	249.4	25.9	17.6	51.9
17SW-17_E1	Sahwave	14389.37	1.136	0.445	40.11713	-119.0759	238.8	23.7	39.7	65.1
17SW-17_E2	Sahwave	13803.64	1.128	0.367	40.11713	-119.0759	245.1	17.9	18.7	64.9
17SW-17_F2	Sahwave	14514.69	1.163	0.635	40.11713	-119.0759	262.7	10.1	0.8	38.5
17SW-17_F3	Sahwave	13504.09	1.145	0.451	40.11713	-119.0759	256.9	4.4	352.9	53.5
17SW-17_G1	Sahwave	14059.52	1.11	0.284	40.11713	-119.0759	246.4	2.6	338.2	34.5
17SW-17_G2	Sahwave	12740.45	1.134	0.533	40.11713	-119.0759	72.2	5.4	336.6	45.6
17SW-17_H2	Sahwave	13869.82	1.124	0.712	40.11713	-119.0759	254	0.1	344.1	41.1
17SW-18_A1	Sahwave	10715.58	1.13	0.288	40.11656	-119.07676	250.7	33.6	39.9	52.3
17SW-18_A2	Sahwave	11142.08	1.15	-0.393	40.11656	-119.07676	241.6	32.7	8.7	43.3
17SW-18_B1	Sahwave	9402.673	1.137	0.465	40.11656	-119.07676	246.4	14.6	9.3	64.4
17SW-18_C1	Sahwave	11555.32	1.147	0.255	40.11656	-119.07676	239.9	23.8	20.4	60.2
17SW-18_C2	Sahwave	7010.184	1.097	0.317	40.11656	-119.07676	249.9	25.3	32.1	59.1
17SW-18_C3	Sahwave	10063.56	1.121	0.105	40.11656	-119.07676	250.9	26.3	26.5	55.4
17SW-18_D1	Sahwave	9759.998	1.105	0.56	40.11656	-119.07676	249.6	29.4	84.4	59.7
17SW-18_D2	Sahwave	7912.401	1.115	0.044	40.11656	-119.07676	237.4	35.5	16.4	46.6
17SW-18_D3	Sahwave	11261.61	1.134	0.654	40.11656	-119.07676	244.2	32.2	43.3	56
17SW-18_E1	Sahwave	10074.43	1.131	0.374	40.11656	-119.07676	270.8	33.8	58.1	51.5
17SW-18_E2	Sahwave	7165.305	1.087	-0.064	40.11656	-119.07676	261.5	37.3	46	46.9
17SW-18_F1	Sahwave	11924.58	1.118	0.329	40.11656	-119.07676	273.8	34.9	40.5	40.6
17SW-18_F1	Sahwave	11227.13	1.139	0.259	40.11656	-119.07676	261.1	35.9	22.3	35.6
17SW-18_F2	Sahwave	12299.17	1.131	-0.14	40.11656	-119.07676	262.7	36.2	42.8	46.4
17SW-18_G1	Sahwave	9405.69	1.106	0.07	40.11656	-119.07676	248.4	41.4	30.1	41.7
17SW-18_G2	Sahwave	10599.48	1.135	0.167	40.11656	-119.07676	259	41.7	43.2	42.3
17SW-18_G3	Sahwave	13246.67	1.181	0.419	40.11656	-119.07676	255.8	42.8	24.2	33.9
17SW-18_H1	Sahwave	13563.76	1.165	0.187	40.11656	-119.07676	22.5	38.2	289.9	3.4
17SW-18_H3	Sahwave	10622.33	1.13	-0.306	40.11656	-119.07676	245.7	38.2	79.1	51.1
17SW-18_H7	Sahwave	11867.34	1.133	0.173	40.11656	-119.07676	241.3	39.4	92.6	46.1
17SW-19_A	Sahwave	14982.88	1.162	0.122	40.11604	-119.07714	260.7	8.9	49.8	79.7
17SW-19_B1	Sahwave	10634.4	1.115	0.462	40.11604	-119.07714	244.6	8.3	142.4	55.3
17SW-19_B2	Sahwave	10184.07	1.091	0.166	40.11604	-119.07714	242.1	8.4	134.3	64
17SW-19_C1	Sahwave	13502.67	1.139	0.529	40.11604	-119.07714	68.7	26.8	206.5	55.7
17SW-19_E1	Sahwave	11121.92	1.121	0.248	40.11604	-119.07714	63.5	8.6	170.7	62.9
17SW-19_E2	Sahwave	10544.42	1.124	0.34	40.11604	-119.07714	73.1	10	175.7	51
17SW-19_F	Sahwave	11985.43	1.175	0.03	40.11604	-119.07714	74.5	26.8	186.4	36.4

17SW-19_G1	Sahwave	9605.639	1.107	-0.039	40.11604	-119.07714	70.3	59.4	281.2	26.9
17SW-19_G2	Sahwave	9908.61	1.101	0.418	40.11604	-119.07714	65.4	45.9	273.2	40.6
17SW-20_A1	Sahwave	11625.22	1.136	0.255	40.11618	-119.07804	76.9	12.4	337.9	35.3
17SW-20_A2	Sahwave	12197.79	1.169	0.581	40.11618	-119.07804	78	5.3	342.8	44.1
17SW-20_B2	Sahwave	11283.3	1.163	0.248	40.11618	-119.07804	82.7	10.2	344.2	39.4
17SW-20_C1	Sahwave	11908.72	1.154	0.746	40.11618	-119.07804	78.6	8.3	346.3	15.6
17SW-20_C2	Sahwave	9990.421	1.152	0.438	40.11618	-119.07804	79.1	11.8	334.7	49.9
17SW-20_C3	Sahwave	12737	1.147	0.381	40.11618	-119.07804	77.8	7.1	343.2	32.9
17SW-20_D1	Sahwave	8527.417	1.109	0.312	40.11618	-119.07804	273.4	35	8.5	7.2
17SW-20_E1	Sahwave	12121.34	1.13	0.226	40.11618	-119.07804	72.3	32.7	326	23.6
17SW-20_F	Sahwave	12239.37	1.144	0.428	40.11618	-119.07804	87.1	23.4	333.2	43.1
17SW-20_G1	Sahwave	11024.13	1.16	0.407	40.11618	-119.07804	136.6	29.6	313.8	60.4
17SW-20_G2	Sahwave	14901.44	1.179	0.312	40.11618	-119.07804	144.4	37.6	324.6	52.4
17SW-22_A2	Sahwave	327.5415	1.022	0.203	40.11381	-119.07126	185	62.1	301.6	13.3
17SW-22_B1	Sahwave	284.0798	1.046	-0.081	40.11381	-119.07126	263.4	53.9	166.5	5
17SW-22_C2	Sahwave	541.6908	1.022	0.53	40.11381	-119.07126	242.9	67.9	336	1.2
17SW-22_D1	Sahwave	209.6642	1.023	-0.089	40.11381	-119.07126	247.4	29.3	94	57.8
17SW-22_E1	Sahwave	194.3872	1.005	0.324	40.11381	-119.07126	264.2	61.2	151.5	12
17SW-22_F1	Sahwave	180.8967	1.011	0.018	40.11381	-119.07126	270	30.2	177.5	4.3
17SW-22_G1	Sahwave	214.7614	1.033	0.156	40.11381	-119.07126	295.1	47	40.5	13.9
17SW-22_H	Sahwave	281.4184	1.046	0.766	40.11381	-119.07126	256.7	16.7	21.3	62.2
17SW-29_A	Sahwave	11666.03	1.14	0.55	40.10995	-119.07747	225.1	37	59.6	52.1
17SW-29_B	Sahwave	13580.59	1.137	0.013	40.10995	-119.07747	242.8	46.1	138.9	13.1
17SW-29_C	Sahwave	13931.29	1.106	0.596	40.10995	-119.07747	238.4	36.2	123.4	30
17SW-29_D	Sahwave	13567.14	1.084	0.514	40.10995	-119.07747	233.2	39	89.2	44.9
17SW-29_E1	Sahwave	14158.97	1.082	0.379	40.10995	-119.07747	225.1	57.6	33	31.9
17SW-29_E2	Sahwave	12975.07	1.107	0.315	40.10995	-119.07747	227.3	53.9	40.2	35.9
17SW-29_F	Sahwave	11487.14	1.06	0.461	40.10995	-119.07747	229.4	22.1	133.6	13.8
17SW-31_A1	Sahwave	12374.12	1.158	0.113	40.10764	-119.08115	231.9	2.7	43.8	87.3
17SW-31_A2	Sahwave	13241.26	1.165	0.516	40.10764	-119.08115	65	3.3	272	86.2
17SW-31_B	Sahwave	13252.54	1.139	0.407	40.10764	-119.08115	241.1	19	46.9	70.4
17SW-31_C	Sahwave	12077.05	1.144	0.145	40.10764	-119.08115	299.5	12.7	48.9	55.8
17SW-31_D	Sahwave	15243.65	1.154	0.442	40.10764	-119.08115	261.9	23.9	16.9	43.6
17SW-31_E	Sahwave	13926.52	1.152	0.225	40.10764	-119.08115	64.2	18.2	306.4	54.9
17SW-31_F	Sahwave	11574.63	1.154	0.419	40.10764	-119.08115	74.8	9.4	331.3	54.6
17SW-31_G	Sahwave	12563.55	1.168	0.35	40.10764	-119.08115	76.8	3.2	341	60.7
17SW-31_H	Sahwave	12571.8	1.147	0.143	40.10764	-119.08115	77.1	3.9	341.6	54.7
17SW-31_I	Sahwave	11311.03	1.108	0.296	40.10764	-119.08115	252	20.6	87.9	68.7
17SW-31_J	Sahwave	11259.42	1.114	0.219	40.10764	-119.08115	254.9	33.8	79.3	56.1

17SW-34_A1	Sahwave	10134.63	1.083	0.158	40.10154	-119.07285	57.1	2.2	324.8	47.1
17SW-34_A2	Sahwave	8126.133	1.072	0.279	40.10154	-119.07285	58.4	14.9	317.7	34.9
17SW-34_B1	Sahwave	9193.659	1.077	0.537	40.10154	-119.07285	34.7	5	124.8	1.1
17SW-34_B2	Sahwave	8673.923	1.097	0.44	40.10154	-119.07285	43.3	14.6	308.1	18.9
17SW-34_C1	Sahwave	9441.854	1.115	0.504	40.10154	-119.07285	42.1	6	304.5	51.5
17SW-34_D1	Sahwave	9330.209	1.091	0.757	40.10154	-119.07285	46.2	12.1	240.1	77.5
17SW-34_E1	Sahwave	9666.934	1.1	0.6	40.10154	-119.07285	49.3	12.7	294.4	61.7
17SW-34_F1	Sahwave	13343.46	1.112	0.42	40.10154	-119.07285	60.2	14.7	282.7	70.5
17SW-34_G1	Sahwave	8865.9	1.069	0.589	40.10154	-119.07285	74.6	1.6	341.4	62.4
17SW-34_G2	Sahwave	9871.413	1.066	0.684	40.10154	-119.07285	254.1	2.2	355.2	78.8
17SW-34_H	Sahwave	8524.49	1.083	0.718	40.10154	-119.07285	223.9	4.4	323.1	64.3
17SW-34_I1	Sahwave	11116.11	1.101	0.696	40.10154	-119.07285	239.1	11.3	341.1	46.3
17SW-34_I2	Sahwave	8612.72	1.07	0.215	40.10154	-119.07285	238.9	7.4	333.4	31.5
17SW-36_A1	Sahwave	15805.32	1.174	-0.049	40.10282	-119.07223	205.9	17.6	7.4	71.5
17SW-36_A3	Sahwave	15450.53	1.139	0.077	40.10282	-119.07223	196	14.5	36.6	74.5
17SW-36_B	Sahwave	14378.77	1.164	0.345	40.10282	-119.07223	227.2	28.2	6.6	54.8
17SW-36_C	Sahwave	19029.81	1.201	0.327	40.10282	-119.07223	229.3	27.1	37.7	62.5
17SW-36_C2	Sahwave	13076.25	1.186	0.225	40.10282	-119.07223	229.4	20.6	0.5	60.2
17SW-36_D	Sahwave	13837.06	1.153	0.426	40.10282	-119.07223	339	68.5	219.2	11.1
17SW-36_F	Sahwave	13090.65	1.148	0.357	40.10282	-119.07223	30.9	20.5	212.2	69.5
17SW-37_A1	Sahwave	15636.27	1.111	0.473	40.1049	-119.07403	342.1	6.2	222.2	77.7
17SW-37_A2	Sahwave	15280.59	1.103	0.536	40.1049	-119.07403	338.9	2.1	72.4	59.4
17SW-37_B	Sahwave	19562.52	1.13	0.341	40.1049	-119.07403	332.6	12.3	108.3	73
17SW-37_C	Sahwave	16653.7	1.108	0.199	40.1049	-119.07403	329.8	12.7	96.3	69.2
17SW-37_D	Sahwave	14620.58	1.105	0.26	40.1049	-119.07403	323.2	25.6	115.2	61.5
17SW-37_E	Sahwave	14916.98	1.113	0.168	40.1049	-119.07403	340.5	8.3	127.8	80.2
17SW-37_F	Sahwave	11891.63	1.088	0.368	40.1049	-119.07403	356.8	10.5	130.7	75
17SW-37_G	Sahwave	11956.86	1.081	0.534	40.1049	-119.07403	329.8	13.2	70.7	39
17SW-39_A	Sahwave	7082.011	1.054	-0.191	40.10519	-119.08795	229.7	28.3	104.6	46.9
17SW-39_B	Sahwave	7790.563	1.073	0.127	40.10519	-119.08795	215.3	20.5	81.8	61.5
17SW-39_C	Sahwave	7083.67	1.044	0.495	40.10519	-119.08795	217.7	61.2	87.4	19.6
17SW-39_D	Sahwave	5817.948	1.056	0.587	40.10519	-119.08795	209.1	37.6	113.6	7.1
17SW-39_E	Sahwave	7393.458	1.068	0.438	40.10519	-119.08795	203	34.1	48.6	53
17SW-39_F	Sahwave	8202.956	1.047	0.3	40.10519	-119.08795	226.1	34	109	34.1
17SW-40_A1	Sahwave	2654.518	1.055	0.131	40.10452	-119.09306	167.8	19.9	58.6	42.3
17SW-40_A2	Sahwave	3171.676	1.058	0.194	40.10452	-119.09306	162	24.1	50.7	39.1
17SW-40_A3	Sahwave	3474.449	1.074	0.472	40.10452	-119.09306	168.7	24.2	69.8	19.1
17SW-40_B	Sahwave	2529.887	1.06	0.631	40.10452	-119.09306	7.3	2.7	274.8	43.6
17SW-40_C	Sahwave	2381.173	1.073	0.507	40.10452	-119.09306	358.8	14.4	94.2	20.2

17SW-40_D	Sahwave	1873.566	1.061	0.269	40.10452	-119.09306	0.9	4	92.7	24.1
17SW-40_E	Sahwave	1863.839	1.109	0.489	40.10452	-119.09306	25.6	0.8	115.9	24.7
17SW-40_F1	Sahwave	1482.15	1.066	-0.414	40.10452	-119.09306	11.1	0.5	101.9	53.8
17SW-40_F2	Sahwave	3397.328	1.114	0.816	40.10452	-119.09306	33.7	4	125.7	26.4
17SW-40_G	Sahwave	3392.081	1.082	0.276	40.10452	-119.09306	193.1	1.3	102.3	33.6
17SW-40_H	Sahwave	2274.872	1.053	0.532	40.10452	-119.09306	183.4	3.2	89.5	51.3
17SW-40_I	Sahwave	1955.469	1.08	0.454	40.10452	-119.09306	355.9	3.2	263.7	34.8
17SW-41_A1	Sahwave	4063.897	1.029	0.018	40.10126	-119.09812	3.8	20	220.1	65.7
17SW-41_A2	Sahwave	4356.916	1.052	0.165	40.10126	-119.09812	352.1	26.9	87.1	9.6
17SW-41_B	Sahwave	11021.57	1.102	0.403	40.10126	-119.09812	315	14.2	175.6	71.5
17SW-41_C	Sahwave	4111.343	1.02	0.136	40.10126	-119.09812	353.7	0.3	263.6	27.4
17SW-41_D	Sahwave	4788.797	1.022	0.251	40.10126	-119.09812	334.5	33.7	132.6	54.3
17SW-41_E1	Sahwave	3586.39	1.025	-0.296	40.10126	-119.09812	164.5	16.4	62.2	36.1
17SW-41_E2	Sahwave	4773.33	1.029	0.216	40.10126	-119.09812	155.3	13	250.3	20.6
17SW-41_F	Sahwave	3825.025	1.017	0.224	40.10126	-119.09812	182.7	5.1	278	45.7
17SW-41_G1	Sahwave	7611.146	1.028	0.597	40.10126	-119.09812	1	0.3	91.1	23.3
17SW-41_G2	Sahwave	4749.556	1.042	0.354	40.10126	-119.09812	163	6.7	255.5	20.3
17SW-41_H1	Sahwave	3548.574	1.025	-0.175	40.10126	-119.09812	323.2	12.3	57.1	17.3
17SW-41_H2	Sahwave	4262.754	1.026	0.293	40.10126	-119.09812	191.7	3.1	99.1	40
17SW-41_I1	Sahwave	6819.589	1.047	0.682	40.10126	-119.09812	354.2	9.8	87.5	18.1
17SW-41_I2	Sahwave	5080.84	1.028	0.104	40.10126	-119.09812	345.5	22.4	92.8	35.8
17SW-42_A1	Sahwave	9390.412	1.03	-0.279	40.09856	-119.09882	33.1	16	127.9	16.2
17SW-42_B1	Sahwave	7209.503	1.043	-0.3	40.09856	-119.09882	10.8	25.7	274.3	13.2
17SW-42_B2	Sahwave	7647.875	1.057	0.561	40.09856	-119.09882	8.3	47.9	146.8	34.1
17SW-42_C1	Sahwave	8080.06	1.034	-0.291	40.09856	-119.09882	270.2	69.9	136.1	14.3
17SW-42_C2	Sahwave	8400.105	1.043	0.062	40.09856	-119.09882	8.9	56.8	269.4	6.2
17SW-42_D1	Sahwave	7103.67	1.021	0.249	40.09856	-119.09882	351	62.9	111.2	14.4
17SW-42_D2	Sahwave	7584.843	1.059	0.402	40.09856	-119.09882	3.1	33	105.2	17.9
17SW-42_E1	Sahwave	9189.36	1.043	0.079	40.09856	-119.09882	3.8	70.3	129.2	11.7
17SW-42_E2	Sahwave	7993.221	1.043	0.115	40.09856	-119.09882	1	37.9	96.2	6.6
17SW-42_F1	Sahwave	7519.732	1.023	-0.241	40.09856	-119.09882	357.8	56.9	117.4	17.8
17SW-42_F2	Sahwave	8973.461	1.037	0.377	40.09856	-119.09882	352.9	71.6	166.6	18.3
17SW-42_G1	Sahwave	8211.025	1.029	0.392	40.09856	-119.09882	35	13.8	183.7	74
17SW-42_G2	Sahwave	7312.465	1.031	-0.634	40.09856	-119.09882	8.3	56.5	169.8	32.1
17SW-42_H1	Sahwave	8411.593	1.035	-0.291	40.09856	-119.09882	318.5	78.1	142.9	11.9
17SW-44_A	Sahwave	6229.603	1.044	0.451	40.10035	-119.0715	217.6	29.6	95.6	43.1
17SW-44_B	Sahwave	10352.08	1.065	0.352	40.10035	-119.0715	157.1	34.7	41.7	31.8
17SW-44_C	Sahwave	10073.83	1.08	0.367	40.10035	-119.0715	193	28.1	89.7	23.3
17SW-44_D1	Sahwave	9919.056	1.088	0.106	40.10035	-119.0715	206.6	46	91.2	22.5

17SW-44_D2	Sahwave	9952.13	1.081	0.044	40.10035	-119.0715	202.6	48.6	76	27.7
17SW-44_E1	Sahwave	9474.482	1.075	0.542	40.10035	-119.0715	201.7	32.8	82.8	36.8
17SW-44_E2	Sahwave	7554.979	1.074	0.297	40.10035	-119.0715	193.8	35.8	89.7	18.7
17SW-44_F1	Sahwave	9684.872	1.076	0.074	40.10035	-119.0715	205.9	26.7	106.7	17.8
17SW-44_G1	Sahwave	8746.053	1.059	0.199	40.10035	-119.0715	229.6	41	82	44.1
17SW-44_G2	Sahwave	9713.973	1.067	-0.276	40.10035	-119.0715	199.2	23.2	85.5	43.2
17SW-45_C	Sahwave	3320.708	1.056	-0.135	40.10033	-119.10853	232.6	60.1	43.9	29.6
17SW-45_D1	Sahwave	3761.095	1.035	0.266	40.10033	-119.10853	176.8	52.2	13.6	36.6
17SW-45_D2	Sahwave	3109.593	1.047	-0.084	40.10033	-119.10853	184.9	68.2	43.3	17.4
17SW-45_E	Sahwave	3490.906	1.05	-0.089	40.10033	-119.10853	238.9	28	11.8	52
17SW-45_F	Sahwave	3205.274	1.079	0.57	40.10033	-119.10853	223.1	46.2	119.5	12.7
17SW-45_G	Sahwave	2989.332	1.028	0.417	40.10033	-119.10853	227.4	67.4	104	12.9
17SW-45_H	Sahwave	3796.638	1.062	0.136	40.10033	-119.10853	293.6	62.5	196.8	3.5